Wrocław University of Science and Technology

CSIC
Consejo Superior de Investigaciones Científicas

Doctoral thesis

Modified graphene materials for electrochemical sensing applications

Modyfikowane materiały grafenowe do zastosowania w sensorach elektrochemicznych

Daria Minta

Supervisor:

Prof. dr hab. inż. Grażyna Gryglewicz, Wrocław University of Science and Technology

Assistant Supervisor:

Dr Zoraida González, Insituto de Ciencia y Tecnología del Carbono, INCAR-CSIC, Oviedo (Spain)

Wrocław 2023

I would like to express my deepest appreciation to Supervisor Prof. Grażyna Gryglewicz for invaluable contribution into my research career and creation of this thesis, helpful and practical advice and huge amount of time spent on valuable discussions on new ideas. I would also like to extend my deepest gratitude to Co-supervisor Dr Zoraida Gonzalez for profound belief in my work, practical and insightful suggestions and time spent on creation new ideas.

I'm extremely grateful to my parents, Alicja and Dariusz for giving me possibility to develop my passions on every level of my education route and my fiancée Piotr for tremendous support and motivation during this PhD journey. I'd also like to extend my gratitude to my sister Agnieszka and grandmother Halina for their unvavering support.

I could have not to forget to thank my lab colleagues: Karolina, Iza, Gosia, Kasia, Natalia, Denis, Bartek, Aleksander, whom I would like to thank for many hours of supportive conversations and substantive support in solving scientific problems.

I also had great pleasure of working in two scientific groups: at Wrocław University of Science and Technology and at the Institute of Carbon Science and Technology, I would like to thank all members of this groups for pleasant environment for learning and support in developing my scientific knowledge.

Table of content

1 Introduction

In the last years, a great research interest for an easy detection of a wide range of analytes has markedly raised. Scientists are seeking for highly sensitive and selective techniques for the control and monitoring of biomolecules, water pollutants and many other compounds with potential negative impact on human life and environment. One of the potential approaches which enables performing measurements quickly, with high sensitivity, selectivity and applying non-complicated measurement setups is electrochemical detection [1,2]. In this context, great efforts are being carried out to propose electrochemical sensors with enhanced working parameters such as limit of detection (LOD) or working linear range (LR). To achieve improved sensor working parameters different bare and/or modified working electrodes are being proposed.

Nowadays, among the extensive of available electrode modifiers, graphene-related materials and their composites are being widely assessed, due to their unique properties. Graphene, isolated in 2004 using mechanical exfoliation of graphite by Geim and Novoselov, is a one-layer 2D material consisted of sp^2 hybridized carbon atoms [3]. It presents, among others, an extremely high electron mobility at room temperature and a high volume to surface ratio, both being the key parameters from the point of view of electrochemical detection [3,4]. Moreover, it has been proved that, in electrochemical detection, the surface chemistry of active materials also plays a crucial role. Graphene offers a tunable surface chemistry, so it is facile to properly functionalize the material structure to make it suitable towards a wide range of analytes detection. Nevertheless, this modification can lead to a decrease of its electrical conductivity. In this context, and to partially restore electrical properties of the material, different strategies are being applied, as deoxygenation, heteroatom doping and preparation of composite materials. In the latter case, metals, metal oxides and their nanoparticles (NPs) appear as promising candidates to be combined with graphene-based materials. NPs can increase the surface area accessible for target analytes attachment. They can also catalyze related redox processes. One the other hand, conducting polymers (CPs) are also under evaluation as suitable electrode modifiers as their long polymeric chains, with functional groups, can enhance the interactions between the electrode surface and the target analyte. In addition, CPs due to their intrinsic electrical conductivity could positively contribute to the electrochemical response of the setup [5].

Previously reported results have led to investigations concerning the preparation of suitable graphene-related materials and derived nanocomposites for successful electrochemical

detection of different target analytes, which is the main goal of this thesis. For this purpose, three groups of active materials are proposed. The starting graphene-based materials, their nanocomposites with metal nanoparticles and conductive polymers have been assessed and compared towards the electrochemical detection of several analytes of interest as dopamine (DA), ascorbic acid (AA) and uric acid (UA). In addition, materials have been also tested towards diclofenac (DCF - water contaminant of emerging concern), providing a new sight into the electrochemical detection of this compound. In addition, a novel concept of sensor based on graphene materials, developed by inkjet-printing technology, is proposed towards DCF monitoring widening the available collection of electrochemical sensing platforms.

2 Literature review

2.1 Target analytes in human healthcare and environmental applications

Nowadays, as a result of the increasing interest on monitoring human health-state and environment protection, there is an urgent need of developing appropriate detection systems for several electroactive analytes as neurotransmitters and water pollutants, respectively. Neurotransmitters are chemical compounds playing a crucial role in the functioning of the central and peripheral nervous systems [6]. Colloquially, they are called “body’s chemical messengers” as they are responsible for signals transfer between neurons through synapses and from nerve cells into gland and muscle cells. Indeed, their main role is transformation of the electric signal into a chemical one. This transition takes place in the synapse which is a bridge between pre- and postsynaptic cells. This process is called neurotransmission [7]. Currently, there are about 100 known neurotransmitters, acting as stimulants or inhibitors. Glutamate, γ-aminobutyric acid, acetylcholine, noradrenaline, dopamine, and serotonin are being the most important ones. In all the cases their excess or deficiency can indicate several disorders and organism malfunctions. At this point it is important to remark that, due to the similar molecular structure of these compounds, and their low concentrations in the human fluids it is highly desirable to detect them with a high sensitivity, selectivity and accuracy [6].

Regarding environmental control and monitoring, electrochemical detection of water pollutants is critical. There is a wide group of these substances such as pesticides, heavy metals, inorganic salts and pharmaceuticals, which in extreme concentrations are devastating for natural habitat [8]. Among them pharmaceuticals or drugs are considered as potentially dangerous and the fastest spreading compounds in the environment due to the fast development of the

pharmaceutical industry. Drugs can end up in the environment as a result of the improper industrial wastewater treatment or their unsuitable recycling by consumers. Moreover, there is a great number of drugs applied in farm animals' treatment. In this way, drugs can be released to environment in the form of excrements, or even at a long time after animal death due to corpse decomposition.

2.1.1 Dopamine (DA) and interfering species

One of the most relevant neurotransmitters in the human body is dopamine (DA). DA is a chemical compound from the family of catecholamines [4]. They consist of a benzene ring with two carboxyl groups and ethylene side chain terminated with an amino group [9]. DA, similarly, to the other neurotransmitters, is synthesized in a two-step process from L-tyrosine (Figure 1) [10]. The first step of DA synthesis is phenylalanine hydroxylation. The product of this reaction – L-tyrosine – is subsequently converted to levodopa which is decarboxylated to DA molecule through an enzymatic reaction [11].

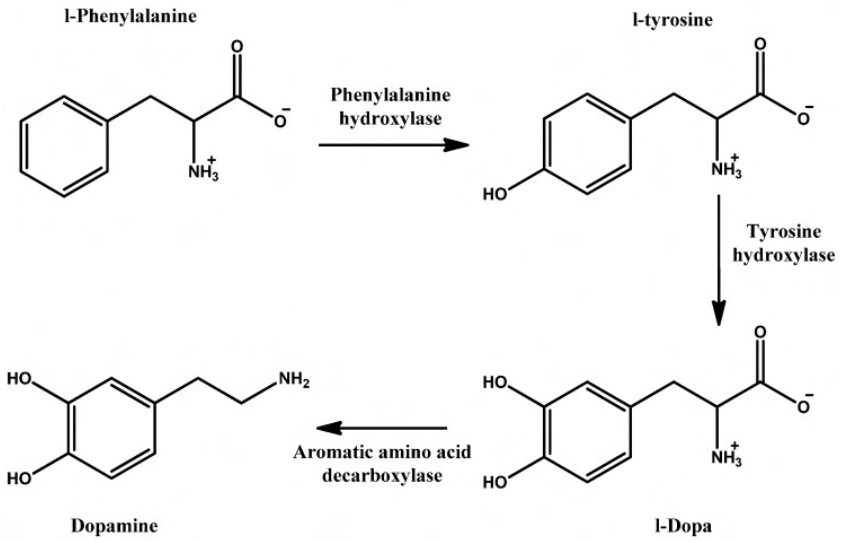

Figure 1. Synthesis route of DA [11].

DA and levodopa molecules, due to their high polarity, cannot move through the lipid membrane and cross the blood-brain barrier (BBB) [12]. Due to this fact DA is mainly synthesized in a nerve terminal, directly responsible for neurotransmitters release, being a part of neuron in a substantia nigra and also in ventral tegmental area and hypothalamus in the central nervous system (CNS) [13–15]. However, there is a protein, large amino acid transporter (LAT), responsible for levodopa transfer through the lipid membrane [16]. Therefore, in the treatment of several diseases levodopa is dosed and then converted into DA.

Depending on the place of localization, DA plays different roles. It takes part directly and indirectly in almost all physiological function in the CNS [17]. In the pyramidal tracts DA is indirectly responsible for movement coordination and muscles tension modulating the activity of basal ganglia [18]. It is well known as pleasure and reward neurotransmitter. In the limbic system DA is related to our emotions connected with reward and aversion [19]. DA occurs also in peripheral nervous systems regulating gastric functions, cardiovascular, hormonal and renal systems. In the hormonal system it acts as inhibitor reducing prolactin release [20].

Both, excess and shortage of DA in the organism have fatal consequences for human health. Moreover, improper levels of DA can indicate that certain disorders occur in the organism. Significant changes of DA levels are observed during the sleep-wake cycle. For example, impoverishment of DA levels can eliminate rapid-eye-movement (REM) phase which subsequently can reduce ability to learn and leads to memory issues [21,22]. Briefly, in schizophrenia the dopaminergic activity in the brain is too high affecting one type of receptors increasing its activity which results in hallucinations and delusions. On the other hand, the low dopaminergic activity in prefrontal cortex and nucleus caudatus results in lower activity of corresponding receptor which provokes misery, demotivation and speaking disorders [23]. Deficiency of DA in Parkinson disease caused by degeneration of neurons in CNS, leads to disorders resulting in stiff movements, which are one of the most characteristic signs of this sickness [24]. Moreover, assessment of DA levels is crucial for depression diagnosis and treatment. Depression is psychiatric disability affecting 3.8 % of population according to Institute of Health Metrics and Evaluation [25,26]. People who suffer from depression usually exhibit symptoms such as anhedonia, lack of motivation, problems with experiencing pleasure. All these signs are the result of a decreased activity of DA receptors in central dopaminergic system [27]. Nevertheless, the above mentioned are only a fragment of disorders related to DA levels. Catecholamine levels are usually measured in the urea. The suitable level of DA referred to the properly functioning organism during standard evaluation including collection of the urine for 24 hours should be below 3300 nmol [28]. One of the proposed quantitative methods of DA detection in human serum, plasma and cell culture supernatants is colorimetric method using Dopamine ELISA kit. However, this set is dedicated only for research application, not for diagnosis. Moreover, a lot of additional equipment and chemicals are required for measurements. These drawbacks combined with the relatively high cost of the test (about £7) and its limited working concentration range hinder the introduction of this kind of test for commercial purpose [29]. Moreover, DA can be monitored using spectroscopic techniques or

high-performance liquid chromatography (HPLC). Both techniques are time-consuming and advanced equipment is necessary to performed measurements.

DA exhibits an electrochemical activity which is beneficial from the point of view of electrochemical detection of this compound. The redox processes ascribed to DA are facile, which makes this analyte suitable for electrochemical detection [30]. Faradaic reactions of DA are shown in Figure 2. The pK_a value of DA is 8.93, therefore if pH value is below 8.93 DA occurs in its cationic form [31]. Firstly, cationic DA specie is reversibly oxidized to o-dopaminoquinone (Figure 2, Reactions I and II) through a two-electron process, resulting in the development of the anodic and cathodic peaks at potential values close to 0.2 and 0.1 V, respectively (vs. Ag/AgCl reference electrode). Part of these o-dopaminoquinone molecules is transformed into leucodopaminochrome by chemical reaction. Then, in another two-electron process leucodopaminochrome is reversibly converted into dopaminochrome leading to development of another pair of related redox peaks at negative potentials (Figure 2, Reactions III and IV) [32,33].

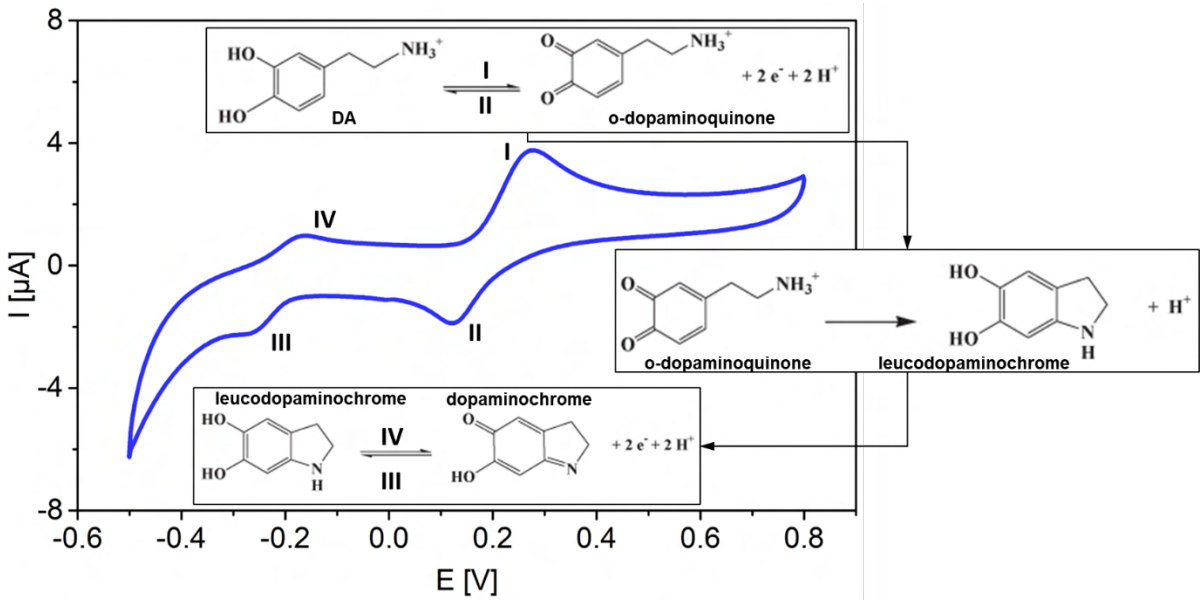

Figure 2. Cyclic voltammogram summarizing the redox processes related to DA electrochemical detection [32].

DA usually coexists in the organism with ascorbic acid (AA) and uric acid (UA), both of them display similar oxidation potentials to that of DA acting as interfering species. That is why it is key to select the most appropriate technique that allows the selective detection of DA.

AA - 2-oxo-L-threo-hexono-1,4-lactone2,3-enediol is an organic substance widely known as vitamin C. Human body is not able to produce AA on its own due to the lack of enzyme (gulonolactone oxidase) which participates in this process [34]. AA is mainly supplied with

natural food products in which it occurs in low amounts. Proper supplementation of AA is crucial for remaining in a good shape since AA is quickly removed from the human body [35]. As stated, AA is involved into a lot of organism actions. AA is one of the most attractive antioxidants playing an important role in a cell functioning. It plays a very important role, among others, in collagen production which is involved in an appropriate functioning of the vascular system lowering the risk of atherogenesis [36]. Moreover, AA occurs in the immediate surroundings of some neurotransmitters, where plays neuro-modulatory functions [37]. It acts in the catecholamines biosynthesis among others as co-factor of the enzyme dopamine-β-hydroxylase [34]. Vitamin C is also applied in a treatment of many diseases for example common cold [38] scurvy [39] and it can also reduce the strength of several allergic reactions [40]. Even though it performs many important functions in the human body, its excess can be also destructive. The suitable amount of AA in human body is in the range between 0.6 – 2 mg/dL [37]. Above this value it can cause side effect as, for example, nausea and digestive stress [41]. Worldwide AA levels are being estimated using HPLC which, as stated before is a suitable and accurate technique. However, several improvements are still required depending on the occurrence and kind of AA to be determined [42].

Electrochemical oxidation of AA is a one-step irreversible process including exchange of two electrons (Figure 3). pK_a value of AA is 4.17, therefore above this value it is in anionic form [43]. The product of oxidation is dehydroascorbic acid. The reaction occurs at the potential value between 0.0 - 0.2 V (vs. Ag/AgCl) [41].

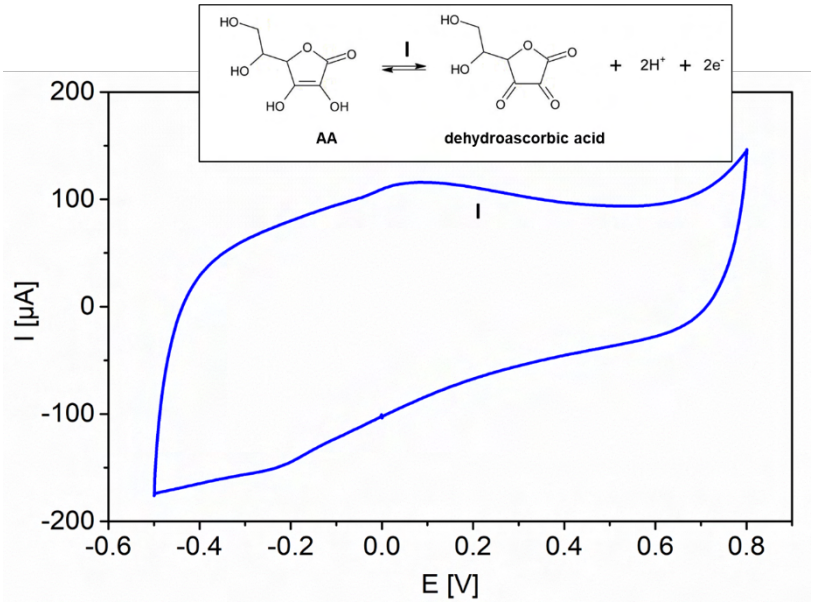

Figure 3. Cyclic voltammogram and reactions characteristic for AA electrochemical detection [41].

As previously mentioned, another interfering compound in the DA detection is 2,6,8-trioxypurine (UA). In the human organism it is a final product of purines decomposition. The beneficial role of UA in the organism has not been discovered so far, nevertheless it is stated that UA shows antioxidant activity [44]. In its regular amounts it is facile excreted from the organism through kidneys in the urine, however its excess can lead to many problems [45]. The reference value of UA in the blood should be in the range between 1.5 to 6.0 mg/dL for woman and 2.5 to 7.0 mg/dL for man. Above this values UA crystals are formed and accumulated in the organism. Deposition of UA in joints and tendons is characteristic among others for gout and Lesch-Nyhan syndrome resulting in a soreness in touch and reduced mobility [43]. At neutral pH value UA is presented in the anionic form due to the pK_a value of 5.75 [43]. Currently the levels of UA in the human body are determined using blood or urine test by means of, among others, colorimetric method even though this methodology can provide an overestimated result. Globally, the most popular methods are spectrophotometry and HPLC, although they are time consuming and require well trained staff [46].

The electrochemical reaction of UA includes a one-step giving oxidation peak at a potential of about 0.4 V (vs. Ag/AgCl) (Figure 4) [43].

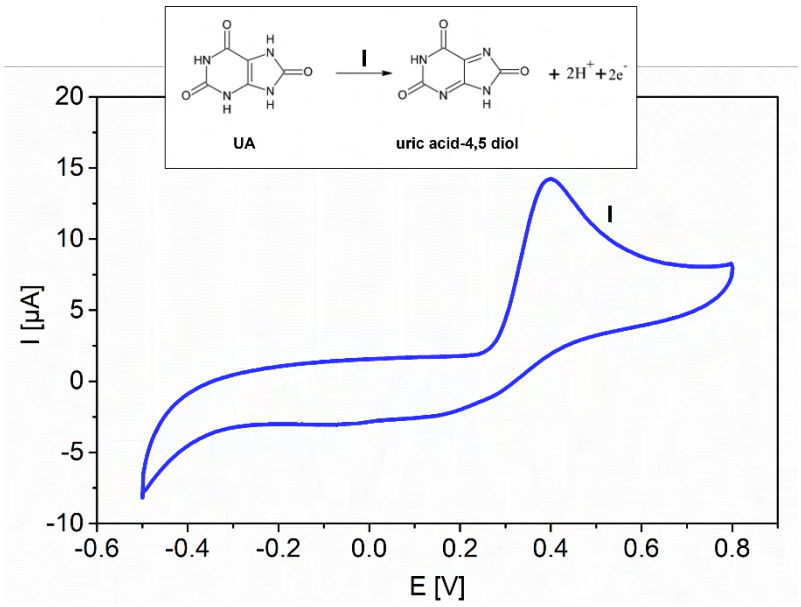

Figure 4. Cyclic voltammogram displaying common faradaic reactions related to UA electrochemical detection [43].

Due to the ease of electrooxidation of above-mentioned molecules and their common presence in the human organism it is highly desirable to detect them using facile electrochemical techniques. However, selectivity and sensitivity drawbacks must be overcome by the development and improvement of electrochemical detection setups.

2.1.2 Diclofenac (DCF)

DCF (2-(2-((2,6-dichlorophenyl) amino) phenyl) acetic acid) is an anti-inflammatory medicine from the group of nonsteroidal drugs (NSAIDs) [47]. Usually, DCF occurs in pharmaceutical products as sodium or potassium salt to increase its solubility [47]. Being a main component of a wide range of commercially available drugs as for example Acoflam, Diclac, Monoflam and Voltaren it is widely applied in the treatment of many disorders such as arthritis or pneumonia [48]. Nevertheless, its overdose has negative impact on the human organism resulting in gastrointestinal disorders or aplastic anemia [47]. Moreover, DCF can contribute to environmental pollution, as the result of improperly post-processing water cleaning or inadequate utilization of medicines by consumers. Thus, due to its low biodegradation, DCF is highly dangerous for the environment even in low concentrations as 1 μg/L [47]. Moreover, utilization of this medicine in a cattle treatment results in its appearance in vultures organisms, with a very negative impact on the population of this specie [49]. In the consequence, there is a high interest on development of an accurate and reliable technique for DCF detection in order to meet EU regulations and protect environment [48]. DCF has been then included in the list of substances which must be monitored in the environment by EU countries [48]. Currently, among available methods for DCF detection spectroscopic, spectrophotometric, fluorimetric, potentiometric and chromatographic technologies are commonly used. Furthermore, commercially available methods accepted by European and United Stated Pharmacopoeias are mainly those based on titration, spectrophotometry and on liquid chromatography (LC). Again, these methodologies are laborious and complex, as they require a multi-step sample preparation procedure [50,51]. At this point, electrochemical techniques also arise as potential alternatives. The electrochemical detection of DCF is a multi-stage process (Figure 5). At neutral pH, DCF is in its anionic form due to the pK_a value of 4.15. In the first step it is oxidized with exchange of one electron. The anodic peak corresponding to this reaction is recorded at 0.6 V (vs. Ag/AgCl). The product of this reaction is then chemically decomposed to 2,6-dichloroaniline and 2,2-hydroxyphenyl acetic acid molecules. The second compound is then reduced (at 0.3 V vs. Ag/AgCl) and in the next cycle reversibly oxidized (at ~0.35 V vs. Ag/AgCl) into the initial form [52].

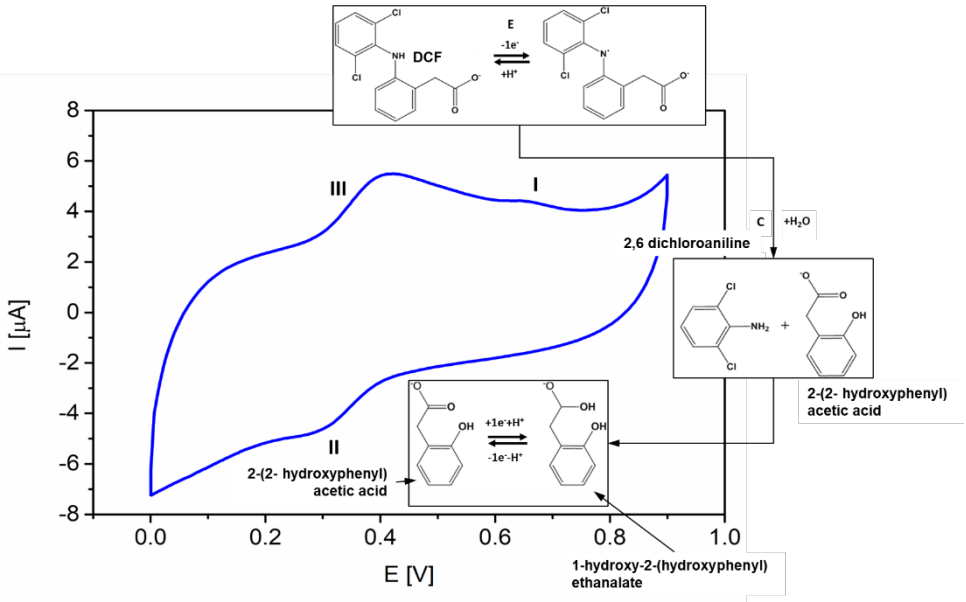

Figure 5. Cyclic voltammogram displaying the faradaic processes related to DCF electrochemical detection [52].

Due to the complex electrochemistry of DCF, it is essential to design and develop novel electrochemical setups which enable its detection following both, a direct and/or non-direct procedure.

2.2 Sensing techniques

Due to the growing demand to control and monitor target analytes in the human body and in the environment, a plenty of detection techniques are being proposed. As previously stated, among currently available DA, its interfering species and water pollutants detection techniques, high performance liquid chromatography (HPLC), different types of chemical sensors based on luminescence, spectroscopy, and nanoplasmonic sensors are commonly used [53–56]. Nevertheless, HPLC suffers from lack of selectivity, low sensitivity, time-consuming sample pre-treatment and need for qualified staff. According to IUPAC, a chemical sensor is "*a device which transforms chemical information, from a chemical reaction of the analyte or from a physical property of the investigated system, into an analytical useful signal*" [57]. As shown in Figure 6, a chemical sensor consists of two basic elements: a chemically selective recognition system (receptor) and a transducer. Besides, there is usually sample delivery unit and electronics containing data processor [58]. The main role of the receptor is the transformation of chemical information into energy, which can be subsequently measured by a transducer. This transducer is responsible for conversion of the measured parameter into useful electrical,

optical, or acoustic signal, which is then amplified and processed into practical data. Thus, the proper selection and combination of receptor/transducer is relevant in the analyte detection. There are two main types of receptors considering trigger signal, i.e., chemical (including biochemical) and physical ones [1,58].

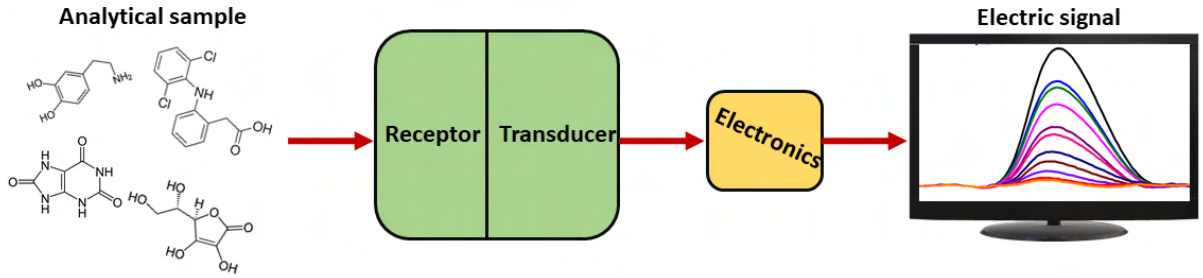

Figure 6. Diagram of operation of a chemical sensor, according to IUPAC.

Thus, they can be classified into thermal, mass, electrochemical, electrical, magnetic and optical, depending on the type of selected transducer [1,58]. Briefly, thermal sensors can be characterized as devices which measure heat effects caused by chemical reactions or adsorption of the analyte. This group involves catalytic sensors and sensors based on optothermal effects. Then, mass-sensitive detectors record the mass change resulting from the accumulation of the analyte on the receptor surface. They can be divided in two groups: piezoelectric and surface acoustic wave devices. The basis of electrochemical sensing is to record electrochemical interactions between the electrode and the analyte and transform them into current or potential. These reactions can occur spontaneously or can be stimulated by an electrical impulse. In contrast, electrical sensor measurement (not being developed electrochemical reactions) is based on the change of electrical properties as a result of interactions between the receptor and the analyte. This group includes metal oxide semiconductor, electronic conductivity and electric permittivity sensors. A wide group of chemical sensing devices is that related to optical sensors which are based on the changes of the optical effects resulting from interaction between the receptor and the analyte. Optical properties which can be measured in this particular case are absorbance, reflectance, luminescence, fluorescence, refractive index, optothermal effect and light scattering. Moreover, wide group of other sensing devices according to the operating principle of the transducer such as α, β, γ or X radiation sensors can be pointed. Among above presented group of chemical sensors, the electrochemical ones are the most promising alternative to overcome difficulties regarding detection of the analytes, in comparison with traditionally used methods [1,59,60].

2.2.1 Principles of electrochemical sensing

Electrochemical sensors enable to perform rapid measurements with a high sensitivity providing simple setting up and compact size of detection cells [1,59,60]. To perform electrochemical measurements, and as mentioned in section 2.2, a potentiostat and a data processor are required. However, the electrochemical cell equipped with appropriate electrodes exhibits the key role. It consists of three electrodes: the working electrode (WE), the reference electrode (RE) and the counter electrode (CE). From the point of view of electrochemical detection, the WE is the main component as on its surface take place processes related to detection step. Considering previous assumptions, WE plays receptor and transducer roles, mainly due to its homogenous structure. It has to be polarizable and should have a small surface thus measuring relatively low currents and ensuring an appropriate long-term performance. Contrarily, the RE is unpolarizable and its surface must be large enough to maintain stable value of the potential during the electric current flow through it. These two electrodes are sufficient to provide a closed electrical circuit. However, to ensure a stable RE potential value, a CE is widely used. Then, the current flows through CE instead of RE. The three electrodes are commonly immersed in the supporting electrolyte solution which acts as a charge transporter, which concentration is significantly higher than that of the target analyte. Moreover, the selected electrolyte cannot participate in any electrochemical and chemical reaction. Another requirement of the electrochemical setup is its electroneutrality (i.e positive and negative charges must be equal). The last property defining electrochemical sensors is the electrical character of the charge transfer within the transducer. Nevertheless, charge transfer in the electrode/electrolyte interface can be electronic, ionic, or mixed. In the ionic and mixed mechanism, electron transfer and, sporadically, electrolysis which has a significant impact on the electrochemical sensor performance can be observed [1,60].

As previously described, the principle of operation of the electrochemical sensor is also based on the interactions between the WE surface, and the target analyte dissolved in the supporting electrolyte (electroactive specie) as in other chemical sensors. The first stage involves transfer of the electroactive compound from the solution to the WE surface. Then, in the second step, the electrode reaction occurs. After that the resulting products can react with other ions present on the electrode surface or can be directly transferred into the bulk solution. These products can be also permanently adsorbed on the electrode surface resulting in electrode fouling and diminishing the electrochemical sensing performance of the set [1,61].

Considering the measured electrical current, electrochemical sensors are generally classified into four groups (Table 1).

Table 1. Classification of electrochemical sensors in relation to the measured electrical current

Type of electrochemical sensor	Measured parameter
Coulometric	charge
Conductometric	conductivity (resistance)
Potentiometric	potential
Amperometric (including voltammetric)	current

Coulometric sensors are based on Faraday's laws. The concentration of detected analyte is determined by measuring the amount of charge required to change the oxidation state of the molecule (direct coulometry). Thus, the mass of electrolysis product is directly proportional to the amount of charge flowing through the WE (Equation 1). By combining it with the second Faraday's law, which states that the charge required to exchange one mole of electrons is equal to Faraday's constant (Equation 2), we can simply state the formula which allows to determine the mass of analyte (Equation 3). In the derived equation all parameters are known except charge, which is defined during coulometric measurement.

$$m = kIt = kQ \tag{1}$$

where:

m – mass of the electrolysis product [g], k – Faraday's electrochemical equivalent [$\frac{g}{C}$], I – electric current [A], Q – electric charge [C] and t – electrolysis time [s].

$$F = \frac{M}{nk} \tag{2}$$

where:

F – Faraday's constant (C/mol), M – molar mass of ion (g/mol) and n – number of the electrons

$$m = \frac{MQ}{nF} \tag{3}$$

Coulometric techniques can be divided into processes performed under constant potential of the WE (controlled-potential coulometry – CPC) or under constant electric current (controlled-current coulometry – CCC). In coulometric analysis, calibration curve is not needed, representing a significant advantage of this method comparing to the other electrochemical techniques and being applied in the detection of inorganic substances and noble metals [60]. One of the requirements according to coulometry is the yield of the electrode reaction, which must be equal to 100%. However, it also presents disadvantages as its long operation time due

to the requirement of 100% yield of the reaction [62]. Canciani et al. [63] analyzed plutonium in a solution containing uranium using CPC. The electrochemical cell used in these measurements was equipped with gold as WE, a saturated calomel RE and platinum mesh CE (Figure 7). They succeed in the detection of the Pu even at high concentration of U. However, this technique implies a difficult sample preparation and application of a complex setup. Moreover, the measured medium must be properly selected due to the complexation ability of sulfate ions towards Pu^{4+}.

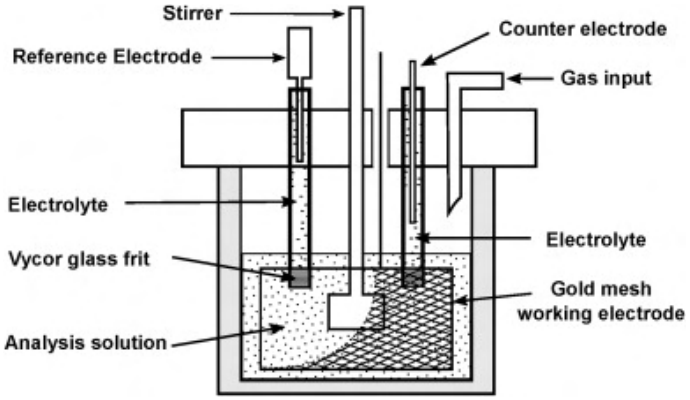

Figure 7. Experimental setup previously reported for coulometric experiments [63].

In case of detection of non-electroactive molecules, coulometric titration (CCC) has been proposed. In this case, the charge necessary to produce titrant, which then react with target analyte, is measured. Considering the non-direct analysis of the non-electroactive specie the end-point of the reaction is usually identified by applying an additional detection technique as, for example, spectrophotometry, potentiometry, amperometry or the most affordable visual observations [62,63]. Coulometric titration has been previously reported for the detection of CO_2 by Trapp et al. [64]. They proposed an electrochemical cell based on Severinghaus CO_2 electrode equipped with pH-meter (iridium oxide as WE). During the procedure, OH^- (titrant ions) are produced at the cathode and react with target analyte, resulting in a pH decrease. This method relies on several chemical reactions which can cause difficulties in measurements repeatability.

Coulometric techniques are not the most popular ones in electrochemical detection systems. More often conductometry, potentiometry and amperometry methodologies are applied (Figure 8).

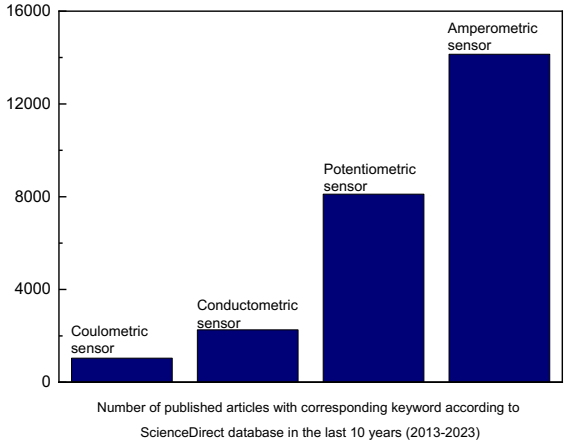

Figure 8. Plot illustrating number of published papers with corresponding keywords: coulometric sensor, conductometric sensor, potentiometric sensor and amperometric sensor in the last 10 years.

Conductometric sensors rely on conductivity changes of the receptor layer resulting from adsorption of molecules of target analytes, which can be non-electroactive, on its surface [1,60]. Moreover, in some cases, changes of the conductivity of the electrolyte are being recorded and are base of chemical information about the sample. Conductometry is commonly focused on non-complex samples measurements consisted of just few molecules/ions. It is important to comply with this requirement because all ions present in the tested solution can affect conductivity of the receptor layer/electrolyte [60]. In a multi-analyte solution problem with selectivity arise and accuracy of measurements drastically decreases. In this regard, conductometry is an easy approach for qualitative, rather not quantitative analysis of the samples, applicable in non-conductive environments as in gas phases [65]. Usually, receptor layers are made of metal oxides. Thus, Bharathi et al. [66] proposed NO_2 gas sensors based on Co-incorporated MoS_2 nanosheets achieving a LOD value of 7 ppm. The proposed system is based on an easy gas sensing mechanism. Briefly, in the air samples, oxygen is adsorbed on the receptor surface leading to a high concentration of the holes. Then, NO_2 reacts with adsorbed oxygen resulting in NO_2 adsorbed by physical interactions on the surface of the receptor material. It results in an increased number of the holes (decrease of the electron number from MoS_2) and movement of the Fermi level into conduction band and subsequent reduction of resistance. Moreover, the increased surface area of the composite, due to Co ions introduction, enables the enhancement of active sites accessible for gas adsorption thus improving the response. Even though conductometric sensors are widely applied, they can detect narrow group of analytes, and the improvement of measurements accuracy is still addressed.

The key point regarding **potentiometric sensors** is to measure the potential, under non-current conditions, between ion selective WE and RE (this last one being characterized by a known potential value). Potentiometric measurements are based on Nernst equation in which potential is described as a logarithmic function of activity of the ions in the measured sample:

$$E = E_0 + \frac{RT}{nF} \ln \frac{a_{ox}}{a_{red}} \quad (4)$$

where:

E – electrode potential [V], E_0 – standard electrode potential [V], R – gas constant = 8,314 $J \cdot K^{-1}$ mol^{-1}, T – temperature [K], F – Faraday constant = 96485 $C \cdot mol^{-1}$, a – molar activity of chemical compounds involved in red-ox reactions in the oxidized (ox) and reduced (red) forms.

All ions in the solution contribute to the generated potential value, which can cause problems with selectivity towards specific ions. Therefore, potentiometric sensors are divided into three groups, considering the contribution of molecules to the charge transfer: selectively permeable, semi-permeable and non-selective. The first group of sensors enables crossing the interphase only to one type of ions. In the second group, it is one type of ions which cannot pass the interphase. Finally, non-selective sensors are characterized for being permeable to all kind of ions. One of the most popular applications of the potentiometric sensors are oxygen detectors (e.g., Lambda probes) and pH-meters. Lambda probes are worldwide applied in all types of cars and facilitate the adjustment of fuel and air quantities to obtain a stoichiometric mixture, thus increasing the effectivity of fuel burning and decreasing the number of toxic substances in fumes. In a perfect operational combustion system, $\lambda = 1$, representing the ideal ratio between fuel and oxygen. In Lambda potentiometric sensor systems, electrodes made of transition metal oxides (for example Zr or Y) are usually proposed. In this kind of systems both electrodes are exposed to gas, even though one of them is treated with air, with an adjusted oxygen content, acting as reference. The another one is exposed to fumes, with an unknown oxygen content (Figure 9) [67].

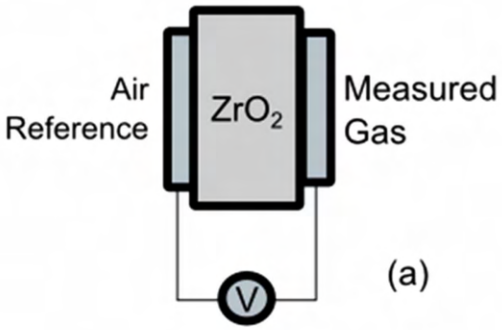

Figure 9. Schematic illustration of a Lambda system based on ZrO_2 [67].

The operation principle of the electromotive force of the cell (EMF) covers logarithmic relationship between partial pressure oxygen on the electrodes (Equation 5).

$$EMF = \frac{RT}{4F} \log \left(\frac{pO_2 air}{pO_2 fumes}\right) \quad (5)$$

Another potentiometric sensor can be found at **pH-meters,** it is consisted of a selectively permeable membrane which allows only H^+ to cross the interphase. Park et al. [68] proposed a pH-meter based on a polyaniline (PANI, conductive polymer) nanofiber array and Ag/AgCl as RE printed on flexible poly(ethylene terephthalate) (PET) [1,68]. The proposed setup is characterized by reaching an excellent sensitivity of 62 mV/pH and displaying a short response time (12.8 s). Due to its flexibility, the proposed sensor enables to measure for example pH of apple samples.

The most highly developed group of electrochemical sensors are the **amperometric** ones in which changes of generated current during applied constant potential are recorded. The current changes are the result of electrochemical oxidation and/or reduction reactions being developed on the electrode/electrolyte interface and are strictly correlated with the concentration of the electroactive specie of interest. According to the applied potential, and the developed reaction, the WE can act as anode or cathode. Generally, amperometric sensors are used in measurements of liquid and gaseous samples. One of their most popular analytical applications is that related to the electrochemical setup proposed by Leland C. Clark, Jr, which enables to estimate oxygen activity, for example oxygenation level, of the biological fluids [60]. It consists of two or three electrodes, platinum (Pt) or gold (Au) as cathode (WE) and Ag/AgCl (RE) immersed in KCl solution as anode. The third electrode is also an anode and diminishes the current flowing through RE improving measurement accuracy. Clark introduced into this electrochemical setup a permeable membrane aiming to protect Pt electrode from fouling and degradation, facilitating estimation of the oxygen diffusion distance. It is usually made of a polymeric material, as Teflon, which is highly permeable for oxygen, and stops the other compounds present in the sample. During the measurement, oxygen crosses the membrane and directly contacts the cathode, where it is reduced following the reaction:

$$O_2 + 4H^+ + 4e^- \longrightarrow 2H_2O$$

The electrons required for this reduction process come from the silver oxidation reaction, being developed at the same time:

$$4Ag + 4Cl^- \longrightarrow 4AgCl + 4e^-$$

The generated electric current is proportional to the partial pressure of oxygen (pO_2) in the electrolyte, and it allows the estimation of the oxygenation level of the fluid [60,61].

Modifications of Clark electrode enable to detect other gaseous compounds as NO_x, Cl_2 or H_2S [1]. Another application based on amperometry is polarography. In polarography, the electrode with changing surface is applied as WE, for example dropping mercury electrode (DME) or hanging mercury drop electrode (HMDE). The principle of drop exchange in DME and HMDE is different. In DME the drop formation is ripped off mechanically using an electromagnetic hammer. However, in HMDE the drop is pushed out using a piston equipped with a micrometer screw. In the first measurements conducted by Heyrovsky [69,70], "the pool" of the mercury at the bottom of the cell played a double role (as RE and CE), but subsequently separated electrodes had been introduced. The remarkable advantage of using this type of electrodes is that measurements are performed on clean and renewable electrode (mercury drop surface) at real-time. Polarography has been widely applied for detection of trace metals in pharmacy, blood serum diagnosis and antibiotics determination [70]. Nevertheless, currently due to the high mercury expenditure and interferences from DME, the above technique is not often applied [60]. The setup required for detection with amperometric technique is facile to construct and the measurement is relatively quick. However, it also presents limitations. The concentration of target analytes cannot be as low as in potentiometric sensor. Moreover, interference drawbacks must be considered, because electrochemical reactions of numerous analytes take place at the same potential value, which can rise problems with overlapping of the voltammetric responses of different substances and make detection impossible or decrease selectivity and accuracy of the measurements. Nevertheless, above mentioned limitations can be easily overcome by adjusting measurements conditions to diminish electrochemical processes originated from interference substances. It can be done by applying suitable amperometric technique or by modifying the WE with proper materials [60].

2.2.2 Electrochemical techniques

There are a great variety of amperometric techniques applied in electrochemical detection measurements. Application of the most suitable one can enhance sensor working performance by decreasing LOD value or improving sensitivity or selectivity towards the analyte of interest. The most common techniques applied in electrochemical detection systems are linear sweep voltammetry (LSV), cyclic voltammetry (CV), differential pulse voltammetry (DPV), square wave voltammetry (SWV), normal pulse voltammetry (NPV) and their modifications. LSV is an electrochemical technique in which a linearly changed potential is applied and the scan is not reversed back. In this technique red-ox reaction of interest takes place after time, when the

potential reaches the required value for the occurrence of the specific process. The corresponding redox peak is developed as a result of recorded currents in a function of applied potential. At the beginning, when increasing the potential applied to the electrode, the rate of the related electrochemical reaction is higher. Then the current reaches the maximum value, and it starts decreasing, due to the lower diffusion of the electroactive species to the electrode surface. LSV is commonly applied in determination of the potential of redox reactions. It is also widely applied in case of determination of species exhibiting not reversible redox, and reverse scan is not necessary [2]. CV can be considered as an improvement of LSV, because it covers also reverse scan and enables monitoring of both reactions: reduction and oxidation. After recording the first scan between potential values from E_1 to E_2 it is reversed back (Figure 10a). The result of reverse scan introduction in the electrochemical detection is a duck-shape voltammogram (Figure 10b).

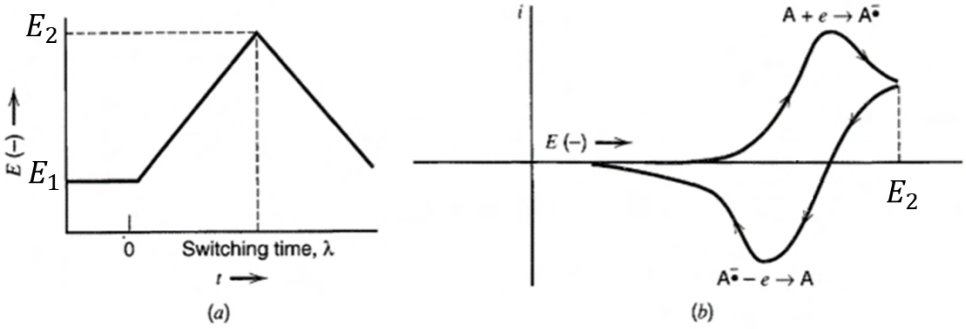

Figure 10. (a) Principle of cyclic potential sweep (b) resulting "duck" shaped voltammogram [2].

CV gives more information about electrochemical processes related to electroactive species allowing the estimation of the process reversibility. In case of reversible processes, the calculation of the number of electrons which are exchanged in electrochemical reactions is performed from the following equation:

$$\Delta E\ [V] = E_{pa} - E_{pc} = \frac{0.059}{n} \quad (6)$$

where:

E_{pa}, E_{pc} – potential at which oxidation and reduction reactions take place, respectively,

n – number of transferred electrons.

LSV and CV techniques are being widely applied mainly in preliminary studies in electrochemical sensing. However, several researchers also applied these techniques for determination of sensor working parameters. Chelly et al. [71] applied LSV in DA and riboflavin (RF) electrochemical sensing using screen-printed carbon electrodes (SPCEs)

modified with gold nanoparticles (AuNPs) as WEs. The peaks corresponding to DA and RF oxidation reactions are clearly distinguishable on the corresponding LSV plots (Figure 11).

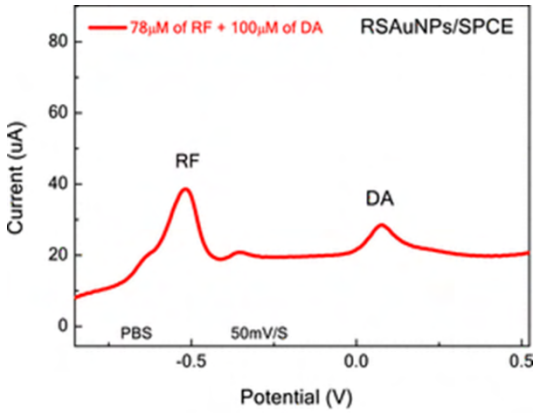

Figure 11. LSV showing the well-separated anodic peaks attributed to the oxidation of DA and RF [71].

The calculated LOD values were 0.2 and 0.07 μM for DA and RF, respectively. Nevertheless, the main drawback of both techniques is the capacitive current being the result of the formation of the electrical double layer (EDL). To diminish this capacitive current and improve sensor working parameters, pulsed techniques, as DPV, are commonly used. The principle of DPV is double sampling of the current during step change of the potential. This current, resulting from the development of the corresponding Faradaic reaction and the previously mentioned EDL formation increases with the same rate, however, capacitive current decreases quicker. Measurement of the current before and after the pulse potential enables to diminish impact of the capacitive current, mainly recording Faradaic current, strictly correlated with the electrochemical reaction [2].

In case of SWV, a combination of staircase and square correction is imposed on the linear potential sweep. The current is probed twice at the end of the first scan and then at the end of the backward scan, shortly before changing of the potential direction. This fact enables to eliminate the capacitive current contribution. In the NPV on the constant potential value, linearly increasing amplitude is imposed. Measurement at the end of the pulse diminishes the capacitive current. Considering modification of applied potential pulse, speed, accuracy and facility of the measurement, several pulsed techniques can be pointed out. The most sensitive one, which enables the fastest measurements is SWV. However, due to easy measurement performance and relatively high sensitivity and accuracy, DPV technique is the most commonly applied [72] According to ScienceDirect database, and considering the last 10 years, there are about 13,400 papers including keywords: *electrochemical detection and differential pulse*

voltammetry. In case of electrochemical detection using SWV and NPV there are about 9500 and 5000 papers, respectively. DPV has been successfully applied in the detection of a wide range of analytes such as DCF, DA, calycosin, Pb and Cd ions, hydroquinone, resorcinol, nitrites, caffeic acid and many others [73–77]. Beni et al. [78] compared cyclic and pulsed techniques in the electrochemical detection of DA. They performed detection in the interface between two immiscible electrolyte solutions (ITIES) mode. CV and DPV/SWV measurements revealed that application of the pulse techniques enables to decrease the LOD value to 2 μM in comparison to 100 μM obtained by CV.

2.2.3 Working electrodes

Far from selecting the most appropriate electrochemical technique, improvement of sensors performance can be obviously addressed by choosing a suitable WE. The most used WEs are:

- carbon based electrodes: glassy carbon electrodes (GCEs), carbon paste electrodes (CPEs), pencile graphite leads (PGEs), boron doped diamond electrodes (BDDEs) [58,79],
- metal-based and noble metal-based electrodes, as Pd, Pt or Au [80]; electrodes with variable surface based on mercury (DME) mentioned in the paragraph 2.3.1,
- metal oxide-based electrodes, as indium tin oxide (ITO) [58].

In order to select the most appropriate WE for the electrochemical setup, not only the related physicochemical properties, but also economic issues must be taken into consideration. GCE is the most widely applied in electrochemical sensing, despite its high cost of fabrication, as it provides chemical inertness, homogenous surface, low electrical resistance, and easy modification. Moreover, it offers a high mechanical strength, which gives possibility to polish it in a facile way and reuse [81,82]. Metal electrodes, such as Pt or Au, although displaying a fast electron transfer and, in consequence, a good electrochemical performance, are very expensive and operate in a narrower potential window (in comparison to carbon-based electrodes). For example, the inert potential window for GCE is -0.76 – 1.96 V vs. -0.38 – 1.44 V for Au in 0.1 M sodium acetate (pH = 7.2 – 7.8) [83], this last is limited due to Au surface oxidation. The as-created oxide layer can result in background current contribution, having a negative impact on the electron transfer rate, and/or can react with target analyte resulting in low accuracy and repeatability of measurements [58]. On the other hand, Pt is a highly effective catalyst for hydrogen evolution reaction. However, in the presence of trace levels of water or in acidic environment, the H_2 evolution reaction could limit its operational cathodic range [84].

An interesting and cheaper alternative for GCE are CPEs. However, they suffer from poor mechanical strength resulting in high susceptibility for destroying.

In the last years, strong research interest is focused on screen-printed and inkjet-printed electrodes (SPEs and IPEs, respectively). Both can be applied in commercial applications and enable miniaturization of the electrochemical detection setups applied in the laboratory tests. At this point it is important to remark that miniaturization is desirable to work with lower volume of samples, when their storage or availability are limited. SPEs enable to place all three electrodes, required to set up an electrochemical cell, on one substrate. The fabrication of these electrodes covers the deposition of selected inks through pressing them by designed form, which must be prepared. Between these printing steps, solidification is also required. Usually, screen-printing procedure demands work in highly clean rooms. Particularly, the formulation of suitable inks for the WE, CE and RE depends on the sensor substrate and required electrochemical properties. The most frequently used inks are based on silver, gold and carbon materials. Gold and carbon usually act as WE. However, carbon-based active materials are widely selected due to their lower cost. On the other hand, silver-based inks are usually printed as RE. Screen printing is possible on a plenty of rigid and flexible substrates such as epidermis, stress ball made of neoprene, underwater garment, paper, PET and many others [85]. Nevertheless, the prices of the equipment required to print using screen printing technique vary from 1000 to 25000 $ depending on the number of directions in which printing is performed (XY or XYZ) [85].

Recently, an interesting alternative for screen printing is inkjet printing technology, which offers the possibility of electrodes fabrication with lower active materials consumption, also offering a high resolution (>2μm) [86]. The resulting inkjet-printed electrodes (IPEs) look similar to the SPEs, even though inkjet printing devices mainly enable to print on flexible substrates such as thin glasses, polyacetate, paper, photographic paper, metal foils, textile fabrics or Kapton®. The inks for achieving a successful printing by means of this technology must meet a number of requirements, mainly in terms of appropriate viscosity/rheology. In this sense, previously reported formulations have assessed the suitability of a great variety of substances starting from metals, carbon materials, conductive polymers, semiconducting metal oxides and dielectric materials [87]. However, there are still some drawbacks which need to be overcome, as the elimination of the necessary additives and stabilizers which negatively impact on the conductivity of the inks. In addition, the speed of printing is slow, and in case of multi layers printing on the substrate a drying step is required. The equipment applied in inkjet printing is usually cheaper that printers applied in screen printing technologies, but still

expensive. Nevertheless, it is possible to adapt a common office printer to print on many substrates. As previously stated, the optimization of inks formulation, matching them with a proper substrate and the optimization of the printing parameters have arisen in a great research interest in recent years [87]. Tortorich et al. [88] applied HP Deskjet 5650 printer. They printed water-based ink composed of carbon nanotubes (CNTs) and additive sodium n-dodecyl sulfate (SDS) as stabilizer on transparency film. As-prepared IPE was compared with commonly applied gold electrode. The electrodes were tested towards Fe^{2+}/Fe^{3+} redox reaction. On both electrodes peaks corresponding to the redox processes are clearly visible. However, the potential values recorded on the CNT IPE were higher than on gold electrode and the intensity of anodic and cathodic peaks was lower, which indicates the importance of improving sensor working parameters.

Bare working electrodes usually perform not satisfactory in electrochemical detection systems. To improve electrochemical detection, different WE modifiers are being applied. When the objective is to measure the potential of electrochemical reaction, the size and shape of the electrode is not of the greatest interest, however they are highly important in electrochemical detection, in which electric currents are recorded. Remembering that capacitive currents can be reduced by applying a suitable detection technique, as stated in the paragraph 2.3.2, a potential approach to enhance the electrochemical detection of target analytes is to decrease the size/surface of the electrode, even though at the same time the number of active sites accessible for detected analyte is reduced. Contrarily to our goal this can worsen sensor working parameters [61]. It is necessary to find a compromise between the minimization of capacitive current by using a suitable active electrode material or electrochemical detection technique and the increase of active sites accessible for target analyte.

2.3 Graphene and related materials

One of the most widely applied group of materials, from carbon family, in electrochemical sensing are graphene-related materials. Graphene is a 2D allotropic form of carbon firstly isolated by Geim and Novoselow in 2004 [3]. It consists of sp^2 hybridized carbon atoms resembling a honeycomb, constituting the basic building unit for all graphitic materials (Figure 12).

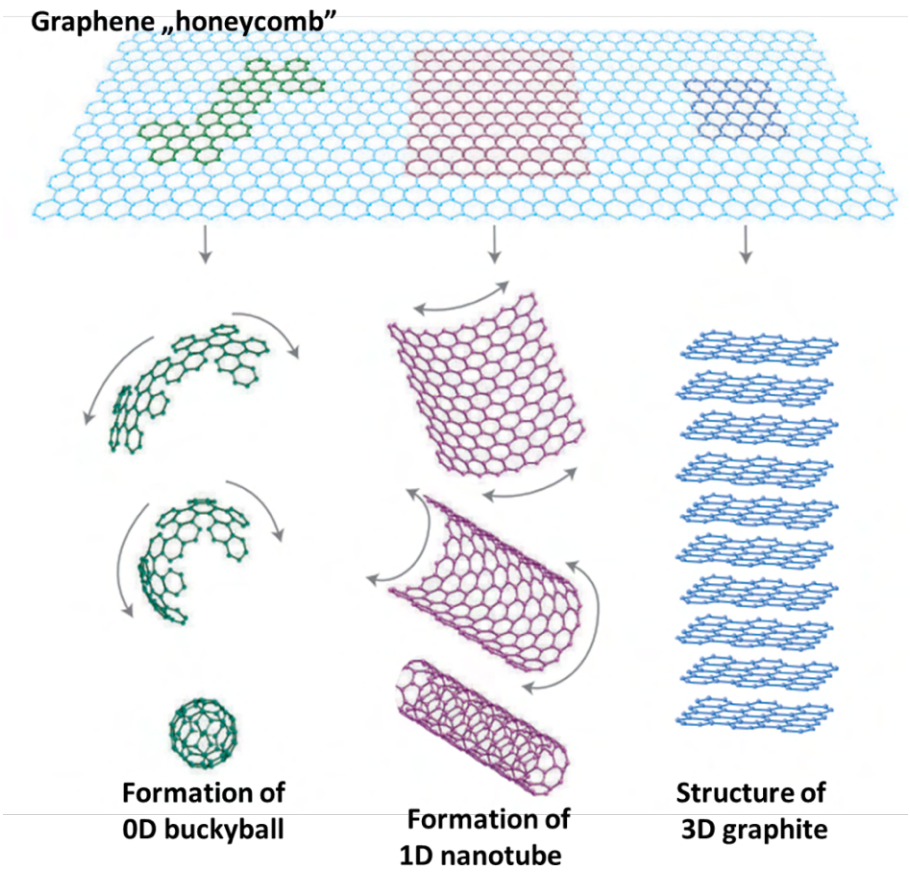

Figure 12. Representation of graphitic materials constructed from graphene layers [3].

Due to unique properties resulting from its structure, high application expectations are associated with graphene. The pristine graphene exhibits high electron mobility ($2.5 \cdot 10^5$ cm^2 V^{-1} s^{-1} at room temperature), excellent electrical conductivity, high thermal conductivity (3000-5000 W mK^{-1}), low thickness of about 0.34 nm and high transparency (optical absorption 2.3 %) [89]. Even though according to its definition, it is a one-layer, non-defective material, in practice it is arduous to obtain graphene without any defects and impurities. Due to the ease of functionalization, graphene can be doped by different functional groups as oxygen, nitrogen, phosphorous, sulfur or boron. Referring to the above, different graphene-based materials are widely used as graphene oxide (GO), reduced graphene oxide (rGO) and doped graphene materials. Due to the hardness of isolation of the single layer, the graphene materials are usually consisted of few graphene layers, with and interlayer distance between 0.35 – 0.36 nm, being called flake graphene [89]. There is a great variety of synthesis routes to obtain graphene materials, thus yielding to final products with different composition, number of defects and associated properties. Kim et al. [90] proposed the division of such synthesis routes of graphene materials into top-down and bottom-up (Table 2).

Table 2. Overview of top-down and bottom-up synthesis routes of graphene materials

Bottom-up	Top-down
Chemical vapor deposition (CVD) Epitaxial methods (e.g., growth on SiC) Chemical conversion Arc discharge Reduction of CO Unzipping carbon nanotubes	Separation/exfoliation of graphite

The most often applied synthesis routes are graphite exfoliation, epitaxial methods, and CVD. Despite the group of top-down techniques is lower in number they are usually applied in commercial production mainly due to economic aspects as they enable to obtain higher quantity of product, even though with a not high quality. Bottom-up techniques enable to obtain graphene-based materials with higher purity, lower number of defects and better quality. However, the amount of as-obtained products is relatively low which makes the commercial production more expensive [90]. Materials obtained by bottom-up techniques are desired in electronic applications, where the quality of applied material is on the great importance. Briefly, epitaxial methods cover deposition of ultrathin layer on the crystalline substrate. The epitaxial growth on SiC seems to be the most promising, involving sublimation of Si atoms from the crystal structure at high temperatures (1000-2000 °C). The C atoms recreate substrate structure resulting in high-quality graphene layer [91,92]. Considering electronic applications, this technique is highly advantageous over others due to deposition of graphene layer directly on the substrate (elimination of transfer step which can raise defects) [93]. Another bottom-up technique, CVD, involves deposition of carbon atoms from different precursors on catalytically active substrate, mostly copper (Cu) and nickel (Ni). Depending on the precursor and substrate the final product can vary. Generally, aliphatic hydrocarbons (methane, ethane, propane) mixed with H_2 are applied as carbon precursors. However, there are also other, environmentally friendly precursors as camphor ($C_{10}H_{16}O$). A reproducible thermal CVD was performed on Ni substrate by camphor evaporation and pyrolysis [94]. The final product in the form of planar few layers nano-graphene (PFLGs) with a size similar to that obtained by epitaxial growth on SiC was obtained. However, this technique has one main drawback which is necessity of scratching of the final product from the substrate surface. The application of camphor as carbon source is suitable due to the molecular structure of its molecule which allows facile formation of hexagonal and pentagonal carbon rings during molecule decomposition (Figure 13).

Camphor is a cheap and natural precursor, nevertheless, depending on the final application of graphene material usually it is more suitable to apply precursors which yield only hexagonal rings to eliminate final product impurities by pentagonal rings [94].

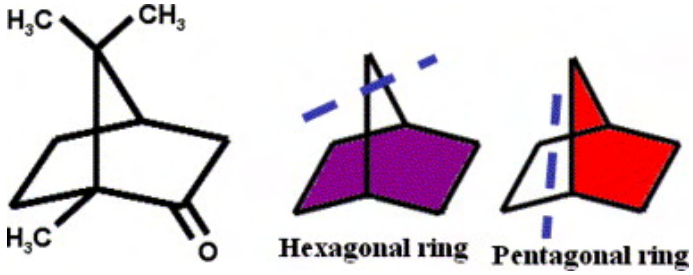

Figure 13. Illustrations of breaking of camphor molecule allowing creation of pentagonal and hexagonal rings [94].

Therefore, simple hydrocarbons as carbon precursors are mostly used in the synthesis of graphene materials by CVD. The challenge is to produce a graphene in a monolayered form by CVD. This technique is widely applied in the production of carbon nanofibers/carbon nanotubes (CNFs/CNTs) that raises considerable risk of graphene-material contamination by another carbon allotrope. It is highly necessary to adjust and set proper synthesis parameters and choose suitable substrates to obtain graphene material overwhelmingly. Generally, CVD technique enable to obtain larger sheets of graphene layers compared to top-down methods, even though the quantity of product is lower [93].

The second group of techniques which enable to obtain graphene-based materials (top-down) focuses mainly on graphite exfoliation. The conditions of top-down techniques do not allow to eliminate all defects and heteroatoms; therefore, the resulting products are graphene-based materials, not pristine graphene. There are two main types of exfoliations: mechanical and chemical, but in the recent years the research interest into electrochemical exfoliation is being also developed. Mechanical exfoliation was used to isolate the graphene layer for the first time by Geim and Novoselov. This technique is widely known as “Scotch tape approach” and it involves removing of graphene layers, one by one, by scotch tape from highly oriented pyrolytic graphite (HOPG). The biggest advantage of this process is ease and possibility of production of single layer graphene. However, high quality of material excludes large dimensions [95]. Electrochemical exfoliation of graphite was firstly performed in 1934 by Thiele et al. [96]. Shortly, it relies on immersing a working electrode made of graphite (foil, HOPG, rod, plate) in the electrolyte solution [97]. Mostly H_2SO_4 or $LiSO_4$ are applied due to the comparable size of SO_4^{2-} ions (0.460 nm) to an average interlayer distance between the graphene layers in graphite (~0.334 nm). The process can be performed under anodic or cathodic conditions. It

covers attraction of ions to the graphite surface, their intercalation between graphene sheets and graphene sheets repealing from the WE surface [98]. Significantly more often chemical exfoliation techniques are being applied. Even though being more complex, they enable to obtain higher quantity of tailored graphene-based materials in a facile way. The schematic representation of graphene-based materials production following this route is shown in Figure 14.

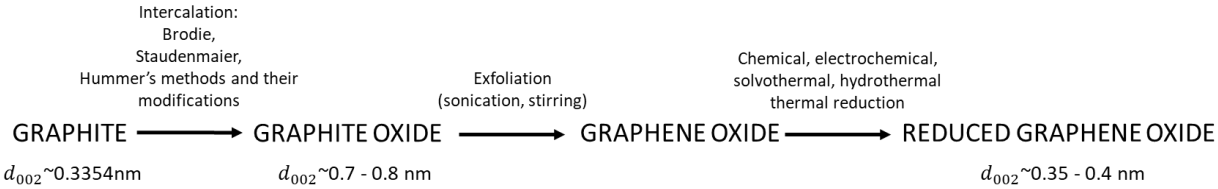

Figure 14. Schematic representation of the graphene-based materials production by chemical exfoliation and subsequent reduction.

There are three main chemical exfoliation methodologies based on the intercalation of graphite: Brodie, Staudenmaier, and Hummers [91,99,100]. Brodie's method, which is the oldest one, relies on the treatment of graphite with $KClO_3$ in fuming HNO_3+NO_2. Staudenmaier modified Brodie's method replacing $KClO_3$ with H_2SO_4. Nowadays, the most popular is Hummer's method in which graphite is oxidized by a mixture of H_2SO_4, $NaNO_3$ and $KMnO_4$. There are also several modifications of Hummer's method which results in materials with varied structures and properties. Despite using different oxidants, the principle of all above methods is the same, being focused on the introduction of oxygen moieties/functional groups in order to increase an average interlayer distance between graphene sheets in graphite also weakening Van der Waals interactions between them. Due to the aggressive reaction environment, the Csp^2 bonds are partially destroyed resulting in defects. The first product/intermediate of intercalation in acidic media is acid-graphite intercalated compound which is then converted to the oxidized form of graphite – graphite oxide (GrO), displaying an average interlayer distance of ~0.8 nm. Apart from functional groups introduced between the graphene layers, different ions and water molecules occur between these layers in GrO, which enable to keep them expanded [91,99,100]. To obtain graphene oxide (GO), post processing of GrO is necessary mainly involving sonication, mixing or thermal expansion. Mixing is the least effective approach in the separation of layers. A very high yield of GO is obtained by sonication; however, a damage of graphene flakes can take place during this treatment resulting in a decrease of their sizes [101]. According to the model proposed by Lerf-Klinowski (Figure 15), GO possesses defects and oxygen functional groups (epoxy and hydroxyl on the basal plane and carbonyl, carboxyl and lactone

on the edges) in its structure which makes it almost an insulator. Therefore, subsequent oxygen groups removal is required to obtain higher quality graphene-based materials (reduced graphene oxide, rGO).

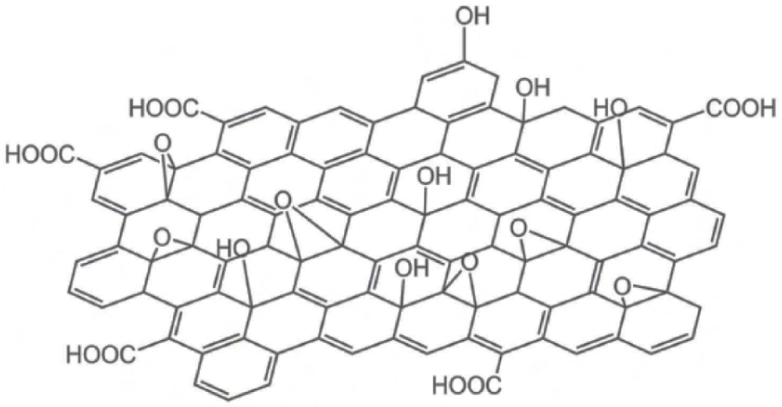

Figure 15. Lerf-Klinowski model of GO [102].

rGO, with partially restored Csp^2 network resulting in higher electrical conductivity, can be obtained by reduction of GO using several methods. For example, chemical, electrochemical, thermal, hydrothermal and solvothermal reduction methodologies. The most popular reducing agent in chemical techniques is hydrazine, as it allows to achieve a high degree of reduction. Hydrazine enables to remove mainly epoxy and hydroxyl groups, while simultaneously introducing nitrogen into the material structure. However, and due to the high toxicity of hydrazine, environmentally friendly reducing agents have been searched in recent years. One of the alternatives for hydrazine is AA, although the degree of oxygen removal is lower, varying an average oxygen content in obtained rGO between 17.5 and 25.4 at.% [103,104]. Plant extracts are also being considered, for example aloe vera, caffeic acid, grapes, tea or pomegranate juice. Nevertheless the reduction degree achieved and the final structure of the product highly dependent on the reducing properties of selected extract [101]. It must be underlined that chemical reduction usually requires removal of residual amounts of reducing agent.

Another approach for obtaining rGO is the electrochemical reduction starting from GO previously deposited on a conductive substrate (coating-reducing method) and subsequently placed in the electrolyte solution. After that, an electric potential is being applied and the electrolyte decomposes emitting hydrogen which acts as reducing agent according to the reaction [92].

$$GO + aH^+ + be^- \rightarrow rGO + cH_2O$$

In the coating-reducing method the morphology and thickness of the final product is mainly dependent on the thickness of deposited GO layer. Moreover, electrochemical reduction can be performed from the GO suspension. In this approach, a WE is immersed into the GO solution and the final product (ERGO) is deposited on the above mentioned electrode surface. Since mechanism of electrochemical reduction is not fully known and depends on the applied potential value, Tong et al. [105] proposed a theory in which carboxyl groups on the edges of graphene layers loose electrons which form new covalent bonds with existing electrons. Nevertheless, according to the content of carboxyl groups presented in GO which is quite low comparing to other oxygen moieties, the expected final reduction degree should be low. Following below reactions (Figure 16), decarboxylation and radical dimerization steps occur:

$$RCOO^- \rightarrow RCOO\cdot + e^-$$

$$RCOO\cdot \rightarrow R\cdot + CO_2$$

$$R\cdot + R \rightarrow R - R$$

Figure 16. Decarboxylation and radical dimerization of carboxyl groups [105].

Carboxyl groups can be also reduced to hydroxyl groups on the cathode. Depending on the deposition time, the final product can be in the form of 3D porous material or film. Electrochemical approach is a promising alternative to chemical route due to elimination of toxic reducing agents and ease of controlling the reaction by regulating the applied potential and time [106] even though it limits the amount of produced rGO.

rGO can be obtained by thermal reduction as well. This process starts with GrO and involves simultaneous exfoliation and reduction in one single step. The precursor is subjected to fast heating at high temperatures (usually 900-1100ºC) in an inert atmosphere leading to decomposition of oxygen functional groups. The formed gaseous products (CO_2, H_2O, CO) are located between graphene layers and their rapid evolution leads to the separation of graphene nanosheets. Practically, the generated pressure depends on the temperature of thermal treatment and usually has a value in the range of 40 - 130 MPa, which is much higher than necessary pressure to separate graphene layers. Unfortunately, the simultaneous thermal exfoliation and reduction leads to plenty of structural defects due to fast heating/reaction rate [107,108]. There is also two-step thermal method combining flash pyrolysis and further heat treatment with slow rate heating. This technique enables to obtain products with tunable properties. During fast heating rate (flash pyrolysis) there is a rapid elimination of oxygen functional groups generating pressure which results in “explosion” leading to separation of the graphene layers. Then during further ramp heating up to the final temperature of the process, deoxygenation proceeds

followed by changes in the structure of the resultant rGO. Unfortunately, the second step could also contribute to final graphene layers aggregation [109].

Recently, due to the ease of process, elimination of toxic reducing agent and purity of final products, hydrothermal reduction of GO has been also assessed. Moreover, hydrothermal treatment excludes possibility of introducing heteroatoms derived from reducing agents. Usually, hydrothermal treatment is performed at temperatures up to 200°C under autogenous or increased pressure. In this technique superheated water plays a key role as reducing agent, catalyzing decomposition of oxygen functional groups [110]. Huang et al. [111] examined hydrothermal reduction process in detail. They compared the physicochemical characteristics of rGOs obtained at 200 °C at different reduction times (0.5, 1, 2, 4, 8 and 10h). Depending on the time of reduction, the obtained products differ in properties and, subsequently, final application. Due to a significant content of oxygen groups after applying a short reduction time, the resulting rGO displayed high hydrophilicity and layer interspacing, this last parameter being similar to that of graphite. The chemical surface composition, determined by XPS, for the samples reduced for 0.5 h revealed a low decrease of epoxy/hydroxyl groups content. This is the result of decomposition of thermally unstable epoxy groups. However, the peak corresponding to this group is still presented, due to the higher stability of hydroxyl groups which are attached to the edges of graphene sheets. The degree of reduction is not sufficient to significantly improve the electrical conductivity, even though material can be applied in electrochemical energy storage devices, where interlayer spacing is highly important, or inks formulation due to hydrophilicity of active material. After 2 h of hydrothermal treatment, further decomposition of epoxy and hydroxyl groups has been observed; however, they are not fully eliminated. Longer reduction time, up to 8h, results in improved electronic properties due to lower oxygen content in the final product. Further elimination of hydroxyl and epoxy groups, which are incorporated into the plane of graphene layers, leads to breakdown of rGO sheets resulting in smaller dimensions of the flakes. As expected, the highest reduction degree was recorded for 10h of reaction corresponding to 14.7 at. % of oxygen. However, the structure of as-obtained material is highly damaged.

Díez et al. [110] studied deoxygenation of GO under hydrothermal conditions at lower temperature (180°C) for 5, 8 and 24 h. Moreover, the efficiency of GO reduction was determined when N_2 or H_2 was applied. In the process in which H_2 was introduced into the autoclave, higher pressure up to 40 bar was generated. Thus, while the oxygen content in rGO reduced for 24h conventionally is 15.9 at %, a process performed in the presence of N_2 or H_2

significantly improved the reduction degree leading to 13.6 and 11.2 at. % of oxygen, respectively [110].

Another potential approach is the solvothermal methodology for GO reduction, differing from the previous one in the type of solvent used. The commonly used solvents are N-methyl-2-pyrrolidone (NMP), ethylene glycol, ethanol and N,N-dimethylformamide (DMF) [112]. Some of the above play also a role of dispersion stabilizer. rGO obtained by solvothermal treatment possesses higher degree of crystallinity [113]. It has been proved that application of benzyl alcohol enables to obtain rGO with a C/O ratio and an average interlayer distance similar to that obtained during chemical reduction by hydrazine (d_{002} = 0.354 nm for rGO/solvothermal vs. d_{002} = 0.364 nm for rGO/hydrazine). Solvothermal treatment of GO can be performed in a mixture of concentrated sulfuric acid and organic solvent (DMF or DMSO). The mechanism of GO reduction in the presence of sulfuric acid covers mainly decomposition of epoxy groups to hydroxyl which are then dehydrated. The oxygen content in the final material reduced at 150°C varies from 13.0 to 18.2 at.%. depending on the applied organic solvent, its ratio to sulfuric acid and reduction time [114]. As follows from Table 3, it can be assumed that bottom-up methods are dedicated to obtain the pristine graphene whereas top-down techniques enable production of graphene-based materials with adequate properties for electrochemical sensing and energy storage applications. Both bottom-up and top-down methodologies have advantages and drawbacks, therefore there is still challenge to design and develop efficient synthesis techniques.

Table 3. Summary of different aspects of graphene-based materials synthesized by means of bottom-up and top-down techniques

Aspect	Bottom-up (CVD, epitaxial growth)	Top-down (mechanical and chemical exfoliation)
Economy of process	High costs of production	Relatively low cost of production
Transfer of the product	In case of CVD the product usually must be transferred	No need of transfer, product in a bulk except electrochemical reduction
Quality of product	High-quality (low number of defects and heteroatoms)	Low-quality (highly defected structure, with plenty of heteroatoms)
Final application	Electronics	Sensors, inks, water purification systems
Quantity of material	Low	High – depending on the technique

Dimensions of graphene layer	Larger areas than in top-down methods	Flakes with small dimensions
Amount of graphene layers	One or few - controlled number of flakes	Many flakes, more than one

2.3.1 Heteroatom doping of graphene materials

Introduction of proper dopants can significantly improve the physicochemical properties of GO and rGO widening their subsequent applications. Mostly nitrogen, boron, phosphorus and sulfur atoms, are introduced into the structure of graphene-based materials due to their similar characteristics, when comparing to C atoms, in terms of van der Waals radius, electronegativity, electronic configuration, and number of valence electrons (Figure 17) [115].

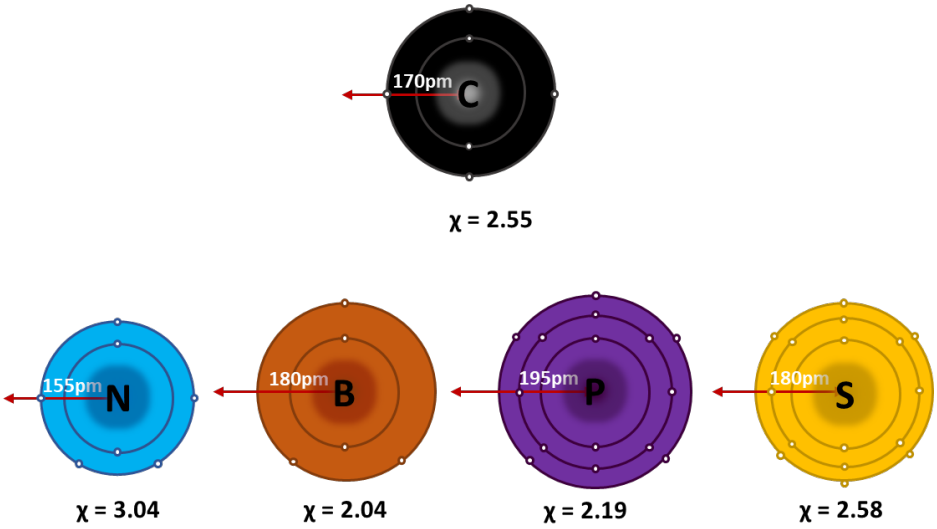

Figure 17. Representation of similarities of nitrogen, boron, phosphorus, and sulfur in comparison carbon atoms.

Generally, phosphorous and sulfur are promising as dopants in case of graphene materials applied in electrochemical energy storage systems. Sulfur tends to replace carbon at the edges of graphene layer. To perform reaction between carbon and sulfur, high energy is demanded. Moreover, the introduction of sulfur into the graphene plane leads to the appearance of a significant number of defects in the structure of graphene-based material mainly due to the higher length of C-S bond in comparison to C-C. Usually, higher number of defects in the material leads to increase of surface area thus resulting in higher capacitance, which even though not being a key parameter when considering electrochemical detection, it could has a positive impact on the electrochemical performance of the material when using it in

electrochemical energy storage devices. Additionally, the presence of oxidized forms of sulfur (sulfone, sulfoxides) and non-oxidized sulfur moieties in the structure of S-doped graphene enhances their capacitance due to pseudocapacitance effect [115,116].

P-doped graphene materials are promising in catalysis because of their high number of valence electrons. Sulphur similarly as phosphorus exhibits a higher atomic radius than C, which results in the appearance of a high number of defects during its incorporation into graphene materials, thus leading to an increased surface area. Moreover, it has been reported that introduction of phosphorus results in the formation of oxidized forms, which can be responsible for pseudocapacitance. P-doping is also positive from the point of view of improving the mechanical strength of the resulting material, as phosphorus enables to create strong bonding between single graphene layers [116].

Boron and nitrogen are significantly easier to be introduced into the graphene structure. Their dimensions are the closest to carbon and they are characterized by similar number of valence electrons. Introduction of boron, as in case of other heteroatoms, leads to changes of electronic structure of graphene-based materials. Due to its lower electronegativity it leads to formation of a p-type conductor. From the point of view of electrochemical detection, and accordingly to the current state of research, nitrogen doping is the most promising and widely investigated approach. Introduction of N to the material structure can boost catalytic activity towards several reactions, as for example oxygen reduction reaction (ORR), due to the high number of active sites accessible for oxygen adsorption. Nitrogen can create both p-type and n-type semiconductors. Nitrogen can be introduced into the graphene materials in different configurations, including amine/amide (N-C), pyrrolic (N-5), pyridinic (N-6), graphitic (N-Q) and N-oxides (N-X) (Figure 18). The nitrogen groups distribution in N-doped material is determined by the type of N-dopant used and the process parameters of N-doping.

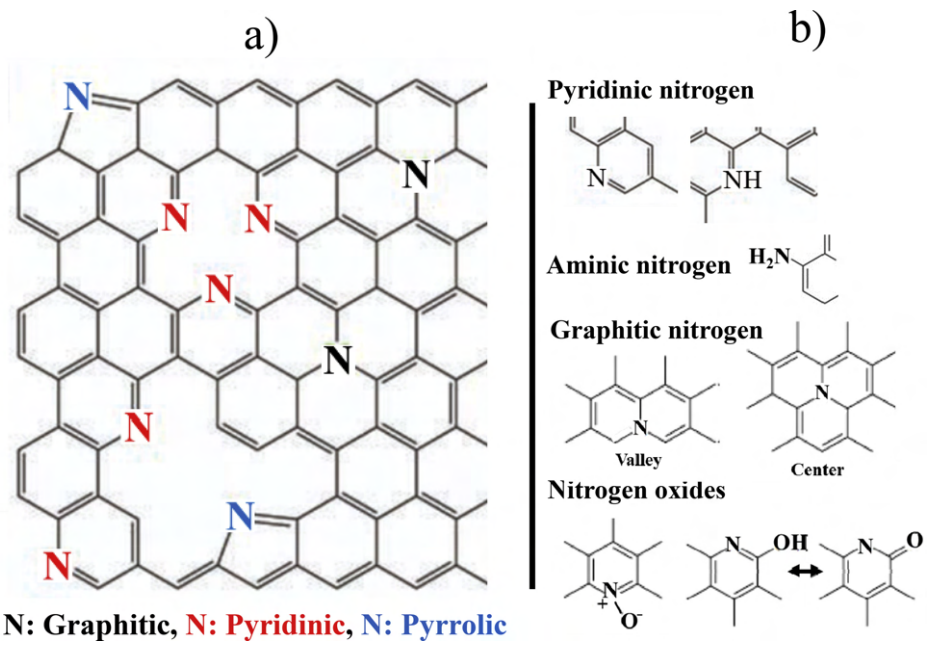

Figure 18. Various configurations of N in N-doped graphene materials [117].

Amine/amide nitrogen bonds are located at the edges of graphene lattice. Contrarily, pyridinic and graphitic form sp^2 hybridized configurations presented in the plane of graphene layers. Pyrrolic moieties (sp^3 hybridization) can be formed at the edges and in the plane of the lattice resulting in intra-structural defects [118]. In relation to the place of incorporation of nitrogen functional groups, pyridinic and pyrrolic groups in high concentration can lead to a decrease of electrical conductivity, due to the high number of defects. Pyridinic and pyrrolic nitrogen result in p-type conductor formation. On the other hand, graphitic nitrogen connected with three carbon atoms does not lead to the appearance of significant structural defects and forms n-type semiconductor [118].

Depending on the final application, also oxygen can be considered as a dopant, disrupting the graphene structure. Although it may be concluded that oxygen atoms show negative impact on graphene material properties, mainly decreasing electrical conductivity and increasing defect quantity, in electrochemical sensing applications electronegative oxygen moieties have a positive role as active sites for adsorption of several analytes.

Table 4. Advantages of heteroatom-doped graphene materials

Dopant	Main advantages of doping considering electrochemical sensing	Ref.
Sulfur	Increase of wettability, enhancement of electrical conductivity, improvement of electrocatalytic activity of redox reactions – generally improvement of sensitivity	[119]

Phosphorus	Enhancement of electrocatalytic activity and electrical conductivity, improvement of mechanical strength	[120]
Boron	Enhancement of conductivity	[115]
Nitrogen	Introduction of electropositively charged active sites for anionic analytes adsorption, increase of electrical conductivity, enhanced electrochemical activity for electrochemical reactions leading to decrease of oxidation/reduction potential values and in improved selectivity	[121]
Oxygen	Introduction of electronegatively charged active sites for cationic analytes adsorption, enhanced selectivity towards cationic analytes determination	[122]

Benefits associate to the use of different dopants are summarized in Table 4. Some of the above-described techniques to obtain graphene materials (paragraph 2.4) are also used for synthesis of doped-graphene materials. For this purpose, numerous modifications of CVD are proposed. Wei et al. [123] deposited N-doped graphene layers by CVD technique from the gaseous mixture of CH_4 and NH_3 on Si substrate modified with Cu as a catalyst. In this process, performed at 800 °C, nitrogen and carbon precursors dissociate on the catalytic sites and then form the final graphene-based material. Ammonia is one of the most often applied doping agents in the synthesis of N-doped graphene by CVD technique. During described procedure, nitrogen is mainly introduced into the graphene layer in the graphitic form leading to n-type semiconductor with increased electrical conductivity [123]. Depending on nitrogen precursor and its concentration the nitrogen content can vary from 0.2 to even 16 at.% [124].

CVD technique was also applied in boron-doped graphene synthesis. In this approach Jafari et al. [125] applied Hot Filament Chemical Vapor Deposition (HFCVD) using a mixture of boron oxide B_2O_3 and ethanol as boron and carbon precursors, respectively, and Cu foil as substrate. Tungsten in a diameter of 0.5 mm was proposed as a hot filament. The gaseous mixture was passed through the setup vertically, contrarily to usually applied horizontal flow (Figure 19). Hot filament, at a fixed temperature of 1500 °C, enables to decompose B and C precursors at 800 °C which, in the next step, form the final product on the substrate. Boron was mainly incorporated into graphene structure in the form of BC_3. However, XPS measurements revealed residual amounts of the starting B_2O_3 which are probably occluded between graphene nanosheets [125].

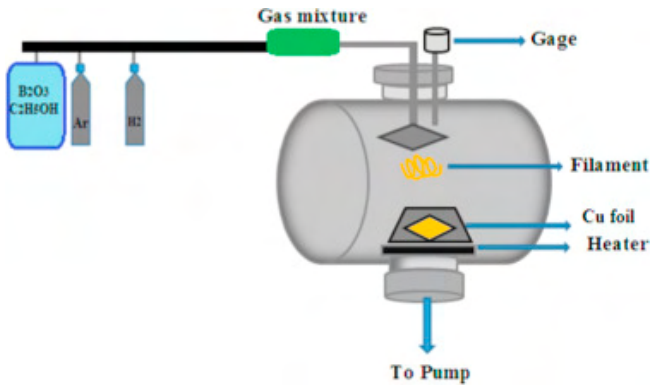

Figure 19. Scheme of HFCVD setup [125].

Interestingly, also epitaxial growth can be applied in the synthesis of B-doped graphene matrials. Norimatsu et al. [126] deposited B_4C films on SiC by thermal vapor deposition (TVD) and pulsed laser deposition (PLD). Modified substrates were then heated at high temperatures (ranging between 1200 – 1500 and 400 – 1600 °C, for TVD and PLD, respectively) under Ar flow. Due to the high concentration of boron in B_4C the final product was highly doped. The boron content was determined based on the correlation with hole concentration. Assuming that one boron atom creates one hole, the boron content in the doped material was 0.64 at.% [126]. Top-down techniques which can combine simultaneous reduction and doping are highly promising alternatives to bottom-up techniques. Considering chemical or thermal reduction of GO, frequently the reducing agent can play a double role acting also as a dopant. Hydrazine and ammonia are the most widely used nitrogen doping agents in chemical reduction, even though chemicals which can be decomposed to NH_3 are also applied, as for example urea, or more complex amines. Long et al. [127] proposed hydrothermal treatment of GO in the presence of chemical reducing agents. They compared two reducing/doping agents, hydrazine, and ammonia. The materials obtained at different temperatures (80, 120, 160 and 200 °C) differed in their elemental composition. When increasing temperature, the quantity of nitrogen decreased. In the samples obtained at lower temperatures (80 and 120 °C), N_2H_4 was adsorbed. At higher temperatures (160 and 200 °C) due to its low stability, N_2H_4 is decomposed leading to the incorporation of nitrogen mainly in the pyridinic form. In this study, a sample reduced chemically at 90 °C using hydrazine and ammonia was prepared for comparative purposed. The incorporation of nitrogen into the graphene structure during chemical reduction was significantly lower (1.21 vs. 5.21 wt.% for sample hydrothermally reduced at 80°C) confirming the key role of hydrothermal environment in nitrogen incorporation [127].

Depending on the precursor the main nitrogen functionality in the N- doped graphene material can be tailored. Wiench et al. [121] demonstrated the impact of N-precursor on the nitrogen

content and its functional distribution in the N-rGO obtained by hydrothermal treatment of GO at 180°C. The use of urea resulted in the majority of pyrrolic nitrogen whereas the reaction with amitrole yielded to rGO enriched in pyridinic nitrogen. In both cases, the GO reduction degree, expressed as oxygen content was similar (9.9 and 10.9 at.% for amitrole and urea, respectively). Amitrole, due to its higher nitrogen content lead to the incorporation of a higher amount of nitrogen compared with urea (11 vs. 7 at.%) into the rGO structure.

The predominant contribution of N as amine/amide was obtained in the rGO synthesized in the presence of guanidine. N-doped graphene material was obtained by hydrothermal treatment of GO in the presence of dopant (N-compound: GO mass ratio = 10:1). Moreover, amitrole and imidazole were also proposed as nitrogen dopants. The highest amount of nitrogen was introduced in the presence of amitrole (13.4 at.%), secondly guanidine (11.9 at.%) and the last imidazole (7.9 at.%). Moreover, oxygen content was similar for all samples, ranging between 9.4 to 10.4 at.%. In agreement with a previous work, amitrole enables to achieve a 0.8 at.% of pyridinic nitrogen [121]. The last dopant, imidazole yielded the highest content of pyrrolic nitrogen moieties [128].

Thermal annealing has been proposed for phosphorus incorporation. A mixture of GO and triphenylphosphine was mixed and heated at 1000 °C for 1h [129]. The resultant P-rGO product was characterized by low oxygen content of about 3.2 and 1.8 at.%. of incorporated phosphorus mainly in the P-O and P-C bonds. Another highly promising dopant is phosphoric acid which was proposed among others by Wen et al. [130]. They impregnated GO with phosphoric acid and then heated the mixture at 800 °C for 30 min. Considering the shorter time and lower temperature of synthesis, the introduced P content was competitive in comparison to triphenylphosphine (1.3 at.%).

Moreover, flash heating was used for nitrogen doping. Intense pulse light (IPL) was a source of heat. The flash heating process enables to heat samples at a temperature of about 1500 °C. The final product, FH-NrGO, was compared with N-rGO obtained using traditional thermal heating at 1500 °C (TH-NrGO), being melamine used as N precursor. Application of this approach resulted in an extremely high nitrogen content of 26 at.%., mainly in the pyridinic and graphitic forms, while it was about 5 times lower (5.38 at .%) when conventional heat treatment was applied. Moreover, application of flash heating with tunable irradiation energy enables to easily control the dopant content [131].

Recently co-doping seems to be highly promising, as it can boost the final material properties due to synergistic effects between dopants [115]. Oxygen functionalized graphene was thermally annealed at 800 °C in the presence of $(NH_4)_3PO_4$ under N_2 flow resulting in NPG

product. During this procedure precursor is decomposed to ammonia and phosphoric acid. Oxygen moieties and structural defects are responsible for binding N and P atoms. The optimal ratio of graphene to precursor which enables to dope graphene material with the highest efficiency was 1:2 (N and P contents: 3.7 and 1.3 at.%., respectively). To prove the significant impact of oxygen functionalities on doping effect, for comparative purposes the sample with lower oxygen content has been prepared by thermal annealing. In this case, the amounts of N and P introduced into rGO structure was considerably lower, 1.3 and 0.6 at.%., respectively, comparing to NPG [132].

2.3.2 Graphene-based nanocomposites

Far from the improvement of graphene-based materials properties by heteroatoms doping, the design and development of composite materials have also increased in interest between the scientific community in the last years. Graphene-based materials are being applied in the synthesis of composites with metal nanoparticles, metal oxides and conducting polymers, among others. From the point of view of their application in electrochemical sensing, the most important properties of metal oxides and metal nanoparticles are their good catalytical properties and enhanced electrical conductivity [133]. Also, the use of conducting polymers enables to achieve an improved electrical conductivity of the resulting composite. In addition, depending on the morphology of polymer, long polymer chains containing charged functional groups can facilitate molecules immobilization on the electrode surface. Summarizing, synthesis and application of composite materials can take advantage of synergistic effects between pure counterparts improving their final electrochemical performance [5,134].

2.3.2.1 Graphene-based composites with metal and metal oxide nanoparticles

Considering electrochemical detection, plenty of metal nanoparticles and metal oxides has been taken into account to produce suitable composites with graphene materials so far. However, nanoparticles or other inorganic counterparts of composites must meet several requirements. For example, it is highly desirable to apply nanoparticles whose sizes are small-scale providing sufficient number of accessible active sites for target analytes. However, smaller nanoparticles result in an enhanced surface area which, at the same time, is responsible for an increase in the capacitive current. For this reason, it is extremely important to find a compromise between the number of active sites and the capacitive current measured on the active material. Moreover, metal nanoparticles or metal oxides should exhibit good catalytic activity to improve the

selectivity of the whole setup. In case of electrochemical detection of biomolecules, also biocompatibility must be considered. The inorganic part of the composite should provide stable connection between the electrode surface and target molecules, protecting them from decomposition or denaturation in case of biomolecules. Thus, mainly noble metals (Au, Ag, Pd, Pt), but also metallic oxides of Fe, Sn, Cu, Mn, Ti, Zn and Ni are considered [133]. Moreover, nanoparticles also have a huge impact on the morphology of the composite preventing graphene layers from aggregation.

Mechanism of metallic nanoparticles formation is shown in Figure 20. Typically, it involves decomposition (hydrolysis in water-based solution or electrolysis under an applied electric potential) of metal precursor and its reduction to metallic nanoparticles using a reducing chemical agent or change of the potential. The process can be terminated before clusters formation, which results in smaller sizes of the as-obtained nanoparticles. As chemical reductants usually AA, sodium borohydride, ethylene glycol, amines and sodium citrate are used [135,136].

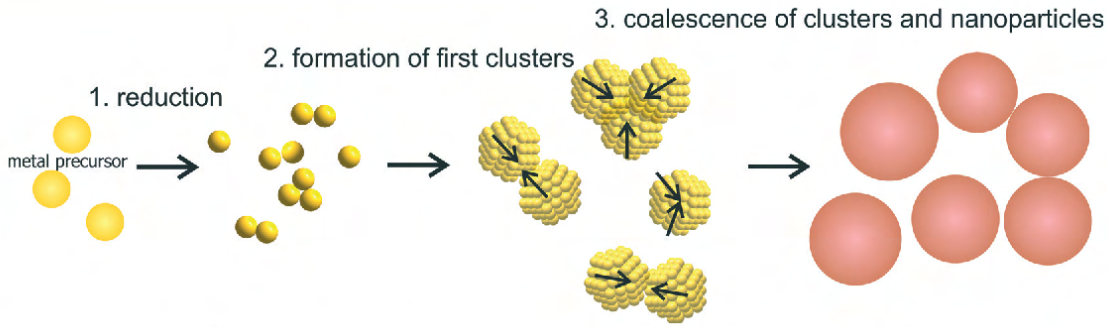

Figure 20. Growth of metallic nanoparticles [135].

There is a wide range of synthesis methods of binary graphene-based composites with metal and metal oxides nanoparticles. Processes can be performed in two ways. The first approach involves modification of the surface of graphene material with metal/metal oxide nanoparticles. It can be typically done by following a simple drop-casting method of previously prepared NPs, for example by chemical reduction or electrochemical deposition from the precursor solution on the graphene material surface.

Cui et al. [137] deposited chemically reduced rGO on the GCE surface. Then PtAu nanoclusters were electrodeposited at a constant potential of - 0.2 V for 400 s from the solution containing $HAuCl_4$ and H_2PtCl_6 as metal precursors. The average diameter of deposited clusters was 200 nm. rGO support is necessary to obtain bimetallic structures which were not observed during deposition on bare GCE. As-prepared composite was applied in hydrogen peroxide electrochemical sensing with high sensitivity, achieving an LOD of 8 nM. High catalytic

activity towards H_2O_2 electrochemical reduction can be ascribed to the sufficient number of PtAu nanoclusters [137].

An easy synthesis method mainly based on the weak Van der Waals interactions between graphene and metal was proposed by Benvidi et al. [138]. They compared the effectiveness of electrochemically deposited AuNPs and chemically reduced drop-casted AuNPs on rGO surface in simultaneous detection of levodopa, uric acid and folic acid. Hydrazine reduced GO was firstly deposited on GCE. In the chemical method, $HAuCl_4$ was reduced by sodium citrate. As-prepared AuNPs were deposited on the rGO/GCE electrode. On the other hand, electrodeposition was performed using chronoamperometry at - 0.2 V. It was revealed that AuNPs deposited by electrochemical technique showed more homogenous distribution indicating on a better control of the morphology of AuNPs by electrochemical techniques (Figure 21). Before electrochemical tests, electrodes were modified with 2-(3,4-dihydroxy phenyl)benzothia-zole (DHB) to increase the number of active sites leading to enhanced peaks currents. Electrochemically deposited AuNPs provided higher surface area for DHB chemisorption resulting in better electrochemical performance towards simultaneous detection.

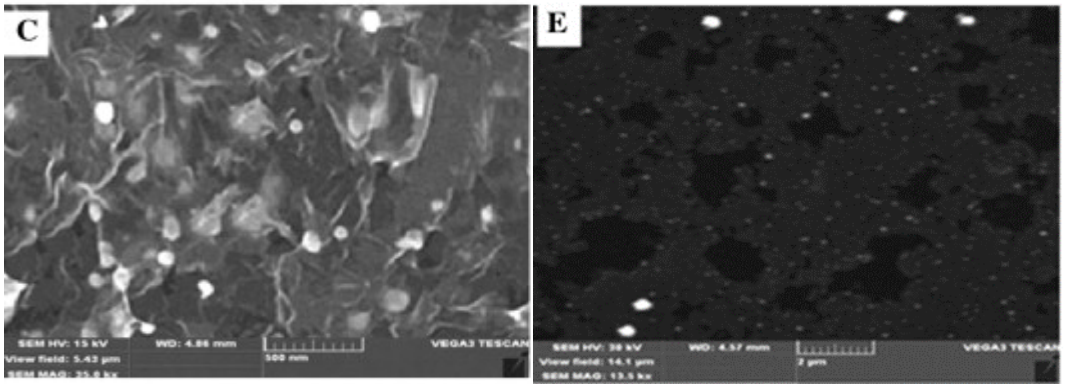

Figure 21. Comparison of rGO modification with AuNPs by electrochemical method (figure on the left) and chemical technique (figure on the right) [138]).

The second approach for obtaining graphene-based binary composites includes simultaneous synthesis of NPs and graphene material. In this approach chemical bonds between carbon from graphene layer and metal can be created, and/or NPs can be occluded by graphene material [139]. Substrates for this kind of synthesis can be metal/metal oxide NPs and graphene material precursors. Cu-rGO composites were prepared by simultaneous electrodeposition on ITO substrate using CV in the potential range between 0.0 and -1.5 V. The starting solution was composed of GO and 1mM $CuSO_4$. This technique enabled to obtain Cu nanoparticles with a size of about 2 nm and successful reduction of GO (increase of C/O ratio from 0.69 to 1.41). The as prepared electrode was applied in electrochemical nitrate detection. The morphology of

the composite was tuned by concentration of GO. A too high content of rGO in the composite implied lower CuNPs presence, negatively affecting its electrochemical performance to nitrate detection. The synergistic effect between composite counterparts was proved indicating an improved rate of charge transfer due to the presence of rGO and high catalytic activity of Cu for NO_3^- reduction reaction [140].

A conventional one-step synthesis procedure of metal NPs/graphene material has been also reported. $PdCl_2$ and GO were mixed in the presence of $NaBH_4$ as reducing agent. PdNPs of uniform sizes (5-10 nm, 29 wt.%) were dispersed onto the rGO graphene nanosheets. It has been proved by several researchers that -OH groups present in the GO structure play a double role as anchoring sites for Pd (or other ions) and as reducing agent. Subsequently, Pd/GO/GCE was applied in paracetamol sensing. The oxidation peak originated from paracetamol redox reaction appeared at lower potentials on this electrode compared to GO/GCE (463 vs. 475 mV). Moreover, the anodic peak current was about twice higher than for such electrode only modified with GO. The improvement of these two parameters clearly indicates synergistic effect between Pd nanoparticles and rGO [141].

Another interesting approach leading to production of metal oxide/graphene-based composites was proposed by Zhang's group [142]. They placed GO and $Cu(CH_3COO)_2 \cdot H_2O$ in an autoclave and treated them hydrothermally at 160 °C for 12 h. Simultaneous reduction of GO and Cu precursor was confirmed by XPS results. Moreover, less intensive peaks corresponding to oxygen moieties in comparison to the starting GO were recorded. In addition, mixed copper oxides were synthesized which was proved by characteristic peaks attributed to Cu_2O and CuO. The synthesized copper oxides particles were of micrometer range (1-3 μm) indicating that hydrothermal approach enables to obtain particles uniformly distributed as shown by SEM, even though with larger sizes than those synthesized by electrochemical techniques. Mixed Cu_xOHM/RGO composite was tested towards glucose sensing. Synergistic effect between RGO and Cu_xOHM was proved showing an improved electrocatalytical activity of the composite in comparison to pure counterparts, reflected by higher intensity of the peak currents. Moreover, graphene layers prevent the aggregation of copper oxides [142].

2.3.2.2 Graphene-based composites with conductive polymers

Due to the low cost and ease of preparation, another promising counterpart of composites with graphene materials for electrochemical sensing applications are conducting polymers (CPs). The most of them consist of conjugated double bonds resulting in delocalized electrons responsible for electrical charge transfer and conductivity. However, CPs can also conduct

electricity basing on ionic conductivity or complexing with charge transfer. In electrochemical applications mainly polymers which conduct electricity through ionic conductivity are being applied, as polyaniline (PANI), polypyrrole (PPy), polythiophenes, and mainly polyethylenedioxythiophene (PEDOT). CPs are usually synthesized following chemical oxidative polymerization procedures or electropolymerization techniques. Similarly, to composites with metallic nanoparticles, composites with CPs can be obtained in two different ways as their synthesis can cover separate production of both counterparts and their subsequent combination or the simultaneous one-pot synthesis of the whole composite. As a result of selected procedure, the final products can differ in their morphology and properties [143]. Furthermore, doping of CPs is a key issue as it can lead to their improved electrical conductivity. This can be achieved by removing or adding electrons from (oxidation, p-doping) or into the polymer structure (reduction, n-doping), respectively [144].

Among available CPs, PANI, which can exist in different oxidation states (Figure 22), is commonly applied in electrochemical detection systems due to the tunability of its properties, environmental stability and high conductivity. Moreover, PANI exhibits positively charged nitrogen moieties which can enhance its affinity to oppositely charged ions during electrochemical detection [145].

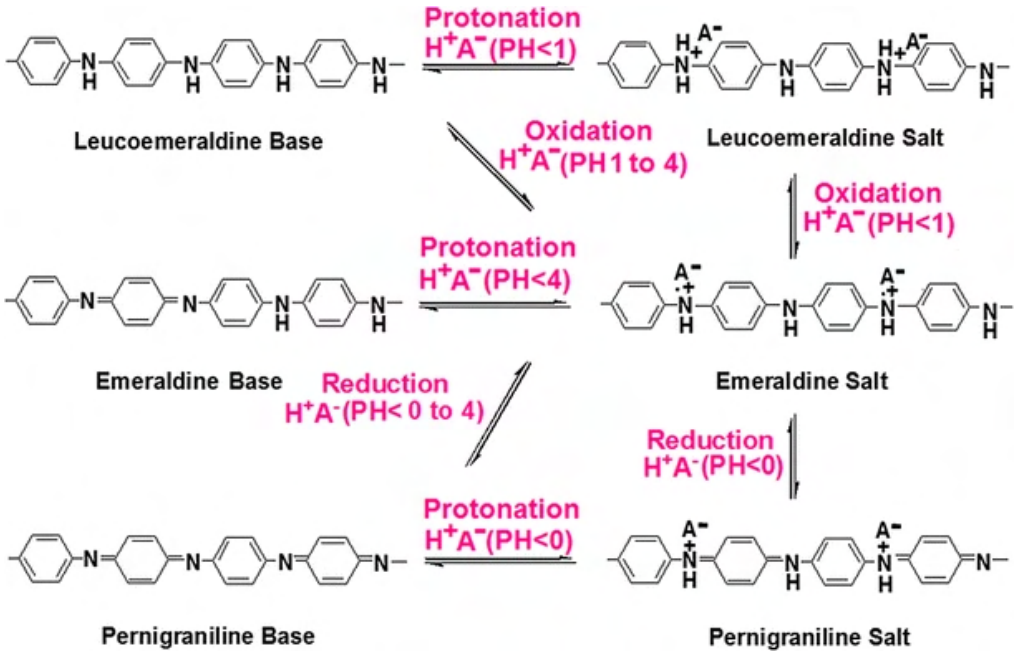

Figure 22. Possible oxidation states of PANI [145].

Depending on the oxidation state, PANI differs in color. Transparent leucoemeraldine is a fully reduced form of PANI, while purple pernigraniline is related to the fully oxidized form, resulting in an insulator. In addition, blue emeraldine base (EB) corresponds to partially

oxidized/reduced PANI form. To obtain conductive PANI it is necessary to perform protonation of EB in acidic medium. In this process, emeraldine salt (ES) which provides the highest electrical conductivity, is synthesized [143].

Regarding potential composites, PANI-GO can be synthesized, as proposed by Muralikrishna et al. [146], by the in-situ oxidative polymerization of aniline monomer in the presence of GO [146]. The synthesis was performed in a HCl solution with ammonium persulfate (APS) at 5 °C. The product was finally heated at 80 °C for 4h to obtain a hydrogel which was then applied as working electrode modifier to Pb^{2+} electrochemical detection. The as-obtained material was characterized by a uniform distribution of PANI nanofibers on GO sheets. EDS studies revealed that PANI-GO composite contained about 14% of nitrogen coming from PANI. GO is mainly responsible for the increased affinity of the electrode surface to Pb^{2+} ions, due to the presence of electronegatively charged oxygen groups. Moreover, the introduction of PANI in the composite resulted in a lowered resistivity and higher electron transfer rate in comparison to pure composite counterparts [146].

Another approach of PANI-containing graphene composites was proposed by Naghib et al. [147]. In the first step FTO (fluorine-doped tin oxide) glass was modified with methacrylated GO (MeGO). Then, aniline monomer was subjected to electropolymerization on the surface of the electrode through CV using a H_2SO_4 solution as electrolyte. The electropolymerization was performed using 20 cycles in the potential range between -0.4 to 1.2 V to obtain a uniform coverage of the electrode surface with PANI flakes. The as-prepared electrode was tested towards AA sensing. Similarly, to previous example, the main role of PANI was the improvement of electrical conductivity negatively impacted by oxygenated groups and methacrylic groups present in GO. On the other side, methacrylic groups are also mainly responsible for the AA attraction to the electrode surface.

Other conductive polymers have been also proposed in electrochemical sensing. Among them PPy shows a high potential in electrochemical detection systems mainly due to its high biocompatibility [148]. Moreover, the high stability of this polymer favors its application in the synthesis of molecularly imprinted polymers (MIPs), which appears as very promising candidates to achieve a suitable electrode material [149]. However, researchers also applied them in the detection of common electroactive molecules such as AA. As an example, a GCE-EG-MIP sensor was proposed by Oliveira et al. [150]. In this work, graphene (EG) was obtained by electrochemical exfoliation of a graphite electrode, in $(NH_4)_2SO_4$ solution, and subsequently drop casted on the GCE surface. To obtain the PPy-based MIP active electrode material, electropolymerization in the potential range -0.6 to 0.8 V from the solution containing $LiClO_4$,

pyrrole monomer and target analyte was performed. After that, target analyte was precisely removed from the matrix. By applying MIP in the electrochemical detection of AA it was possible to perform its determination in the pH value of 7.2. As it is known, AA has a pK_a value of 4.17 which results in the formation of anions at pH values close to the physiological one. It can result in the repulsion of the analyte from the electrode surface by the electronegative oxygen groups present in EG. Due to the unique AA print, the selectivity towards its detection was boosted, even though the molecularly imprinted active sites might be permanently fouled decreasing the sensor performance [150].

Going further, PEDOT possess the highest electrical conductivity among the CPs pointed above. Moreover, it can be easily functionalized by negatively charged sulfonic groups which is beneficial in the detection of several molecules in cationic form [151]. rGO-PEDOT:PSS/GCE film was proposed in electrochemical nimesulide and piroxicam detection by Wong et al. [152]. In this work, GO was chemically reduced and mixed with PEDOT:PSS and then dropped casted onto GCE surface. The bonding between rGO and PEDOT:PSS was achieved through hydroxyl groups of rGO and sulfonyl groups of PEDOT:PSS. Moreover, such mixture enabled to disperse PEDOT:PSS homogeneously between rGO nanosheets resulting in avoiding graphene layers aggregation. As a result, the combination of rGO and PEDOT:PSS lead to an improved conductivity and accessibility of surface area for target analytes. Furthermore, PEDOT:PSS provided also functional groups resulting in an enhanced affinity to nimesulide and piroxicam onto the electrode surface [152]. In other work, Huang et al proposed a one-pot approach to the preparation of a PEDOT/GO modified electrode towards UA detection [153]. In this case, a mixture of GO and EDOT monomer was drop casted onto the ITO substrate. The setup was treated under a constant potential (1.2 V) for 150 s to obtain the final working electrode. The proposed procedure enabled, in a facile way, to control the modifier layer thickness by tuning the drop volume. According to previous reports, in the electrochemical UA detection, it is crucial to have available as thinner layers as possible, as they accelerate the electron transfer rate.

Summarizing, there is a variety of techniques in order to obtain binary composites, resulting in materials with different properties and morphology. However, there is still a plenty of novel modifications to be afford, which could facilitate protocols and enhance the electrochemical properties of final materials.

2.3.2.3 Graphene-based ternary composites

To boost the electrochemical performance of different detection setups ternary composites including graphene-based materials, conducting polymers and metal/metal oxides nanoparticles have been recently proposed. As stated, the combination of different components into one material results in improved physical and chemical properties as a result of synergistic effects. Although there are several approaches covering different synthesis combinations, the most popular one is pre-synthesis of graphene-based material/conductive polymer composite and further introduction of metallic nanoparticles or metal oxides.

Demirkan et al. [154] performed oxidative polymerization of PPy in the presence of GO, phosphoric acid and APS. Then, hydrazine was added to reduce GO. After obtaining the binary composite, $PdCl_2$ was added and Pd particles were obtained by microwave assisted synthesis procedure. The as-prepared composite, with an average Pd particles size of about 3 to 4 nm, was applied as GCE modifier and subsequently tested towards the simultaneous AA, DA and UA detection. The proposed ternary composite was resistant in acidic pH environments (pH value of about 3) in which simultaneous detection was performed to avoid undesirable electrode fouling by poly-DOPA, which is created at higher pH values.

Following a similar synthesis procedure, a PANI-based sensor was proposed towards nitrite detection in water samples. GO was mixed with aniline in the presence of HCl and APS. AuNPs, in the form of colloidal solution, was obtained by mixing $HAuCl_4$ with trisodium citrate as reducing agent. Then, binary GO-PANI composite was mixed with AuNPs and stirred for 12h. In situ polymerization resulted in connected GO-PANI network with high number of active sites accessible for the successful attachment of Au precursor. An average size of AuNPs was in the range of 70-80 nm. PANI and AuNPs enhance electron transfer between solution and electrode surface due to improved conductivity. Moreover, homogenously dispersed AuNPs catalyze nitrite oxidation leading to improved sensor performance (LOD = 170 nM) [155].

Other approaches cover one-pot synthesis. For example, Gao et al. [77] proposed methodology in which in the first step EDOT monomer was mixed with H_2PtCl_6. The reaction was performed for 8h and after this time GO was added and subsequently reduced by $NaBH_4$. The second step was performed for 6h resulting in Pt-PEDOT/rGO composite, as PEDOT plays and excellent role as substrate for PtNPs deposition. An average size of Pt-PEDOT was 140 nm. The as synthesized material was applied in detection of caffeic acid. Due to the synergistic effect between composite components, the charge transfer and electrocatalytic properties were

improved, as the intensity of anodic and cathodic peak currents increased in comparison to pure counterparts. As a result, the LOD of caffeic acid was 2 nM in a liner range of 0.005 to 50 μM. Core-shell structures seem to be also highly promising. Au@graphene core-shell nanoparticles (AG)-doped conducting polymer PEDOT were proposed towards paracetamol detection. These core-shell nanostructures protect NPs from aggregation and loss of unique properties. Furthermore, AG-core-shell structures (Figure 23) can be easily obtained by CVD technique. The silica applied as $HAuCl_4$ carrier. The as-obtained powder was placed in a furnace and CVD, using methane as carbon precursor, was performed. In the final step silica was removed by HF. It is well seen that small size nanoparticles were covered by graphene layers (Figure 23b and c). Ternary composite was obtained by electrodeposition in EDOT and PSS solution containing previously prepared AG core-shell nanostructures. This approach enables to incorporate AG nanostructures in the PEDOT film. The peaks corresponding to paracetamol electrochemical reaction were more distinctive in comparison to unmodified GCE and electrodes modified with separate composite components. These good results are explained by the enhanced conductivity and developed active surface area after PEDOT introduction [156].

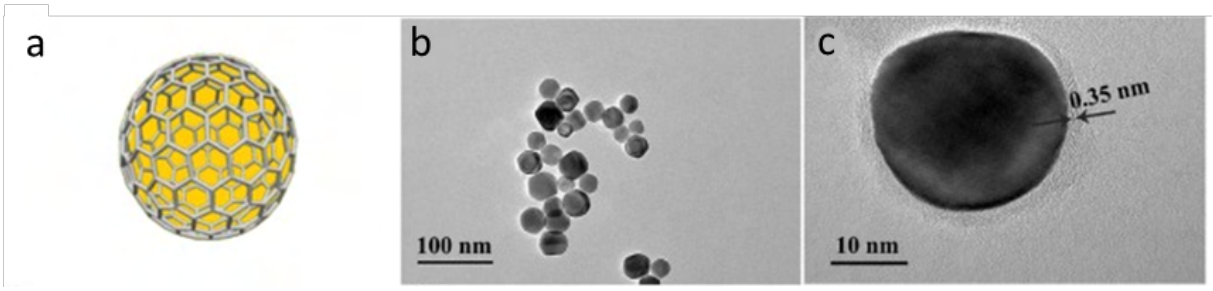

Figure 23. (a) Schematic diagram, (b) TEM image, (c) HR-TEM image of AG core-shell nanoparticles [156].

As an alternative, all ternary composite components can be directly synthesized on the electrode surface using electrochemical techniques. Liu et al [157] firstly deposited rGO and PEDOT on the GCE surface from the solution containing GO and EDOT applying CV in the potential range between -1.5 to 1.1 V. Then, Cu_2O particles were deposited from a $CuSO_4$, citric acid and NaOH solution using chronoamperometry at an applied potential of -1.0 V for 30 s. The as-obtained non-enzymatic sensing platform showed a promising performance towards glucose electrochemical detection. Glucose directly reacts with Cu^{2+} ions originated from Cu_2O oxidation and layered structure enhanced the electron transfer rate, resulting in an increased sensitivity and LOD value of 140 nM.

A hydrothermal treatment has been also proposed to synthesize ternary composites. Fe_2O_3-rGO binary composite was obtained, by mixing $FeCl_2$ in the presence of ammonia with GO and

submitting the mixture to a hydrothermal treatment at 170 °C for 4 h. Then aniline, APS and HCl were mixed with Fe_2O_3-rGO and subsequent oxidative polymerization for 36h at -5 °C was conducted. As a result, PANI particles were homogenously distributed in the whole volume of binary composite which consisted of wrinkled graphene sheets covered with 100 nm size Fe_2O_3 particles. The proposed composite has been applied to hydroquinone detection showing an enhanced charge transfer. PANI fibers improve stability of the composite which resulted in a 2D structure exhibiting an increased surface accessible for hydroquinone detection, which leads to a reduction of the electroactive molecule diffusion time [158].

Facile sandwich-structured nanocomposites show also improved electrochemical potential. They have been proposed, among others, for the AA electrochemical detection. Firstly, a substrate consisting of GO functionalized with carboxyl groups was prepared. Then, it was simultaneously reduced and doped with nitrogen and subsequently deposited onto FTO. Afterwards, a layer of Ag nanoparticles was deposited by chronoamperometry. It resulted in the enhancement of the surface accessible for the last layer, which was PANI, electrodeposited by CV, and acting as protector against AgNPs oxidation. Moreover, the electric currents recorded during oxidation of AA on PANI and NFG/PANI composite were comparable, which agreed with a poor stability of PANI in aqueous solution, lately improved by the AgNPs adhesive layer. The synergism between PANI and AgNPs is highly visible. All mentioned above advantages resulted in an improved stability, electrical conductivity, and charge transfer. Even though AgNPs were mainly coated by PANI, they displayed a huge impact on the improvement of charge transfer during oxidation of AA [159].

Depending on desired properties of composites and requirement from their final application, the selection of the most beneficial synthesis route is crucial. To improve the catalytic properties and increase the available active sites for target analytes, it seems that deposition of metallic nanoparticles on the surface of pre-treated graphene and/or conductive polymer is the most suitable choice. Moreover, typical functional groups present in the structure of graphene-based materials and conductive polymers are great substrates for the attachment, and further reduction, of metallic nanoparticle precursors. As described above, the wide range of approaches and facility of modifications provide a huge field to synthesis structures with unique morphologies.

2.3.3 Recent trends in graphene-based materials for DA and DCF electrochemical detection

Electrochemical detection of DA has been previously reported by using several electrochemical techniques and different electrode modifiers. However, there is still an urgent need to design and develop non-complicated electrode modifiers which enable an improvement of resulting sensors working parameters even in the presence of interferences. In this context, recent advances in the detection of DA are summarized in Table 5. Conductive polymers as PPy and PEDOT have been thoroughly investigated for this application. However, PANI provide a higher potential in such application due to its low preparation cost and excellent electrical properties. Moreover, composites with metallic nanoparticles, mainly noble metal nanoparticles (Pd, Pt, Au) have been commonly tested in electrochemical DA sensing in the last few years. However, it is worth to replace noble metals with cheaper metallic nanoparticles to reduce cost of active electrode materials preparation.

Liao et al. [160] proposed porous graphene complex with surfactant, dimethyldioctadecylammonium (DODA), for DA detection. Firstly, GO was synthesized using a modified Hummer's method. In the next step GO/DODA complex was prepared by mixing the graphene material with DODA dissolved in chloroform. The as-prepared complex was casted onto ITO glass surface and subsequently electrochemically reduced to obtain rGO/DODA in a honeycomb-patterned porous structure. SEM observation revealed high porosity of the complex. During the synthesis, DODA was inserted between GO layers leading to an increase of d-spacing and preventing them from aggregation. Final electrochemical measurements revealed the high electrochemical potential of rGO/DODA complex towards DA, reaching a LOD of 120 nM.

Hsieh et al. [161] proposed a facile approach for developing a non-enzymatic rGO-supported Pd-nanocubes (Pd-NCs) composite. Both, Pd-NCs and rGO were prepared by chemical reduction of 0.01 M H_2PdCl_4 by AA in cetyltrimethylammonium bromide (CTAB) and GO by hydrazine, respectively. Then, counterparts were mixed in the weight ratio of 3:7 (Pd-NCs:rGO). The as-prepared slurry was applied as GCE modifier to be used as working electrode in DA electrochemical detection system. The obtained SEM images revealed that Pd particles, in the form of nanocubes (23 nm of length) were uniformly distributed within rGO layers. Pd-NCs mainly acted as DA oxidation catalyst, even though the anodic peak current intensity was improved by rGO introduction, resulting in an enhanced sensitivity towards target analyte. The

sensor works linearly in the concentration range 20- 220 μM presenting a LOD value of 7 μM [161].

As stated, ternary composites have become more popular, recently. DA was successfully detected using ternary Fe_3O_4@PPy/rGO as GCE modifier. In this approach, oxidative polymerization of PPy was performed in the presence of HCl. Fe_3O_4 in the form of nanorods were uniformly deposited on the PPy/rGO by following a chemical reflux technique in the presence of urea for 28h. Nanorods, showing a length close to 150 nm and a width of 50 nm, increased the roughness of electrode material increasing the number of active sites for successful analyte adsorption. Moreover, they also act as pillars avoiding rGO stacking. Synergistic effect between composite components resulted in detection LOD value to DA sensing of 63 nM in the linear range between 0 to 100 μM [162].

In parallel, DCF is an environment contaminant whose detection has been growing in interest in recent years, due to an increased environmental awareness. Moreover, in the field of electrochemical sensing, and far from obtaining suitable electrode modifiers, another key factor is the size of the electrochemical setup selected to perform the analysis together with the possibility of make measurements in a real time. It is well-seen (Table 5) that there are just few works regarding electrochemical DCF detection applying electrodes based on graphene materials and its composites, none of them applying IPEs.

DCF has been previously detected by Karuppiah et al. [163]. They proposed GO functionalized with carboxyl groups as active electrode material. GO was prepared by a modified Hummer's method, using monochloroacetic acid to convert hydroxyl groups to carboxyl ones. Commonly used GO/GCE presented lower anodic peak currents than GO functionalized with -COOH groups. It has been denoted that -COOH groups are responsible for improvement of mechanical strength and electrical conductivity of electrode material. LOD defined applying LSV technique was 90 nM.

There are also works presenting application of SPCEs toward this analyte. Even though these electrodes are more popular and advanced, at the same time they are also more complex and expensive than IPEs. To simplify and reduce cost of electrodes fabrication maintaining possibility of real time measurements, IPEs are presented as a competitive and promising alternative. Kimuam et al. [164] proposed PtNFs/rGO modified SPE towards DCF electrochemical detection. SPE was made of PVC with screened silver and carbon inks acting as reference and working/counter electrodes, respectively. GO was mixed with PtNFs precursor (H_2PtCl_6) which then was dropped on the SPE. The electrode was treated electrochemically to perform simultaneous GO and H_2PtCl_6 reduction. PtNFs homogenously covered graphene

layers which led to improved sensor working parameters for DCF electrochemical sensing comparing to rGO and PtNFs.

Table 5. Operational parameters of sensors based on graphene-related materials and their composites for DA and DCF sensing (data from articles published between 2013-up to now)

Active electrode material	**WE**	**EC Method**	**LOD [nM]**	**LR [µM]**	**Ref.**
		DA			
rGO/DODA	ITO	DPV	120	0 – 40	[160]
N-rGO-180–8	GCE	DPV	630	2.5 – 100	[122]
Pd-NC/rGO	GCE	AMP	7000	20 – 220	[161]
Ag-rGO	GCE	DPV	1000	10 – 70	[165]
N-rGO/MnO	GCE	DPV	3000	10 – 180	[166]
Pd@α-MnO_2/G	GCE	DPV	86	0.2 - 425	[167]
CdTe QDs-Gr/GC	GCE	DPV	330	1 – 500	[168]
Au@Pt/GO	GCE	AMP	110	0.5 – 177.5	[169]
AuPtNPs/S-NS-GR	GCE	DPV	6	0.001 - 400	[170]
Cu_2O-RGO	GCE	SDLSV[1]	6	0.01 – 10; 10 - 80	[171]
rGO/$BiVO_4$	GCE	SWV	98, 713	0.25 – 5; 10 – 100	[172]
ZnO-rGO-AuNPs	SPE	DPV	294	0.5 – 100	[173]
PANI-GO	GCE	DPV	500	2 – 18	[174]
OPPy/ERGO	GCE	DPV	500	2 – 160	[175]
PPy/Graphene	GCE	AMP	2300	100 - 1000	[176]
NG/PEDOT	GCE	DPV	50	0.2 - 90	[177]
PEDOT-modified LSG	LSG	DPV	330	1.0 – 150	[178]
GO/PEDOT:PSS	Au	DPV	8.0	$0.8 \cdot 10^{-3}$ – 5; 5 - 50	[179]
rGO/Pd@PPy	GCE	DPV	56	10^3 – 10^5	[154]
Fe_3O_4@PPy/rGO	GCE	DPV	63	0 – 100	[162]
		DCF			
GO-COOH	GCE	LSV	90	1.2 – 400	[163]
EGr-$Co_{1.2}Fe_{1.8}O_4$	SPCE	DPV	1	0.001 – 0.01	[180]
PtNFs/rGO	SPE	DPV	40	0.1 – 100	[164]
NiNPs/ERGO	GCE	SWV	90	0.250 – 125	[181]
PDDA-Gr	GCE	DPV	609	10 – 100	[182]
$Co(OH)_2$ -RGO	CPE	SWAdSW[2]	8	0.025 – 1.55	[183]
PANI-RGO	CPE	DPV	3710	16.88 – 27.35	[73]

3 Aims and scope of the thesis

The main aim of this thesis is the design and development of electrochemical sensors based on graphene materials as active sensing GCE modifier for electrochemical sensing of DA, AA, UA and DCF.

Having a broad outlook on recent trends on the topic of electrochemical sensing, on one hand three different groups of graphene-based nanocomposites have been selected as suitable GCE modifiers towards electrochemical detection of abovementioned target analytes. On the other hand, a novel concept of IPEs is proposed for DCF sensing widening the scope of available electrochemical sensors.

To achieve these general goals, several specific objectives have been proposed:

- Synthesis of reduced graphene oxide (RGO) and nitrogen-doped reduced graphene oxide (NRGO), by hydrothermal treatment, which played a role as support for subsequent electrodeposition of gold nanoparticles (AuNPs). Assessment of the impact of N-groups introduced into the rGO structure on the AuNPs deposition. Electrochemical characterization of the as-prepared materials towards individual sensing of DA, AA and UA and for their simultaneous detection (interference study).
- Synthesis of a series of graphene-based nanocomposites (hydrothermal treatment) based on thermally reduced graphene oxide (TRGOs), obtained at different temperatures, and different amounts of PANI as conductive polymer. Evaluation of the influence of the reduction degree of TRGOs on PANI distribution. Research on the electrochemical performance of selected nanocomposites for DA and DCF detection.
- Synthesis (hydrothermal treatment) of binary (Fe_2O_3-SnO_2/RGO) and ternary (Fe_2O_3-SnO_2/RGO/PANI) graphene-based nanocomposites. Investigation of the positive contribution of selected inorganic components (Fe_2O_3 and SnO_2) and PANI on the electrochemical behavior of resulting materials for DA and UA sensing.
- Design and development of a novel concept of miniaturized sensing platforms towards DCF electrochemical detection. Optimization of GO-based inks, inkjet-printing processing parameters and post-processing treatments for obtaining IPEs on Kapton® as flexible substrate.

The scope of this thesis is graphically summarized in Scheme 1.

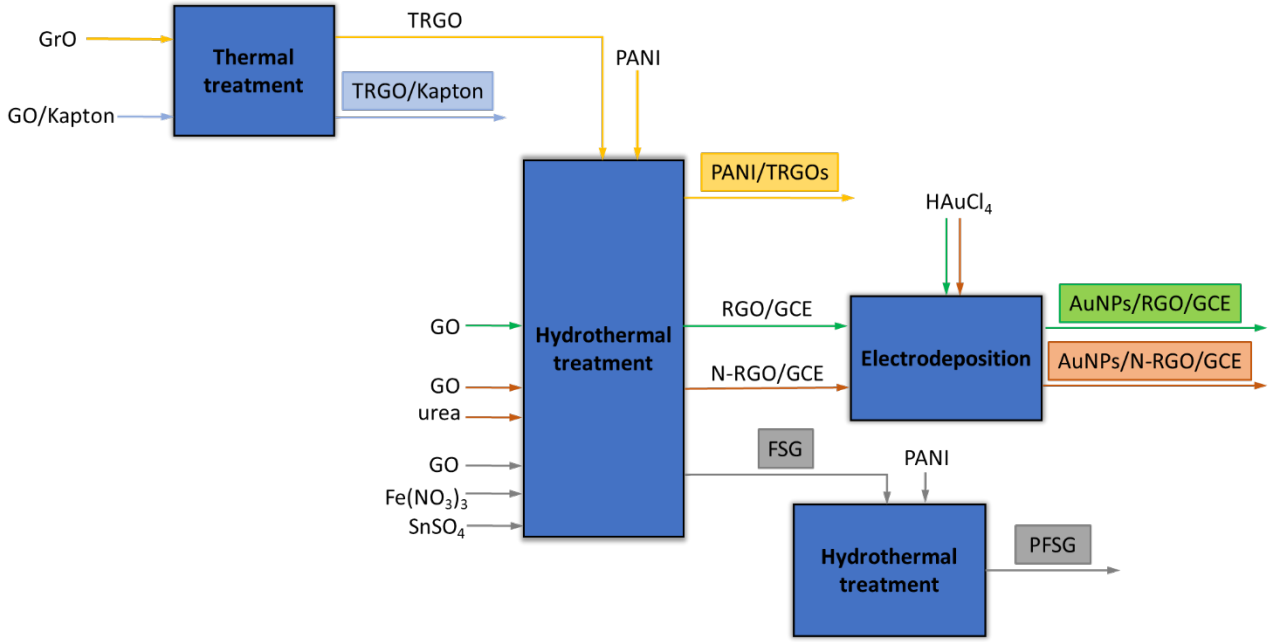

Scheme 1. Scheme of the scope of this thesis.

4 Experimental

4.1 Materials and reagents

- Synthetic graphite AG-239L C-NERGY KS 6L, TimCal,
- Synthetic graphite powder, particle size < 70 μm, from Sigma-Aldrich
- Anthracene oil (AO)- derived graphite
- Urea, CH_4N_2O, Sigma-Aldrich,
- Chloroauric acid, $HAuCl_4 \cdot 3H_2O$ Sigma-Aldrich,
- Allumina oxide, Al_2O_3, grain sizes 300 and 50 nm, Sigma-Aldrich,
- Nafion® D-520 dispersion, 5% w/w in water and 1-propanol, Alfa Aesar
- MilliQ water,
- Dopamine, hydrochloride, $C_8H_{11}NO_2 \cdot HCl$, Sigma-Aldrich,
- L-ascorbic acid, $C_6H_8O_6$, Sigma-Aldrich,
- Uric acid, $C_5H_4N_4O_3$, Sigma-Aldrich,
- Diclofenac sodium salt, $C_{14}H_{10}Cl_2NNaO_2$, Sigma Aldrich
- Potassium dihydrogen phosphate, KH_2PO_4, CHEMPUR
- Dipotasium hydrogen phosphate, K_2HPO_4, CHEMPUR
- N,N-Dimethyloformamide (DMF), C_3H_7NO, POCH

- Ammonium hydroxide, NH_4OH, 25 %, p.a., CHEMPUR
- Triton X-100®, 98 %, Sigma Aldrich
- Sodium dodecyl sulphate, Sigma Aldrich
- Carbon black - VULCAN® XC72 carbon black, CABOT
- Aniline, C_6H_7N, ≥ 99,5 %, Sigma-Aldrich
- Iron nitrate (III), $Fe(NO_3)_3 \cdot 9H_2O$, ≥98 %, Sigma-Aldrich
- Tin sulfate (II), $SnSO_4$, ≥95 %, Sigma-Aldrich
- Acetone, Avantor Performance Materials
- Hydrochloric acid, 1 M HCl, Avantor Performance Materials
- Ammonium persulfate, $(NH_4)_2S_2O_8$, ≥98 %, Sigma-Aldrich
- Creatinine, $C_4H_7N_3O$, Sigma Aldrich
- Trisodium citrate, $Na_3C_6H_5O_7 \cdot 2H_2O$, Sigma Aldrich
- Sodium chloride, NaCl, Eurochem
- Potassium chloride, KCl, Eurochem
- Ammonium chloride, NH_4Cl, CHEMPUR
- Calcium chloride, $CaCl_2 \cdot 2H_2O$, CHEMPUR
- Magnesium sulfate, $MgSO_4 \cdot 7H_2O$, CHEMPUR
- Sodium bicarbonate, $NaHCO_3$, POCH
- Sodium oxalate, $Na_2C_2O_4$, POCH
- Sodium sulfate, Na_2SO_4, CHEMPUR
- Sodium dihydrogen phosphate, NaH_2PO_4, CHEMPUR
- Disodium hydrogen phosphate, Na_2HPO_4, CHEMPUR
- Hydrogen dioxide, H_2O_2, Sigma Aldrich
- DuPont™ Kapton®

4.2 Starting materials

4.2.1 Graphene-based materials

Graphene oxide (GO) was synthesized following a modified Hummer's method [184]. Briefly, 2 g of graphite (C-NERGY KS 6L, TimCal, grain size $d_{50} < 3{,}4$ μm, purity 99,98 %) was placed in a flask and mixed with 96 mL of 98 % H_2SO_4 and 2 g of $NaNO_3$. In the next step, the flask was cooled to 7-9 °C in an ice bath and 12 g of $KMnO_4$ were added to the mixture under constant stirring. The mixture was heated to 35 °C and stirred for 3h. The next step covered addition of

400 mL of H_2O_2 (3 wt.%). The as-obtained graphite oxide (GrO) was washed with Milli-Q water until neutral pH value of supernatant. Finally, GrO was exfoliated in a sonication bath for 2 h, keeping constant cooling, to obtain the GO aqueous suspension.

Reduced graphene oxide (RGO) was prepared by hydrothermal treatment of GO (1 mg mL^{-1}) in an autoclave (PARR 4564 equipped with automatic controller PARR 4848, Parr Instrument Company, Moline, IL, USA, Figure 24). The hydrothermal treatment was performed at 180 °C for 12 h (mixing speed = 200 rpm). When the reaction was finished, the reactor was cooled down to the room temperature under constant stirring. The product was washed with Milli-Q water and isopropanol in a centrifuge at 5000 rpm and subsequently vacuum-dried overnight at 60 °C. NRGO was obtained following the same protocol, but in the presence of urea as nitrogen source. The weight ratio between GO and urea was 1:10.

Figure 24. Autoclave (PARR 4848, Parr Instrument Company, Moline, IL, USA) used for the hydrothermal treatments.

Thermally reduced graphene oxides (TRGOs) were obtained by one step thermal exfoliation/reduction treatment of GrO at INCAR. Selected GrO was previously obtained by the oxidative treatment of an anthracene oil (AO)-derived graphite using a modified Hummers method [109]. GrO was then exfoliated and reduced by flash pyrolysis in a tubular furnace at a controlled temperature (below 300 °C) and then ramp-heated (5 °C min^{-1}) up to the final temperature (400, 700 and 1000 °C, t_R=1 h) under inert atmosphere (N_2 flow of 200 mL min^{-1}) [109]. The as-prepared TRGOs were labelled as TRGO400, TRGO700, TRGO1000.

4.2.2 Graphene oxide (GO)-based inks formulation for inkjet printing and post-processing of inkjet-printed electrodes (IPEs)

GO for inks formulation was prepared starting from synthetic graphite powder (particle size < 70 µm, from Sigma-Aldrich) following a modified Hummer's method previously described [184]. The obtained GO aqueous suspension, at a concentration of 12000 ppm, was diluted to 4000, 7000 and 9000 ppm (GO-X, where X is a concentration of GO). Different inks additives were also evaluated. Firstly, impact of suitable surfactants as Triton X-100 (GO_X_TX) and SDS (GO_X_SDS) were assessed by adding them to GO in a 2:1 (w/w) ratio. Then, the incorporation of carbon black (CB) into inks formulation (CB:GO = 1:35 w/w) and its role on resulting properties was investigated. Inks formulations under evaluation were labeled as GO-X_S_CB, where S is tested surfactant. Graphical summary of the steps followed in the optimization is presented in Scheme 2. After printing of GO-based inks on Kapton®, the resulting IPEs were thermally treated at 400 °C (t_R=1h, heating rate 2°C min^{-1}) in a tubular furnace under inert atmosphere (N_2 flow: 200 mL min^{-1}) obtaining GO-X_S_CB_TR400/K.

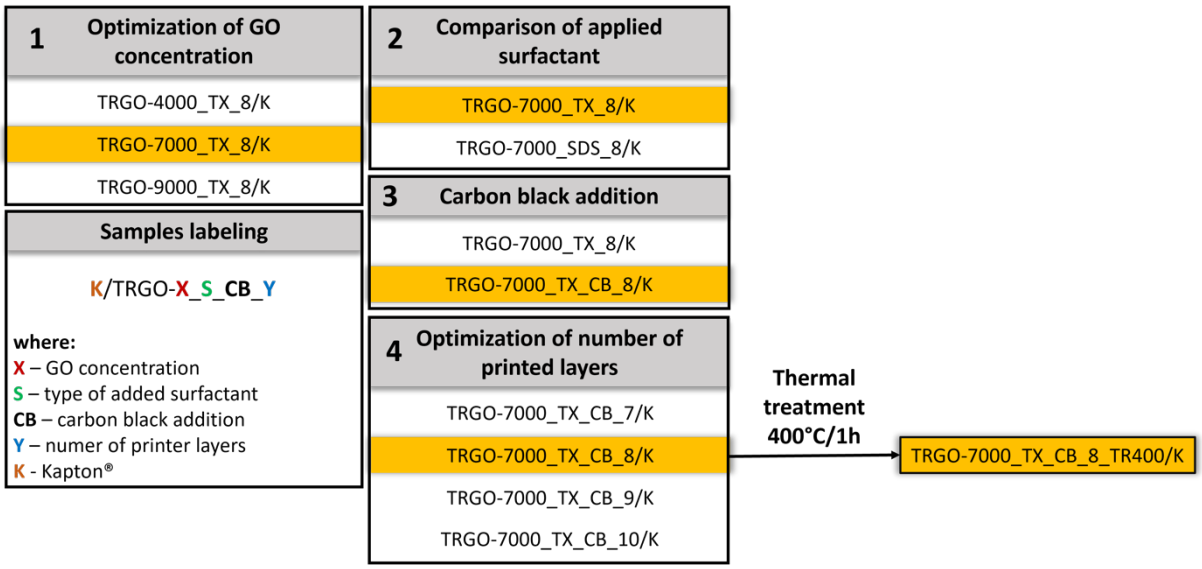

Scheme 2. Graphical summary of the steps followed for inks formulation.

4.2.3 Polyaniline (PANI)

PANI was prepared using an oxidative polymerization procedure [185]. Briefly, 500 mg of aniline was mixed with 5 mg of Triton X-100, 20 mL of Milli-Q water and 10 mL of 1 M HCl. The dispersion was sonicated in an ultrasounds bath for 30 min between 0 and 5 °C. Next, ammonium persulfate (APS), as a polymerization initiator, was added and the mixture was

stirred in a flask. The polymerization was carried out in the temperature range between 0 and 5 °C for 6 h. The obtained product was filtered and washed with Milli-Q water and methanol until the supernatant reached a neutral pH. Finally, PANI was dried under vacuum at 60 °C for 12 h.

4.3 Graphene-based nanocomposites

4.3.1 Graphene-based nanocomposites with gold nanoparticles (AuNPs)

Hydrothermally obtained RGOs and NRGOs were first applied as GCEs modifiers and subsequently modified with AuNPs. The electrodeposition was performed in a 1 mM aqueous $HAuCl_4$ solution (pH ~5) in the potential range between -0.1 to -0.9 V (vs. Ag/AgCl) at a scan rate of 50 mV s^{-1}. For both materials, the number of electrodeposition cycles was optimized (30 cycles for RGOs and 20 cycles for NRGOs).

4.3.2 Graphene-based nanocomposites with PANI

PANI/TRGO nanocomposites were prepared using a simple one-step hydrothermal treatment. Firstly, nanocomposites starting from TRGO400 were prepared using different PANI:TRGO ratios (1:3, 1:1, 3:1). Before TRGO was ultrasonicated (Milli-Q water, 30 min). Afterwards, suitable amounts of PANI were added to the dispersion and ultrasonicated. The dispersion was then placed into an autoclave and the reaction was performed for 8 h following the hydrothermal protocol described in section 4.2.1. The autogenic pressure was ~8.8 bar. After the reaction, the product was washed with Milli-Q water and finally vacuum dried overnight at 60 °C. After optimization of suitable PANI:TRGO ratio (weight ratio 1:1), and following the same protocol, nanocomposites based on TRGO700 and TRGO1000 were also prepared for comparative purposes.

4.3.3 Graphene-based binary nanocomposites with iron oxide-tin oxide (FSGs)

A series of FSGs nanocomposites were obtained by the hydrothermal treatment of GO in the presence of $Fe(NO_3)_3$ and $SnSO_4$, with different GO to Fe_2O_3-SnO_2 ratios. The mass ratios (Fe_2O_3-SnO_2:RGO) finally selected were 33:67 and 15:85. Summarizing, the synthesis procedure consisted on mixing 100 mL of GO aqueous solution (1.35 mg mL^{-1}) with suitable amounts of $Fe(NO_3)_3$ and $SnSO_4$ following ultrasonication for 1 h. Next, 1 mL of 10% v/v ammonia solution was added to the mixtures to establish a pH value of 9. The prepared

suspensions were placed in an autoclave (Parr Instrument Company, Moline, IL, USA), and subsequently submitted to 180 °C for 8 h under constant stirring (200 rpm). The resulting products were washed with Milli-Q water and vacuum-dried overnight at 60 °C.

4.3.4 Graphene-based ternary nanocomposites, with iron oxide-tin oxide and PANI (PFSGs)

Ternary nanocomposites were synthesized using a secondary hydrothermal treatment. Firstly, previously obtained FSG (33:67 mass ratio) was dispersed in Milli-Q water and ultrasonicated for 30 min. Then, a suitable amount of PANI (mass ratio PANI:FSG = 1:1) was added and ultrasonicated for additional 30 min. After that, the sonicated mixture was placed in an autoclave and submitted to 180 °C for 12 h under constant stirring (200 rpm). After the reaction was finished, the product was centrifuged with Milli-Q water and isopropanol and dried overnight at 60 °C. The expected mass ratio (PANI:Fe_2O_3-SnO_2:RGO) of obtained composites was 50:17:33.

4.4 Physicochemical characterization of the synthesized materials

Starting graphene-based materials and subsequent nanocomposites were thoroughly characterized by a wide spectrum of advanced techniques as field emission scanning electron microscopy (FESEM), X-ray photoelectron spectroscopy (XPS), elemental analysis (EA), high resolution transmission electron microscopy (HRTEM), X-ray diffraction (XRD), sheet resistance measurements and N_2 adsorption-desorption at 77 K measurements. All these characterization techniques are described in detail below.

Field emission scanning electron microscopy (FESEM)

The morphology of the different materials was investigated by FESEM, using the following instruments:

- Ga-FIB FEI Helios NanoLab 600i in the Nanores Lab (Wrocław, Poland).
- FEI Quanta FEG 650 in INCAR-CSIC (Oviedo, Spain),
- FIB–FEI HELIOS NANOLAB 450 HP in Sieć Badawcza Łukasiewicz PORT (Wrocław, Poland),
- SEM, MERLIN Zeiss with EDS X-Flash®5010 Bruker Nano detector in the Faculty of Chemistry at the University of Warsaw (Warsaw, Poland)

X-ray photoelectron spectroscopy (XPS)

The surface chemistry of the materials was determined by XPS analysis using:

- A VG-Microtech Multilab 3000 spectrometer (SPECS, Germany) equipped with a hemispherical electron analyzer and a MgKα (hυ = 1253.6 eV) X-ray source at INCAR-CSIC (Oviedo, Spain).
- A PHI 5000 VersaProbe Instrument (Kanagawa, Japan) at the Institute of Physical Chemistry in Polish Academy of Sciences (Warsaw, Poland).

The type of carbon bonding and the oxygen and nitrogen functional groups present in the samples were estimated by curve fitting of the C1s and N1s spectra using a Gaussian–Lorentzian (70:30) peak shape after performing a Shirley background correction using CasaXPS software. Deconvolutions were performed using the following binding energies:

C1s spectrum:

284.5 ± 0.2 eV – Csp^2

285.4 ± 0.2 eV – Csp^3

286.5 ± 0.3 eV – hydroxyl, epoxy, ester, eter, C-N groups, C-N

287.6 ± 0.2 eV – carbonyl and quinone groups

288.9 ± 0.3 eV – carboxyl and lactones

290.4 ± 0.4 eV – electrons in aromatic ring [π-π*].

N1s spectrum of graphene materials:

398.7 ± 0.3 eV – pyridinic groups (N6)

399.7 ± 0.2 eV – amide, imide, lactams, nitriles (NC)

400.3 ± 0.3 eV – pyrrolic groups (N5)

401.4 ± 0.5 eV – graphitic nitrogen (NQ)

402-405 eV – pyridine oxides (NX)

N1s spectrum of PANI and related composites:

398.2 ± 0.3 eV – imine (-N=)

399.6 ± 0.2 eV – amine (-NH-)

400.9 ± 0.3 eV – oxidized amine ($-NH^+$)

402.5 ± 0.5 eV – protonated imine (=N^+)

Elemental analysis (EA)

Elemental analysis was performed to determine the percentage weight of carbon, nitrogen, hydrogen and oxygen. The total O content of the whole samples was determined directly in a LECO VTF-900 furnace coupled to a LECO-CHNS-935 mircoanalyzer. Moreover, C, H and N contents of the samples were determined with a LECO–CHNS-932 microanalyzer (Geleen, The Netherlands). The analysis was performed at INCAR-CSIC (Oviedo, Spain).

High resolution transmission electron microscopy (HRTEM)

High Resolution Transmission Electron Microscopy was applied to determine the structure of the different materials. The observations were performed using a FEI TITAN3 G2 60-300 in Sieć Badawcza Łukasiewicz PORT (Wrocław, Poland).

X-ray diffraction (XRD)

The crystalline structure of selected materials was determined using X-ray diffraction (XRD, Bruker D8 Advance diffractometer, operating at 40 kV and 40 mA, Karlsruhe, Germany). The measurements were performed at INCAR-CSIC (Oviedo, Spain).

The d_{002} parameter was calculated using the Bragg equation:

$$d_{002} = \frac{n\lambda}{2sin\theta}$$

where: n – diffraction order, λ – X-ray wavelength, θ – deflection angle at maximum band intensity.

Sheet resistance measurements

The electrical resistance was evaluated using the four-point methodology (Jandel RM3000+ test unit attached to a Jandel cylindrical four-point probe head - *Jandel Engineering*, *Leighton Buzzard*, *UK).* The measurements were performed at the School of Engineering, University of East Anglia, Norwich Research Park, (Norwich, United Kingdom).

Nitrogen adsorption measurements

The specific surface area (S_{BET}) of selected materials was determined by applying the Brunauer-Emmett-Teller (BET) equation to the nitrogen adsorption isotherms obtained at 77 K on an Autosorb IQ gas sorption analyser (Quantachrome, Boynton Beach, FL, USA). The measurements were performed at Wrocław University of Science and Technology in the

Department of Process Engineering and Technology of Carbon and Polymer Materials (Wrocław, Poland).

4.5 Electrochemical characterization

4.5.1 Three-electrode cell experimental set up

GCE preparation

GCEs were firstly properly polished on felt using alumina oxide slurry with grain sizes of 0.3 and 0.05 μm. Then electrodes were sonicated in the water/ethanol solution (v/v 1:1) to remove residual amounts of alumina oxide slurry and rinsed with Milli-Q water. Subsequently GCEs were modified with dispersions of the as-synthesized materials to act as working electrodes (WEs). For this purpose, selected active materials were crushed and sieved to obtain grain sizes lower than 50 μm. 4 mg of corresponding material were then dispersed in 1 mL of water:DMF solution (v/v 1:1). In case of more complex materials (FSG and PFSG), 10 μL of nafion was added to the dispersion to increase adhesion of the active material to the electrode surface. The as prepared suspensions were sonicated in an ultrasound bath for 3h. WEs were prepared by drop-casting of 2.5 μL of prepared dispersions and dried under infrared lamp or in the furnace at 60 °C till dried.

Configuration of the three-electrode cell experimental setup

The electrochemical characterization of previously prepared WEs was performed in a three-electrode setup configuration (Figure 25). Apart from selected WE the cell consisted of graphite rod/Pt wire and Ag/AgCl/3.5 M KCl as CE and RE, respectively. Measurements were carried out in a phosphate buffer solution (PBS) as electrolyte, at a fixed pH, and the corresponding target analyte. All measurements were recorded using a VMP3 potentiostat/galvanostat (BioLogic, France).

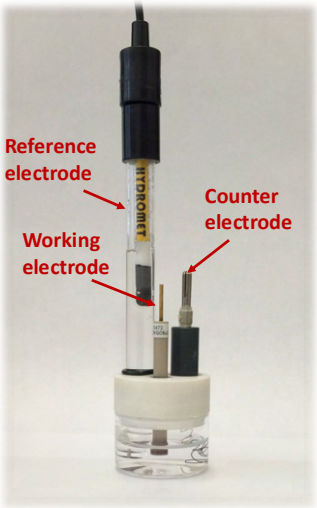

Figure 25. Three-electrode electrochemical setup.

4.5.2 Miniaturized setup containing inkjet printed electrode

Printing procedure

IPEs were printed using a commercial EPSON EcoTank ET-M2120 printer. Kapton® (DuPont™) was selected as flexible substrate for printing due to its high thermal stability (up to 450 °C). Prior to printing, the printer cartridge was washed several times with Mili-Q water to remove residual amounts of previously applied ink. All inks formulations were homogenized for 10 min at 2000 rpm using SpeedMixter (German Engineering by Hauschild, type DAC 150.1 FVZ-K) and filtered using 0.45-micron syringe filters before being introduced into the printer cartridge. GO-based inks were introduced into the cartridge using a syringe applying constant and slow ink flow to avoid bubbles formation. Cartridge, filling process, cartridge filled with GO-based inks and resulting printed patterns are presented in Figure 26.

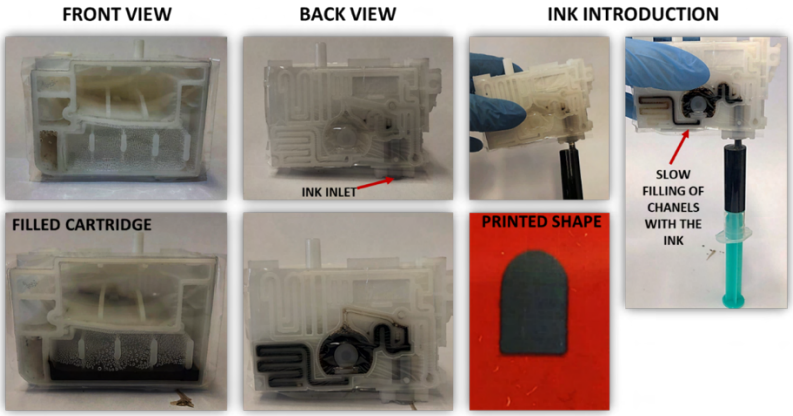

Figure 26. (a – f) Schematic representation of filling of the printer cartridge. (g) Image of a printed pattern on Kapton®.

Assembly of three-electrode miniaturized electrochemical setup

A novel three-electrode miniaturized electrochemical setup is presented in Figure 27. It consists of selected IPE as WE, a micro-Ag/AgCl as RE and a graphite rod as CE.

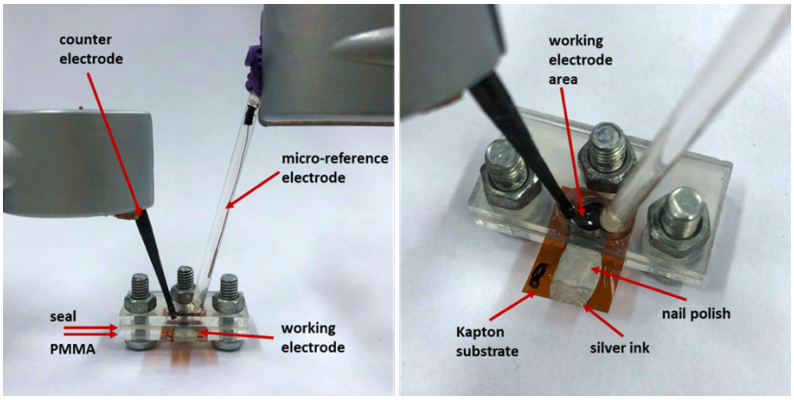

Figure 27. Miniaturized electrochemical setup using inkjet-printed TRGO/Kapton as a WE.

4.5.3 Electrochemical techniques and measurements conditions

Electrochemical characterization of the different active electrode materials under investigation was determined by cyclic voltammetry (CV) and differential pulsed voltammetry (DPV).

The first stage of the assessment of related electrochemical performances included **preliminary CV studies** carried out in PBS solutions containing target analyte of interest at a concentration of 100 µM in the potential range between -0.5 to 0.8 V for DA, AA and UA, 0.0 to 0.9 V for DCF and -0.3 to 1.0 V for the same analyte but using IPEs. **pH optimization** was performed in the pH range between 5.8-8.0 using the same settings and conditions. **Kinetics of electrodes reactions** was determined by CV measurements at increasing scan rates (2-250 mV s^{-1}). **Electrochemical working parameters of the electrodes** were determined using DPV technique. The measurements were performed at increasing concentration of target analyte. Firstly, DPV technique parameters (accumulation time, pulse width, pulse height, time and amplitude of the pulse) were optimized. DPV curves were baseline corrected and calibration curves were defined. Limit of detection (LOD) values were calculated following equation 7:

$$LOD\ [\mu M] = \frac{3S}{b} \quad (7)$$

where S is the standard deviation of the blank sample and b is the slope of the related calibration curve (signal to noise ratio S/N=3). Moreover, sensitivity of measurements, which is equal to the slope of the corresponding calibration curve [µA μM^{-1}], was defined. DPV technique was also applied for evaluating the impact of interferences and/or simultaneous determination, reproducibility, repeatability, stability, and real sample measurements. **Reproducibility of the**

WEs was evaluated by preparation of five different electrodes and subsequent comparison of their anodic responses towards 100 μM solution of target analyte. The relative standard deviation (% RSD) of the series of measurements was calculated. **Repeatability of the measurements** was determined by five consecutive measurements with the same electrode in 5 different target analyte solutions at a concentration of 100 μM. **The long-term stability** of tested electrodes was evaluated by daily measurements of the anodic peak currents for seven days. After 30 days, control measurement was also performed. Between measurements, electrodes were stored in a 0.1 PBS solution at optimized pH value. **Interference studies/simultaneous detection** were performed in the presence of commonly interfering species. **Real sample analysis** was performed in an artificial urine solution prepared following a protocol proposed by Chutipongtanate and Thingboonkerd [186]. The artificial urine was composed of 2.427g urea, 0.034g uric acid, 0.900g creatinine, 0.297g $Na_3C_6H_5O_7 \cdot 2H_2O$, 0.634g NaCl, 0.450g KCl, 0.161g NH_4Cl, 0.089g $CaCl_2 \cdot 2H_2O$, 0.100g $MgSO_4 \cdot 7H_2O$, 0.034g $NaHCO_3$, 0.003g NaC_2O_4, 0.258g Na_2SO_4, 0.100g $NaH_2PO_4 \cdot H_2O$, 0.011g Na_2HPO_4 and 200 mL of Milli-Q water.

5 Results and discussion

5.1 Graphene-based nanocomposites in electrochemical sensing

5.1.1 Graphene-based nanocomposites with gold nanoparticles towards electrochemical detection of DA, ascorbic acid (AA), uric acid (UA) and their simultaneous detection

5.1.1.1 Morphology and structure of active electrode materials

FESEM images present RGO and NRGO morphologies (Figure 28a and b, respectively). According to the literature, urea was selected as nitrogen source as its introduction positively contribute to achieve a suitable chemical composition ensuring an effective electrochemical performance for DA sensing [121]. As it can be seen both graphene materials, consisted of aggregated flame-like graphene sheets with comparable thickness [110,187].

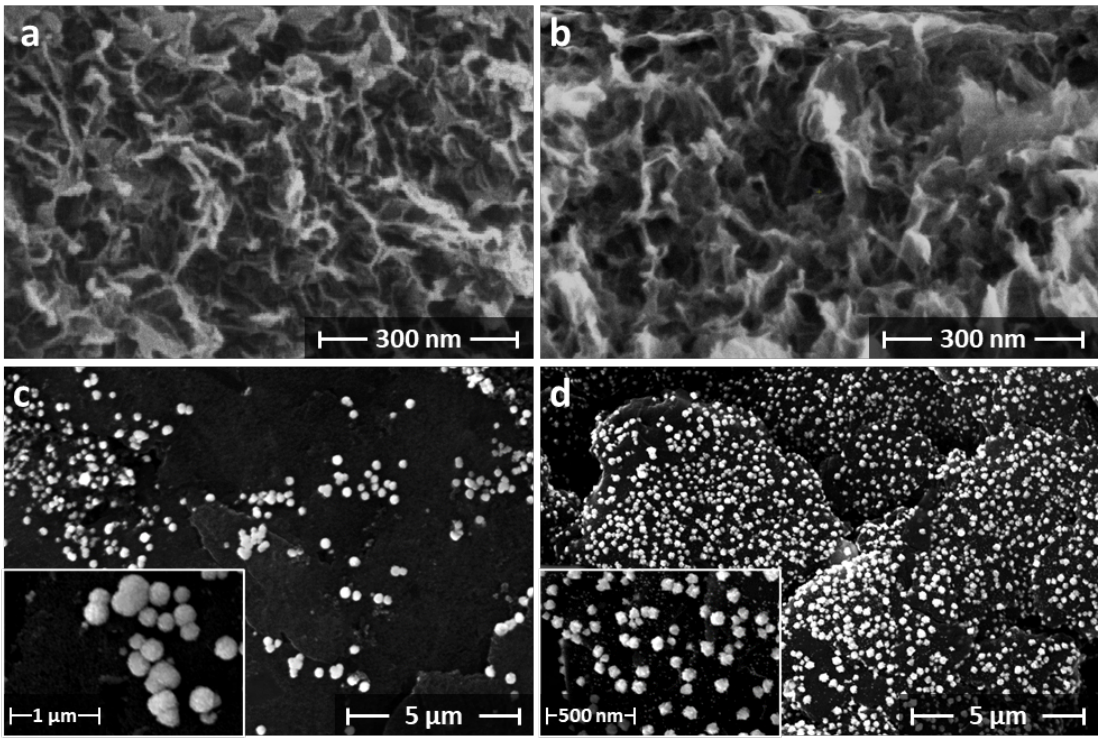

Figure 28. FESEM images of (a) RGO, (b) NRGO, (c) AuNPs/RGO, and (d), AuNPs/NRGO.

The impact of N-doping of RGO on the subsequent electrodeposition of AuNPs on RGO and NRGO was examined (Figures 28c and d). The number of electrodeposition cycles was optimized on both RGO/GCE and NRGO/GCE considering their corresponding electrochemical responses towards DA (Figures 29a and b).

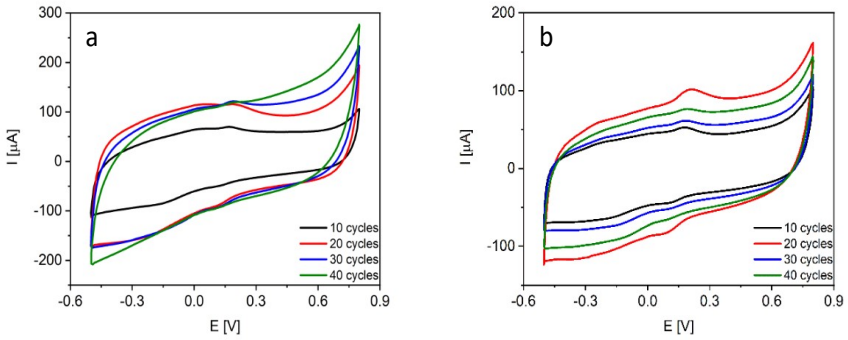

Figure 29. CVs recorded on (a) AuNPs/RGO/GCE and (b) AuNPs/NRGO/GCE, obtained by applying a different number of electrodeposition cycles (10-40 cycles), in a 0.1 M PBS solution (pH = 7.0) with 100 µM of DA.

According to the results, the capacitive current measured on the RGO/GCE increased when increasing the number of electrodeposition cycles. However, the anodic peak related to DA oxidation was the most distinctive when applying 30 electrodeposition cycles (121.7 µA).

Regarding NRGO/GCE, the mechanism of AuNPs deposition seems to be quite different as the capacitive current firstly increases when increasing the number of electrodeposition cycles reaching the maximum value of DA oxidation peak current at 20 cycles (101.8 μA). Then, capacitive current starts to decrease which could be explained considering the decrease of the surface area of the material as a result of formation of AuNPs aggregates. Moreover, and following the morphology of synthesized nanocomposites (Figs 28c and d), the different mechanism of AuNPs deposition on both graphene materials is reflected by differences in the AuNPs distribution. Despite the lower number of electrodeposition cycles a higher amount of AuNPs was electrodeposited on the surface of doped material (NRGO/GCE). Insets in Figures 28c and d present magnified AuNPs enriched areas, corroborating marked differences in the distribution, shape and size of AuNPs. In case of NRGO, 20 electrodeposition cycles are sufficient to homogeneously cover the whole surface of NRGO/GCE with uniform tetrahedral shape and size (20-250 nm) nanoparticles. On the other hand, on RGO/GCE AuNPs appear as bigger spherical aggregates (50-450 nm).

Table 6. Surface chemistry of RGO, NRGO, and their nanocomposites with AuNPs determined by XPS (at.%)

Sample	C	N	O	Au
RGO	83.3	-	16.7	-
AuNPs/RGO	79.1	-	14.4	6.5
NRGO	84.8	6.4	8.8	-
AuNPs/NRGO	80.7	2.7	9.0	7.6

The chemical surface composition of the materials was determined by XPS (Table 6). As expected, the carbon content decreases in both materials after electrodeposition of AuNPs. This fact together with the presence of Au confirms successful electrodeposition of AuNPs on the surface of graphene materials. Moreover, and in agreement with previously shown SEM images, the amount of AuNPs on the NRGO surface is higher than on the RGO surface (7.6 and 6.5 at.%, respectively). For RGO, the oxygen content decreases after electrodeposition presumably due to the reduction of oxygen functional groups during such electrochemical process in the potential range between -0.1 to -0.9 V [188]. It is also worth to note that the AuNPs electrodeposition time was shorter in case of NRGO than that of RGO. The starting NRGO possess significantly lower oxygen content than RGO which made the electrochemical reduction more difficult [188]. Therefore, the oxygen content in the starting NRGO is comparable to AuNPs/NRGO (8.8 and 9.0 at.%, respectively) and the nitrogen content

markedly decreases after electrodeposition of AuNPs, which suggest that nitrogen enriched areas are preferential for nucleation and growth of AuNPs. The deconvoluted C1s spectra of the materials are presented in Figure 30. The C1s spectrum can be divided into four components corresponding to sp^2 hybridized carbon (284.5 eV), hydroxyl, epoxy and C-N groups (286.5 eV), carbonyl and quinone bonds (287.6 eV) and carboxylic groups (289.0 eV). As follows from the deconvoluted spectra the most intensive band for all materials is at a binding energy of 284.5 eV which is assigned to Csp^2 hybridized carbon. This is in agreement with previously reported studies on graphene-based materials and confirm successful GO reduction by hydrothermal treatment [110]. Considering the surface chemistry in detail (Table 7), it is clear that electrodeposition of AuNPs on RGO mainly leads to the decrease of Csp^2 content, indicating a random distribution of metallic nanoparticles. The intensity of the peak at 286.5 eV is higher for NRGO than RGO, due to a significant C-N contribution. On the other hand, electrodeposition of AuNPs on NRGO leads to a significant decrease of carbonyl and carboxyl groups (Table 7). It could be explained by both, transformation of carbonyl groups to hydroxyl groups during electrodeposition and electrodeposition of AuNPs on -COOH functional groups [189,190]. N1s deconvoluted spectra are shown for NRGO and AuNPs/NRGO in Figure 31 a and b, respectively. Both spectra can be resolved into five and four components in NRGO and AuNPs/NRGO, respectively: pyridinic nitrogen (N6, 398.7 eV), amine, amide and lactams (NC, 399.7 eV), pyrrolic (N5, 400.3 eV), quaternary (NQ, 401.4 eV) and pyridine N-oxides (402-405 eV) (Figure 31). The main nitrogen functionalities in NRGO are pyridine and pyrrolic groups. According to the literature, doping RGO with urea lead to a significant contribution of pyrrolic groups [121]. During hydrothermal treatment transformation of pyrrolic groups to quaternary nitrogen can be observed [191]. As it can be seen there is a significant decrease of almost all nitrogen functionalities after electrodeposition indicating the high impact of nitrogen on AuNPs anchoring, as for example a strong interaction of pyridinic nitrogen and gold has been previously reported [192]. It is consistent with XPS results as the N6 content decreases from 2.6 to 0.7 at.% [193]. In addition, pyrrolic nitrogen also interacts with Au leading to its decrease from 1.9 to 0.7 at.% after electrodeposition [194]. Furthermore, nitrogen in the form of pyridine oxide entirely disappeared after electrodeposition of AuNPs, also confirming its involvement in AuNPs anchoring due to its complexation ability [195]. The content of amide/amine/lactam functional groups increases after AuNPs electrodeposition which can be the result of transformation of nitrogen functionalities under potential and preferential deposition of AuNPs on pyridinic, pyrrolic, pyridinic oxides and quaternary nitrogen functionalities. Figs. 32 a and b show the Au4f deconvolutions for AuNPs/RGO and

AuNPs/NRGO. The spectra clearly confirm the successful deposition of AuNPs in the metallic form as two distinctive peaks at binding energies of 84.0 ($Au4f_{7/2}$) and 87.7 ($Au4f_{5/2}$) are distinguishable [196].

Table 7. Type and distribution of C and N surface functional groups, at.%

Sample	C1s peak deconvolution				N1s peak deconvolution				
	Csp^2	C-OH/C-N	C=O	O=C-OH	N6	NC	N5	NQ	NX
RGO	54.1	18.0	5.8	5.3	-	-	-	-	-
AuNPs/RGO	41.3	22.9	8.9	6.1	-	-	-	-	-
NRGO	50.3	24.8	7.7	2.0	2.6	0.5	1.9	0.9	0.5
AuNPs/NRGO	48.9	26.3	4.6	0.9	0.7	1.0	0.7	0.3	-

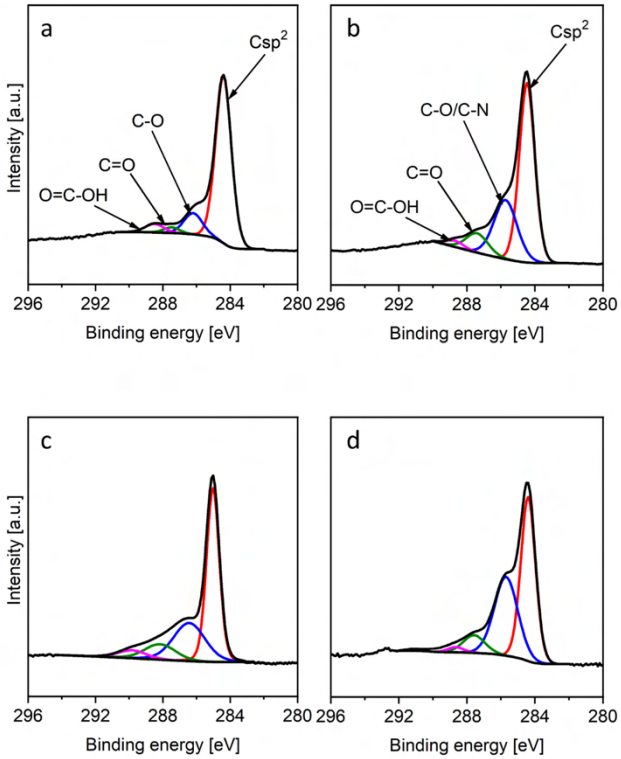

Figure 30. Deconvolutions of the C1s core-level XPS spectra of (a) RGO, (b) NRGO, (c) AuNPs/RGO and (d) AuNPs/NRGO.

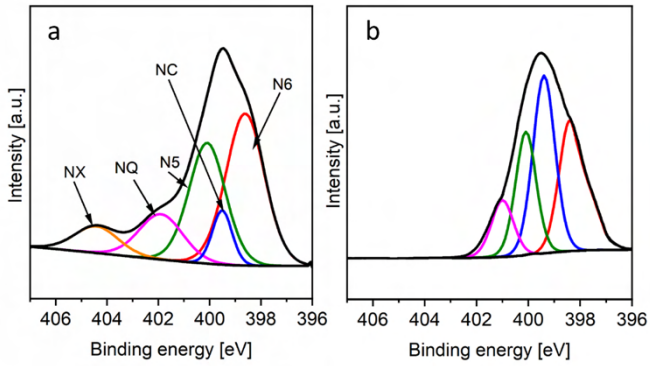

Figure 31. Deconvolutions of the N1s core-level XPS spectra of (a) NRGO, (b) AuNPs/NRGO.

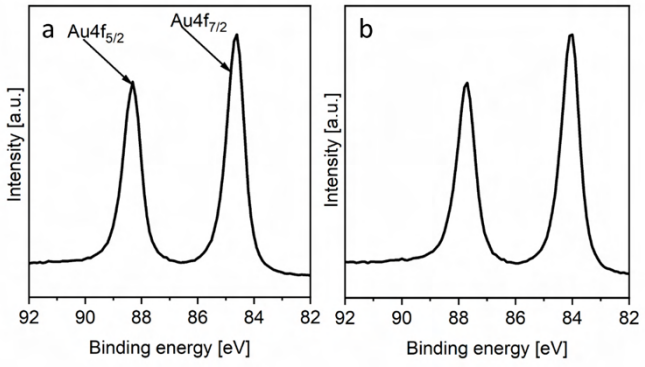

Figure 32. Deconvolutions of the Au4f core-level XPS spectra of (a) AuNPs/RGO, (b) AuNPs/NRGO.

5.1.1.2 Electrochemical detection of DA

All previously characterized samples were assessed as active electrode materials for the electrochemical detection of DA as target analyte. In the first step, preliminary CV experiments were performed on the different electrodes under evaluation using a PBS (pH = 7.0) solution containing 100 μM DA as electrolyte (Figures 33a and b). The non-modified GCE presents a nearly negligible response for DA oxidation (5.2 μA at 178.2 mV, Figure 33a). After its modification with RGO a significant increase of capacitive current is observed, as a result of enhanced electrode surface area [197]. Surprisingly, after electrodeposition of AuNPs such capacitive current decreases, which could suggest a decrease in previously developed surface area due to formation of large AuNPs aggregates. Contrarily, the modification of GCE with AuNPs/NRGO results in an enlargement of surface area as a result of homogenously distributed AuNPs exhibiting smaller sizes (Figure 33b) [198]. Nevertheless, the anodic peak corresponding to DA oxidation is clearly visible on both electrodes reaching current values of 121.62 μA and 101.85 μA on AuNPs/RGO/GCE and AuNPs/NRGO/GCE, respectively. The anodic peak current recorded on AuNPs/NRGO/GCE reaches a lower current value, however it is better resolved, which is the result of lower capacitive current comparing to AuNPs/RGO/GCE.

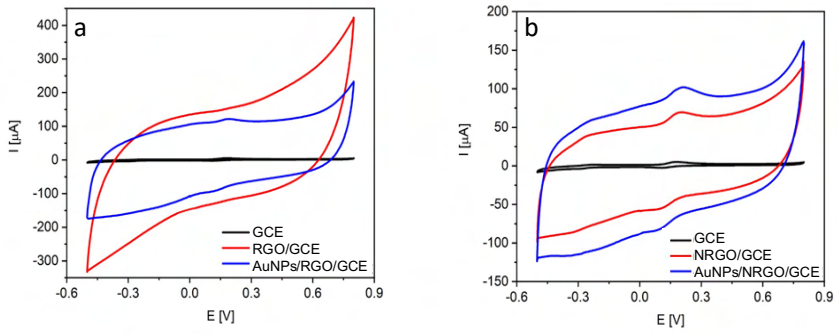

Figure 33. CVs recorded on the different electrodes under evaluation in a 0.1 M PBS solution (pH = 7.0) containing 100 µM of DA.

In order to enhance the electrochemical response of the electrodes for DA sensing, the next step covered optimization of their working pH values (Figure 34). Relationships between anodic peak currents vs. pH and overpotential values vs. pH are also presented. The optimization was performed in PBS solutions containing 100 µM of DA in the pH range from 5.8 to 8.0. On RGO/GCE (Figures 34a and b) the maximum anodic peak current was recorded at pH 7.4 (292.8 µA, 231.0 mV). However, on NRGO/GCE (Figures 34c and d) and AuNPs/RGO/GCE (Figures 34e and f) a pH value of 7.0 was selected as the optimized one, as the value of anodic peak currents are the highest (189.4 and 146.8 µA, respectively). Moreover, overpotential of DA oxidation present a value of 260.8 and 248.2 mV for NRGO/GCE and AuNPs/RGO/GCE, respectively. Regarding AuNPs/NRGO/GCE (Figures 34g and h) the maximum anodic peak current was recorded at pH ~ 6.6 (122.5 µA,280.2 mV), even though, measurement at pH 7.0 revealed a just imperceptibly lower current (120.6 µA) but a significantly lower overpotential (256.2 mV). On RGO/GCE the anodic peak current measured at pH 7.0 (287.4 µA, 246.1 mV) is comparable to that recorded at pH 7.4, which gives the possibility to perform measurements at the former pH. To compare electrochemical performance of all electrodes towards DA electrochemical sensing further studies were performed at the same pH value. Searching for a compromise between the anodic peak current and the overpotential of the DA oxidation, pH of 7.0 was selected as the optimized one for all the electrodes. Moreover, this value is close to the physiological one (pH = 7.4) which increases the potential application of proposed electrodes in real sample analysis [199].

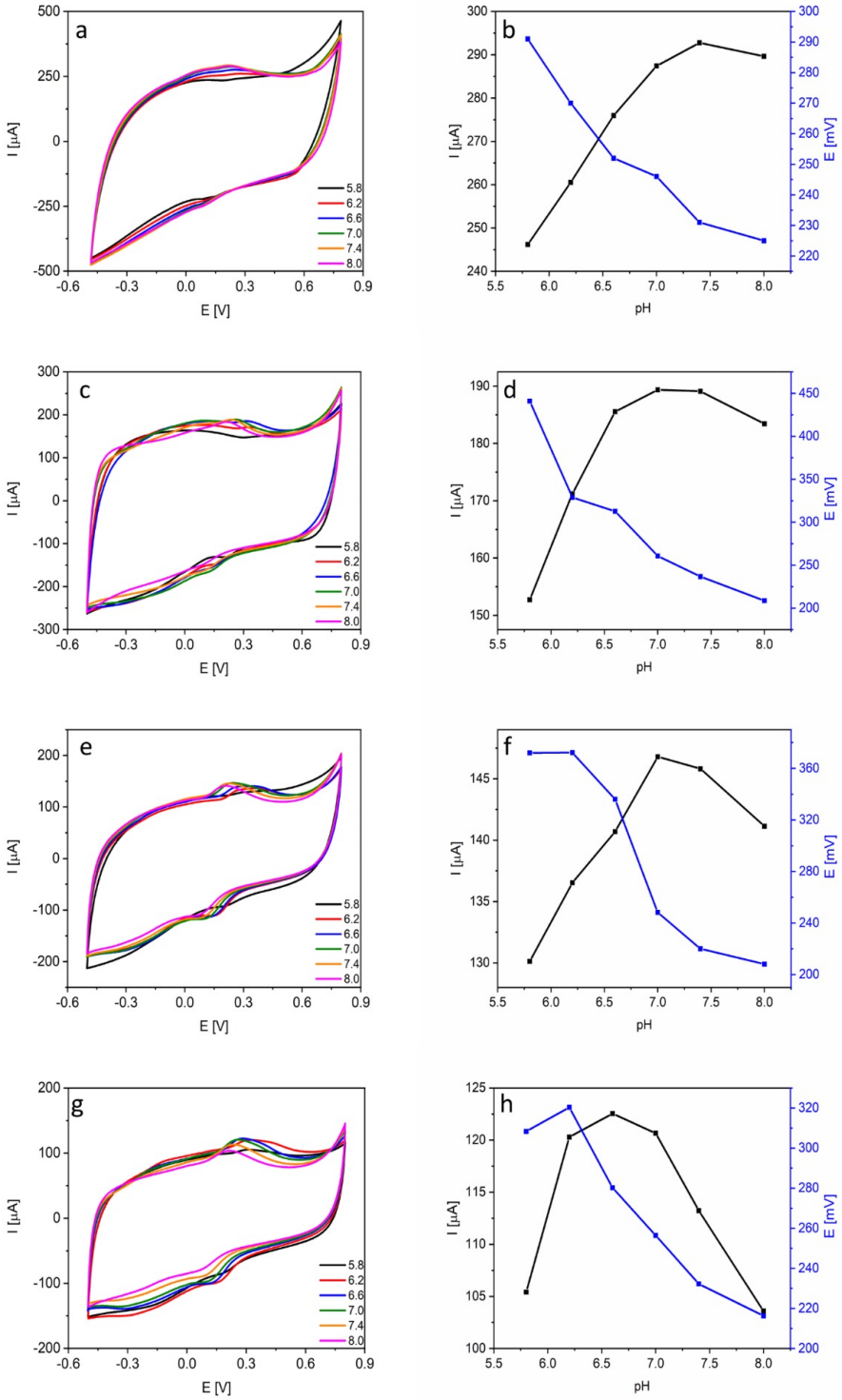

Figure 34. CVs recorded (υ_{scan} = 100 mV s^{-1}) at increasing pH values on (a) RGO/GCE, (c) NRGO/GCE, (e) AuNPs/RGO/GCE and (g) AuNPs/NRGO/GCE in 0.1 M PBS solution containing 100 µM of DA. Influence of the pH on the anodic current and peak potential values recorded on (b) RGO/GCE, (d) NRGO/GCE, (f) AuNPs/RGO/GCE and (h) AuNPs/NRGO/GCE.

Further research was conducted in order to determine the main mechanism controlling DA oxidation. With this purpose, CV measurements were performed, on the different electrodes, in a 0.1 PBS (pH = 7.0) solution containing 100 μM DA at increasing scan rates (2-250 mV s^{-1}, Figure 35). As expected, the anodic peak potential increases with the scan rate on all the electrodes. In addition, measured currents also increase, as a result of a diffusion rate higher than the rate of reaction, thus more ions reaching electrode surface. Moreover, the relationship between anodic peak currents and square root of scan rate is linear on all electrodes. To clearly identify the main mechanism controlling DA oxidation, the logarithmic relationship between scan rate and anodic peak current was defined. The slope of derived curves was 0.75 on RGO/GCE (Figure 35c), 0.67 on NRGO/GCE (Figure 35f), 0.74 on AuNPs/RGO/GCE (Figure 35i), and 0.75 on AuNPs/NRGO/GCE (Figure 35l). Both findings are consistent with diffusion as main mechanism controlling the reaction [200].

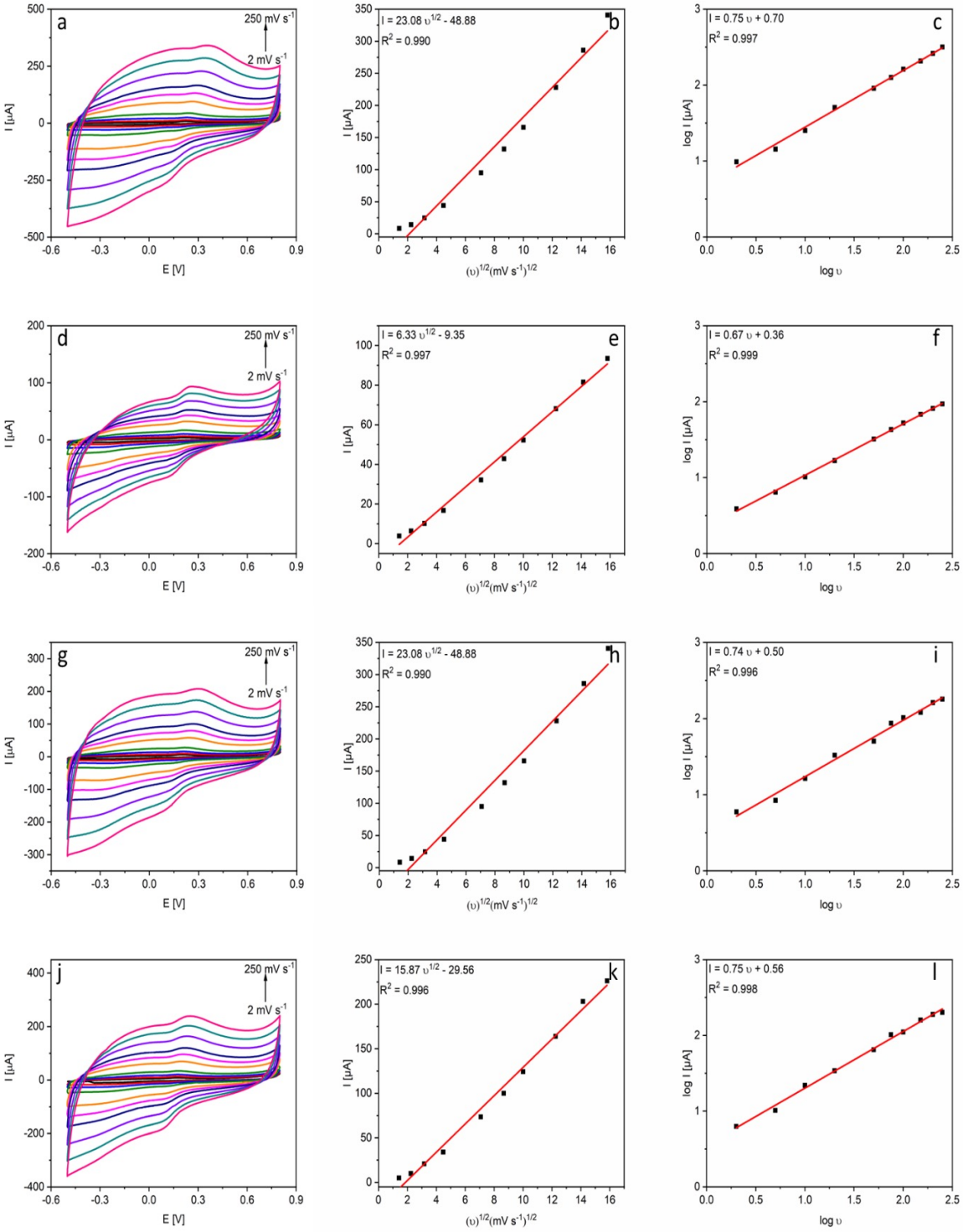

Figure 35. CVs recorded at increasing scan rates (2, 5, 10, 20, 50, 75, 100, 150, 200, 250) on (a) RGO/RGO, (c) NRGO/GCE, (e) AuNPs/RGO/GCE and (g) AuNPs/NRGO/GCE in a 0.1 M PBS (pH = 7.0) solution with 100µM of DA. Relationships between maximum anodic peak current and overpotential and square root of scan rate recorded on (b) RGO/GCE, (d) NRGO/GCE, (f) AuNPs/RGO/GCE and (h) AuNPs/NRGO/GCE. The logarithmic relationship

between scan rate and anodic peak current recorded on (c) RGO/GCE, (f) NRGO/GCE, (i) AuNPs/RGO/GCE and (l) AuNPs/NRGO/GCE.

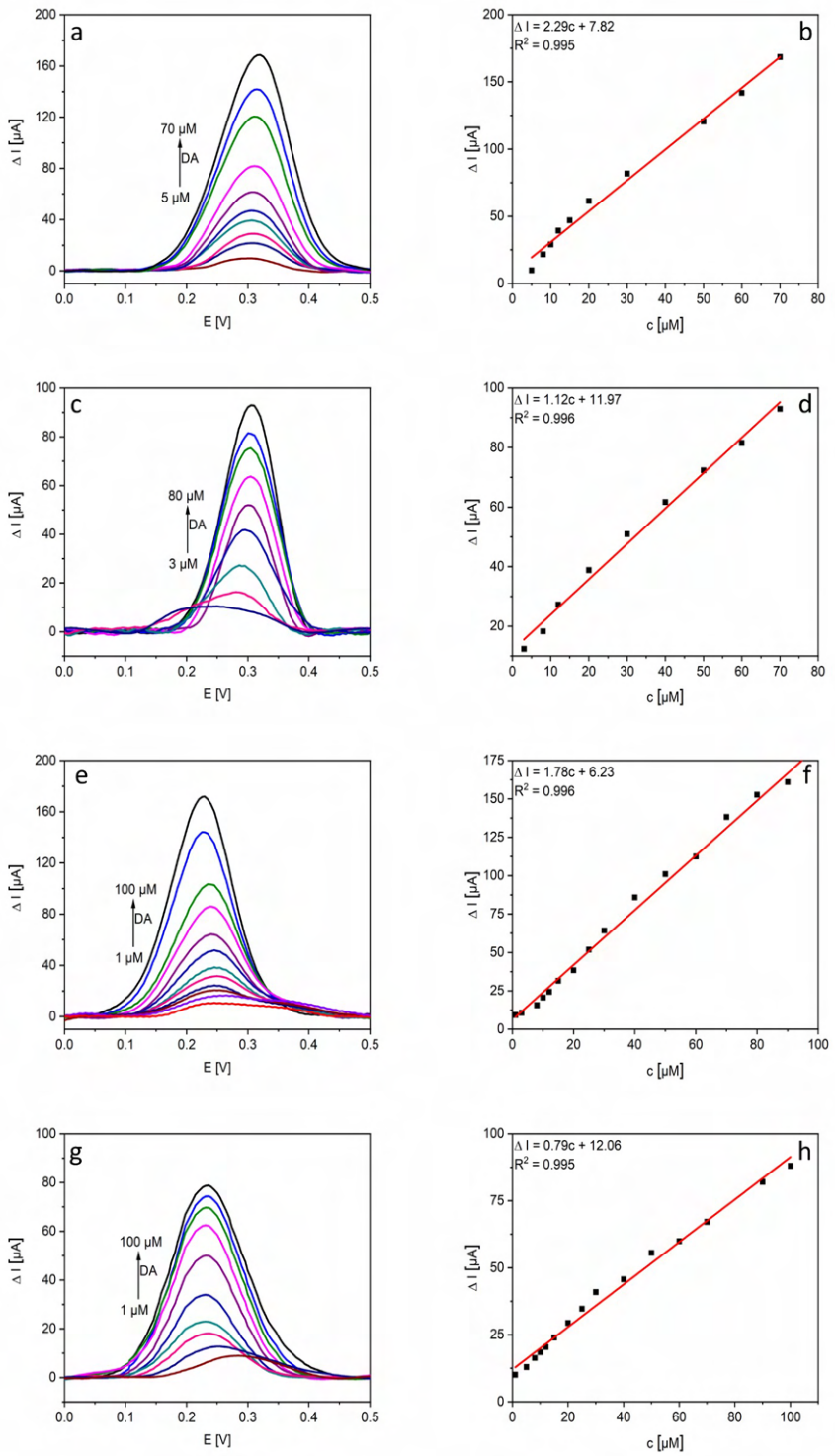

Figure 36. Baseline-corrected DPVs recorded on (a) RGO/GCE, (c) NRGO/GCE, (e) AuNPs/RGO/GCE and (g) AuNPs/NRGO/GCE in a 0.1 M PBS solution (pH = 7.0) with

increasing concentration of DA. Calibration curves for (b) RGO/GCE, (d) NRGO/GCE, (f) AuNPs/RGO/GCE and (h) AuNPs/NRGO/GCE.

DPV measurements at increasing DA concentrations (from 0.1 to 300 μM) were performed to determine calibration curves (Figure 36) of the electrodes under evaluation. Then, the range in which sensors worked linearly was selected (Table 8). Thus, working linear ranges for RGO/GCE and NRGO/GCE are 5 – 70 and 3 – 80 μM, respectively. After modification of both electrodes with AuNPs linear ranges were expanded to 1 – 100 μM. These results confirmed the beneficial impact of AuNPs on the electrochemical sensing performance, as they increased the electrochemically active surface area for target analyte, also favoring stable connection between electrode surface and analyzed molecule [133,198]. Furthermore, LODs for DA sensing were significantly lower after electrodeposition of AuNPs. This result can be explained considering the increased electrical conductivity of the sensing platforms also due to the lower oxygen content in the active material [201]. It has been reported that amine groups are able to create covalent bonds with gold surfaces [202]. Therefore, homogenously distributed AuNPs enhance the attachment of DA molecules through amine group presented in its structure. Nevertheless, according to the literature and previous studies, electronegatively charged oxygen moieties present on the electrode surface also have a marked impact for DA detection [122]. At a pH value of 7.0 DA is in cationic form (pK_a value = 8.93) [31]. It leads to creation of electrostatic interactions between cationic DA form and negatively charged oxygen groups increasing the stability of connection between the electrode surface and analyte. Moreover, AuNPs present high biocompatibility and impact on molecule attachment to the electrode surface [133]. From all these interesting results, it seems highly important to find a compromise between the properties of sensing platforms, which allow to ensure the creation of suitable bonding between the active electrode material and DA without decreasing the electrical conductivity. In this context, it is reasonable that the highest LOD (998 nM) was measured on RGO/GCE (16.7 at.% O). However, AuNPs/RGO/GCE, displaying a lower oxygen content (14.6 at.% O), provided an improved LOD (700 nM). Similarly, on NRGO/GCE (8.8 at.% O) the calculated LOD was 812 nM, being this value improved up to 385 nM on AuNPs/NRGO/GCE (9.0 at.% O). On the other hand, when comparing NRGO/GCE and AuNPs/RGO/GCE the at.% O significantly differs the LODs were not so far away from each other, thus probing that AuNPs can compensate electrical conductivity loses caused by the presence of oxygen functional groups. Moreover, in case of RGO/GCE and NRGO/GCE after electrodeposition of AuNPs, the overpotentials of DA oxidation significantly decreased proving

the electrocatalytic activity of AuNPs in DA oxidation [133]. All sensors worked in a wide LR, reaching high correlation coefficients (from 0.995 to 0.996). Even though DA oxidation products are highly reactive and could deposit on the electrode surface, these high correlation coefficients indicate the absence of fouling on the electrodes surface [203].

Table 8. Electrochemical performance of the different electrodes under evaluation towards DA electrochemical sensing

Sensor	LOD nM	LR µM	Sensitivity µA μM^{-1}	Reproducibility RSD %	Repeatability RSD %
RGO/GCE	998	5-70	2.29	7.7	6.7
NRGO/GCE	812	3-70	1.12	6.2	4.8
AuNPs/RGO/GCE	700	1-100	1.78	7.6	6.4
AuNPs/NRGO/GCE	385	1-100	0.79	4.3	2.7

Following the assessment of the potential application of these sensors, reproducibility and repeatability studies were performed on all the electrodes under evaluation (Table 8). According to the obtained results, both parameters were improved after electrodeposition of AuNPs. Moreover, the low % RSD value related to repeatability on AuNPs/NRGO/GCE (2.7 %) corroborates previous assumption regarding absence of fouling by the oxidized DA products, due to the presence of uniformly deposited AuNPs. It can be also pointed out that this parameter was better for NRGO/GCE (in comparison to RGO/GCE 4.8 and 6.7 %, respectively) which could be also a probe of the antifouling abilities of nitrogen functional groups.

Additionally, long-term stability tests were carried out (Figure 37). Obtained results revealed that on RGO/GCE, NRGO/GCE, and AuNPs/RGO/GCE the intensity of the recorded signal decreased linearly. However, on AuNPs/NRGO/GCE measurements remained almost unaffected even after 30 days (91% of the initial oxidation signal). It indicates that the homogenous distribution of AuNPs on this electrode has a key role on the stability of its electrochemical performance, preventing oxidation of nitrogenated groups [204,205].

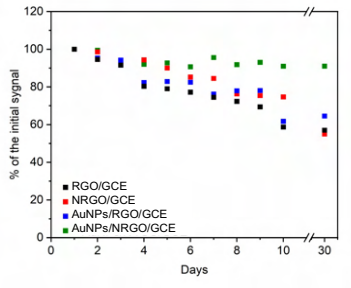

Figure 37. Long-term stability tests performed on the RGO/GCE, NRGO/GCE, AuNPs/RGO/GCE and AuNPs/NRGO/GCE.

Considering the best results recorded on AuNPs/NRGO/GCE, selectivity studies were performed on this electrode, using as electrolyte a 0.1 PBS solution (pH = 7.0) containing DA, glucose and NaCl. The electrochemical response of this electrode in the presence of the three analytes was measured and the resulting data (using the equation designated from calibration curve) are summarized in Table 9. An average calculated value, when adding 50 μM of DA to 100 μM NaCl and 100 μM glucose containing solution, was 48.3 μM. These results corroborates the high potential application of this sensors for DA sensing in the presence of selected interferences.

Table 9. Selectivity studies of AuNPs/NRGO/GCE in the presence of glucose and NaCl

Analyte	Added μM	Measured μM	Detection performance %	RSD %
DA	50	50.7	101.4	3.5
		46.8	93.6	
		47.5	95.0	

5.1.1.3 Electrochemical detection of AA

The next stage on the evaluation of the electrochemical performance of the proposed electrodes was checking their application for multi-analyte sensing. For this purpose, the electrodes were tested towards interfering species as AA, which also occurs in the human organisms along with DA. Preliminary studies were performed using CV in a 0.1 M PBS solution (pH = 7.0) containing 100 μM AA (Figure 38). It can be observed that recorded capacitive currents were quite similar to those showed when sensing DA (Figure 38a and b). However, the anodic peak related to AA oxidation was significantly wider, which could indicate a slower electron transfer rate for this redox process. After modification of both graphene-based sensing platforms with AuNPs, results significantly improved as the anodic peak current increased and overpotential values decreased for AA oxidation (115.9 μA-86.7 mV for AuNPs/RGO/GCE and 38.0 μA-114.7 mV for AuNPs/NRGO/GCE). In addition, the oxidation peaks were better developed on electrodes modified with AuNPs. Thus, and also due to better performance of these two electrodes for DA sensing as target analyte, they both were tested in further studies.

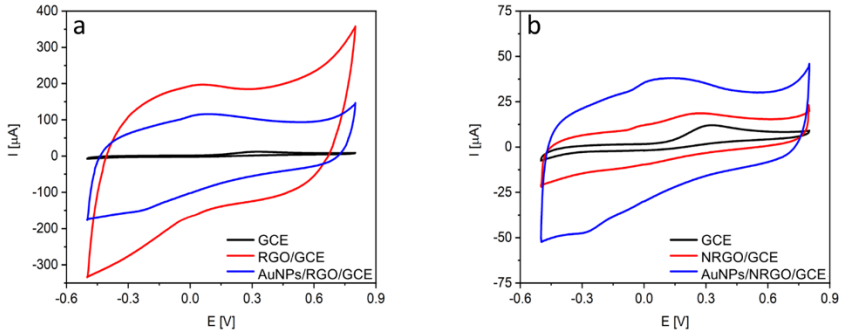

Figure 38. CVs recorded on the different electrodes in a 0.1 M PBS solution (pH = 7.0) containing 100 µM of AA.

The impact of pH on their electrochemical response towards AA was also tested (Figure 39). On both electrodes the highest anodic peak currents were recorded at pH 6.6 (97.2 and 38.8 µA, for AuNPs/RGO/GCE (Figures 39a and b) and AuNPs/NRGO/GCE (Figures 39c and d). When comparing results recorded on AuNPs/RGO/GCE at pH 6.6 and 7.0, there were negligible differences between anodic peak currents (only a 2 µA drop at pH 7.0). However, the anodic overpotential significantly decreased from 181 to 113 mV. Similar results were obtained when evaluating AuNPs/NRGO/GCE the corresponding anodic peak current displayed almost the same intensity (38.8 and 38.6 µA at pH 6.6 and 7.0, respectively) while overpotential dropped from 83 to 71 mV. Maintaining the optimized pH value for DA (pH = 7.0), which is the main target analyte in this thesis, and trying to achieve a compromise between the highest anodic peak current and the lowest overpotential, further measurements were performed at pH 7.0.

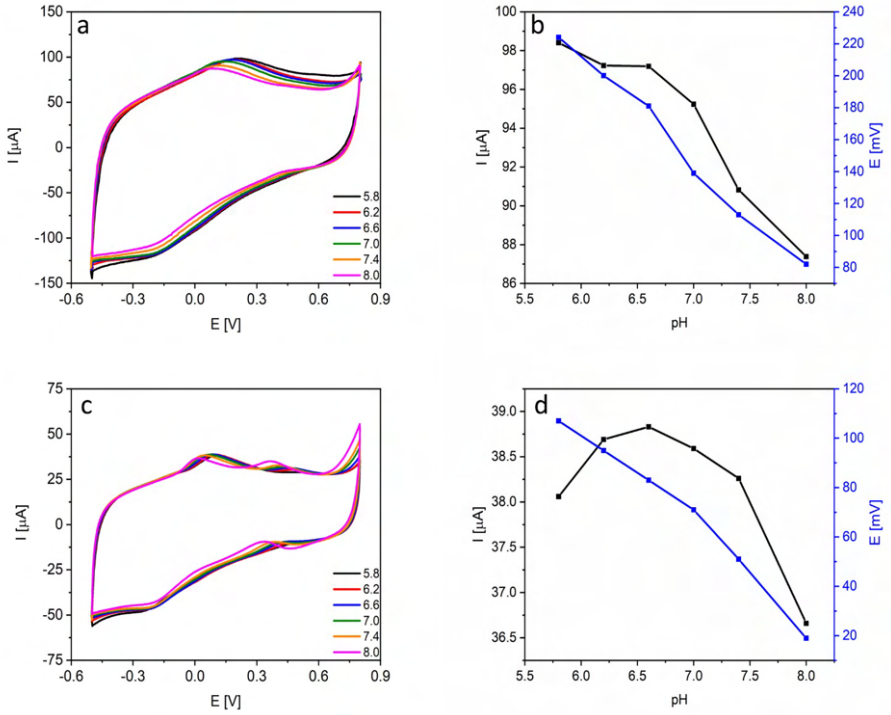

Figure 39. CVs recorded (υ_{scan} = 100 mV s^{-1}) at increasing pH values on (a) AuNPs/RGO/GCE, (c) AuNPs/NRGO/GCE in a 0.1 M PBS solution containing 100 µM of AA. Influence of the selected pH on the oxidation peak currents and potential values for (b) AuNPs/RGO/GCE, (d) AuNPs/NRGO/GCE.

CV measurements at increasing scan rates were performed on both electrodes (Figure 40). Again, the anodic peak potential values increased when increasing the scan rate. The relationship between measured anodic peak currents and the square root of scan rate was linear. Moreover, the logarithmic relationship between scan rate and anodic peak current revealed slope values of 0.70 AuNPs/RGO/GCE (Figure 40c) and 0.65 for AuNPs/NRGO/GCE (Figure 40f), which is in agreement with diffusion as the main mechanism controlling AA oxidation [200].

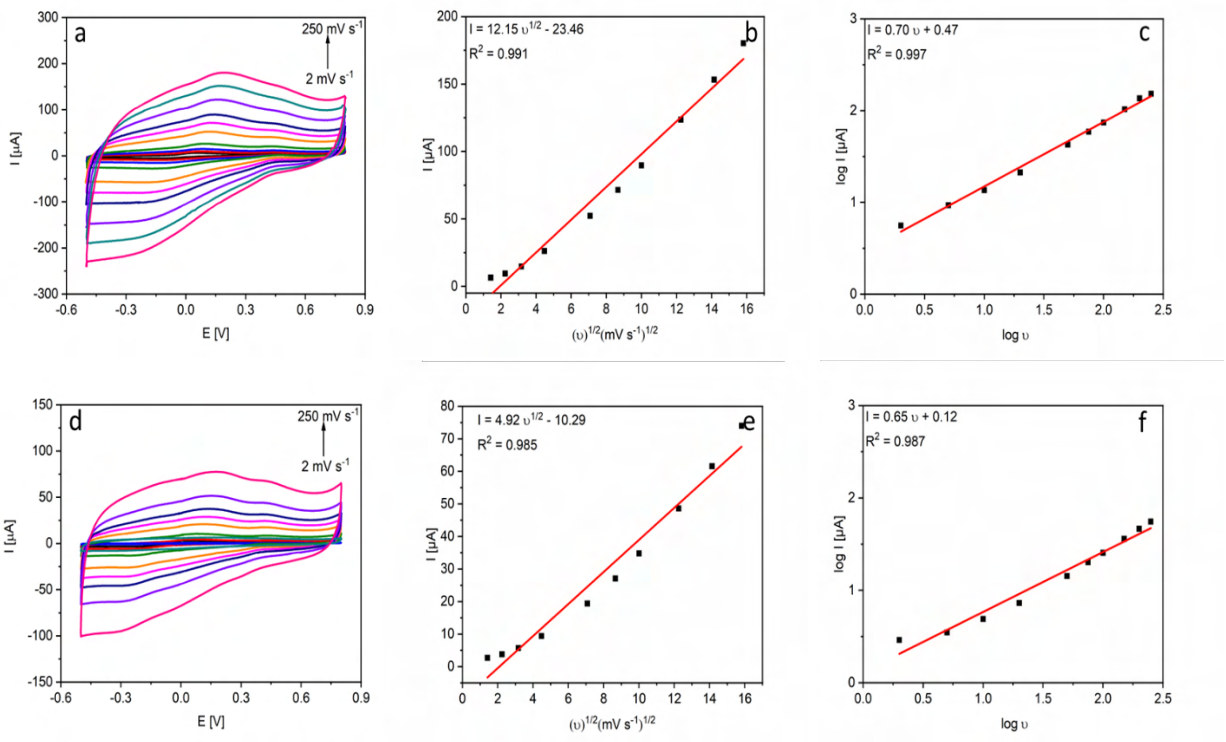

Figure 40. CVs recorded at increasing scan rates (2, 5, 10, 20, 50, 75, 100, 150, 200, 250) on (a) AuNPs/RGO/RGO, (c) AuNPs/NRGO/GCE in a 0.1 M PBS solution (pH = 7.0) with 100 µM of DA. Relationships between the maximum anodic peak current and overpotential and square root of scan rate recorded on (b) AuNPs/RGO/GCE, (d) AuNPs/NRGO/GCE. The logarithmic relationship between scan rate and anodic peak current recorded on (c) AuNPs/RGO/GCE, (f) AuNPs/NRGO/GCE.

Due to the lack of AA oxidation signal at low concentrations, DPV curves were recorded in extended concentration range (0.1 - 2500 µM, Figure 41). For AuNPs/RGO/GCE the LR was 100 to 2000 µM (Figure 41b) and for AuNPs/NRGO/GCE 200 to 1000 µM (Figure 41d). This unexpected result could be explained considering the strong adsorption of AA on the electrode surface and subsequent electrode fouling which, at higher concentrations, diminish AA oxidation signal. This assumption could be also supported by its lower sensitivity. Nevertheless, LOD calculated for both electrodes was comparable (Table 10). Slightly better LOD for AuNPs/NRGO/GCE can be the result of a stronger affinity between AA (which at the selected experimental conditions is in its anionic form, $pK_a = 4.17$ [43]) and positively charged nitrogen groups presented in the active material (2.7 at.% of nitrogen) [206]. In addition, the AA oxidation potential recorded on AuNPs/RGO/GCE and AuNPs/NRGO/GCE were 117.2 and 99.9 mV, respectively which gave the possibility to test both materials in a simultaneous detection of AA and DA as no interference should be expected, due to significantly differing

overpotential values. The overpotential of AA oxidation is lower on AuNPs/NRGO/GCE which proves that homogenously distributed, smaller AuNPs possess higher electrocatalytic activity towards AA oxidation reaction than randomly deposited bigger aggregates.

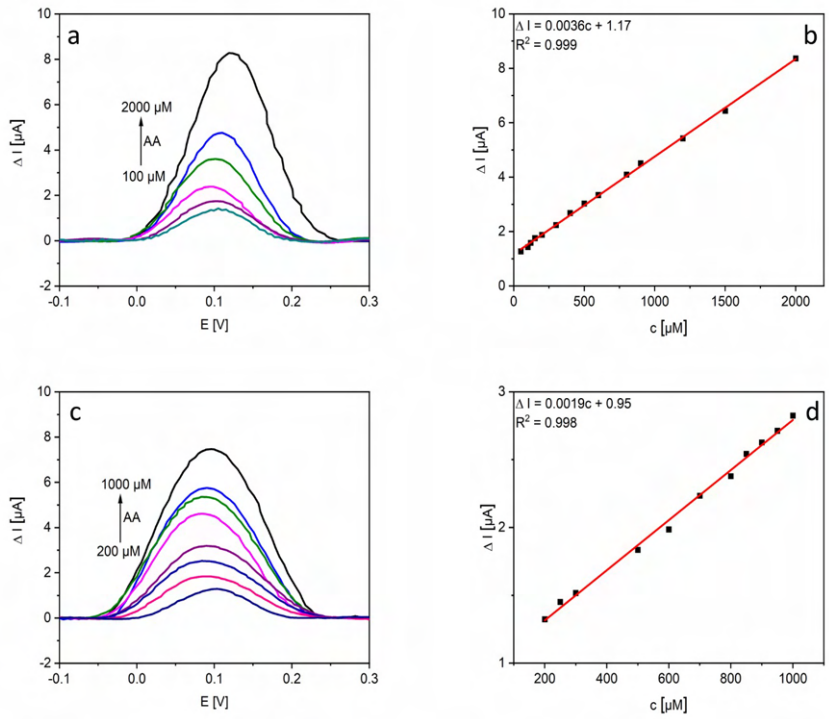

Figure 41. Baseline-corrected DPVs recorded on (a) AuNPs/RGO/GCE, (c) AuNPs/NRGO/GCE in a 0.1 M PBS solution (pH=7.0) at increasing concentrations of AA. Corresponding calibration curves for (b) AuNPs/RGO/GCE, (d) AuNPs/NRGO/GCE.

Table 10. Electrochemical performance of AuNPs/RGO/GCE and AuNPs/NRGO/GCE towards AA sensing

Sensor	LOD µM	LR µM	Sensitivity µA μM^{-1}	Reproducibility RSD %	Repeatability RSD %
AuNPs/RGO/GCE	56	100-2000	0.004	7.8	7.3
AuNPs/NRGO/GCE	44	200-1000	0.002	4.9	4.6

Reproducibility and repeatability tests revealed that both values were higher than when evaluating electrodes towards DA sensing (Table 10). It can be correlated with a higher fouling of electrodes with AA oxidation products as it is an irreversible process. Following slightly better results recorded on AuNPs/NRGO/GCE, further selectivity studies were performed on this electrode using a 0.1 PBS solution (pH = 7.0) in the presence of glucose and NaCl as electrolyte. 600 µM of AA was added to the solution containing 100 µM of NaCl and glucose. The intensity of recorded oxidation peaks was measured and the calculated values (using the

equation designated from calibration curve) are presented in Table 11. An average calculated value during addition of 600 µM to the solution with NaCl and glucose was 478 µM indicating on weakening of the signal by interferences species.

Table 11. Selectivity studies of AuNPs/NRGO/GCE in the presence of glucose and NaCl

Analyte	Added µM	Measured µM	Detection performance %	RSD %
AA	600	485.0	80.8	5.2
		505.0	84.2	
		445.0	74.2	

5.1.1.4 Electrochemical detection of UA

Another potential interfering compound is UA, as it also occurs in human body. In this context, and to assess the possibility of UA determination, preliminary CV experiments were performed in a PBS solution (pH = 7.0) containing 100 µM of this compound (Figure 42). A similar trend to that shown in previous DA and AA studies can be observed. The current recorded on bare GCE presents a value of 14.2 µA at an overpotential of 397.9 mV. Modification of GCE with RGO (Figure 42a) and NRGO (Figure 42b) results in the appearance of capacitive current, even though the most distinctive UA oxidation peaks at lower overpotential values were recorded on AuNPs/RGO/GCE (111.6 µA at 330.8 mV) and AuNPs/NRGO/GCE (58.1 µA at 326.8 mV) electrodes. Hence further studies concerning UA electrochemical detection were performed on these two electrodes.

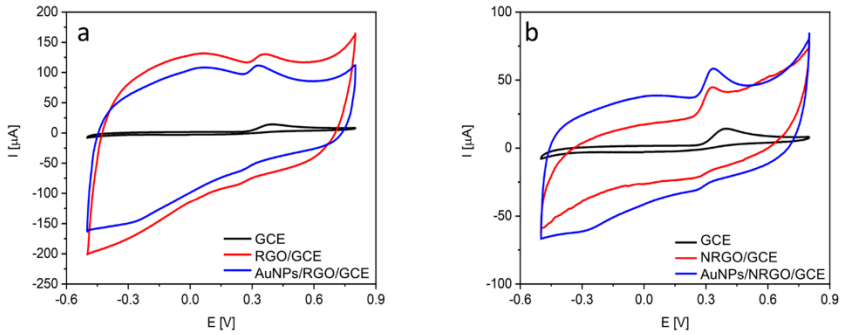

Figure 42. CVs recorded on the different electrodes in a 0.1 M PBS solution (pH = 7.0) containing 100 µM of UA.

Following previously proposed protocol, CV measurements at increasing pH values were also performed to determine the optimum experimental value (Figure 43). As it can be seen, the highest anodic peak current was recorded at pH 6.2 on both electrodes (80.0 and 36.4 µA for AuNPs/RGO/GCE (Figure 43a and b) and AuNPs/NRGO/GCE (Figure 43c and d),

respectively). When comparing values recorded on AuNPs/RGO/GCE at pH 6.2 and 7.0, a negligible drop of anodic peak current, from 80.0 to 78.9 µA, can be observed. Nevertheless, the related overpotential values decrease significantly from 421 to 381 mV. Similarly, on the other electrode the anodic peak current presents almost the same intensity, independently of the pH (36.4 vs. 35.5 at pH 6.2 and 7.0), while the overpotential value differs of about 49 mV. Taking into account the previously optimized pH value for DA and AA detection (7.0) and the overpotential of UA oxidation at pH 7.0, this value was selected as the most suitable for further measurements.

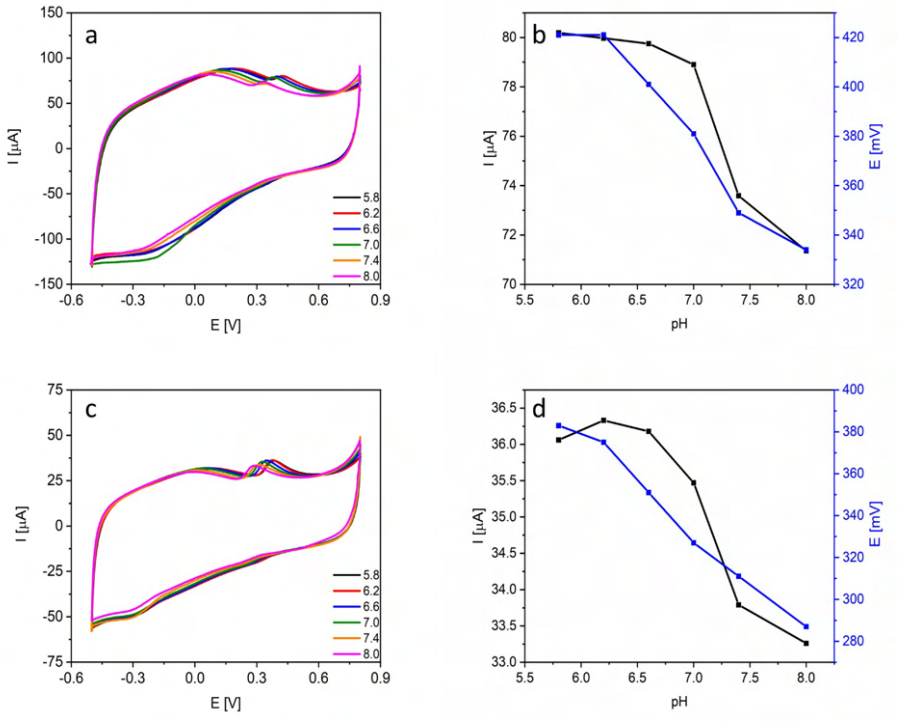

Figure 43. CVs recorded (υ_{scan} = 100 mV s^{-1}) at increasing pH values on (a) AuNPs/RGO/GCE and (c) AuNPs/NRGO/GCE in a 0.1 M PBS solution containing 100 µM of UA. Influence of the selected pH on the oxidation current and peak potential values recorded on (b) AuNPs/RGO/GCE and (d) AuNPs/NRGO/GCE.

CVs were also recorded on these electrodes at increasing scan rates (2 – 250 mV s^{-1}), maintaining previously optimized experimental parameters (Figure 44). The relationship between the square root of scan rate and the maximum peak current results linear (Figure 44b and d). Moreover, the slope of the curve related to the relationship between logarithm of scan rate and logarithm of maximum of anodic peak current is 0.72 for both electrodes. As in previous cases, it indicates that UA oxidation is mainly controlled by diffusion [200].

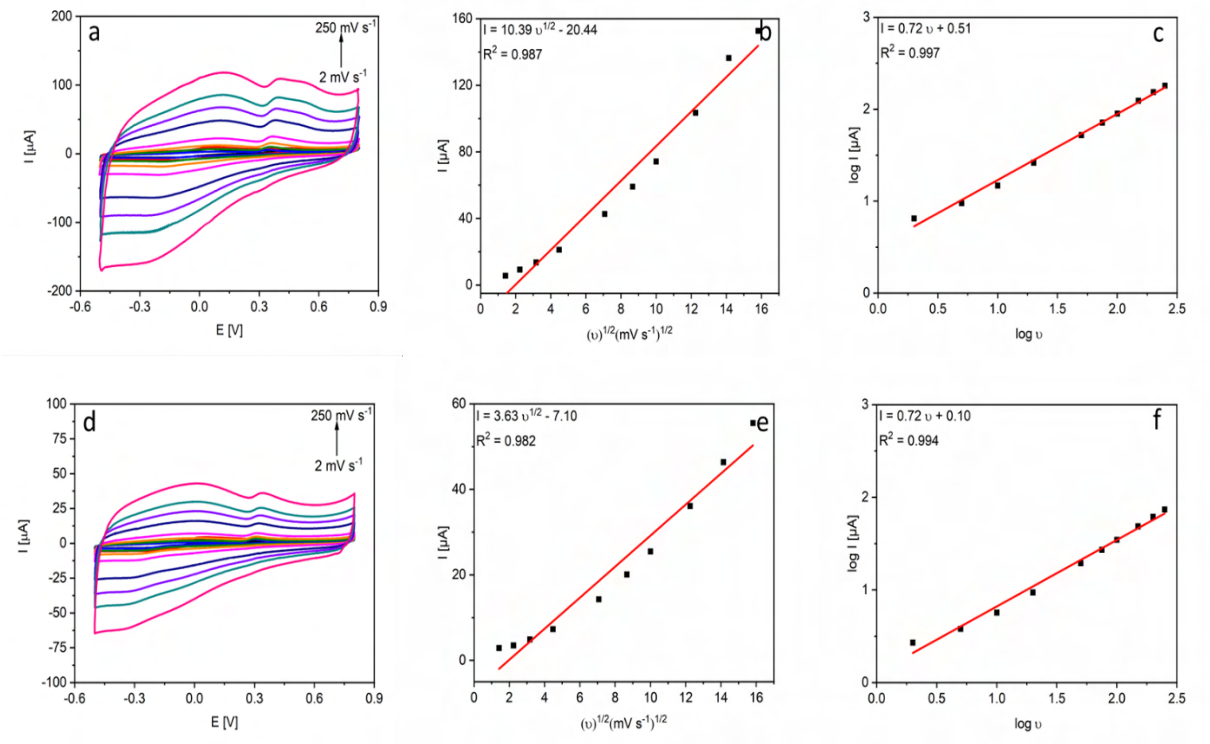

Figure 44. CVs recorded at increasing scan rates (2, 5, 10, 20, 50, 75, 100, 150, 200, 250) on (a) AuNPs/RGO/GCE, (c) AuNPs/NRGO/GCE in a 0.1 M PBS solution (pH=7.0) containing 100µM of UA. Relationships between maximum anodic peak current and square root of scan rate recorded on (b) AuNPs/RGO/GCE, (d) AuNPs/NRGO/GCE. The logarithmic relationship between scan rate and anodic peak current recorded on (c) AuNPs/RGO/GCE, (f) AuNPs/NRGO/GCE.

Subsequently, DPV measurements at increasing UA concentrations (from 0.1 to 1000 µM) were performed to determine the corresponding calibration curves (Figure 45). Two electrodes under evaluation worked linearly in the ranges 20 – 500 and 1– 100 µM, respectively. AuNPs/NRGO/GCE presents a narrower linear range as a result of the strong interactions of the anionic form of UA and positively charged nitrogen functionalities (2.7 at.% N) [206]. Regarding LOD values, marked differences were observed as AuNPs/RGO/GCE enabled to detect 17 µM of UA while a LOD of 2.7 µM was reached at AuNPs/NRGO/GCE (Table 12). This fact, together with the higher sensitivity can prove that interaction of UA with nitrogen moieties has a significant positive impact on its electrochemical detection. In addition, homogenously distributed AuNPs can also imply strong interactions with target analyte as it contains in its structure amine functional groups [207]. As a result, overpotential values of UA oxidation were 476.1 and 412.1 mV on AuNPs/RGO/GCE and AuNPs/NRGO/GCE, corroborating the high catalytic activity of these metallic nanoparticles [133]. All these results

rise the possibility of applying both active electrode materials towards simultaneous detection of DA, AA and UA as the overpotential of oxidation of these three electroactive compounds significantly differs (which is crucial to achieve high resolution and low interference effects).

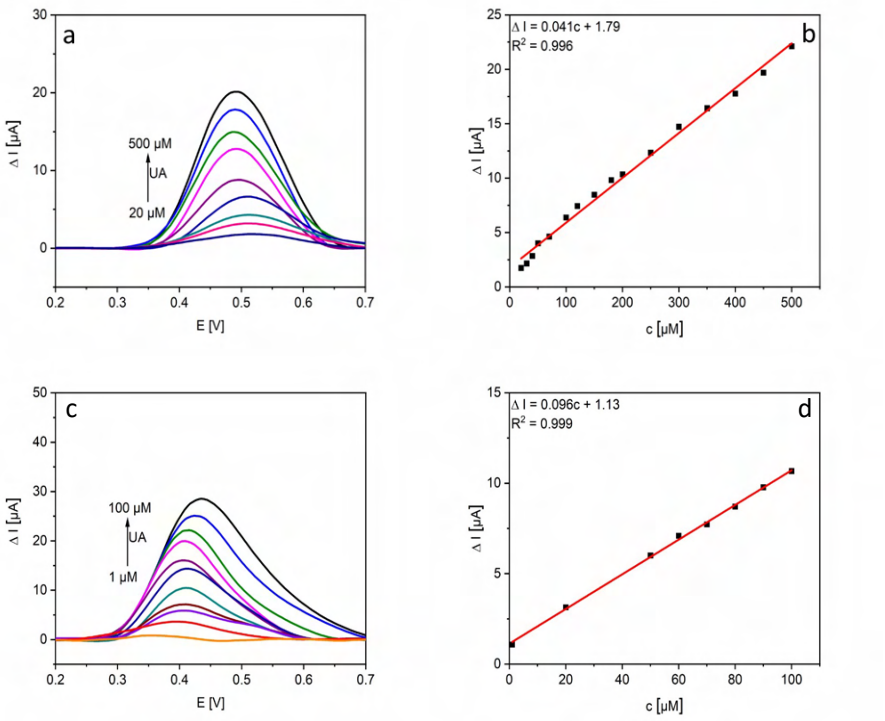

Figure 45. Baseline-corrected DPVs recorded on (a) AuNPs/RGO/GCE, (c) AuNPs/NRGO/GCE in a 0.1 M PBS solution (pH=7.0) at increasing concentrations of UA. Corresponding calibration curves for (b) AuNPs/RGO/GCE, (d) AuNPs/NRGO/GCE.

Table 12. Electrochemical performance of AuNPs/RGO/GCE and AuNPs/NRGO/GCE sensors towards UA detection

Sensor	LOD μM	LR μM	Sensitivity μA μM^{-1}	Reproducibility RSD %	Repeatability RSD %
AuNPs/RGO/GCE	17	20-500	0.04	7.2	6.9
AuNPs/NRGO/GCE	2.7	1-100	0.10	4.5	3.8

Considering reproducibility and repeatability of evaluated sensors for UA detection, similar results to that corresponding to DA sensing were obtained (Table 12). It should be pointed that, the repeatability on both electrodes resulted lower than that related to AA measurements, which could be assigned to the good reversibility of UA electrochemical reactions and a lower electrode-fouling.

From the most improved sensor working parameters recorded on AuNPs/NRGO/GCE, selectivity studies were performed on this electrode in a 0.1 PBS solution (pH = 7.0) containing

a known concentration of target analyte, glucose and NaCl (100 μM of each interfering compound). The calculated values, using measured signal intensities and corresponding calibration curves (Figure 45d) are presented in Table 13. An average calculated value when adding 100 μM of UA to the solution was 80.5%, indicating that NaCl and glucose displayed a low impact on UA oxidation signal.

Table 13. Selectivity studies of AuNPs/NRGO/GCE in the presence of glucose and NaCl

Analyte	Added μM	Measured μM	Detection performance %	RSD %
UA	100	82.4	82.4	1.6
		79.7	79.7	
		79.4	79.4	

5.1.1.5 Simultaneous detection of target analytes

Previous results recorded in individual aqueous solutions of DA, AA and UA revealed the high potential of AuNPs/RGO/GCE and AuNPs/NRGO/GCE for the simultaneous detection of these three electroactive compounds, as their corresponding anodic peaks were well-developed at different potential values. Thus, further experiments were performed for varying concentrations of each analyte in the presence of constant concentrations of the two other species. The baseline corrected DPVs recorded on AuNPs/RGO/GCE and AuNPs/NRGO/GCE in a 0.1 M PBS solution (pH = 7.0) containing constant concentrations of AA and UA and increasing concentration of DA and the corresponding calibration curves are presented in Figure 46. It can be observed that the anodic peaks related to the oxidation of the three species are well-resolved. Peak potential separations (AA-DA, DA-UA and AA-UA) recorded on AuNPs/RGO/GCE were 0.22, 0.20 and 0.41 V (Figure 46a) while for AuNPs/NRGO/GCE these values were 0.34, 0.20 and 0.54 V (Figure 46c). These results clearly indicate the highest catalytic activity of homogenously distributed AuNPs in AuNPs/NRGO/GCE [133]. As expected, the anodic peak current corresponding to DA oxidation increases when increasing its concentration on both electrodes in the linear ranges 8 – 80 and 3 – 100 μM on AuNPs/RGO/GCE (Figure 46b) and AuNPs/NRGO/GCE (Figure 46d). These LRs were narrower than those obtained for individual DA detection, thus corroborating the interference from AA and UA. While AA oxidation peak was stable when increasing DA concentration, the peak corresponding to UA decreased in intensity, this suggests the occupation of active sites by UA molecules which were then replaced by DA. The LOD of DA in the simultaneous sensing is higher than that obtained during individual detection, which also proves above conclusion (Table 14). Moreover, sensitivity

decreased in the simultaneous detection, corroborating the occupation of active sites not only by DA as target analyte but also by the two other interfering compounds.

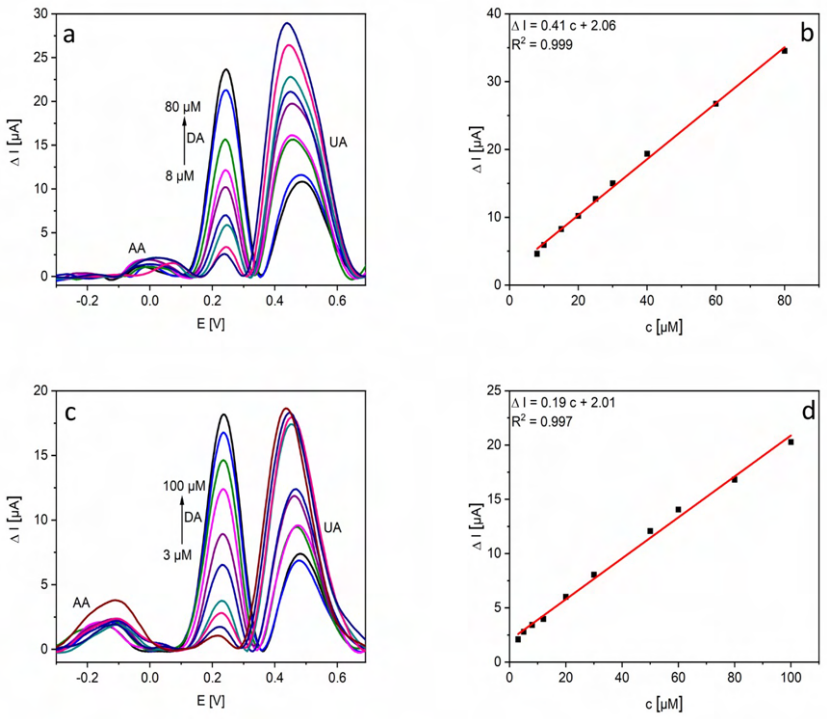

Figure 46. Baseline-corrected DPVs recorded on (a) AuNPs/RGO/GCE, (c) AuNPs/NRGO/GCE in a 0.1 M PBS solution (pH=7.0) at increasing concentrations of DA and constant concentration of AA and UA (300 µM). Corresponding calibration curves for (b) AuNPs/RGO/GCE, (d) AuNPs/NRGO/GCE.

Similar studies were also developed for AA as target analyte in the presence of DA and UA as interfering compounds (Figure 47). The anodic peak current of AA increases when increasing its concentration on both electrodes under evaluation, in the linear ranges 150 – 1500 (Figure 47b) and 550 – 150 µM (Figure 47d). However, the simultaneous determination was only possible on AuNPs/NRGO/GCE as the UA oxidation peak was negligible on the other electrode. This can be explained considering the higher occupation of active sites by DA. However, in the structure of AuNPs/NRGO/GCE positively charged nitrogen is presented leading to the repulsion of some DA molecules and subsequent attachment of AA molecules. Moreover, the LR on AuNPs/NRGO/GCE was narrower than that on AuNPs/RGO/GCE which can be the result of a strong occupation of active sites on the former not only by target analyte but also by DA and UA. The LOD values for AA detection calculated on both electrodes were 57 and 58 µM, respectively (Table 14), which were close to those calculated in the individual AA sensing (56 and 44 for AuNPs/RGO/GCE and AuNPs/NRGO/GCE).

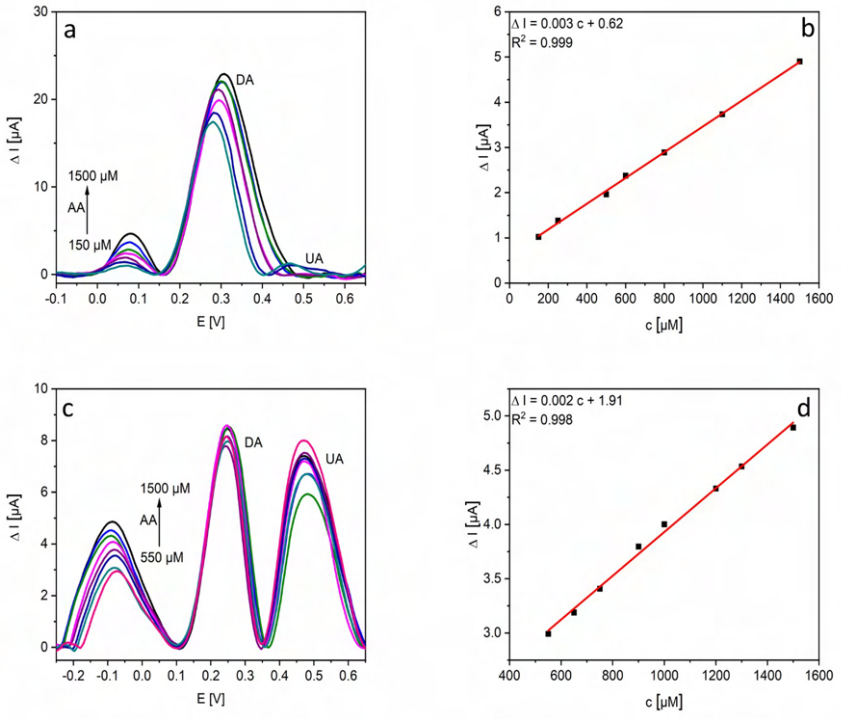

Figure 47. Baseline-corrected DPVs recorded on (a) AuNPs/RGO/GCE, (c) AuNPs/NRGO/GCE in a 0.1 M PBS solution (pH=7.0) at increasing AA concentrations and constant DA (100 µM) and UA (300 µM) concentrations. Corresponding calibration curves for (b) AuNPs/RGO/GCE, (d) AuNPs/NRGO/GCE.

UA was also tested in the presence of DA and AA as interfering compounds (Figure 48). According to the results, the three expected peaks were well-resolved even at high DA concentration. Nevertheless, the peak corresponding to AA oxidation on AuNPs/NRGO/GCE has significantly lower intensity than those corresponding to DA and UA. Moreover, peak currents of DA and AA oxidation decreased when UA concentration was increased. Both sensors worked linearly in the concentration ranges 250 – 1500 and 20 – 1000 µM (Figures 48b and 48d). Calculated LRs were significantly wider than those obtained in the solution containing individual UA, which would indicate potential interference from AA and DA. The calculated LOD values were 68 and 8.7, respectively (Table 14). As expected, the values were higher to those obtained in case of individual determination of UA.

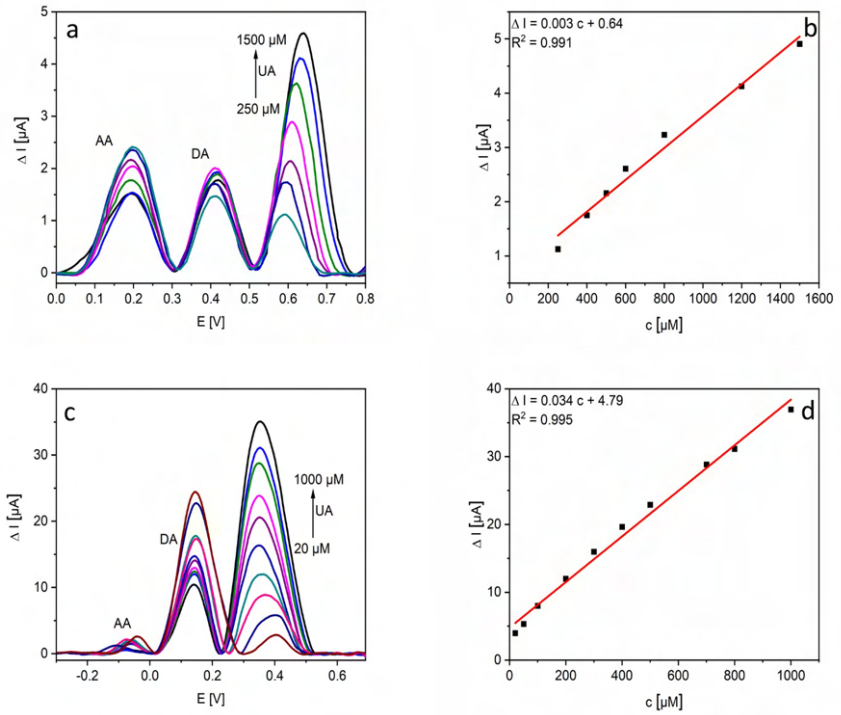

Figure 48. Baseline-corrected DPVs recorded on (a) AuNPs/RGO/GCE, (c) AuNPs/NRGO/GCE in a 0.1 M PBS solution (pH=7.0) at increasing concentrations of UA and constant AA (300 μM) and DA (100 μM) concentrations. Corresponding calibration curves for (b) AuNPs/RGO/GCE, (d) AuNPs/NRGO/GCE.

Sensitivity in the simultaneous determination of three analytes decreased comparing to their individual detection, which was in agreement with interference studies results. Nevertheless, both active electrode materials provided good resolution of the peaks corresponding to DA, AA and UA oxidation in their simultaneous determination.

Table 14. Electrochemical performance of AuNPs/RGO/GCE and AuNPs/NRGO/GCE electrodes towards DA, AA and UA simultaneous detection

Sensor	LOD, μM			LR, μM			Sensitivity, μA μM^{-1}		
	DA	AA	UA	DA	AA	UA	DA	AA	UA
AuNPs/RGO/GCE	3.9	57	68	8–80	100–1500	250–1500	0.41	0.003	0.003
AuNPs/NRGO/GCE	2.4	58	8.7	3–100	550–1500	20–1000	0.19	0.002	0.034

Summary

The impact of nitrogen functional groups presented into the RGO structure on the subsequent distribution of AuNPs and further electrochemical performance for target analytes detection

was determined. RGO and NRGO were synthesized using hydrothermal treatment at 180 ˚C for 12h. The use of urea as a nitrogen source enabled obtaining NRGO with 6.4 at.% of nitrogen. AuNPs were electrochemically deposited directly on the surface of RGO/GCE and NRGO/GCE reaching metallic nanoparticles contents of 6.2 and 7.6 at.%, respectively. A higher amount of smaller AuNPs was homogenously deposited on the NRGO/GCE electrode despite shorter electrodeposition time. The comparison of sensing performance of modified GCEs towards DA demonstrated the beneficial impact of nitrogen groups, which was further enhanced by deposition of AuNPs, leading to a lower LOD value (385 nM) and to an improved reproducibility and repeatability. Determination of AA and UA using AuNPs/RGO/GCE and AuNPs/NRGO/GCE revealed that electrode containing nitrogen groups also performed better for detecting interfering compounds, reaching LOD values of 44 and 2.7 μM for UA and AA, respectively. Nanocomposites of graphene materials and AuNPs were also tested for the simultaneous detection of AA, DA and UA. According to the results, the obtained LOD values were higher than those corresponding to the detection of individual analytes. Moreover, sensitivity of measurements also decreased which could be the result of electrode fouling issues by products of redox reactions of interfering species.

5.1.2 Graphene-based nanocomposites with PANI

5.1.2.1 Morphology and structure of nanocomposites

The morphology of starting (Figure 49) and nanocomposite materials (Figure 50) was thoroughly investigated by FESEM. PANI synthesized by oxidative polymerization procedure (Figure 49a) displayed typical coral-shape nanoparticles [208]. On the other hand, TRGOs showed corrugated layers, typical for materials obtained by thermal exfoliation and reduction of GrO [209]. Comparing TRGO400 (Figure 49b), TRGO700 (Figure 49c) and TRGO1000 (Figure 49d), different exfoliation degree of resulting materials was observed. In case of TRGO1000 (Figure 49d) several accordion type structures were clearly distinguishable [209]. When applying 400°C, the temperature resulted too low to fully exfoliate graphene layers, therefore numerous graphene layer aggregates were still observed. On the other hand, exfoliation and reduction at 1000°C lead not only to an improved removal of oxygen functional groups, but also to the formation of graphene layers aggregates [209].

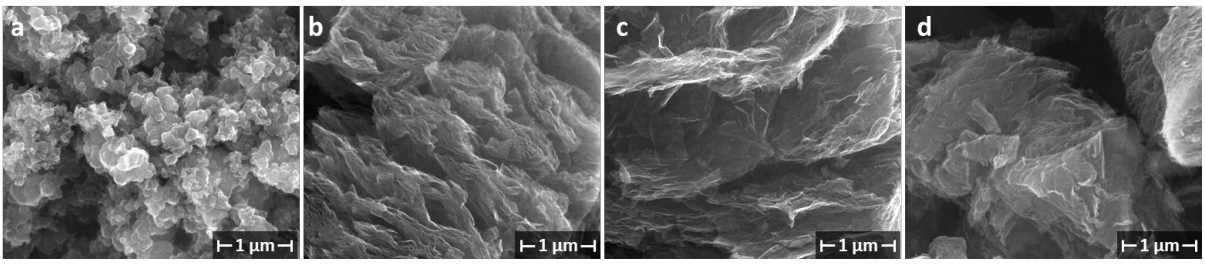

Figure 49. FESEM images of starting materials (a) PANI, (b) TRGO400, (c) TRGO700, (d), TRGO1000.

Hydrothermal synthesis of PANI-TRGOs nanocomposites resulted in different morphologies depending on the starting TRGO and the PANI:TRGO ratio (Figure 50). As an example, figures 50a, b, and c present the nanocomposites synthesized using TRGO400 and different amounts of PANI (PANI:TRGO400 ratios 1:3, 1:1 and 3:1, respectively). When increasing amount of PANI more corral-shape aggregates were observed in the resulting nanocomposites. As previously stated, the temperature of thermal treatment of GrO has a significant impact on the morphology of final TRGOs, and subsequently on the further distribution of PANI. Differences in the morphology of composites obtained from TRGO400, TRGO700 and TRGO1000 with the same PANI contribution are clearly visible (Figures 50b, d, e). Considering PANI-TRGO400 1:1, aggregated PANI particles mainly cover the surface of graphene layer (Figure 50b). On the other hand, due to the better exfoliation degree of the graphene material, a more homogenous distribution of PANI particles was observed in PANI-TRGO700 1:1 (Figure 50d). Polymer particles were homogenously deposited not only on the graphene layers, but also between them. Looking at the morphology of PANI-TRGO1000 1:1, conductive polymer is mainly located between graphene layer (Figure 50e). Table 15 presents the chemical composition, sheet resistance, average interlayer distance, and surface area of the materials under evaluation.

Table 15. Physicochemical properties of starting materials and PANI-TRGOs nanocomposites under evaluation

Sample	Elemental analysis wt.%				Sheet resistance Ω sq^{-1}	d_{002} nm	S_{BET} m^2/g
	C	H	O	N			
PANI	64.95	3.93	21.39	9.73	6.22 x 10^7	-	35
TRGO400	80.80	1.00	18.00	0.20	3.20 x 10^6	0.3651	494
TRGO700	90.32	1.45	8.09	0.14	2.37 x 10^4	0.3465	523
TRGO1000	-	-	-	-	-	0.3559	278
PANI-TRGO400	-	-	-	-	-	-	225
PANI-TRGO400	74.31	2.59	17.49	5.61	1.86 x 10^6	0.3641	131
PANI-TRGO400	-	-	-	-	-	-	73
PANI-TRGO700	79.96	2.74	11.71	5.60	9.84 x 10^4	0.3497	143
PANI-TRGO1000	-	-	-	-	-	0.3571	173

To gain insight into the distribution of PANI within and/or onto the different TRGOs materials, XRD measurements were performed, and the corresponding average interlayer distance (d_{002}) was calculated (Table 15). According to the data, this value resulted higher for TRGO400 when comparing to PANI-TRGO400 1:1 (0.3651 nm vs. 0.3641 nm, respectively) which can indicate that PANI particles in this nanocomposite were mainly deposited onto the surface of graphene layers leading to their compression. Contrarily, d_{002} value was higher in the PANI-TRGO700 1:1 than in the starting graphene material (0.3465 vs. 0.3497 nm) indicating the preferential deposition of PANI particles between the graphene layers, leading to their separation. Considering TRGO1000, d_{002} also increased after PANI incorporation to form the nanocomposite (0.3559 vs. 0.3571 nm) pointing that also several PANI aggregates are being introduced between graphene layers leading to their separation. According to N_2 isotherms measurements, (Table 15) PANI presented the lowest S_{BET} value while TRGOs provided specific surface areas at around 500 m^2/g. After incorporation of PANI, S_{BET} of resulting nanocomposites significantly decreased indicating their successful synthesis. Such a decrease of S_{BET} can have a beneficial impact on electrochemical detection, lowering the capacitive current [122].

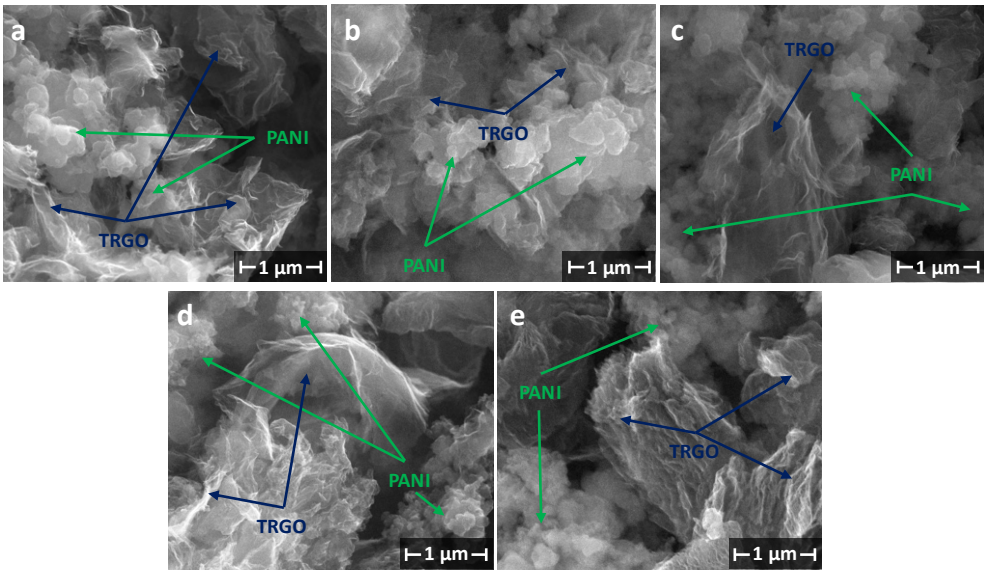

Figure 50. FESEM images of (a) PANI-TRGO400 1:3, (b) PANI-TRGO400 1:1, (c) PANI-TRGO400 3:1, (d) PANI-TRGO700 1:1, (e) PANI-TRGO1000 1:1.

The chemical surface composition of starting and nanocomposite materials was determined by XPS (Table 16). As expected, the oxygen content of TRGOs decreased when increasing the thermal treatment temperature, being the same trend observed for subsequent nanocomposites with PANI. Regarding N content, it was higher for PANI-TRGO400 nanocomposites, mainly at the higher ratio (3:1, 4.6 at. %). Comparing nanocomposites obtained from different TRGOs but adding the same amount of polymer, the highest nitrogen content was obtained for PANI-TRGO400 1:1, also corroborating the higher amount of PANI particles deposited on the surface of the graphene layers. Elemental analysis was also performed (for selected materials) and compared with XPS. The bulk nitrogen content for PANI-TRGO400 1:1 and PANI-TRGO700 1:1 was comparable (~5.6 wt.%). However, the N surface content for PANI-TRGO700 1:1 was lower than that for PANI-TRGO400 1:1 (3.5 vs. 2.5 at.%) suggesting that in the former PANI was distributed not only on the surface of graphene layers but also within them.

Table 16. Chemical surface composition of starting and nanocomposite materials determined by XPS (at.%)

Sample	C	N	O
PANI	82.2	8.2	9.6
TRGO400	89.9	-	10.1
TRGO700	94.9	-	5.1
TRGO1000	98.1	-	1.9
PANI-TRGO400 1:3	89.6	1.1	9.3
PANI-TRGO400 1:1	87.8	3.5	8.7
PANI-TRGO400 3:1	86.6	4.6	8.8
PANI-TRGO700 1:1	91.4	2.5	6.1
PANI-TRGO1000 1:1	93.1	2.2	4.7

The chemical composition of starting and nanocomposite materials was studied in detail (Table 17). The C1s spectra of PANI, TRGO400, TRGO700 and TRGO1000 can be divided into five components corresponding to sp^2 hybridized carbon (284.5 eV), sp^3 hybridized carbon and C-N groups (285.4 eV), hydroxyl and epoxy (286.5 eV), carbonyl and quinone bonds (287.6 eV) and carboxylic groups (289.0 eV) (Figure 51) [210]. The peak at binding energy of 284.5 eV corresponding to sp^2 hybridized carbon has the highest intensity for all TRGOs. These results corroborated previously reported ones, where the contribution of sp^2 hybridized carbon increased and peaks corresponding to oxygen and carbon connections decreased when increasing the temperature of the thermal treatment thus proving successful reduction [211]. C1s deconvoluted spectra were also presented for nanocomposite materials (Figure 52). Hydrothermal treatment of TRGOs in the presence of PANI resulted in a decrease of the Csp^2 content and subsequent increase of Csp^3/C-N. Moreover, PANI-TRGO700 1:1 exhibited the highest amount of hydroxyl and carboxyl groups which can have a positive influence on its electrochemical performance for DA detection [122]. For the series of composites with increasing PANI:TRGO ratio, the contribution of Csp^3/C-N also increased, proving the successful incorporation of greater amounts of PANI. Furthermore, comparing PANI/TRGOs obtained from TRGOs reduced at different temperatures, the Csp^2 contribution increased when increasing the temperature of the thermal treatment [209].

In parallel, N1s deconvoluted spectra are shown for PANI and nanocomposite materials (Figure 53). N1s spectra can be resolved into four peaks corresponding to imine (-N=, 398.2 eV), amine (-NH-, 399.6 eV), oxidized amine (-NH^+, 400.9 eV), protonated imine (=N^+, 402.5 eV) [210]. Moreover, the protonation degree (P_s) was calculated as the ratio between positively charged nitrogen groups and total nitrogen content [212]. All composites present the highest intensity

of peak at binding energy at 399.5 eV corresponding to amine nitrogen species [213]. The composites differ in the contribution of positively charged nitrogen. The highest P_s corresponded to PANI-TRGO700 1:1.

For selected materials sheet resistance measurements were also performed (Table 15). TRGO700 was characterized by a lower sheet resistance (2.37 x 10^4 Ω sq^{-1}) than TRGO400 (3.20 x 10^6 Ω sq^{-1}), which can directly results from a higher restoration of the Csp^2 network (Csp^2 contribution 66.5 vs. 55.2 at.%, respectively). Introduction of PANI into TRGOs leads to an increase of sheets resistance, even though the resulting values were at the same order that those for the corresponding starting materials (9.84 x 10^4 vs. 1.86 x 10^6 Ω sq^{-1} for PANI-TRGO700 1:1 and PANI-TRGO400 1:1).

Table 17. Type and distribution of C and N functional groups, at.%

Sample	C1s peak deconvolution					N1s peak deconvolution				
	Csp^2	Csp^3/C-N	C-OH	C=O	O=C-OH	-N=	-NH-	-NH+	=N+	Ps %
PANI	43.1	21.2	7.0	4.7	4.2	0.2	5.9	1.9	0.2	25.6
TRGO400	55.2	7.4	12.6	3.4	11.3	-	-	-	-	-
TRGO700	66.5	9.1	7.6	4.3	7.4	-	-	-	-	-
TRGO1000	77.2	11.2	5.2	2.2	2.3	-	-	-	-	-
PANI-TRGO400 1:3	51.0	14.9	11.9	7.4	4.4	0.1	0.9	0.1	0.0	9.1
PANI-TRGO400 1:1	50.9	17.1	7.1	7.4	5.3	0.1	3.0	0.3	0.1	11.4
PANI-TRGO400 3:1	49.5	20.1	8.1	4.4	4.5	0.2	3.7	0.6	0.1	15.2
PANI-TRGO700 1:1	56.4	17.5	8.9	3.0	5.6	0.1	1.9	0.5	0.0	20.0
PANI-TRGO1000	66.5	14.1	5.0	3.3	4.2	0.1	2.0	0.1	0.0	4.5

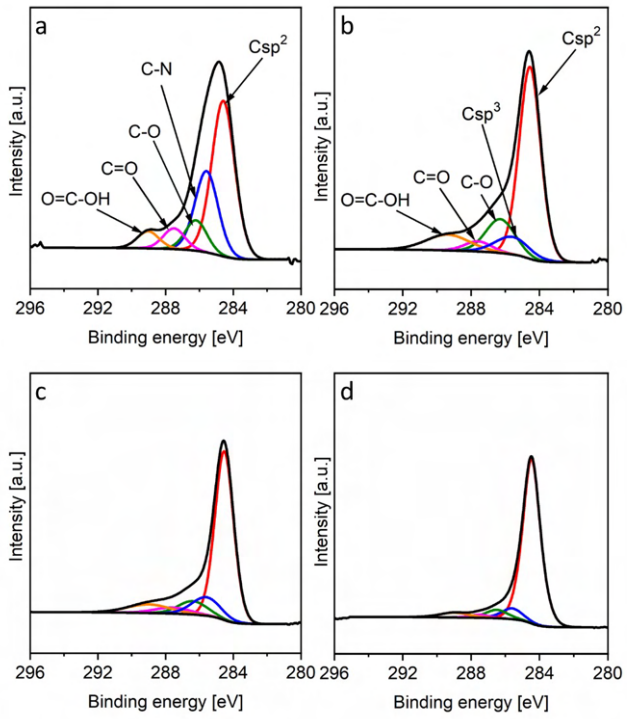

Figure 51. Deconvolutions of C1s core-level XPS spectra of starting (a) PANI, (b) TRGO400, (c) TRGO700 and (d) TRGO1000.

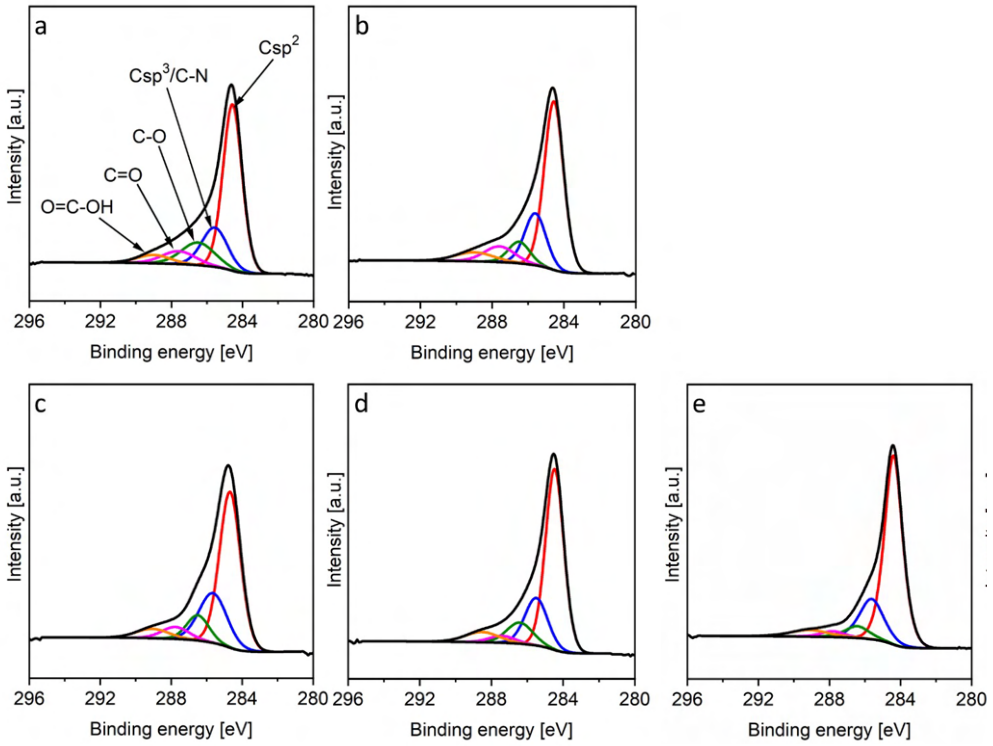

Figure 52. Deconvolutions of C1s core-level XPS spectra of (a) PANI-TRGO400 1:3, (b) PANI-TRGO400 1:1, (c) PANI-TRGO400 3:1, (d) PANI-TRGO700 1:1, (e) PANI-TRGO1000 1:1.

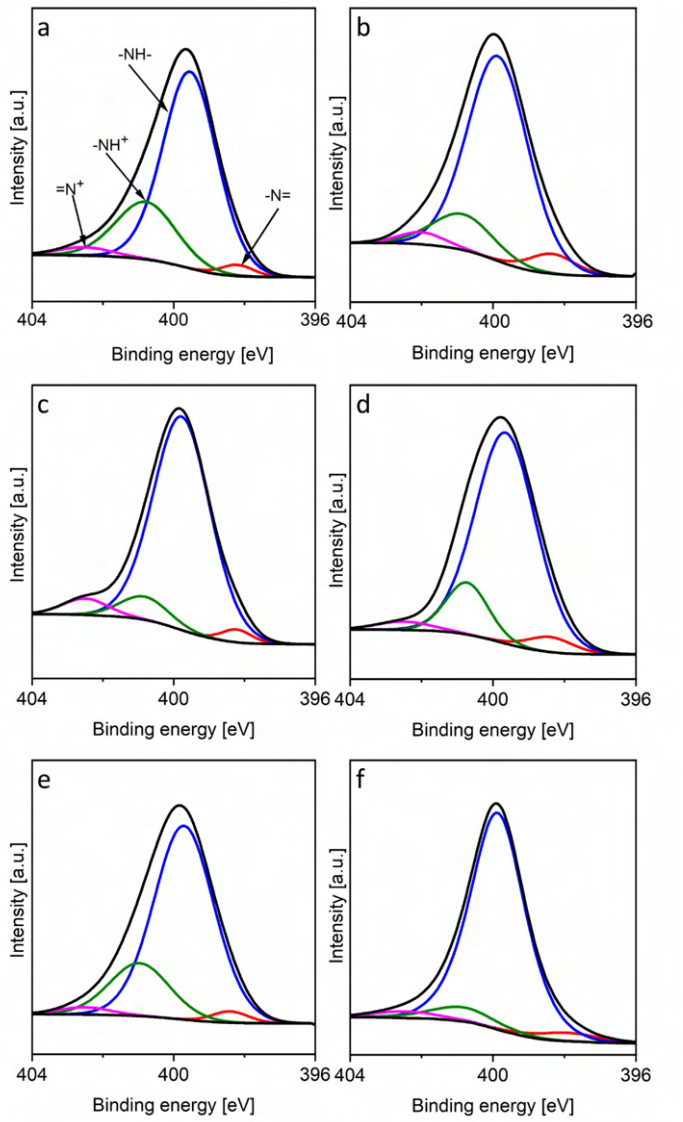

Figure 53. Deconvolutions of N1s core-level XPS spectra of (a) PANI, (b) PANI-TRGO400 1:3, (c) PANI-TRGO400 1:1, (d) PANI-TRGO400 3:1, (e) PANI-TRGO700 1:1, (f) PANI-TRGO1000 1:1.

5.1.2.2 Electrochemical detection of DA

Impact of PANI on DA sensing

As a first approach, the influence of PANI in the final nanocomposite structure, and its subsequent impact on the DA sensing was evaluated. For this purpose, a series of PANI-TRGO400 samples, synthesized varying the weight ratio of polymer:graphene material, was tested. CVs recorded on GCE, PANI/GCE, TRGO400/GCE, PANI-TRGO400 1:3/GCE, PANI-TRGO400 1:1/GCE and PANI-TRGO400 3:1/GCE are presented in Figure 54. On all electrodes, a well-developed DA oxidation peak was observed, except the PANI/GCE, on

which very broad and low current intensity peak was recorded (13.9 µA at 293.1 mV) [214]. On the other hand, modification of GCE with TRGO400 and derived nanocomposites lead to an increased capacitive current (probably due to an o enhanced active electrode surface area). Thus, the highest anodic peak current was recorded on TRGO400/GCE (89.5 µA at 261.1 mV), as result of the highest S_{BET} of this graphene material (494 m^2/g) and its highest capacitive current contribution. Anodic peak currents recorded on nanocomposites presented lower values (70.6, 48.8, and 36.8 µA for PANI-TRGO400 1:3/GCE, PANI-TRGO400 1:1/GCE and PANI-TRGO400 3:1/GCE, respectively) due to their lower S_{BET} values. However, these peaks were recorded at lower overpotentials comparing to that of TRGO400/GCE (~240 and 261 mV for nanocomposites and TRGO400). To select the most suitable active electrode material for DA sensing further studies were carried out.

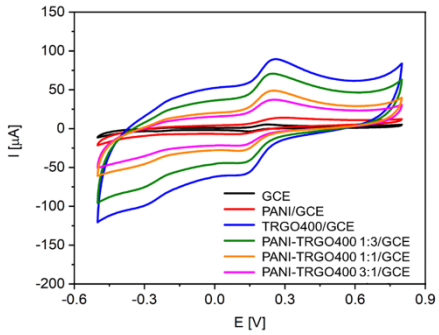

Figure 54. CVs recorded on modified GCEs in a 0.1 M PBS solution (pH = 7.0) containing 100 µM of DA.

To perform electrochemical measurements with the highest effectiveness, pH optimization was performed (Figure 55a). Relationships regarding the anodic peak current vs. pH and the overpotential vs. pH were presented (Figure 55b). The optimization was performed in a PBS solution containing 100 µM of DA, varying the pH from 5.8 to 8.0, on all the electrodes under investigation. Nevertheless, to compare their electrochemical performance, for all electrodes the same pH value was sought looking for a compromise between the higher anodic peak current, lower overpotential and possible application in real samples analysis. For PANI/GCE (Figures 55a and b) the highest anodic peak current was recorded at pH 5.8 (70.9 µA at 525.4 mV). This high overpotential value allowed us to discard this electrode, considering potential interference issues in the presence of UA, having a similar oxidation potential. Moreover, the additional peak corresponding to cationic radicals' creation in PANI structure at more acidic pH values is highly distinctive [215]. Considering TRGO400/GCE (Figures 55c and d), the highest anodic peak current was recorded at pH 6.2 (79.9 µA at 281.1 mV). For PANI-

TRGO400 1:3/GCE, PANI-TRGO400 1:1/GCE, PANI-TRGO400 3.1/GCE the highest anodic peak currents were recorded at pH values of 6.6 (115.4 μA at 248.3 mV), 6.6 (43.7 μA at 241.4 mV) and 7.0 (49.8 μA at 229.3 mV). In case of TRGO400/GCE there was a significant decrease of overpotential when measurement was performed at higher pH value (281.2 vs. 217.2, for 6.2 and 7.0, respectively) while the anodic peak current was almost unaffected (79.9 vs. 78.6 μA, for 6.2 and 7.0, respectively). Similarly, for PANI-TRGO400 1:3/GCE the overpotential decreased from 248.3 to 232.3 mV for 6.6 and 7.0 pH values, and anodic peak current only decreased by 0.7 μA. In addition, on PANI-TRGO400 1:1/GCE the overpotential at pH 7.0 is lower of about 16.1 mV in comparison to pH 6.6 and anodic peak current dropped by 0.5 μA. Taking into account all materials under evaluation and the physiological pH value, the final optimized pH value was 7.0.

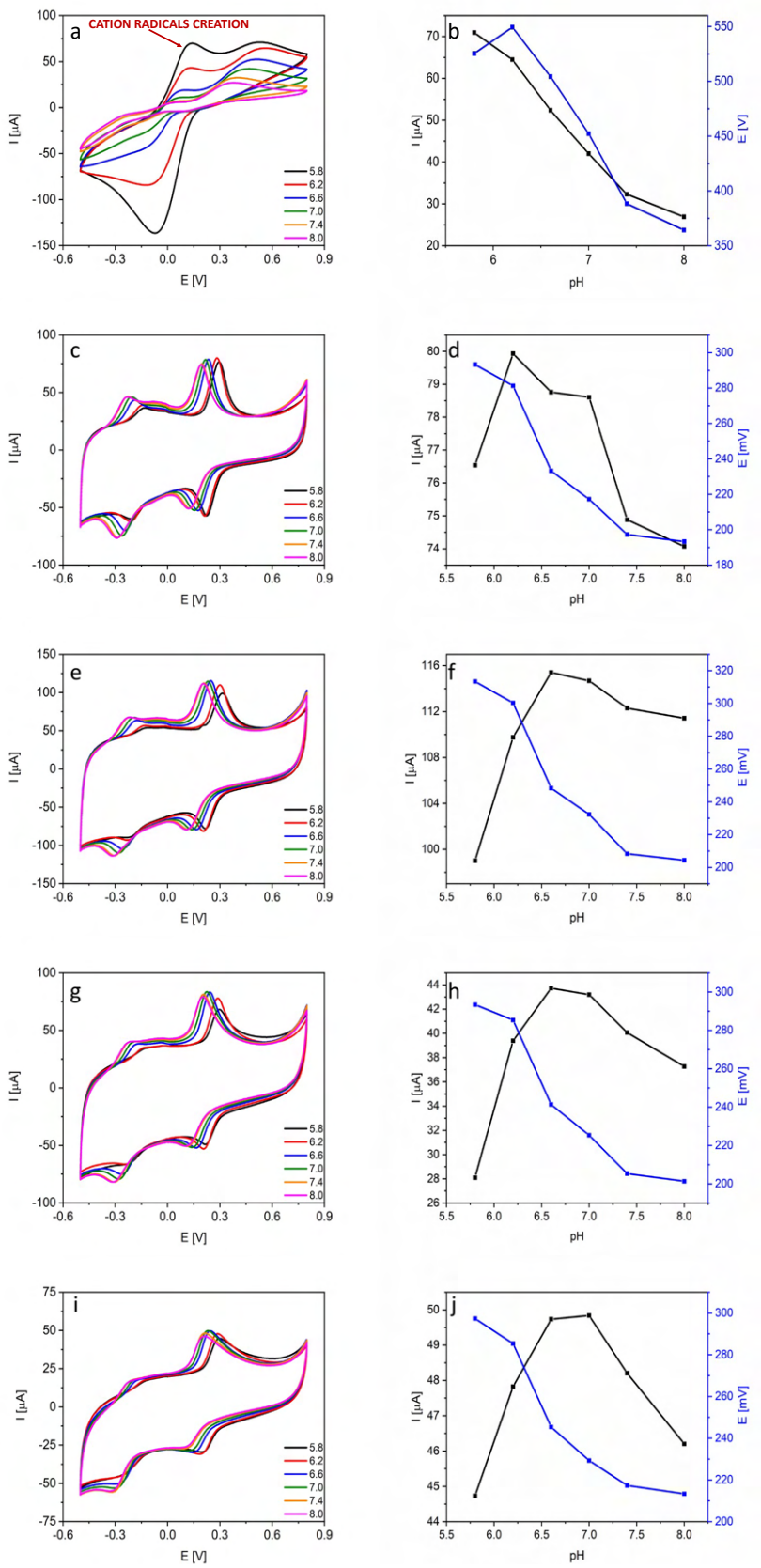

Figure 55. CVs recorded (v_{scan} = 100 mV s^{-1}) at increasing pH values on (a) PANI/GCE, (c) TRGO400/GCE, (e) PANI-TRGO400 1:3/GCE and (g) PANI-TRGO400 1:1/GCE, and (i) PANI-TRGO400 3:1/GCE in a 0.1 M PBS solution containing 100 µM of DA. Influence of the

selected pH value on the oxidation current and peak potential values recorded on (b) PANI/GCE, (d) TRGO400/GCE, (f) PANI-TRGO400 1:3/GCE (h) PANI-TRGO400 1:1/GCE, and (j) PANI-TRGO400 3:1/GCE.

To determine the main mechanism controlling DA oxidation CV measurements at increasing scan rates (2 – 250 mV s^{-1}) were carried out in a 0.1 M PBS solution (pH = 7.0) containing 100 µM DA (Figure 56). According to the results, all assessed electrodes displayed a linear relationship between the anodic peak current and the square root of the scan rate. In addition, the logarithmic relationship between both parameters was plotted, varying the related slopes from 0.16 for PANI/GCE to 0.63 for TRGO400/GCE and 0.58, 0.50 and 0.46 for PANI/TRGO400 1:3/GCE, PANI/TRGO400 1:1/GCE and PANI/TRGO400 3:1, respectively (Figures 56c, f, i, l, o). From all these results, it can be assumed that DA oxidation is a mainly diffusion-controlled process [200,216].

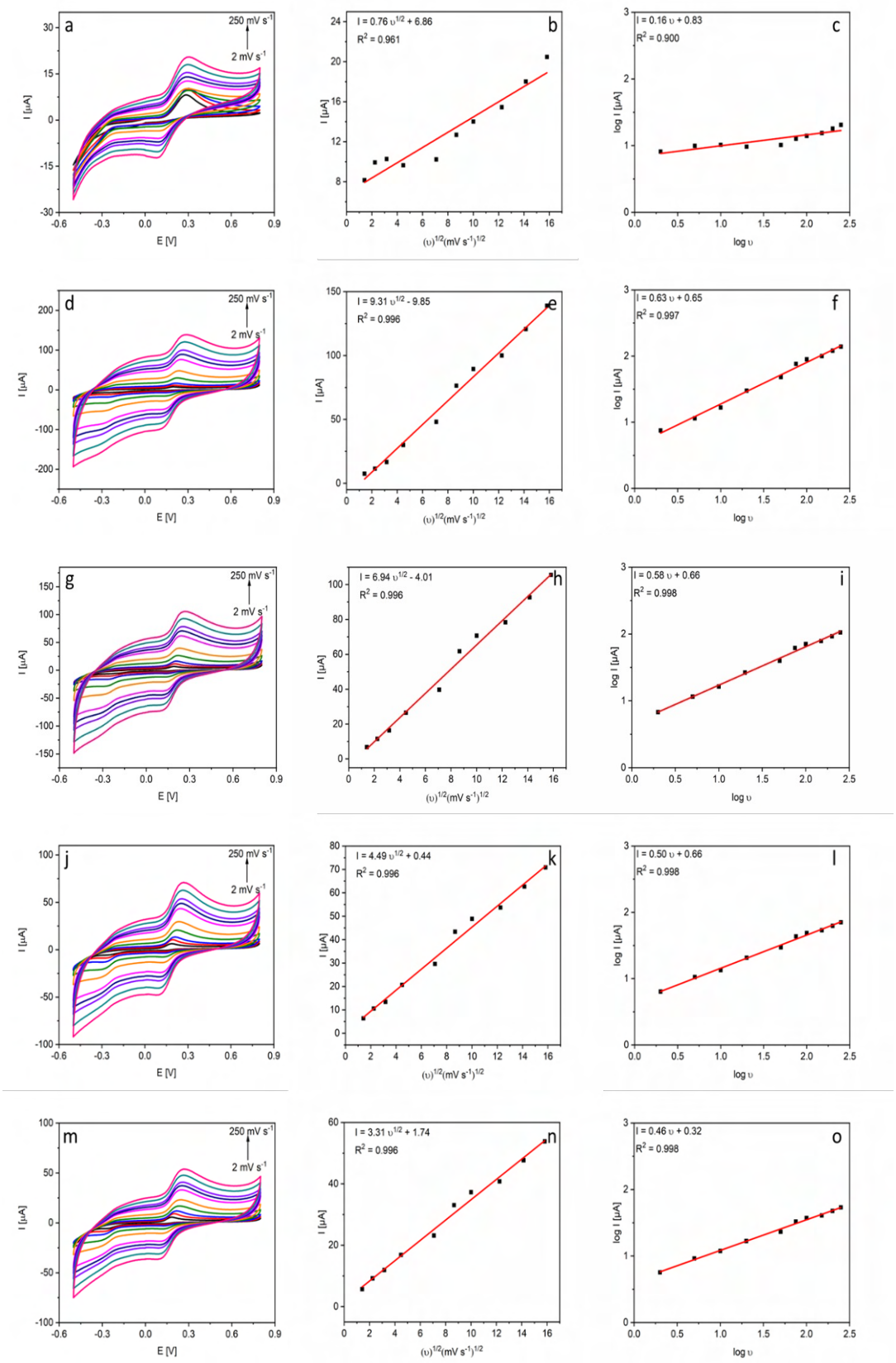

Figure 56. CVs recorded at increasing scan rates (2, 5, 10, 20, 50, 75, 100, 150, 200, 250) on (a) PANI/GCE, (c) TRGO400/GCE, (e) PANI-TRGO400 1:3/GCE, (g) PANI-TRGO400 1:1/GCE, and (i) PANI-TRGO400 3:1/GCE in a 0.1 M PBS solution (pH=7.0) with 100µM of

DA. Relationships between maximum anodic peak current and square root of scan rate on (b) PANI/RGO, (d) TRGO400/GCE, (f) PANI-TRGO400 1:3/GCE, (h) PANI-TRGO400 1:1/GCE, and (j) PANI-TRGO400 3:1/GCE. The logarithmic relationship between scan rate and anodic peak current recorded on (c) PANI/GCE, (f) TRGO400/GCE, (i) PANI-TRGO400 1:3/GCE and (l) PANI-TRGO400 1:1/GCE (o) PANI-TRGO400 3:1/GCE.

The last stage covered DPV measurements at increasing DA concentration (0.1 - 300 μM) and optimized pH value (pH 7.0) (Figure 57). The linear range achieved on GCEs modified with starting materials (PANI/GCE and TRGO400/GCE) was 1-25 μM (Figures 57b and d) (Table 18). Moreover, the high correlation coefficients indicated on suitable estimation of operational sensors parameters. However, TRGO400/GCE provided a significantly lower LOD than PANI/GCE. This result could be explained considering the presence of positively charged nitrogen functional groups in the structure of PANI which contributed to the repulsion of the cationic form of the analyte from the electrode surface [217]. On the other hand, PANI enabled to perform measurements with higher resolution (sensitivity of 4.34 $\mu A\ \mu M^{-1}$ for PANI/GCE vs. 3.58 for TRGO400/GCE). While evaluating subsequent nanocomposites, addition of 25 and 50 wt.% of conductive polymer to TRGO400 led to a significant improvement of LOD and LR for DA (Figures 57f and h). At the selected pH value, DA (pK_a = 8.93) is in its cationic form, therefore it is crucial to introduce oppositively charged functionalities, as oxygen groups. Bearing in mind that these oxygen groups lead to lower electrical conductivity of the material, it is crucial to find a compromise relating to the suitable oxygen contribution [122]. Thus, LOD value calculated for PANI-TRGO400 1:3/GCE was still higher than the corresponding for TRGO400/GCE despite having similar oxygen content (~ 9.5 at%.). This is in agreement with the presence of positively charged N moieties in the nanocomposite, which led to the target analyte repulsion. Considering above shown SEM images, PANI aggregates were mainly on the surface of graphene layers for the series of nanocomposites under study, which could negatively impact on sensors performance. The more improved LOD value was recorded on PANI-TRGO400 1:1/GCE, as a consequence of its moderate oxygen content (8.7 at.%), without significant impact on electrical conductivity. Moreover, this good result can be correlated with the higher protonation degree of this electrode, positively contributing to the electrical conductivity (11.4 % vs. 9.1 for PANI-TRGO400 1:3/GCE and PANI-TRGO400 1:1/GCE, respectively). Going one step further, the LOD for PANI-TRGO400 3:1/GCE was almost the same as for PANI/GCE, corroborating that 75 wt.% of PANI is to high amount to effectively detect DA. The oxygen content for PANI-TRGO400 1:1/GCE and PANI-TRGO400 3:1/GCE

was comparable (8.7 vs. 8.8 at.%), even though the latter one presented a higher N content (4.6 at.%), mainly in the form of amine groups which were also in DA structure leading to the repulsion of target analyte. On the other hand, PANI can increase affinity of DA to the electrode surface due to the π- π interactions [218]. Taking into account the overpotential of DA oxidation, the value decreased from 249.2 for TRGO400/GCE to 234.2, 224.3 and 234.3 mV for PANI-TRGO400 1:3/GCE, PANI-TRGO400 1:1/GCE and PANI-TRGO400 3:1/GCE, indicating an enhanced electron transfer in the nanocomposite materials.

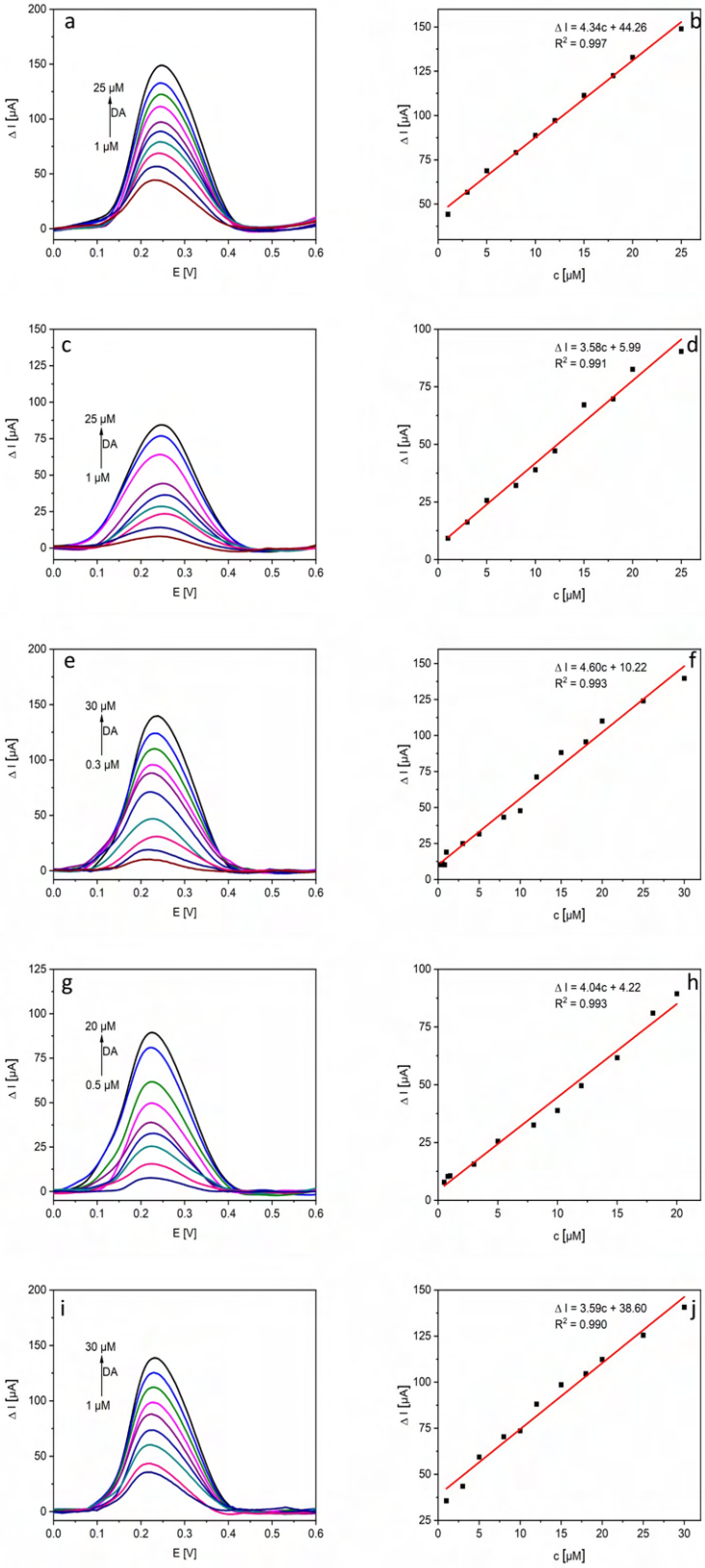

Figure 57. Baseline-corrected DPVs recorded on (a) PANI/RGO, (c) TRGO400/GCE, (e) PANI-TRGO400 1:3/GCE, (g) PANI-TRGO400 1:1/GCE, and (i) PANI-TRGO400 3:1/GCE in a 0.1 M PBS solution (pH=7.0) with increasing concentration of DA. Corresponding

calibration curves for (b) PANI/GCE, (d) TRGO400/GCE, (f) PANI-TRGO400 1:3/GCE, (h) PANI-TRGO400 1:1/GCE, and (j) PANI-TRGO400 3:1/GCE.

Table 18. Electrochemical performance of PANI/GCE, TRGO400/GCE, PANI-TRGO400 1:3/GCE, PANI-TRGO400 1:1/GCE and PANI-TRGO400 3:1/GCE electrodes towards DA sensing

Sensor	LOD nM	LR μM	Sensitivity μA μM^{-1}	Reproducibility RSD %	Repeatability RSD %
PANI/GCE	1570	1 – 25	4.34	7.9	3.8
TRGO-400/GCE	883	1 – 25	3.58	9.7	2.8
PANI-TRGO400 1:3/GCE	1180	0.3 – 30	4.60	9.3	3.1
PANI-TRGO400 1:1/GCE	701	0.5 – 30	3.63	6.6	5.5
PANI-TRGO400 3:1/GCE	1550	1 – 30	3.59	4.0	1.6

Reproducibility and repeatability measurements revealed the successful modification of GCEs with all the active materials, mainly after PANI addition. Repeatability of the measurements on all the modified GCEs did not exceed the RSD range of 1.6 – 5.5 %. Concluding, from the above discussed nanocomposites evaluation, that containing the 50 wt.% of PANI was selected as the most suitable for DA sensing, as it provided the most improved sensor working parameters.

Impact of selected TRGO on DA sensing

Once optimized the amount of conductive polymer, the impact of selected TRGO material on sensors performance for DA was evaluated. As previously stated, temperature of the thermal treatment has a high impact on the morphology of the resulting graphene material, as different exfoliation degrees can be achieved, thus to different porosities. Then, exfoliation of TRGO determines the distribution of PANI in the nanocomposite which implies differences in the contribution of the surface functional groups. Therefore, it is facile to modulate the contribution of functional groups originated from PANI on the surface of the material and in the bulk. Among synthesized PANI/TRGO nanocomposites, the most homogenous distribution of PANI was observed for PANI/TRGO-700 1:1. This composite had the same nitrogen bulk content as PANI/TRGO-400 1:1 (5.6 wt.%), however lower surface N content (2.5 vs. 3.5 at.%). PANI/TRGO-1000 1:1 was characterized by the lowest surface N content (2.2 at. %). Moreover, it could be observed that higher amount of PANI in the nanocomposite led to

decreased S_{BET} which can be beneficial in electrochemical detection as lower capacitive currents are recorded.

Preliminary CV measurements were performed in a 0.1 M PBS solution (pH = 7.0) containing 100 µM DA (Figure 58). Due to the developed S_{BET} (523 m^2/g) of the graphene material, TRGO-700/GCE displayed a high capacitive current and an anodic peak current of 175.3 µA at 241.4 mV (Figure 58a). Further modification of GCE with PANI-TRGO700 1:1 led to a lower capacitive current and a lower anodic peak current (28.1 µA at. 213.1 mV). Interestingly, opposite behavior could be observed on TRGO-1000/GCE and PANI-TRGO-1000 1:1/GCE (Figure 58b). In this last case, the capacitive current increased despite graphene material has lower S_{BET} (173 vs. 278 m^2/g for TRGO700), reaching an anodic peak current of 32.5µA at 252.2 mV. TRGO1000/GCE presented an anodic peak current of 16.5 5µA at 252.2 mV which can be explained considering its lower oxygen content (1.9 vs. 5.9 at.% for PANI-TRGO1000 1:1, respectively) in TRGO1000 and problems with wettability [219,220]. In case of TRGO700-based nanocomposites, lower overpotential values for DA oxidation was observed after PANI introduction. Comparing PANI-TRGO700 1:1/GCE with PANI-TRGO400 1:1/GCE the overpotential recorded on the first electrode was lower (213.4 vs. 241.3 mV). This results was in agreement with a better electrical conductivity (as follows from related sheet resistance measurements: 1.86 x 10^6 vs. 9.84 x 10^4 Ω sq^{-1} for PANI-TRGO400 and PANI-TRGO700) and, consequently, with a faster electron transfer.

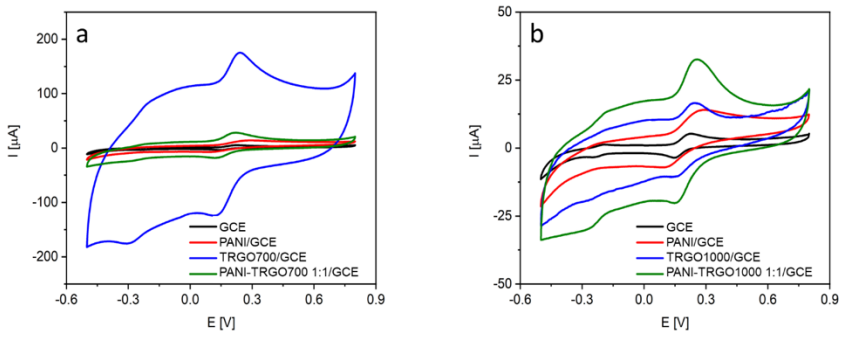

Figure 58. CVs recorded on the different electrodes in a 0.1 M PBS solution (pH = 7.0) containing 100 µM of DA.

Optimization of working pH was performed in the 5.8 to 8.0 range (Figure 59). Relationships between the peak current vs. pH and the overpotential vs. pH are also presented. The highest anodic peak current on TRGO700/GCE was recorded at pH 6.2 (71.7 µA), which was comparable to that recorded on the same electrode at pH 7.0 Regarding the overpotential of DA

oxidation, it was significantly lower at pH 7.0 than 6.2 (265.3 vs. 201.4 mV). On the other hand, the optimal pH value for TRGO1000/GCE was 7.0 (55.8 μA at 243.9 mV) (Figure 59d). However, optimum pH values for the nanocomposites-based electrodes were 6.6 and 6.2 (Figures 59f and h). The anodic peak current decreased only by 0.5 μA on PANI-TRGO700 1:1/GCE at pH 7.0 while related overpotential dropped of 16.0 mV. For PANI-TRGO1000 1:1/GCE DA oxidation overpotential reached a value lower by 24.2 mV while the anodic peak current decreased by 0.9 μA. All the above results corroborated pH 7.0 as the most suitable for further electrochemical measurements.

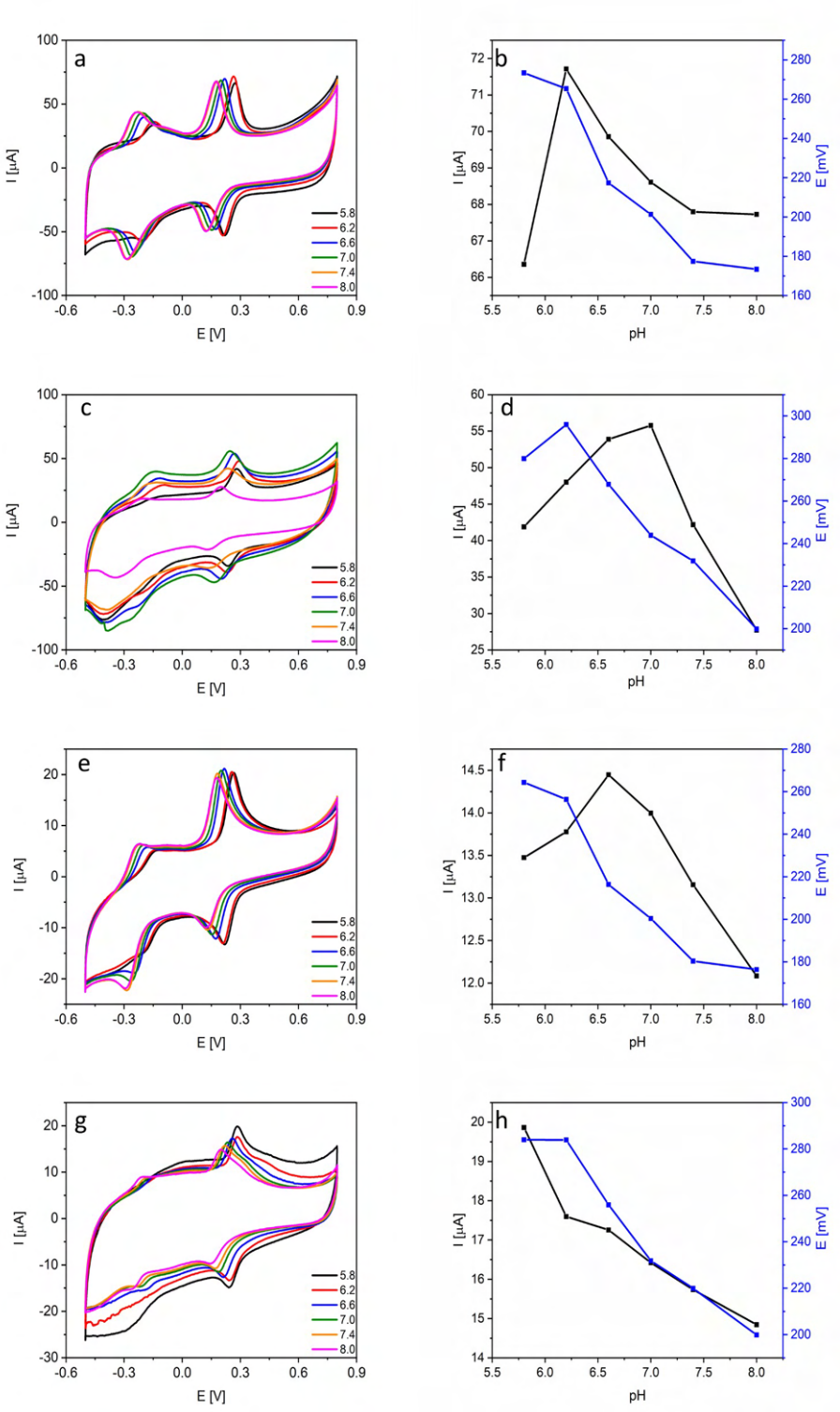

Figure 59. CVs recorded (v_{scan} = 100 mV s^{-1}) at increasing pH values on (a) TRGO700/GCE, (c) TRGO1000/GCE, (e) PANI-TRGO700 1:1/GCE and (g) PANI-TRGO1000 1:1/GCE in a 0.1 M PBS solution containing 100 µM of DA. Influence of the selected pH on the anodic peak current and overpotential values recorded on (b) TRGO700/GCE, (d) TRGO1000/GCE, (f) PANI-TRGO700 1:1/GCE and (h) PANI-TRGO1000 1:1/GCE.

Scan rate measurements in the scan rate range of 2-250 mV s^{-1} were performed to determine the main mechanism controlling DA oxidation (Figure 60). Relationship between maximum anodic peak current and the square root of scan rate was linear on all tested electrodes reaching correlation coefficient varying between 0.968 – 0.996. Moreover, the slopes from the logarithmic relationship between the scan rate and the anodic peak current (0.74 for TRGO700/GCE, 0.47 for TRGO1000/GCE and 0.54 and 0.55 for nanocomposites) also indicated diffusion as the main mechanism controlling DA oxidation [200].

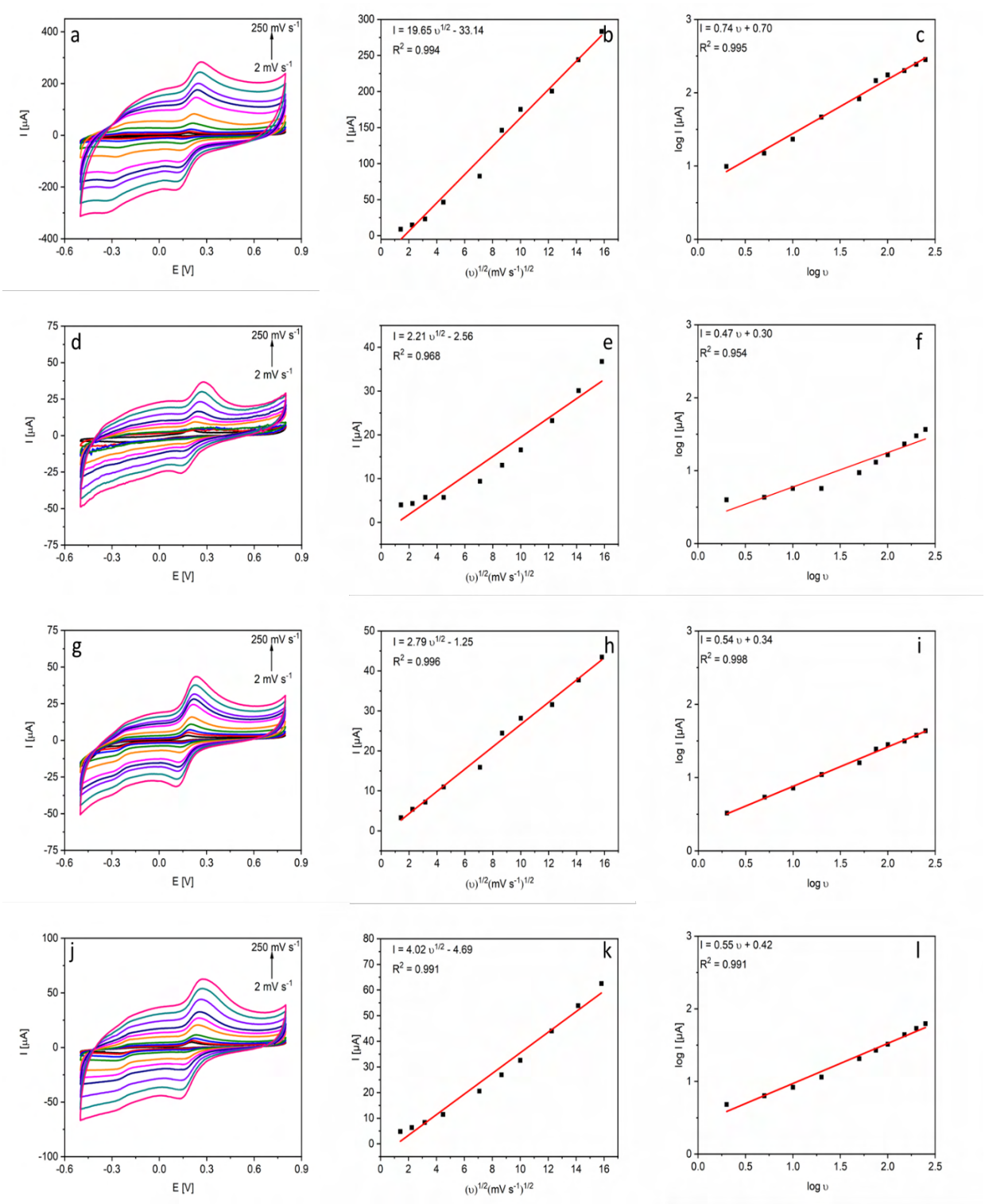

Figure 60. CVs recorded at increasing scan rates (2, 5, 10, 20, 50, 75, 100, 150, 200, 250) on (a) TRGO700/GCE, (c) TRGO1000/GCE, (e) PANI-TRGO700 1:1/GCE and (g) PANI-TRGO1000 1:1/GCE in a 0.1 M PBS solution (pH=7.0) with 100µM of DA. Relationships between maximum anodic peak current and square root of scan rate recorded on (b) TRGO700/GCE, (d) TRGO1000/GCE, (f) PANI-TRGO700 1:1/GCE and (h) PANI-

TRGO1000 1:1/GCE. The logarithmic relationship between scan rate and anodic peak current recorded on (c) TRGO700/GCE, (f) TRGO1000/GCE, (i) PANI-TRGO700 1:1/GCE and (l) PANI-TRGO1000 1:1/GCE.

DPV measurements (in the DA concentration range 0.1 – 300 μM) were also performed on all the electrodes under evaluation to determine the calibration curves and sensors working parameters (Figure 61). Then, ranges in which sensors worked linearly were selected (Table 19). As it can be seen, LR was significantly improved on the nanocomposites-based sensors. Moreover, the correlation coefficients were high for all the tested electrodes indicating the suitable selection of LRs. Comparing PANI-TRGO700 1:1/GCE (Figures 61e and f) and PANI-TRGO1000 1:1/GCE (Figures 61g and h) with PANI/GCE, TRGO700/GCE and TRGO1000/GCE) the improvement of sensors working parameters (in terms of LOD and LR) was significant. Among them, PANI-TRGO700 1:1/GCE sensor provided the best performance, with the lowest LOD (430 nM) and the highest sensitivity (6.71 $\mu A\ \mu M^{-1}$) for DA sensing (Table 19). These good results could be explained considering its highest protonation degree (20 %) and subsequent better electrical conductivity. Furthermore, PANI can slightly increase attachment of DA molecules due to π-π interactions [218]. The lower oxygen content in PANI-TRGO1000 1:1/GCE resulted in a higher LOD as fewer active sites, facilitating attachment of DA to the electrode surface, were available. All the above discussed results clearly indicate that it is key to find a compromise between the oxygen content and the restoration of electrical conductivity for achieving a suitable active material towards DA detection. Comparing PANI-TRGO700 1:1/GCE to previously tested PANI-TRGO400 1:1/GCE the former sensor provided better working parameters, as a result of a more homogenous distribution of PANI within the graphene layers and synergistic effect between composite counterparts providing suitable oxygen and PANI contents. PANI-TRGO700 1:1/GCE, even having a lower oxygen content (6.1 vs. 8.7 at.%,), presented a suitable amount of surface oxygen groups enabling the attachment of DA while preserving and appropriate electrical conductivity. In parallel, PANI-TRGO1000 1:1/GCE also showed better electrochemical performance towards DA than PANI-TRGO400 1:1/GCE despite its lower protonation degree (4.5 vs. 11.4 %) and oxygen content (4.7 vs. 8.7 at.%). Bearing in mind previously shown d_{002} values for TRGOs and their nanocomposites with PANI, this parameter decreased after PANI introduction for TRGO400 and increased for TRGO700 and TRGO1000. This suggest that homogenous distribution of PANI particles within TRGO layers is crucial for effective DA determination. Moreover, after PANI introduction the DA oxidation also

decreased, reaching the lowest value of 214.2 mV on PANI-TRGO700 1:1/GCE indicating an enhanced electrocatalytic effect of the nanocomposite.

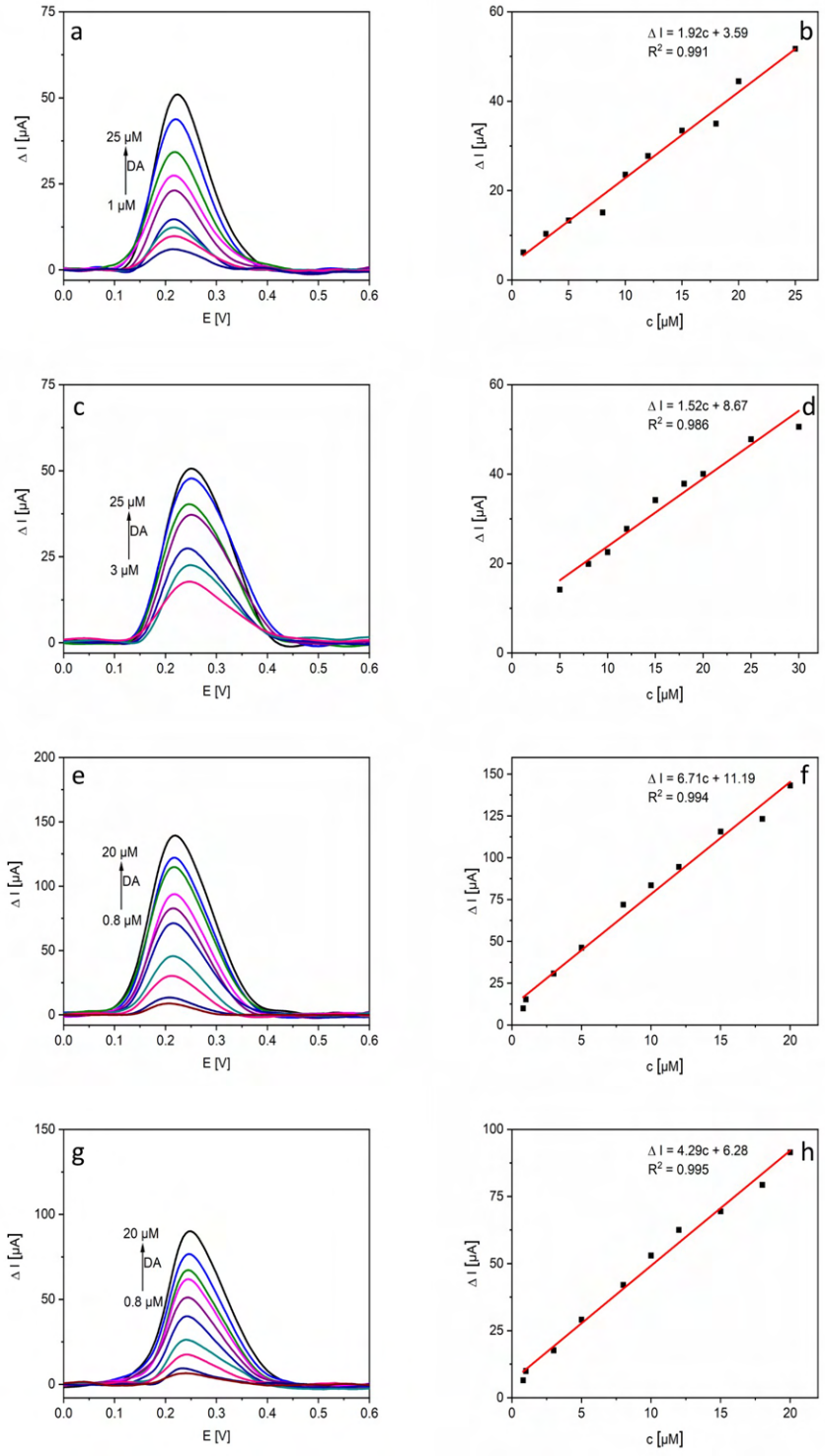

Figure 61. Baseline-corrected DPVs recorded on (a) TRGO700/GCE, (c) TRGO1000/GCE, (e) PANI-TRGO700 1:1/GCE and (g) PANI-TRGO1000 1:1/GCE in a 0.1 M PBS solution (pH = 7.0) with increasing concentration of DA. Corresponding calibration curves recorded on (b)

TRGO700/GCE, (d) TRGO1000/GCE, (f) PANI-TRGO700 1:1/GCE and (h) PANI-TRGO1000 1:1/GCE.

As mentioned, the highest sensitivity was calculated for PANI-TRGO700 1:1:/GCE (6.71 vs. 3.63 μA μM^{-1} for PANI-TRGO400 1:1/GCE) as a result of its lower sheet resistance (9.84 x 10^4 vs. 1.86 x 10^6 for PANI-TRGO4001:1/GCE). Considering repeatability and reproducibility, it is accepted that the crucial factor to improve both parameters is the synergetic effect between PANI particles and graphene layers of TRGOs, as the lowest values were obtained for nanocomposites [221]. In addition, a homogenous distribution of PANI within TRGOs layers enabled to achieve satisfactory values of both parameters.

Table 19. Electrochemical performance of TRGO-700/GCE, TRGO-1000/GCE, PANI-TRGO700 1:1/RGO/GCE and PANI-TRGO1000 1:1/GCE electrodes towards DA sensing

Sensor	LOD nM	LR μM	Sensitivity μA μM^{-1}	Reproducibility RSD %	Repeatability RSD %
TRGO-700/GCE	965	1 – 25	1.92	7.2	2.5
TRGO-1000/GCE	1213	3 – 25	1.52	6.9	2.4
PANI-TRGO-700/GCE	430	0.8 – 20	6.71	4.0	1.0
PANI-TRGO-1000/GCE	506	0.8 – 20	4.28	5.1	3.4

Selectivity studies were performed on PANI-TRGO700 1:1/GCE as this sensor showed the highest improvement of performance for DA sensing. DPV measurements were performed in a 0.1 M PBS solution containing 300 μM of AA and UA (as interfering compounds) and increasing concentration of DA (Figure 65). Sensor worked linearly in the concentration range of 0.8 - 20 μM, which is the same as in the detection of individual DA. The obtained results seemed to be highly promising as DA-UA oxidation peaks separation presented a value of 135 mV. However, it can be noticed (Figure 65a) that when increasing concentration of DA the intensity of UA oxidation signal decreased. This could suggest the occupation of several electrode active sites by UA, as protonated amine moieties (20% of total N content) can increase affinity of anionic UA form to electrode surface. Then, when increasing DA concentration, UA molecules are removed from the electrode surface. The LOD for DA increased from 430 to 842 nM which can be explained by marked interference issues, mainly originated from UA, as the peak corresponding to AA was not presented. Consequently, the sensitivity of the sensor dropped from 6.71 to 4.16 μA μM^{-1} (Table 20).

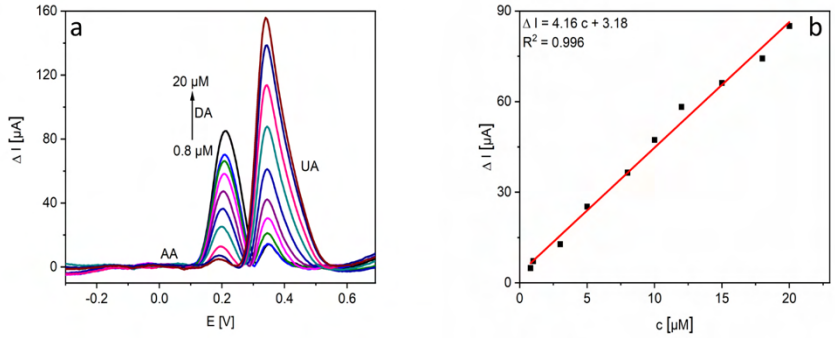

Figure 65. Baseline-corrected DPVs recorded on (a) PANI-TRGO700 1:1/GCE in a 0.1 M PBS solution (pH=7.0) with increasing concentration of DA and 300 μM of AA and UA. Corresponding calibration curves for (b) PANI-TRGO700 1:1/GCE.

Table 20. Electrochemical performance of PANI-TRGO700 1:1/GCE towards DA sensing in the presence of interfering compounds (300 μM of AA and UA)

Sensor	LOD nM	LR μM	Sensitivity μA μM^{-1}
PANI-TRGO-700/GCE	842	0.8 – 20	4.16

Extended interference studies were performed on PANI-TRGO700 1:1/GCE to assess its potential application when analyzing complex samples from different sources. Thus, impact of 800 μM creatinine, 1000 μM glucose, 600 μM KCl and 1100 μM NaCl on DA oxidation signal was tested using DPV measurements (Figure 66a). As it can be observed, a well-developed anodic peak was recorded maintaining the same LR as during individual sensing of target analyte (Figure 66b). No more additional peaks appeared, confirming the appropriate selectivity of the as-proposed sensor. However, a slight deterioration of the LOD for DA (from 430 to 450 nM) was observed (Table 21). Moreover, the sensitivity decreased from 6.71 to 5.63 μA μM^{-1}. Both observations can be the result of a small interference originated from ions existing in tested solution (i.e. anodic peak ascribed to creatinine oxidation can appear at similar potential value as DA [222].

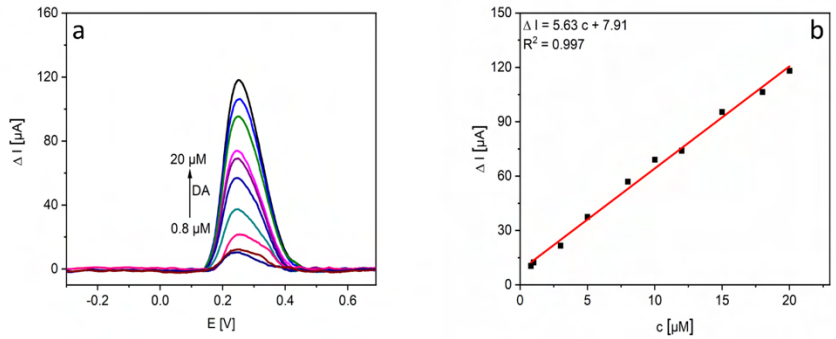

Figure 66. Baseline-corrected DPVs recorded on (a) PANI-TRGO700 1:1/GCE in a 0.1 M PBS solution (pH=7.0) with increasing concentration of DA and 800 μM of creatinine, 1000 μM of glucose, 600 μM of KCl and 1100 μM of NaCl. Corresponding calibration curves for (b) PANI-TRGO700 1:1/GCE.

Table 21. Electrochemical performance of PANI-TRGO700 1:1/GCE towards DA detection in the presence of interferences (800 μM of creatinine, 1000 μM of glucose, 600 μM of KCl and 1100 μM of NaCl)

Sensor	LOD nM	LR μM	Sensitivity μA μM^{-1}
PANI-TRGO-700/GCE	459	0.8 – 20	5.63

Long-term stability was evaluated for TRGO700/GCE and PANI-TRGO700 1:1/GCE sensors (Figure 67). It can be observed that intensity of anodic peak of interest decreased linearly reaching values of 65% of initial signal after 30 days of usage on TRGO700/GCE. However, PANI-TRGO700 1:1/GCE maintained 80 % of initial signal after 30 days, showing a better stability. This can be explained from the synergistic effects between nanocomposite counterparts (increasing the linkage between both composite counterparts) and an increased attachment of active material to the GCE surface by PANI chains [221].

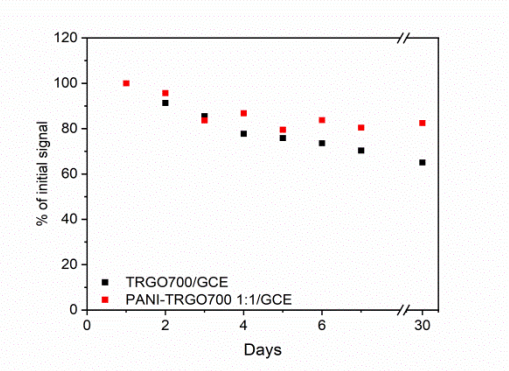

Figure 67. Long-term stability recorded on TRGO700/GCE and PANI-TRGO700 1:1/GCE.

Summary

PANI addition as active electrode material for DA electrochemical detection was evaluated. According to the obtained results, the main role of conductive polymer is to increase the affinity of target analytes to electrode surface and stability of sensor. A series of nanocomposites starting from TRGO400 and PANI at different weight ratios (1:3, 1:1, 3:1) was prepared by hydrothermal treatment (180 °C, 8h) and subsequently tested towards DA sensing. The measurements revealed better electrochemical behavior ascribed to PANI-TRGO400 1:1/GCE. Therefore, the weight ratio 1:1 was selected to prepare similar composites but using as graphene components TRGO700 and TRGO1000. Impact of thermal exfoliation and reduction temperature of TRGO on PANI distribution and resultant electrochemical properties was determined. Thus, significant differences regarding PANI particles distribution on and within graphene layers were revealed, when comparing PANI-TRGO400 1:1, PANI-TRGO700 1:1, and PANI-TRGO1000 1:1. The most homogenous distribution of PANI was observed for PANI-TRGO700 1:1. In addition, d_{002} parameters of PANI-TRGO700 1:1, and PANI-TRGO1000 1:1 nanocomposites resulted higher than that corresponding to the starting graphene materials, indicating introduction of PANI between graphene layers leading to their separation. Furthermore, the highest protonation degree was determined for PANI-TRGO700 1:1. TRGO700 and PANI-TRGO700 1:1 presented lower sheet resistance values than TRGO400 and PANI-TRGO400 1:1. Electrochemical measurements confirmed the lowest LOD and highest sensitivity for DA sensing PANI-TRGO700 1:1/GCE, whose long-term stability was significantly improved after PANI incorporation.

5.1.2.3 Electrochemical detection of DCF

Due to growing environmental demands there is an urgent need for designing and developing appropriate sensing devices for detecting contaminants of emerging concern as some pharmaceuticals (i.e DCF). In this context, TRGOs were also assessed as potential active electrode materials. Electrochemistry of DCF (faradaic and chemical processes under an applied potential) is quite complex as it covers several steps described in detail in paragraph 2.1.2. Most research reports are focused on the first electrochemical reaction of DCF (appearance of first anodic peak) ascribed to the oxidation of DCF anionic form. Aquilar-Lira et al. [52] compared the suitability of detection protocol based on first electrochemical reaction with that corresponding to 1-hydroxy-2-(hydroxyphenyl)ethanalate oxidation (development of a second anodic peak), highlighting the improvement of sensors working parameters when

focusing on second redox reaction. Therefore, in this thesis the second, non-direct redox DCF sensing procedure was considered. TRGOs were preliminary evaluated for this purpose by means of CV measurements in a 0.1 M PBS solution (pH = 7.0) containing 100 µM of DCF (Figure 68). As expected, the bare GCE presented no faradaic response related to DCF oxidation. Subsequent modification of GCE with PANI led to an enhanced capacitive current (due to the increase of S_{BET}), nevertheless no peaks corresponding to DCF electrochemical redox reactions were either observed. However, modification of GCE with TRGOs resulted in the development of anodic peaks with high current intensity ascribed to above mentioned DCF reactions. The highest anodic peak current of 1-hydroxy-2-(hydroxyphenyl)ethanalate oxidation was recorded on TRGO700/GCE (9.6 µA at 372.9 mV). Moreover, both peaks were well-developed on this electrode. The intensity of anodic peak currents recorded on TRGO400/GCE and TRGO100/GCE were lower reaching values of 7.9 µA at 375.4 mV and. 5.0 µA at 356.0 mV, respectively. It can be noticed that overpotential of DCF redox reactions was lower on TRGO1000/GCE comparing to the two other TRGOs, which could be ascribed to its higher electrical conductivity as a results of its better aromatic network restoration (Csp^2 contents of 77.2, 66.5 and 55.2 at.% for TRGO1000, TRGO700 and TRGO400).

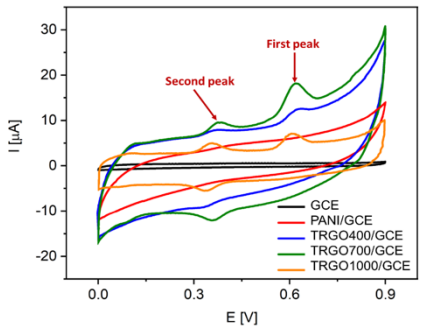

Figure 68. CVs recorded on the different electrodes in a 0.1 M PBS solution (pH = 7.0) containing 100 µM of DCF.

The effect of pH on DCF non-direct detection was also determined (Figure 69). In this regard, relationships between the anodic peak current vs. pH and the overpotential vs. pH were shown (Figure 69). The optimization of pH value (in the 6.2 – 8.0 range) was performed in a 0.1 M PBS solution containing 100 µM of DCF. On TRGO400 (Figure 69b) and TRGO700/GCE (Figure 69d), the maximum anodic peak currents were recorded at pH 6.2 being 9.4 µA at 431.7 mV) and 7.1 µA at 414.2 mV, respectively. However, on TRGO1000/GCE (Figure 69f) the maximum anodic peak current was recorded at pH 7.0 (7.9 µA at 375.5 mV). On this electrode, the anodic peak current recorded at pH 6.2 was 7.2 µA at 414.1 mV. As in previous discussions,

to find a compromise between the most suitable pH value for different TRGOs, 6.2 was selected as the optimum one.

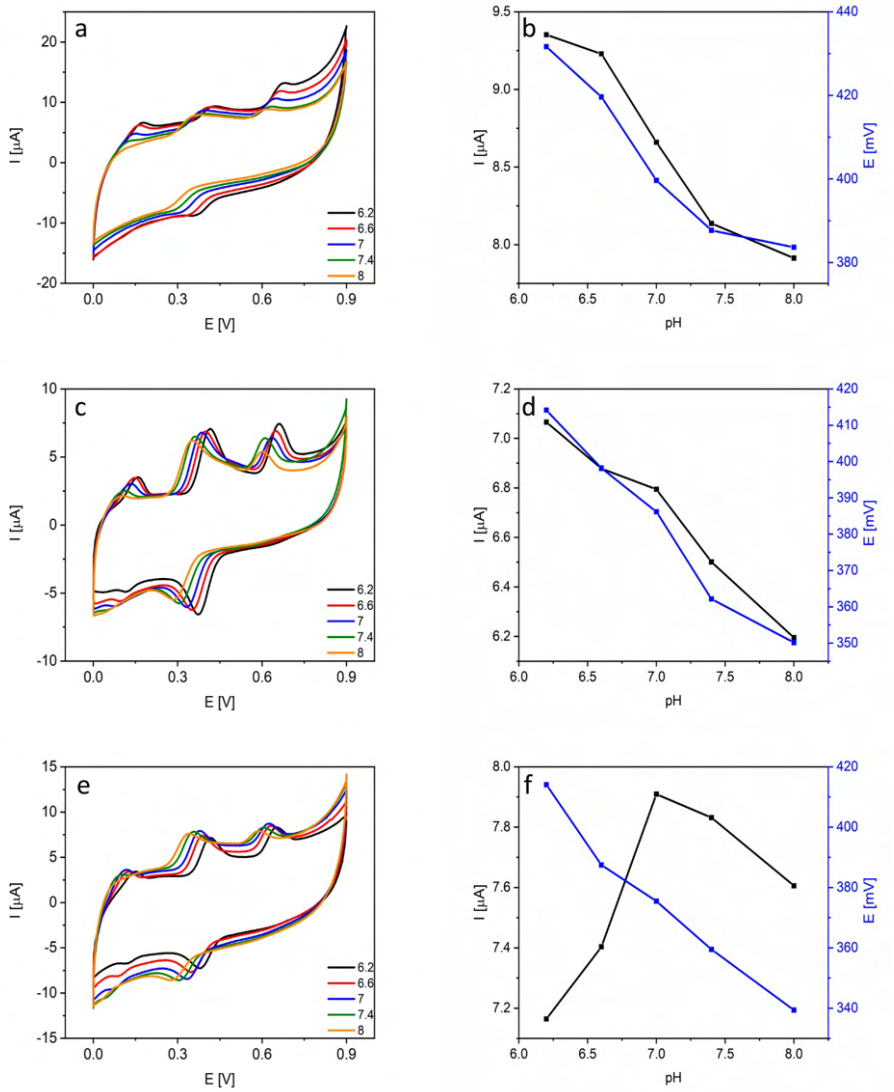

Figure 69. CVs recorded (v_{scan} = 100 mV s^{-1}) at increasing pH values on (a) TRGO400/GCE, (c) TRGO700/GCE, and (e) TRGO1000/GCE in a 0.1 M PBS solution containing 100 µM of DCF. Influence of the selected pH on the anodic peak current and peak potential values recorded on (b) TRGO400/GCE, (d) TRGO700/GCE, and (f) TRGO1000/GCE.

The next step focused on the determination of the main mechanism controlling DCF oxidation. The CV measurements at increasing scan rates (2 – 250 mV s^{-1}) were performed in a 0.1 PBS solution (pH = 6.2) containing 100 µM DCF (Figure 70). As expected, the anodic peak current related to the DCF oxidation increased when increasing the scan rate on all evaluated electrodes. Moreover, relationships between anodic peaks currents and square root of scan rate were linear in all the cases. Furthermore, logarithmic relationships between scan rate and anodic peak

current were plotted. The slopes of resulting plots were 0.41, 0.59 and 0.23 for TRGO400/GCE, TRGO700/GCE and TRGO1000/GCE, respectively (Figures 70c, f and i). According to these results, it can be assumed that the main mechanism controlling DCF oxidation is diffusion [200]. Interestingly, when increasing scan rate the peak corresponding to first electrochemical DCF reaction nearly disappeared, confirming the complete decomposition of DCF to the form of 2,6 dichloroaniline and 2-(2-hydroxyphenyl)acetic acid [52].

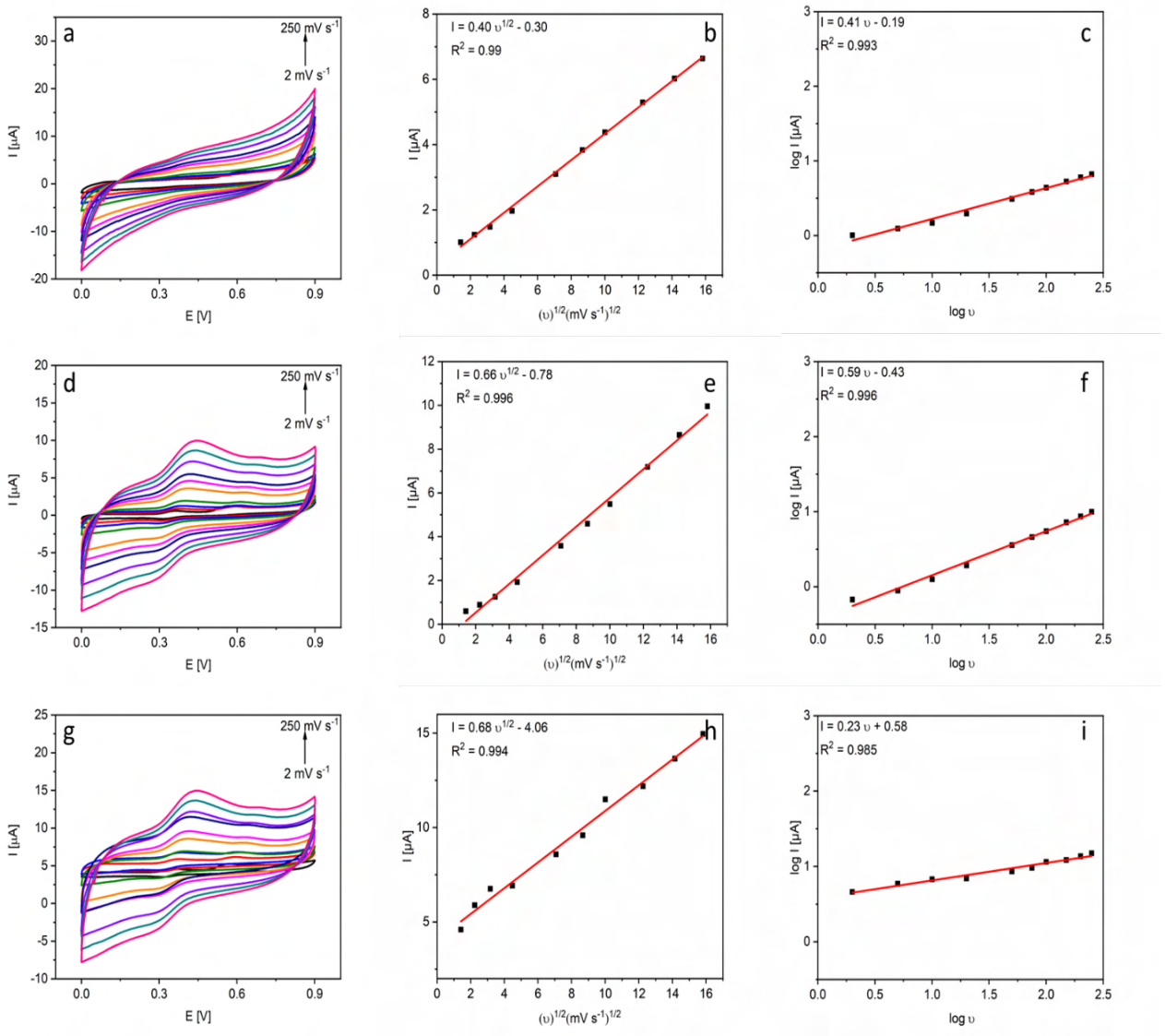

Figure 70. CVs recorded at increasing scan rates (2, 5, 10, 20, 50, 75, 100, 150, 200, 250) on (a) TRGO400/GCE, (c) TRGO700/GCE, and (e) TRGO1000/GCE in a 0.1 M PBS solution (pH=6.2) with 100µM of DCF. Relationships between the maximum anodic peak current and square root of scan rate recorded on (b) TRGO400/GCE, (d) TRGO700/GCE, and (f) TRGO1000/GCE. The logarithmic relationship between scan rate and anodic peak current recorded on (c) TRGO400/GCE, (f) TRGO700/GCE, (i) TRGO1000/GCE.

DPV measurements at increasing DCF concentrations (0.1 – 300 μM) were performed on the different electrodes to determine calibration curves and related sensors working parameters (Figure 71 and Table 22). The widest linear range was recorded on TRGO700/GCE (0.2 – 20 μM, Figure 71d), as a result of its moderate oxygen content enabling to achieve a suitable electrode wettability while maintaining an appropriate electrical conductivity, both parameters crucial in electrochemical sensing [219]. Following the mechanism of DCF redox reactions, firstly it is oxidized and positively charged molecules are created. Then, the resulting product is decomposed and negatively charged 2-(2-hydroxyphenyl) acetic acid appeared. In consequence, it is highly important to select an active material with suitable oxygen content which enables to increase affinity for positively charged molecules while not leading to repulsion of negatively charged molecules in further steps. TRGO400/GCE showing high oxygen content (10.1 at. %) can contribute to repulsion of 2-(2-hydroxyphenyl) acetic acid. On the other hand, TRGO1000/GCE, containing 1.9 at. % of O, can lead to poor attachment of positively charged DCF species. TRGO700/GCE exhibits a moderate oxygen content (5.1 at.%), which could maintain a suitable electrical conductivity while providing enough number of active sites for DCF, thus resulting in a LOD value for DCF of 61 nM. From these promising LOD values, reproducibility of electrode modification and repeatability of measurements were also investigated. Reproducibility and repeatability values were slightly higher than those calculated for similar electrodes for DA sensing due to more complex electrochemical detection mechanism.

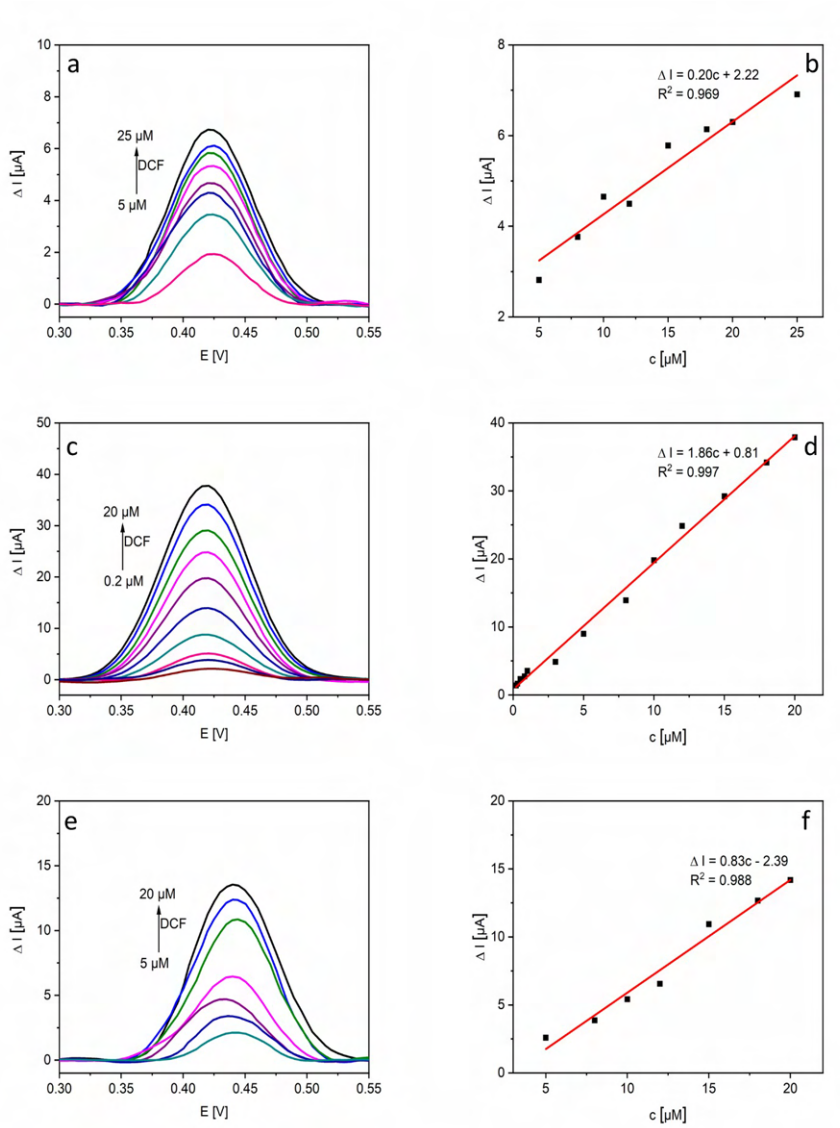

Figure 71. Baseline-corrected DPVs recorded on (a) TRGO400/GCE, (c) TRGO700/GCE, and (e) TRGO1000/GCE in a 0.1 M PBS solution (pH=6.2) with increasing concentration of DCF. Corresponding calibration curves for (b) TRGO400/GCE, (d) TRGO700/GCE, and (f) TRGO1000/GCE.

Table 22. Electrochemical performance of TRGO400/GCE, TRGO700/GCE and TRGO1000/GCE sensors towards DCF sensing

Sensor	LOD nM	LR µM	Sensitivity µA μM^{-1}	Reproducibility RSD %	Repeatability RSD %
TRGO-400/GCE	2.25	5 – 25	0.20	10.5	5.0
TRGO-700/GCE	0.061	0.2 – 20	1.86	11.9	6.4
TRGO-1000/GCE	4.14	5 – 20	0.83	12.3	7.8

According to the data, TRGO700/GCE exhibited better electrochemical performance for DCF non-direct determination, therefore (and considering previous results with nanocomposites for DA detection) PANI addition was also tested. The capacitive current recorded on PANI-TRGO700 1:1/GCE resulted higher than that measured on TRGO700/GCE, leading to a higher anodic peak current (35.0 µA at 377.6 mV). However, the peaks recorded on TRGO700/GCE were more distinctive (Figure 72). To select the most suitable active material towards DCF electrochemical non-direct determination further studies were performed.

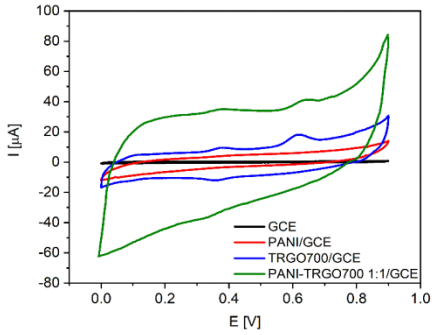

Figure 72. CVs recorded on different electrodes in a 0.1 M PBS solution (pH = 7.0) containing 100 µM of DCF.

The pH optimization was performed (Figure 73a). On PANI-TRGO700 1:1/GCE the highest anodic peak was recorded at pH 8.0 (13.8 µA at 349.2 mV) (Figure 73b). Nevertheless, differences between anodic peak current intensities measured at different pH values were subtle. Therefore, pH of 6.2 (12.5 µA at 414.1 mV) was selected as the optimum for further measurements to compare the performance of tested electrodes.

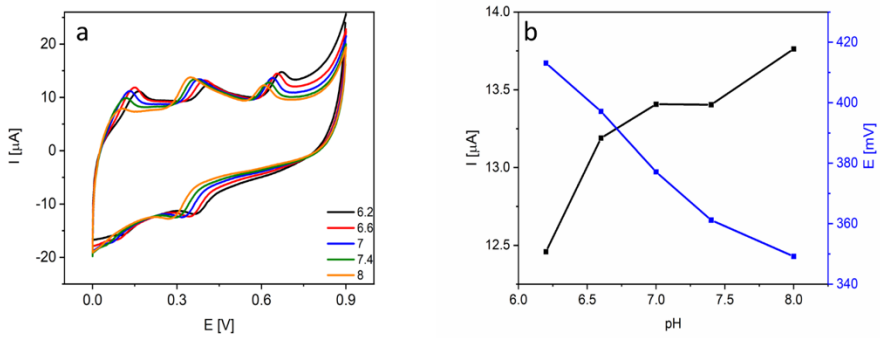

Figure 73. CVs recorded (v_{scan} = 100 mV s^{-1}) at increasing pH values on (a) PANI-TRGO700 1:1/GCE in a 0.1 M PBS solution containing 100 µM of DCF. Influence of the selected pH on the oxidation peak current and peak potential values recorded on (b) PANI-TRGO700 1:1/GCE.

CV experiments at increasing scan rates (2-250 mV s^{-1}) were performed in a 0.1 PBS solution (pH = 6.2) containing 100 µM DCF (Figure 74). The relationship between the square root of scan rate and the maximum anodic peak current was linear, reaching a correlation coefficient of 0.988. Moreover, logarithmic relationship between scan rate and maximum anodic peak current showed a slope of 0.8 (which is close to 1), indicating that the main mechanism controlling DCF non-direct oxidation is adsorption [200,216].

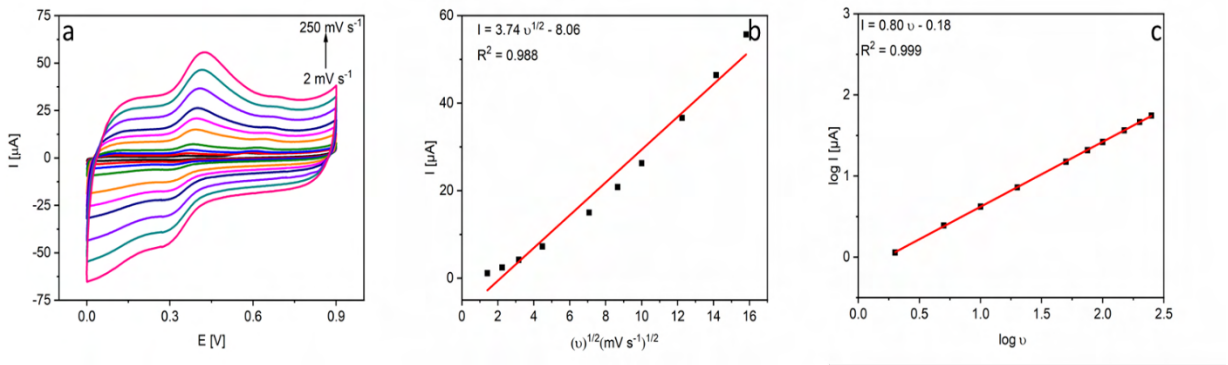

Figure 74. CVs recorded at increasing scan rates (2, 5, 10, 20, 50, 75, 100, 150, 200, 250) on (a) PANI-TRGO700 1:1/GCE with 100 µM of DCF. Relationships between maximum anodic peak current and square root of scan rate recorded on (b) PANI-TRGO700 1:1/GCE. The logarithmic relationship between scan rate and anodic peak current recorded on (c) PANI-TRGO700 1:1/GCE.

DPV measurements (Figure 75a) were also performed to plot calibration curve (Figure 75b). Derived sensor working parameters are presented in Table 23. The LR on PANI-TRGO700 1:1/GCE was almost the same as on TRGO700/GCE (0.2-20 vs. 0.2-25 µM, respectively), even though LOD corresponding to the nanocomposite-based sensors was higher (442 nM) than the corresponding to TRGO700/GCE (61 nM), which can be the result of a decreased electrical conductivity (sheet resistance 2.37 x 10^4 and 9.84 x 10^4 for TRGO700 and PANI-TRGO700 1:1, respectively). Moreover, the protonation degree of 20% and the presence of 0.5 at.% of protonated amine groups in PANI-TRGO700 1:1/GCE can contribute to the repulsion between the positively charged DCF form and electrode surface, thus hindering its appropriate electrochemical performance. Again, reproducibility and repeatability of the sensors were worse than those calculated for DA detection due to the more complex DCF electrochemical detection and electrode fouling [223].

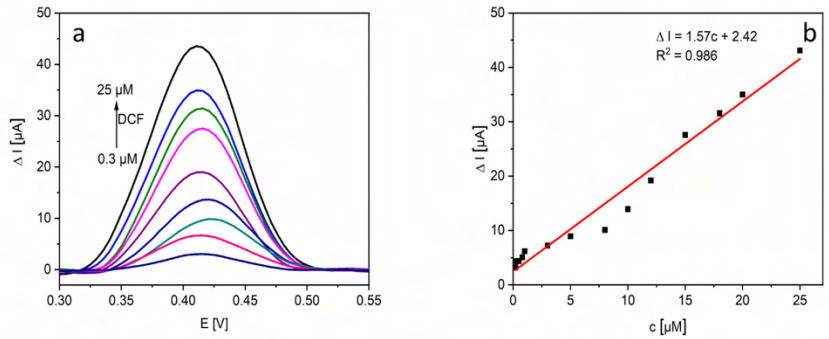

Figure 75. Baseline-corrected DPVs recorded on (a) PANI-TRGO700 1:1/GCE in a 0.1 M PBS solution (pH = 7.0) with increasing concentration of DCF. Corresponding calibration curves for (b) PANI-TRGO700 1:1/GCE.

Table 23. Electrochemical performance of PANI-TRGO700 1:1/GCE sensor towards DCF sensing

Sensor	LOD nM	LR µM	Sensitivity µA μM^{-1}	Reproducibility RSD %	Repeatability RSD %
PANI-TRGO-700/GCE	0.442	0.2 – 25	1.57	12.1	11.0

Selectivity studies were performed on TRGO700/GCE as electrochemical performance towards DCF non-direct detection was the most effective on this electrode (Figure 76). It can be observed that at 0 µM DCF, an unexpected peak was developed, probably due to interfering compound present in the solution. After addition of DCF, such peak intensity increased, thus confirming that interfering redox processes take place at the same redox potential as that corresponding to the target analyte. Due to low selectivity, sensor working parameters were not defined in the presence of interferences.

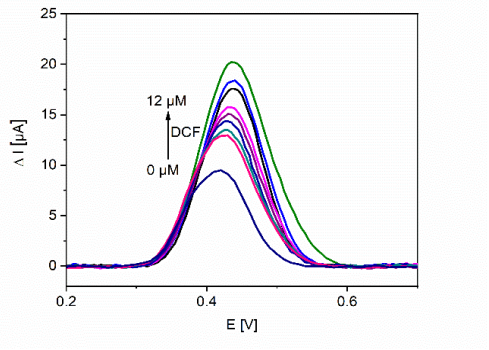

Figure 76. Baseline-corrected DPVs recorded on (a) TRGO700 1:1/GCE in a 0.1 M PBS solution (pH = 7.0) with increasing concentration of DCF and 100 µM of glucose, urea, ascorbic acid, thiourea, glycine, NaCl, $CaCO_3$, $MgSO_4$.

The last parameter investigated was long-term stabilities of TRGO700/GCE and PANI-TRGO700/GCE towards DCF sensing (Figure 77). After 30 days of measurements, on both sensors, the intensity of DCF oxidation peak decreased about 50-60 % of the initial signal, which could be ascribed to an electrode fouling coming from strong adsorption of DCF oxidation by-products.

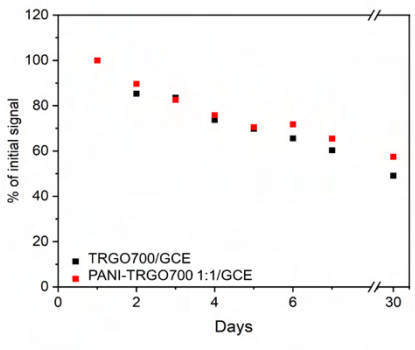

Figure 77. Long-term stability recorded on TRGO700/GCE and PANI-TRGO700 1:1/GCE.

Summary

TRGOs were assessed as potential GCE modifiers towards DCF sensing. TRGOs synthesized in this thesis mainly differed in the chemical surface composition (oxygen content ranging from 1.9 to 10.1 at.%). Electrochemical measurements carried out showed better electrochemical performance of TRGO700/GCE (5.1 at.% O) towards non-direct electrochemical sensing of DCF, reaching a LOD value of 61 nM. Impact of PANI addition to the graphene material was also tested. PANI-TRGO700 1:1 presented a slightly higher oxygen content than TRGO700 (6.1 vs. 5.1 at.%). Moreover, its addition led to the presence of a 2.5 at.% of nitrogen. The sensor working parameters after PANI incorporation were markedly changed as LOD increased from 61 nM on TRGO700/GCE to 442 nM PANI-TRGO700 1:1/GCE. After comparison of the electrochemical performances of TRGOs and their nanocomposites with PANI towards DA and DCF sensing, it can be concluded that addition of conductive polymer is beneficial for DA sensing, but it does not improve sensor working parameters for DCF detection. Nevertheless, PANI introduction resulted in improved stability of the composite materials.

5.1.3 Graphene-based binary and ternary nanocomposites

Following previously discussed promising results towards DA detection using graphene materials, AuNPs and PANI as active electrode materials, in further studies binary

nanocomposites based on graphene materials and mixed transition metal oxides (FSGs), and ternary composites, incorporating PANI to the binary ones (PFSGs), were proposed. Transition metal oxides, as for example Fe_2O_3 or SnO_2, can act as electrocatalysts for target analytes sensing, being significantly cheaper than previously used AuNPs. Moreover, the hydrothermal procedure followed for synthesizing the binary nanocomposites could lead to the distribution of transition metal oxides nanoparticles between graphene layers, thus providing a proper separation between them. Furthermore, addition of PANI as conductive polymer could improve sensors working parameters.

5.1.3.1 Morphology and structure of nanocomposites

XRD measurements were performed on FSG33:67 and PFSG nanocomposites to determine crystalline forms of metal-based nanoparticles incorporated and to confirm the presence of graphene material and conductive polymer (Figure 78). During the hydrothermal treatment of GO in the presence of $SnSO_4$ and $Fe(NO_3)_3$, two separate crystalline phases were formed. As a result, in the XRD patters related to FSG33:67 and PFSG nanocomposites clearly visible peaks, attributed to rhombohedral α-Fe_2O_3 (JCPDS card no. 33-0664) and tetragonal SnO_2 (JCPDS card no. 41-1445), appeared [224,225]. The (012) peak at 24°, corresponding to Fe_2O_3, and (110) peak at 26.5°, corresponding to SnO_2, overlap with the (002) plane of the RGO graphitic structure [226]. After secondary hydrothermal treatment, for PANI incorporation, there were just small changes in these peaks intensities. This fact proved that crystalline structure was well preserved during hydrothermal treatment. For PFSG, an additional peak at 22.3° appeared, being attributed to periodicity related to PANI polymer chains [227].

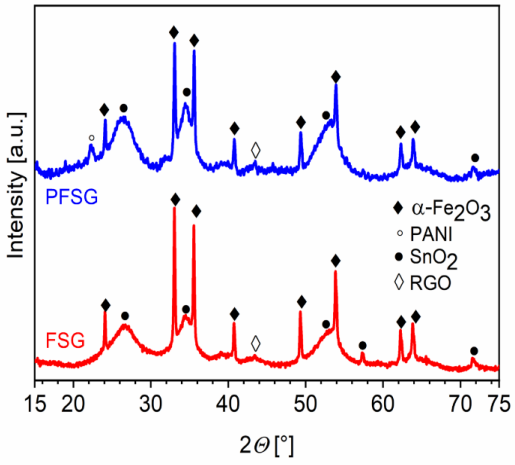

Figure 78. XRD patterns of FSG33:67 and PFSG nanocomposites.

The morphology of the different nanocomposites was investigated using FESEM (Figure 79). From the obtained images, significant differences between FSGs (33:67 and 15:85) and PFSG nanocomposites can be observed. Binary nanocomposites FSG33:67 (Figure 79a) and FSG15:85 (Figure 79b) showed a similar morphology, with clearly visible aggregated structures of graphene layers covered with iron and tin oxide nanoparticles. However, on FSG15:85 the amount and size of such nanoparticles were lower probably due to the lower weight of metal oxides precursors used in its synthesis. Regarding ternary PFSG nanocomposite, PANI coral-shape aggregates appeared both, on the surface of graphene layers and between them (Figure 79c) [208]. Fe_2O_3 nanoparticles in a characteristic cubic form (about 200 nm in size) were also visible [228]. Moreover, PANI aggregates covered such Fe_2O_3 nanostructures leading to the formation of a conductive layer. On the other hand, SnO_2 nanoparticles (50-100 nm in size) were also clearly visible on the RGO nanosheets, maintaining their structure after the secondary hydrothermal treatment.

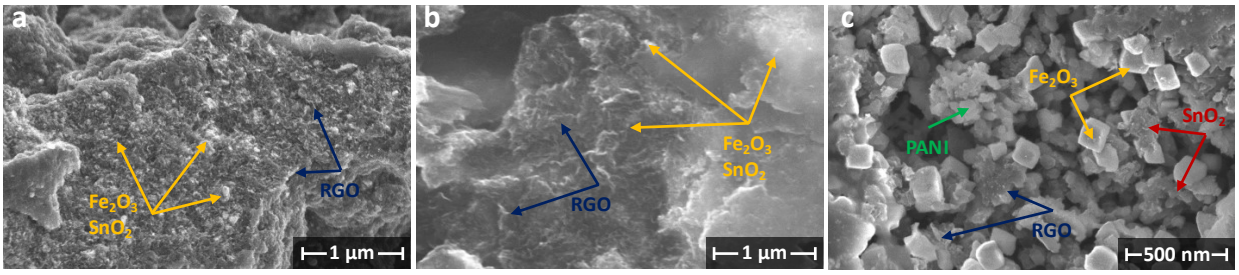

Figure 79. FESEM images of binary (a) FSG33:67, (b) FSG15:85, and ternary (c) PFSG nanocomposites.

To gain insight into the inner structure of ternary nanocomposites, TEM observations were carried out (Figure 80). As it can be seen, characteristic graphene layers with local defects are distinguishable [110]. Moreover, small Fe_2O_3 and SnO_2 nanoparticles were observed, confirming their successful incorporation and distribution within graphene layers. In addition, amorphous structure of PANI particles was visible [229].

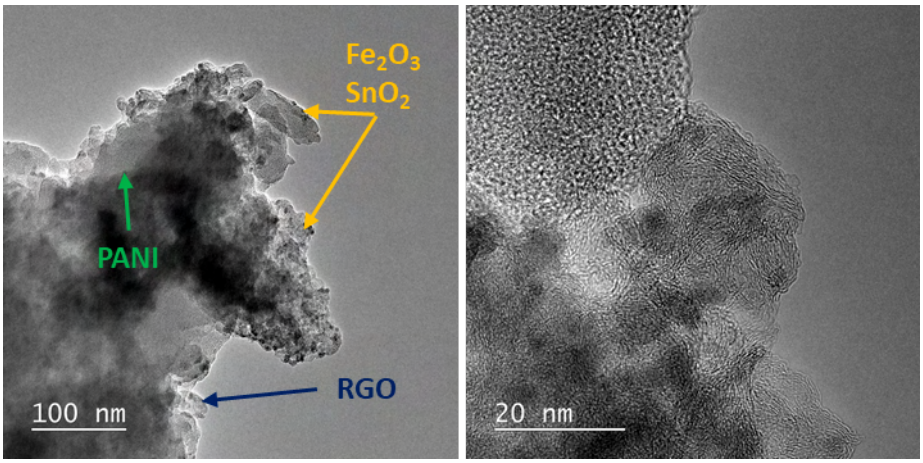

Figure 80. TEM images of PFSG.

Additionally, porosity of the composites was determined using N_2 sorption measurements at 77K (Table 24). FSG composites show well developed porosity. This is the result of incorporation of metallic nanoparticles into composite structure. Moreover, the nanoparticles which are deposited not only on the surface of graphene layers but also between them prevent restacking of graphene layers and further aggregation which also implies enhanced contribution in surface area of the composite materials [230]. The S_{BET} surface area decreases after introduction of PANI to the composite structure from 434 to 206 m_2/g which is the result of introduction of non-porous material into the composite structure. Nevertheless, the secondary hydrothermal treatment is crucial for maintaining the porous structure which can be blocked during conventional one-step hydrothermal treatment [185,226]. The chemical surface composition of binary and ternary composites was determined by XPS (Table 24). The oxygen content was the highest for FSG33:67 due to the highest contribution of metal oxides in the structure of the composite. Nitrogen is presented in the FSGs which is the result of residual amount of ammonia which was applied to adjust reaction medium pH. The highest carbon contribution was presented in FSG15:85 due to the highest RGO content. After secondary hydrothermal treatment of binary FSG33:67 composite in the presence of PANI the significant decrease of oxygen is observed which is the result of the PANI incorporation. PFSG exhibited increased nitrogen content (11.7 at.%). Similar Fe and Sn content is observed for FSG15:85 and PFSG (1.7 vs 1.5 at.% in total) which indicated similar contribution of inorganic part in both materials.

Table 24. Chemical composition of nanocomposite materials determined by XPS (at.%) and S_{BET} surface area values

Sample	C	O	N	Fe	Sn	S_{BET} m^2/g
FSG33:67	63.9	29.8	2.6	0.9	3.0	434
FSG15:85	80.1	15.1	3.1	0.5	1.2	520
PFSG	74.6	12.2	11.7	0.7	0.8	206

Detailed chemical composition of the materials was determined (Table 25). The C1s spectra of starting materials can be divided into five components corresponding to sp^2 hybridized carbon (284.5 eV), sp^3 hybridized carbon and C-N groups (285.4 eV), hydroxyl and epoxy groups (286.5 eV), carbonyl and quinone bonds (287.6 eV) and carboxylic groups (289.0 eV) (Figure 81) [212]. For all materials the peak at a binding energy of 285.4 eV presents the highest intensity. PFSG exhibits the lowest contribution of -COOH (1.9 at.%) which can be explained by their further reduction during secondary hydrothermal treatment. An increase in the content of -OH groups (10.2 at.%) supports above finding. N1s deconvoluted spectra are shown for PFSG (Figure 82). N1s spectra can be resolved into four peaks corresponding to imine (-N=, 398.2 eV), amine (-NH-, 399.6 eV), oxidized amine ($-NH^+$, 400.9 eV), protonated imine ($=N^+$, 402.5 eV). The highest contribution of imine groups is observable. The protonation degree (P_s) was calculated as the ratio of positively charged nitrogen groups and total nitrogen content [212]. Protonated nitrogen functionalities presented in PFSG resulted in the protonation degree of 17 %.

Table 25. Type and distribution of C and N functional groups, at.%

Sample	C1s peak deconvolution						N1s peak deconvolution				
	Csp^2	Csp^3/C-N	C-OH	C=O	O=C-OH	satellites	-N=	-NH-	-NH+	=N+	P_S %
FSG33:67	29.4	14.1	7.5	5.0	4.4	3.5	-	-	-	-	-
FSG15:85	41.5	20.1	8.7	5.1	3.5	1.2	-	-	-	-	-
PFSG	35.4	19.0	10.2	5.3	1.9	2.8	2.5	7.3	1.8	0.1	17

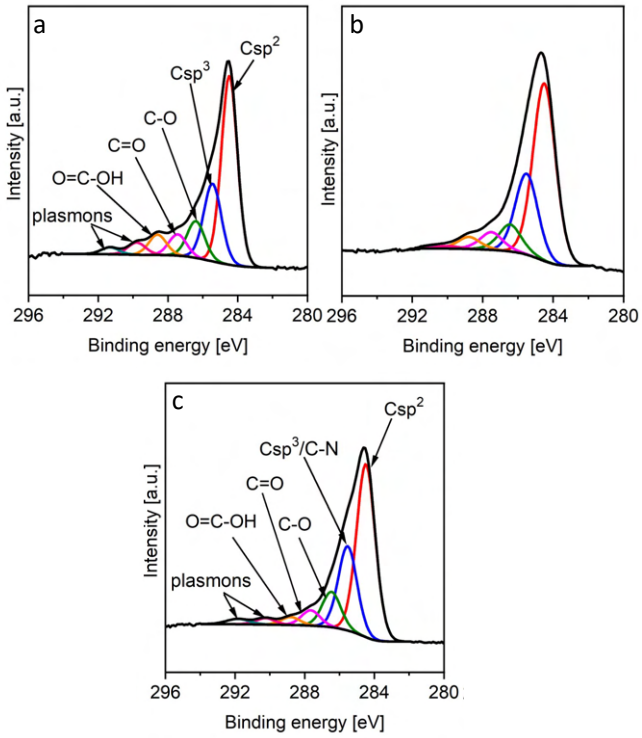

Figure 81. Deconvolutions of the C1s core-level XPS spectra of (a) FSG33:67, (b) FSG15:85, (c) PFSG.

Figures 82 and 83 present deconvoluted XPS spectra of the Fe2p and Sn3d core level of FSGs and PFSG composites. Peaks corresponding to Fe (at binding energies 724.9 and 711.2 eV) and Sn (486.5 and 494.9 eV) in the form of oxides were observed for all materials. Moreover, for FSG33:67 low intensity peak attributed to metallic Fe is presented. This peak disappeared for FSG15:85 and PFSG. It can indicate the preferential formation of metallic Fe particles when the contribution of related precursor is high [231]. During secondary hydrothermal treatment, the peak assigned to metallic Fe disappeared which can be due to the transformation of metallic Fe to Fe_2O_3 form. In Figure 83 peak at binding energy 486.5 eV corresponds to $Sn3d_{3/2}$. It additionally proves the introduction of Sn nanoparticles in the form of metal oxide [232].

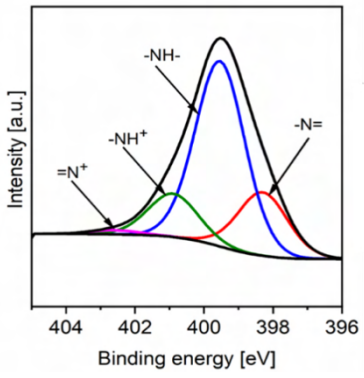

Figure 82. Deconvolutions of N1s core-level XPS spectra of PFSG.

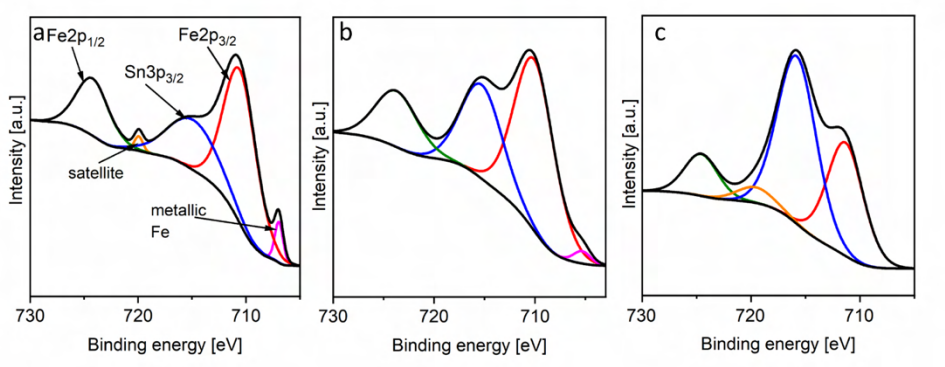

Figure 83. Deconvolutions of Fe2p core-level XPS spectra of binary (a) FSG33:67, (b) FSG15:85 and ternary (c) PFSG nanocomposites.

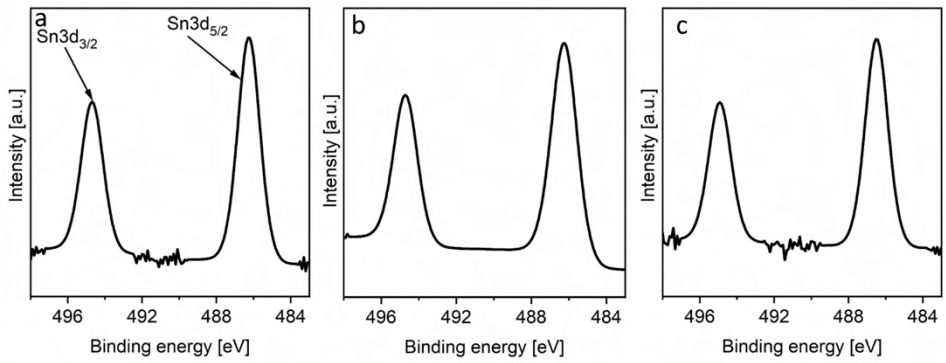

Figure 84. Deconvolutions of Sn3d core-level XPS spectra of binary (a) FSG33:67, (b) FSG15:85 and ternary (c) PFSG nanocomposites.

5.1.3.2 Electrochemical detection of DA

CV measurements in a PBS solution (pH = 7.0) solution containing 100 μM DA (Figure 85) revealed that modification of GCE with binary/ternary nanocomposites resulted in improved response originated from DA redox reactions. The highest capacitive current was recorded on FSG33:67/GCE, as a result of developed surface area (434 m^2/g) [197]. Due to this high capacitive current the DA oxidation peak was not clearly distinguishable on this electrode. However, a well-developed anodic peak was recorded on FSG15:85/GCE (74.8 μA at 255.7mV). In addition, the faradaic process of interest was visible on PFSG/GCE (45.3 μA at 234.2 mV), as the capacitive current significantly decreased due to the lower S_{BET} of the active material after PANI introduction (206 m^2/g). Moreover, a significant decrease of DA oxidation overpotential was noted. This can be due to the PANI introduction into the nanocomposite, enhancing the electrical conductivity and improving accessibility to active Fe_2O_3-SnO_2 sites [233].

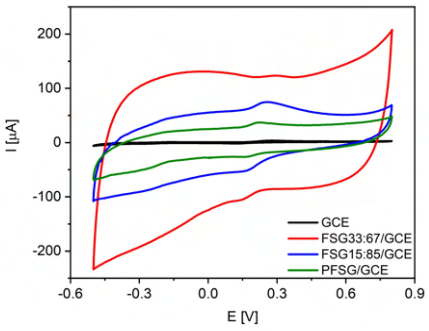

Figure 85. CVs recorded on different electrodes in a 0.1 M PBS solution (pH = 7.0) containing 100 µM of DA.

In the next step, pH optimization (in the range 5.8 – 8.0) was performed (Figure 86). Relationships between anodic peak currents vs. pH and overpotentials vs. pH are also presented. The highest anodic peak current on FSG33:67/GCE was recorded at pH 7.0 (184 µA at 312.8 mV). Regarding FSG15:85/GCE (Figure 86d) and PFSG/GCE (Figure 86f) the highest anodic peak currents were recorded at pH 6.2 (89.9 µA at 301.8 mV) and 6.6 (29.8 µA at 263.8 mV), respectively. A slight drop of anodic peak current (2.4 µA) recorded at pH 7.0 on FSG15:85/GCE was observed, while the overpotential considerable decreased (44.0 mV). On PFSG/GCE, the anodic peak currents recorded at pH 6.6 and 7.0 exhibited almost the same intensity (29.8 vs. 29.7 µA), while the overpotential dropped by 31.9 mV. To find a compromise between the highest anodic peak current and the lowest overpotential vale, a pH of 7.0 was selected as the optimum one for all tested electrodes.

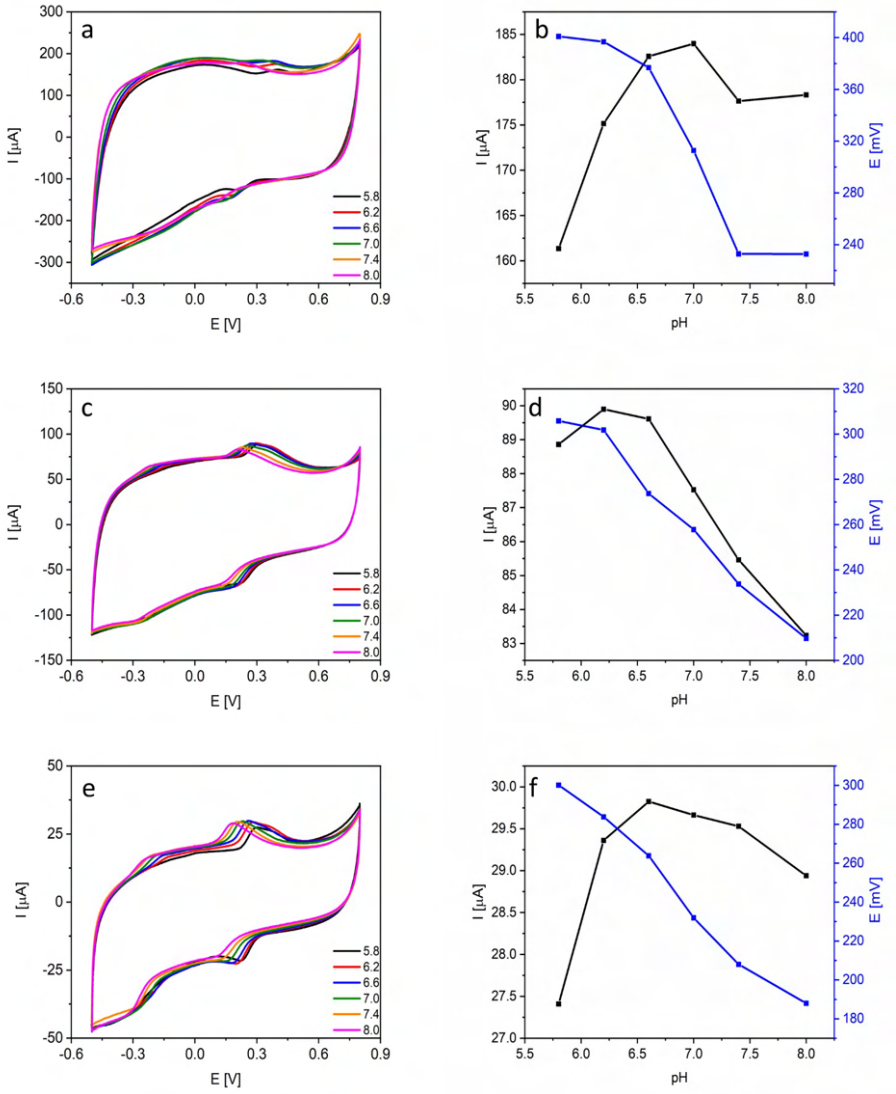

Figure 86. CVs recorded (v_{scan} = 100 mV s^{-1}) at increasing pH values on (a) FSG33:67/GCE, (c) FSG15:85/GCE and (e) PFSG/GCE in a 0.1 M PBS solution containing 100 µM of DA. Influence of pH on the anodic peak current and peak potential values recorded on (b) FSG33:67/GCE, (d) FSG15:85/GCE and (f) PFSG/GCE.

CV measurements at increasing scan rates (2 – 250 mV s^{-1}), in a 0.1 PBS solution (pH = 7.0) containing 100 µM DA, were performed to determine the main mechanism controlling DA oxidation (Figure 87). For all tested electrodes, relationships between anodic peak currents and square root of scan rate were linear. Moreover, slopes from the plots derived from logarithmic relationship between f scan rate and maximum anodic peak current were 0.72, 0.71 and 0.71 for FSG33:67/GCE, FSG15:85/GCE and PFSG/GCE, respectively (Figures 87c, f and i). Thus, it can be assumed that the main mechanism controlling DA oxidation was diffusion [200].

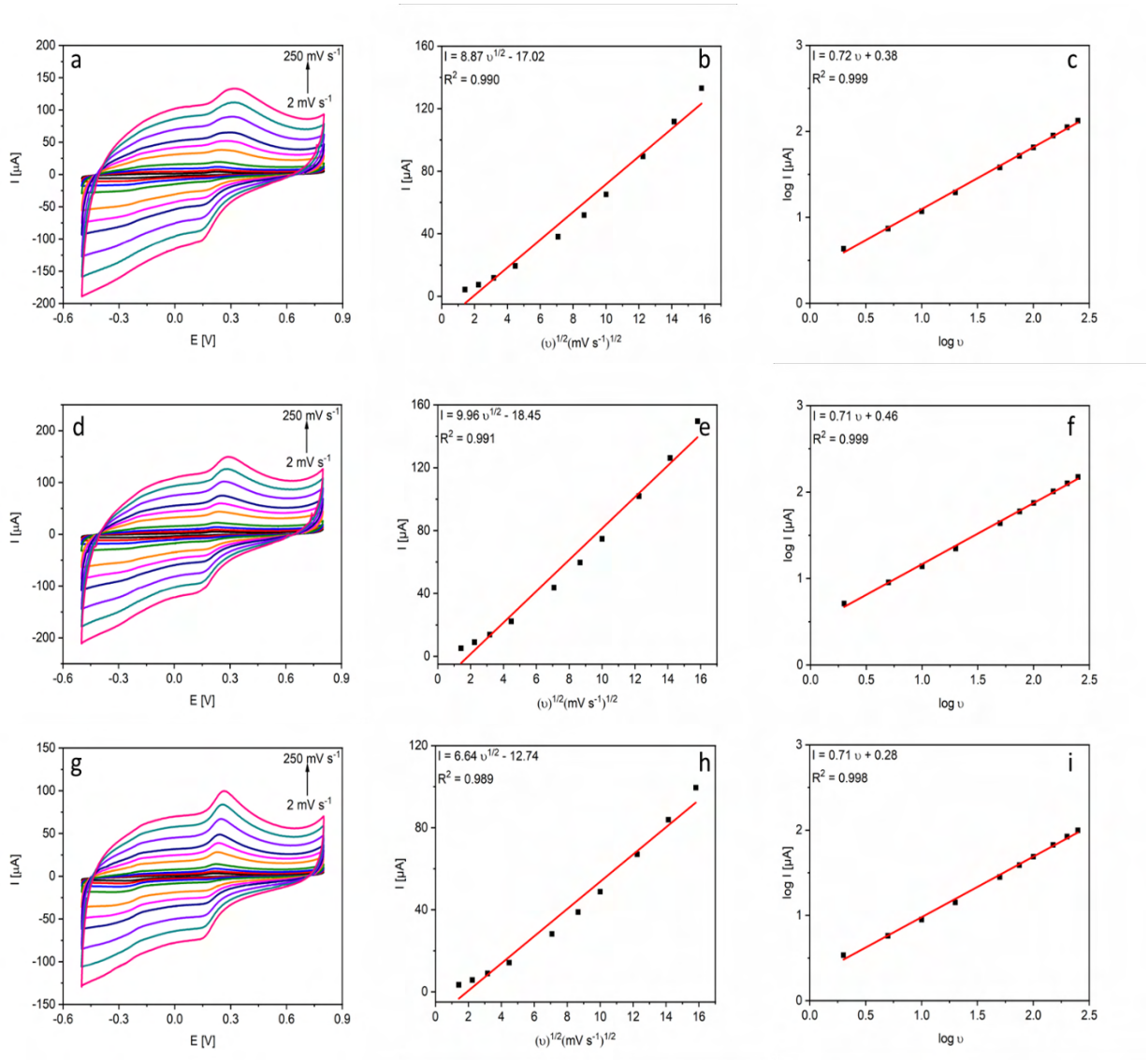

Figure 87. CVs recorded at increasing scan rates (2, 5, 10, 20, 50, 75, 100, 150, 200, 250) on (a) FSG33:67/GCE, (c) FSG15:85/GCE and (e) PFSG in a 0.1 M PBS solution (pH =7 .0) with 100 µM of DA. Relationships between maximum anodic peak current and square root of scan rate recorded on (b) FSG33:67/GCE, (d) FSG15:85/GCE and (f) PFSG/GCE. The logarithmic relationship between scan rate and anodic peak current recorded on (c) FSG33:67/GCE, (f) FSG15:85/GCE and (i) PFSG/GCE.

DPV experiments were carried out at increasing DA concentrations (0.1 to 300 µM) (Figure 88). For all tested electrodes two linear ranges were selected (Table 26). This result indicated that, when increasing analyte concentration, its oxidation products were adsorbed on the electrode surface lowering electron transfer rate and the anodic currents. However, both LRs overlapped, which enabled to detect DA within a broad range of concentrations with high accuracy (R^2: 0.984 – 0.996). The widest LR was recorded on PFSG/GCE (0.1 – 20, 20 – 120

μM) (Figure 88f). Moreover, on this electrode the LOD was the lowest (76 nM). It can be also observed that LOD decreased when decreasing the number of inorganic part contribution in the composite and when increasing nitrogen content. Enhanced sensor working parameters were revealed for PFSG/GCE, which can be attributed to the presence of a more suitable number of electroactive oxygen groups and an improved electrical conductivity due to PANI introduction [122,234]. Moreover, the lowest overpotential of DA oxidation was recorded on this electrode probably due to the separation of FSG layers by conductive polymer chains, which facilitates accessibility of target analyte to active sites. The separation of FSG layers increases accessibility to the inorganic part of the composite for target molecule which can act catalytically [232]. As expected, the sensitivity within the second LR decreased, as a result of the electrode fouling [6,235]. Furthermore, the lowest values of reproducibility and repeatability were also recorded on PFSG/GCE. The conductive polymer acts as a binder increasing the affinity of the active material to GCE surface. For comparative purposes, a calibration curve was recorded on an electrode prepared using dispersion without nafion (PFSGw/o_nafion/GCE). In this case, the LOD for DA detection increased more than ten times. Moreover, LR was limited comparing to PFSG/GCE (Figure 88h). This can be the result of a weaker attachment of ternary PFSG nanocomposite to the electrode surface, which was also confirmed by a poorer sensor reproducibility and repeatability. On the other hand, the sensitivity calculated for electrode with nafion was higher, which is in agreement with the hydrophobic nature of this polymer leading to a slower electron transfer on the corresponding sensor [236].

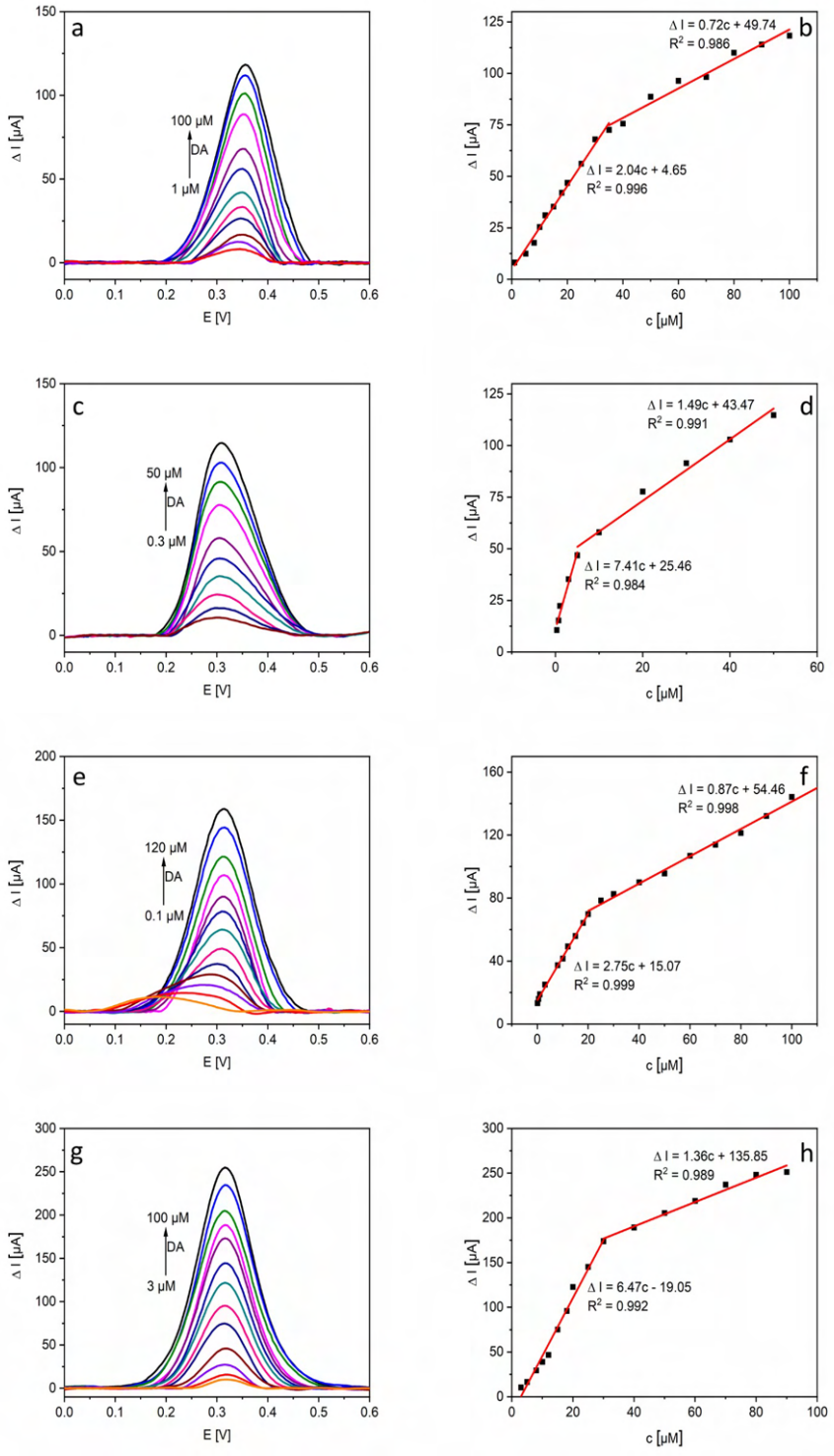

Figure 88. Baseline-corrected DPVs recorded on (a) FSG33:67/GCE, (c) FSG15:85/GCE and (e) PFSG/GCE in a 0.1 M PBS solution (pH=7.0) at increasing DA concertation. Corresponding calibration curves for (b) FSG33:67/GCE, (d) FSG15:85/GCE and (f) PFSG/GCE.

Table 26. Electrochemical performance of FSG33:67/GCE, FSG15:85/GCE, PFSG/GCE and PFSGw/o_nafion/GCE sensors towards DA sensing

Sensor	LOD nM	LR µM	Sensitivity µA µM^{-1}	Reproducibility RSD %	Repeatability RSD %
FSG33:67/GCE	1500	1-35; 35-100	2.04; 0.72	15.1	7.9
FSG15:85/GCE	441	0.3-5; 5-50	7.41; 1.49	15.9	8.9
PFSG/GCE	76	0.1-20; 20-120	2.75; 0.87	3.2	3.3
PFSGw/o_nafion/GCE	833	1-30; 30-90	6.47; 1.36	9.2	8.7

In a following stage, the impact of interfering compounds on DA detection was evaluated on PFSG/GCE. Measurements in the presence of 300 µM of UA and AA (Figures 89a and b) revealed a lower LR in comparison to individual detection of target analyte. This can be a result of occupation of active sites on the electrode by UA molecules. The peak corresponding to AA was not visible, indicating a high selectivity towards DA in the presence of AA. The LOD for DA significantly increased (1.7 µM) as a consequence of the competitive reaction of UA oxidation, which also takes place at comparable overpotentials (Table 27). These studies were expanded to measurements in solutions with constant concentration of DA (100 µM) and increasing concentrations of UA (Figures 89c and 89d). It can be observed that even when UA concentration increased, the DA oxidation peak remains almost unaffected confirming that even in the presence of higher amounts of UA, the selectivity of PFSG/GCE towards DA high enough.

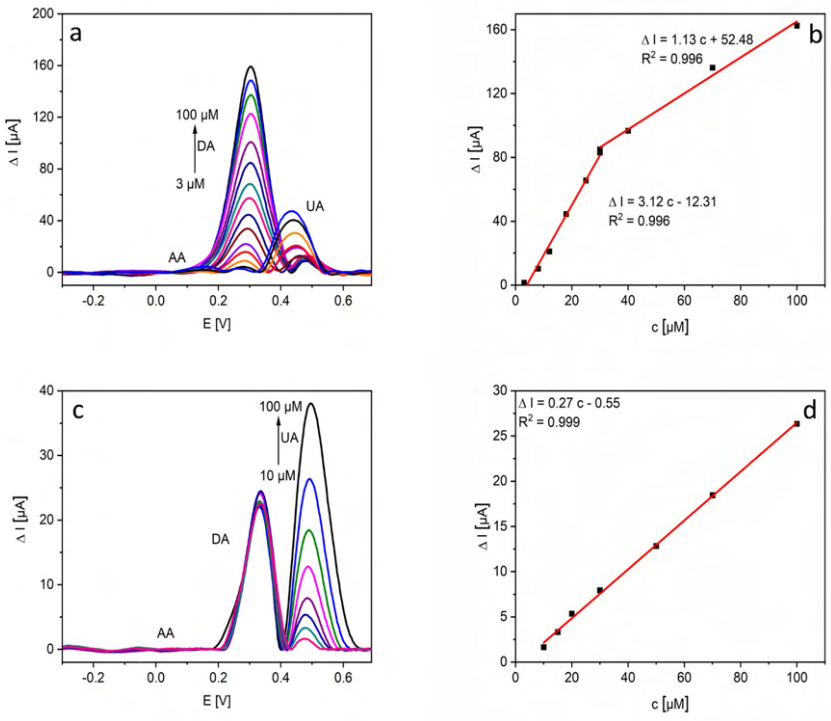

Figure 89. Baseline-corrected DPVs recorded on (a) PFSG/GCE in a 0.1 M PBS solution (pH = 7.0) at increasing DA concentrations and 300 μM of AA and UA. (b) corresponding calibration curve.

Table 27. Electrochemical performance of PFSG/GCE sensor towards DA sensing in presence of interfering compounds (300 μM of AA and UA)

Sensor	LOD nM	LR μM	Sensitivity μA μM^{-1}
PSFS/GCE	1.7	3 – 30	3.12; 1.13

The potential application of PFSG/GCE towards DA detection was also tested in artificial urine samples (Table 28). The intensity of the related anodic peak was measured, and the real value was calculated using previously determined calibration curve. The recovery values for three different concentrations were between 97.7 - 110.9 %. The values higher than 100 % were indicative of impact of interfering compounds having similar oxidation potentials than target analyte.

Table 28. Electrochemical performance of PFSG/GCE sensor towards DA sensing in the presence of interfering compounds

Analyte	Added μM	Measured μM	Detection performance %	RSD %
DA	10	10.5	104.5	6.3
	20	22.2	110.9	
	50	48.8	97.7	

5.1.3.3 Electrochemical detection of UA

Due to the promising electrochemical performance of binary and ternary nanocomposites under study towards DA sensing, they were also assessed for UA detection. For this purpose, CV measurements were performed in a 0.1 M PBS solution (pH = 7.0) containing 100 μM of this analyte (Figure 90). As expected, modification of GCE with nanocomposites resulted in increased capacitive currents. The most distinctive anodic peak related to UA oxidation was recorded on FSG 15:85/GCE (102.3 μA at 400.1 mV), and the lowest one was developed on PFSG/GCE (26.4 μA), although it appeared at lower overpotential (391.9 mV).

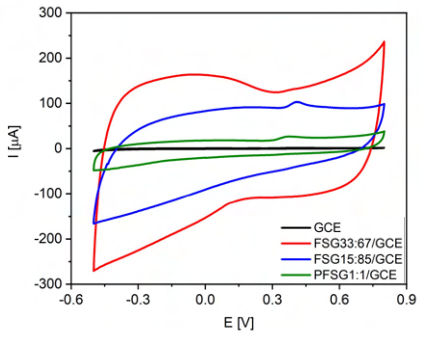

Figure 90. CVs recorded on different electrodes in a 0.1 M PBS solution (pH = 7.0) containing 100 µM of UA.

The pH of the electrolyte was optimized (in the range 5.8 – 8.0) in a 0.1 M PBS solution containing 100 µM of UA (Figure 91). Relationships between the anodic peak current vs. pH and the overpotential vs. pH are also shown. On FSG33:67/GCE (Figure 91b) and PFSG/GCE (Figure 91f) the highest anodic peak currents were recorded at pH value of 6.6 (110.5 µA at 455.8 mV and 19.1 µA at 368.8 mV, respectively). The optimized pH value FSG15:85/GCE (Figure 91d) was 6.2 (108.3 µA at 448.9 mV), however at pH 6.6, current value was almost the same (105.1 µA, at a lower overpotential of 392.8 mV)). Therefore, pH 6.6 was selected as the most suitable one for further investigations.

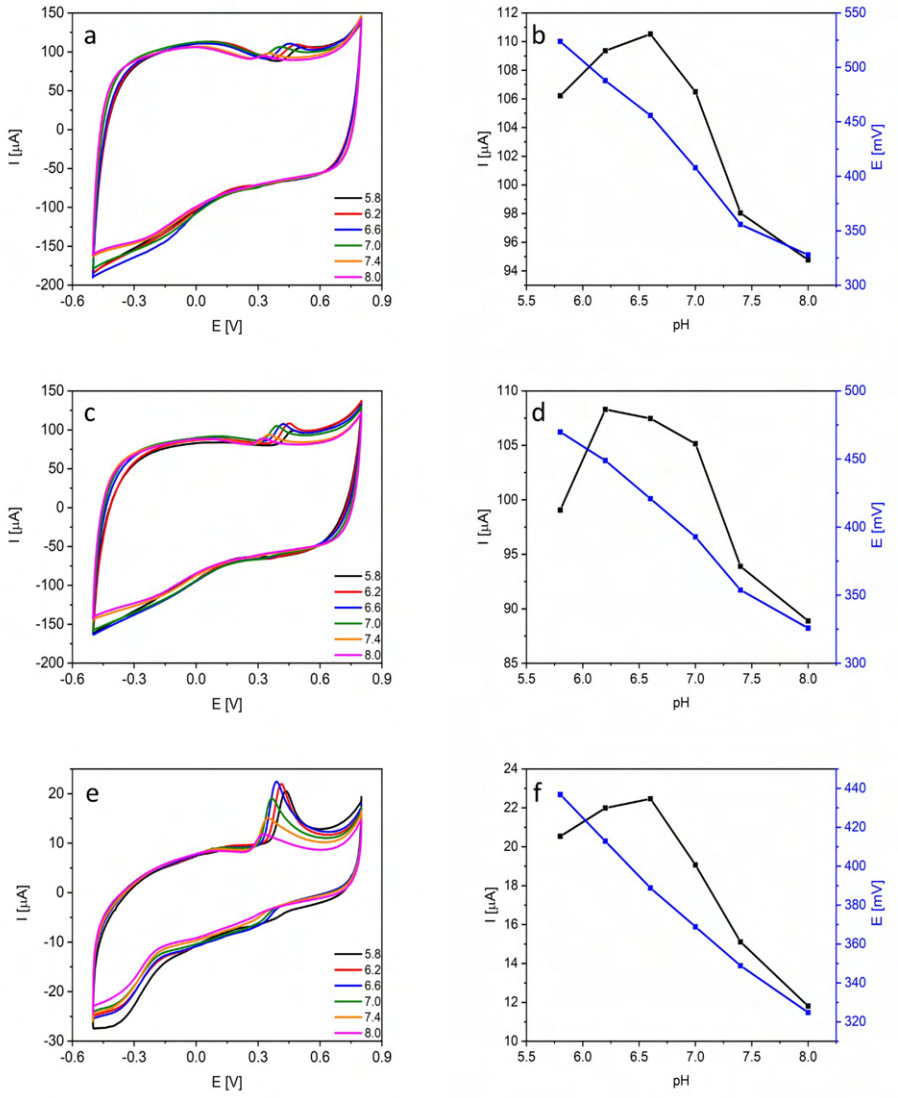

Figure 91. CVs recorded (v_{scan} = 100 mV s^{-1}) at increasing pH values on (a) FSG33:67/GCE, (c) FSG15:85/GCE and (e) PFSG/GCE in a 0.1 M PBS solution containing 100 µM of UA. Influence of the selected pH on the oxidation peak current and peak potential values recorded on (b) FSG33:67/GCE, (d) FSG15:85/GCE and (f) PFSG/GCE.

The main mechanism controlling UA oxidation was determined by CV measurements carried out at increasing scan rates (2 – 250 mV s^{-1}) in a 0.1 PBS solution (pH = 7.0) containing 100 µM UA (Figure 92). Relationship between anodic peak current and square root of scan rate was linear for all tested electrodes. In addition, logarithmic relationship between scan rate and maximum anodic peak current was plotted for all electrodes. The slope of the resulting plots was 0.65, 0.67 and 0.63 on FSG33:67/GCE, FSG15:85/GCE and PFSG/GCE, respectively (Figures 93c, f, and i). Both findings were indicative that the main mechanism controlling UA oxidation was diffusion [200].

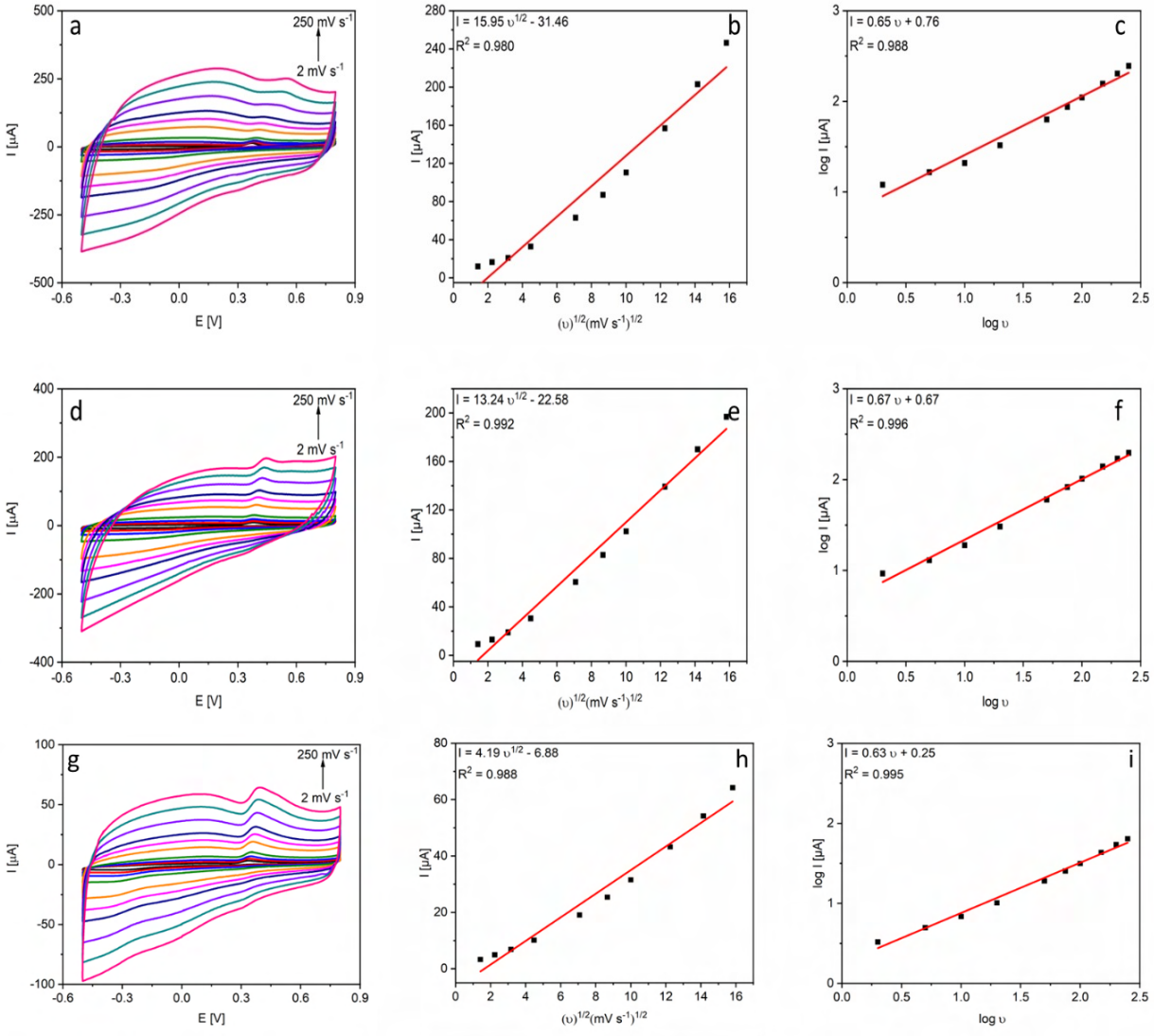

Figure 92. CVs recorded at increasing scan rates (2, 5, 10, 20, 50, 75, 100, 150, 200, 250) on (a) FSG33:67/GCE, (c) FSG15:85/GCE and (e) PFSG/GCE in a 0.1 M PBS solution (pH = 7.0) with 100µM of UA. Relationships between maximum anodic peak current and square root of scan rate recorded on (b) FSG33:67/GCE, (d) FSG15:85/GCE and (f) PFSG/GCE. The logarithmic relationship between scan rate and anodic peak current recorded on (c) FSG33:67/GCE, (f) FSG15:85/GCE and (i) PFSG/GCE.

Further, DPV measurements at increasing concentrations of UA (0.1 – 300 µM) were also performed (Figure 93). For all tested electrodes two linear ranges were selected, similarly as in DA detection (Table 29). Two overlapped linear ranges can be correlated with electrode fouling as at high UA concentrations, products of its oxidation can be adsorbed on the electrode surface [235]. The widest LR was recorded on PFSG/GCE (Figure 93f) (5 – 50 and 50 – 200 µM) which indicated the highest anti-fouling properties of this electrode. Repeatability and reproducibility

measurements on PFSG/GCE presented the lowest values, also corroborating its high anti-fouling properties. It was expected that positively charged nitrogen groups presented in the ternary composite could attract UA to the electrode surface, improving sensor working parameters. However, the protonation degree on PFSG/GCE has a value of 17% which indicate too low number of positively charged nitrogen groups to have a significant impact on UA attraction to the electrode surface. The lowest LOD was recorded on FSG15:85/GCE (Figure 93c), as this active electrode material exhibited the better restoration of the aromatic network (Csp^2 = 41.5 at.%). Thus, it can be concluded that when assessing UA detection, the electrical conductivity is more crucial than the presence of contrary charged functional groups. As an additional probe, in the structure of FSG33:67/GCE a significant contribution of oxygen moieties could be observed (29.8 at.%) which led to a lower electrical conductivity and to worse sensor working parameters.

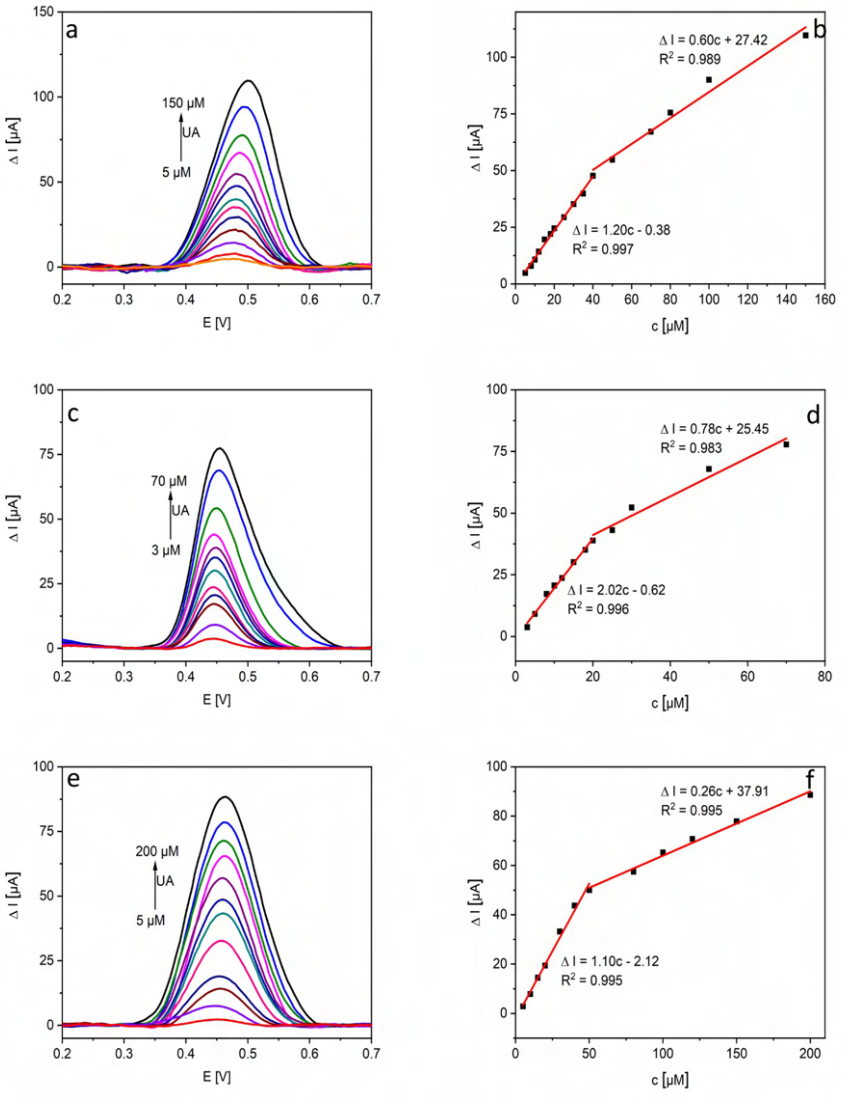

Figure 93. Baseline-corrected DPVs recorded on (a) FSG33:67/GCE, (c) FSG15:85/GCE and (e) PFSG/GCE in a 0.1 M PBS solution (pH=7.0) at increasing UA concentrations. Corresponding calibration curves for (b) FSG33:67/GCE, (d) FSG15:85/GCE and (f) PFSG/GCE.

As above mentioned, enhanced reproducibility and repeatability data were recorded on PFSG/GCE. It can be explained from the presence of PANI in the composite which improved the attachment of the active material to the GCE surface. Repeatability on FSG15:85/GCE was improved in comparison to FSG33:67/GCE due to repulsion of target analyte from the electrode surface by this last one active material, with a markedly higher oxygen content (29.8 vs 15.1 at.%).

Table 29. Electrochemical performance of FSG33:67/GCE, FSG15:85/GCE and PFSG/GCE sensors towards UA sensing

Sensor	LOD nM	LR µM	Sensitivity µA µM^{-1}	Reproducibility RSD %	Repeatability RSD %
FSG33:67/GCE	1.8	5 – 40; 40	1.2; 0.6	16.1	9.5
FSG15:85/GCE	0.328	3 – 20; 20	2.02; 0.78	16.2	6.3
PSFS1:1/GCE	1.6	5 – 50; 50	1.1; 0.3	5.1	3.4

As FSG15:85/GCE showed better performance towards UA detection, interference studies were conducted on this electrode. In this regard, DPV experiments were performed in a 0.1 M PBS solution (pH = 6.6) at increasing concentrations of UA and 300 µM of AA and DA (Figure 94). The LOD increased from 0.328 to 2.6 µM (Table 30), even though this electrode provided a ow LOD for DA detection (441 nM). This fact indicates the occupation of active sites not only by UA but also by DA molecules, which was confirmed by the well-developed anodic peak originated from DA oxidation, which was almost unaffected even at high UA concentrations.

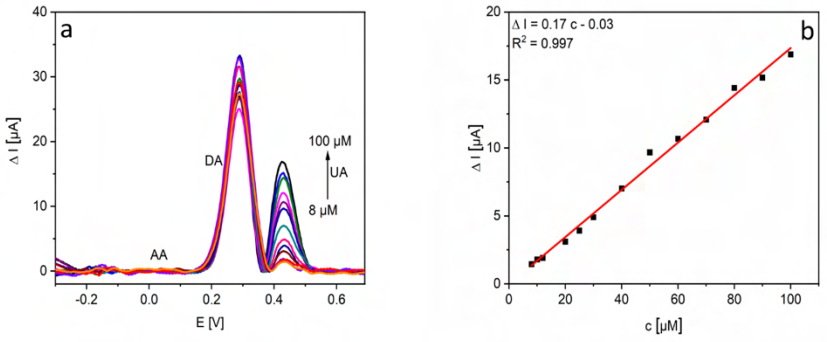

Figure 94. Baseline-corrected DPVs recorded on (a) FSG15:85/GCE in a 0.1 M PBS solution (pH = 6.6) at increasing UA concentrations and 300 μM of AA and DA. (b) Corresponding calibration curve.

Table 30. Electrochemical performance of FSG15:85/GCE sensor towards UA sensing in presence of interfering compounds (300 μM of AA and DA)

Sensor	LOD nM	LR μM	Sensitivity μA μM^{-1}
FSG15:85/GCE	2.6	8 – 100	0.17

Further studies in artificial urine samples were performed on FSG15:85/GCE. Thus, 5, 25, and 50 μM of UA were added to an artificial urine solution (Table 31). The current intensity of the recorded oxidation peak was used to calculate the real value existing in the solution, following previously obtained calibration curve. Recoveries ranged between 80.7 – 92.4 %. When UA concentration increased, the detection performance decreased. It can be explained by the potential adsorption of oxidized UA forms and other compounds presented in the artificial urine samples, resulting in electrode fouling and leading to the decrease of signal intensity [235].

Table 31. Electrochemical performance of FSG15:85/GCE towards UA sensing in the presence of interfering compounds

Analyte	Added μM	Measured μM	Detection performance %	RSD %
UA	5	4.6	92.4	7.1
	25	20.1	83.5	
	50	40.4	80.7	

5.1.3.4 Simultaneous detection

Simultaneous detection of DA and UA was performed on PFSG/GCE, as this electrode showed better performance for DA detection (Figure 95a). Due to differences in the optimized pH values in DA and UA determination (7.0 and 6.6, respectively), the optimization of the pH value was carried out in a solution containing both analytes. The overpotential values ascribed to DA and UA oxidation reactions decreased when increasing pH value. The highest anodic peak current for DA detection was recorded at pH 6.6, although the overpotential was lower at pH 7.0 (Figure 95b). Comparing anodic peak currents measured at pH 6.6 and 7.0, it decreased by 0.8 and 0.4 μA when detecting DA and UA, respectively. For both analytes the overpotential decreased by 16 mV at pH 7.0 comparing to 6.6. Bearing in mind the physiological pH value (7.4), pH 7.0 was selected as the optimal value.

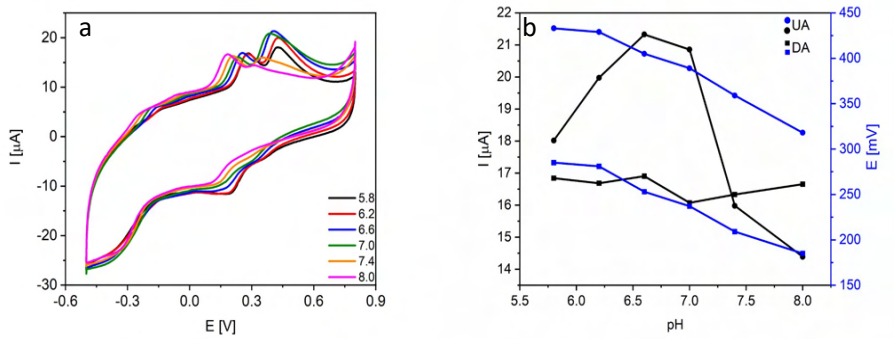

Figure 95. CVs recorded (v_{scan} = 100 mV s^{-1}) at increasing pH values on (a) PFSG/GCE in a 0.1 M PBS solution containing 100 µM of DA and 100 µM of UA. Influence of the selected pH on the oxidation peak current and peak potential values recorded on (b) PFSG/GCE.

CVs at increasing scan rate (2 – 250 mV s^{-1}) were recorded on this electrode in a 0.1 PBS solution (pH = 7.0) containing 100 µM DA and to gain insight into the main mechanism controlling both oxidation processes (Figure 96). Relationships between anodic peak current and square root of scan rate were linear. Moreover, slopes of the plots resulting from the logarithmic relationships between scan rate and maximum anodic peak current were 0.60 for DA and 0.51 for UA (Figure 96c). These results corroborated that diffusion is the main mechanism controlling both anodic reactions [200].

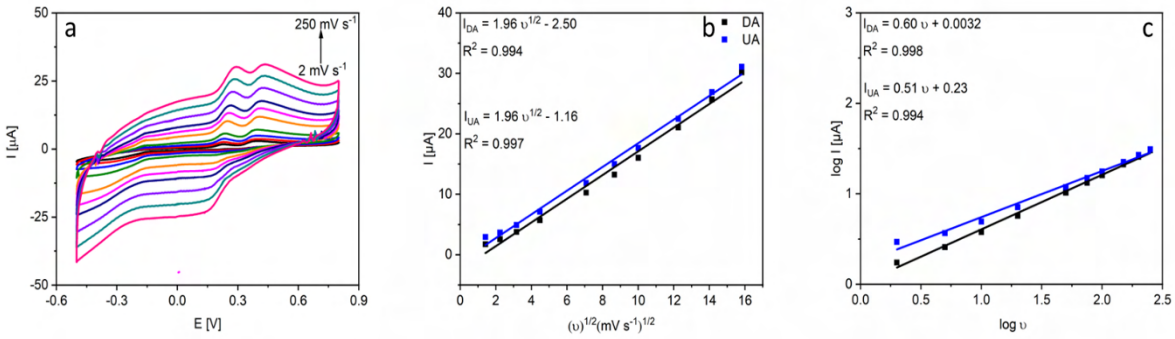

Figure 96. CVs recorded at increasing scan rates (2, 5, 10, 20, 50, 75, 100, 150, 200, 250) on (a) PFSG/GCE in a 0.1 M PBS solution (pH=7.0) with 100µM of UA. Relationship between maximum anodic peak current and square root of scan rate recorded on (b) PFSG/GCE. The logarithmic relationship between scan rate and anodic peak current recorded on (c) PFSG/GCE.

Simultaneous determination plots are shown in Figure 97. The baseline corrected DPVs were recorded on PFSG/GCE in a DA concentration range 2 – 15 µM (Figure 97b) and (Figure 97c) in a UA concentration range 20 - 150 µM, as this last analyte concentration in the human

organism is ten times higher than DA. The oxidation peaks corresponding to both analytes were well-resolved (peak to peak separation 160 mV), while the calculated LOD values were 0.15 and 6.4 µM for DA and UA, respectively (Table 32). These results show a promising potential application of PFSG/GCE in real samples analysis, as determined LOD values were in the same range as that for individual detection.

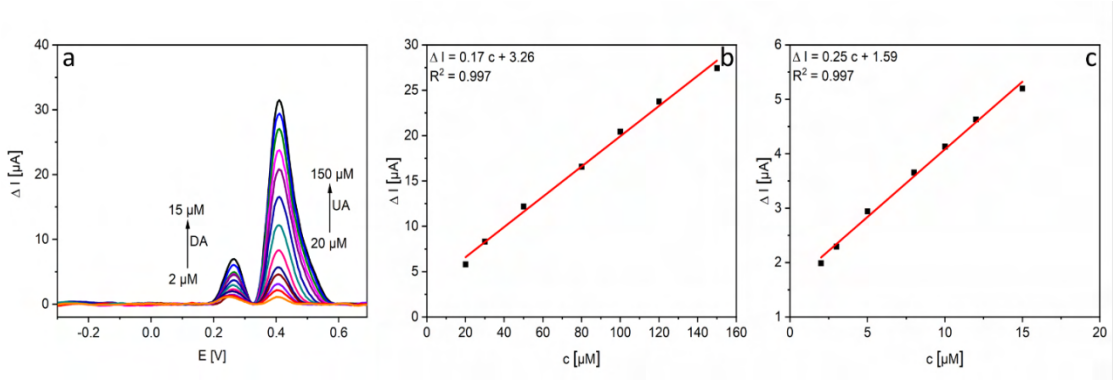

Figure 97. Baseline-corrected DPVs recorded on (a) PFSG/GCE in a 0.1 M PBS solution (pH = 7.0) at increasing concentrations of DA and UA. Corresponding calibration curves for (b) DA and (c) UA.

Table 32. Electrochemical performance of PFSG/GCE towards simultaneous DA and UA sensing

Analyte	LOD nM	LR µM	Sensitivity µA µM^{-1}
DA	0.15	2 – 15	0.17
UA	6.4	20 – 150	0.25

Finally, the long-term stability of PFSG/GCE was investigated (Figure 98). After 7 days, it maintained almost 95 % of initial oxidation signal of both analytes. The signal corresponding to DA was almost unaffected while for UA a drop of 10 % after 30 days of usage was noticed. The long-term stability of the nanocomposite material can be attributed to the synergistic effects between its counterparts. Graphene layers provide sites for PANI attachment during hydrothermal treatment which enables to maintain proper separation between them. On the other hand, PANI chains play a key role as RGO scaffold [221,237].

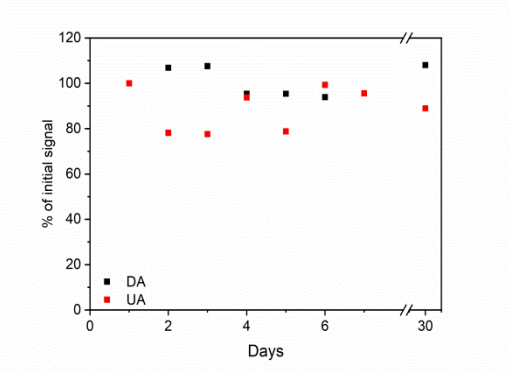

Figure 98. Long-term stability study on PFSG/GCE for the simultaneous DA and UA detection.

Summary

Binary nanocomposites of Fe_2O_3-SnO_2 and RGO, with different weight ratios of the inorganic counterpart, synthesized under hydrothermal treatment (180°C/8h) and ternary nanocomposite synthesized applying a secondary hydrothermal treatment to the binary ones with PANI (180°C/12h) were tested for DA and UA detection. Binary composites differed in both, the inorganic part contribution and the Csp^2 content. FSG15:85 showed a higher contribution of Csp^2 and more developed active surface area, exhibiting the better sensing behavior comparing to FSG33:67. On the other hand ternary PFSG nanocomposite presented the same contribution of Fe_2O_3-SnO_2 as in FSG15:85 (15 wt.%). PFSG nanocomposite contained in its structure a 11.7 at.% N resulting in protonation degree of 17% and leading to the lowest LOD for DA detection (76 nM). Due to successful application of these nanocomposites for DA sensing, their multianalyte sensing properties were also tested. Enhanced electrochemical performance towards UA was revealed on FSG15:85/GCE (LOD = 328 nM), as this active material presented the highest Csp^2 content (41.5 at.%) and the best development of S_{BET}.

5.1.4 IPEs for DCF electrochemical detection

IPEs are a novel and interesting alternative to widely used GCEs or screen-printed electrodes (SPEs) in order to carry out electrochemical measurements of different target analytes. Due to their low cost, scalable, easy manufacture and compact/miniaturized size this type of electrodes has arisen in interest between the scientific community and could be potentially applied thus replacing commercially available electrodes. In this thesis, IPEs are shown as a proof of

concept, trying to show its applicability in electrochemical sensing of DCF which, as previously stated, is considered as water contaminant of emerging concern.

5.1.4.1 Morphology and structure of sensing platforms

The morphology of sensing platforms based on graphene materials and manufactured by means of inkjet-printing on Kapton as flexible substrate (see experimental section) was determined using SEM (Figure 99). It can be observed that both of them (made from GO-based ink or thermally treated in a post-processing step, at a temperature of 400 ºC) exhibited a homogenous coverage of the selected substrate, forming smooth layers. Moreover, carbon black (conductive additive) aggregates were clearly visible [209,238].

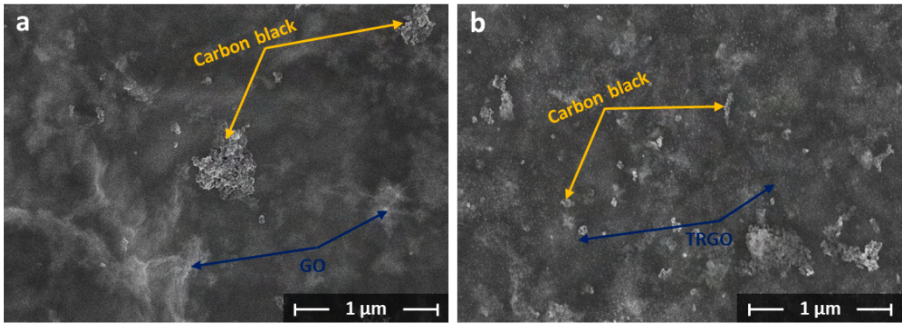

Figure 99. SEM pictures of (a) GO-7000_TX_CB_8/K and (b) GO-7000_TX_CB_8_TR400/K.

The chemical surface composition of both sensing platforms was determined by XPS (Table 33). As expected, a significant decrease of oxygen content was observed after thermal treatment (post-processing step) (31.3 at.% O for GO-7000_TX_CB_8/K and 9.1 at.% O for GO-7000_TX_CB_8_TR400/K), thus confirming the successful thermal reduction of starting GO-based ink. In addition, the chemical composition of GO-7000_TX_CB_8_TR400/K is similar to that determined for TRGO400 powder, produced using a conventional thermal exfoliation/reduction starting from GrO (89.9 at.% C and 10.1 at.% O). The C1s spectra of both IPEs can be divided into five components corresponding to sp^2 hybridized carbon (284.5 eV), sp^3 hybridized carbon (285.4 eV) hydroxyl and epoxy (286.5 eV), carbonyl and quinone bonds (287.6 eV) and lactone and carboxylic groups (289.0 eV) (Figure 100) [210]. Moreover, chemical surface composition is presented in Table 34 in detail. GO-7000_TX_CB_8_TR400/K presented a high contribution of Csp^2. In addition, the content of all functional groups in GO-7000_TX_CB_8_TR400/K is similar to TRGO400 powder. This finding also proved the successful reduction of GO-based ink on Kapton® substrate. The contribution of Csp^3 and hydroxyl and epoxy groups decreased after thermal treatment.

Moreover, an increase of carboxy/lactone peak was observed after thermal treatment which can be explained by a conversion of oxygen moieties which possess lower stability into lactone groups [239,240]. In addition, electrical conductivity measurements were performed on GO-7000_TX_8_TR400/K and GO-7000_TX_CB_8_TR400/K to check the impact of CB incorporation into the GO-based ink formulation. A marked decrease of sheet resistance was recorded on IPE after thermal treatment in the presence of this conductive additive (3.96 vs. 5.10 kΩ sq^{-1} for GO-7000_TX_CB_8_TR400/K and GO-7000_TX_8_TR400/K, respectively). The sheet resistance for GO-7000_TX_CB_8/K presented a value out of measurement device range, as a result of the high isolating character of the GO.

Table 33. Chemical surface composition of IPEs determined by XPS (at.%)

Sample	C	O
GO-7000_TX_CB_8/K	68.7	31.3
GO-7000_TX_CB_8_TR400/K	90.9	9.1

Table 34. Type and distribution of C functional groups, at.%

Sample	C1s peak deconvolution				
	Csp^2	Csp^3	C-OH	C=O	O=C-OH
GO-7000_TX_CB_8/K	42.5	12.1	32.9	7.1	5.4
GO-7000_TX_CB_8_TR400/K	60.9	16.6	13.2	4.3	5.0

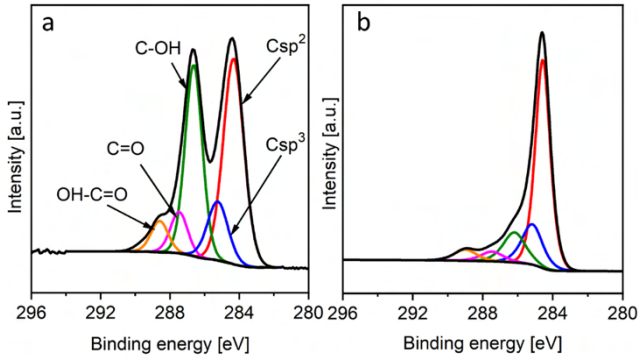

Figure 100. Deconvolutions of the C1s core-level XPS spectra of (a) GO-7000_TX_CB_8/K and (b) GO-7000_TX_CB_8_TR400/K.

5.1.4.2 Electrochemical performance of IPEs (optimization of ink formulation)

Considering previously recorded promising performance of TRGOs for DCF electrochemical sensing they were also considered as active materials for IPEs manufacture and subsequent electrochemical characterization. As stated before, the highest possible temperature applied of GO-based IPEs was 400°C as thermal stability of Kapton® (which was selected as substrate in

this thesis) is 450°C. The electrochemical performance towards the non-direct DCF detection on different IPEs (printed using GO-based inks with different formulations) after thermal treatment (Figure 101) was tested. Firstly, the concentration of starting GO (4000, 7000 and 9000 ppm) was optimized (Figure 101a), fixing the printed layers as 8. The capacitive currents measured on all the electrodes were comparable, indicating the achievement of homogenous layers. However, the anodic peak currents corresponding to DCF oxidation process of interest differed. Related current was significantly lower on GO-4000_TX_Y_TR400/K. Moreover, the overpotential values were also higher on this electrode, when comparing to those measured on GO-7000_TX_Y_TR400/K and GO-9000_TX_Y_TR400/K. The resulting slower electron transfer rate can be explained from the poorer homogeneity of printed layers on this electrode. As CVs recorded on IPEs prepared using inks at higher GO concentrations were comparable, the ink based on GO in lower concentration (7000 ppm) was selected for further measurements. The effectiveness of Triton X-100 and SDS as surfactants was also compared (Figure 101b). Both surfactants were added to a GO-7000 suspension in a weight ratio 2:1. The more distinctive peaks were developed on the IPE with Triton X-100 in the ink formulation. Subsequently, addition of CB to ink formulation was tested (Figure 101c). Even though the incorporation of this conductive additive resulted in higher capacitive currents, a well-developed oxidation peak, with suitable current intensity and overpotential values, was shown reflecting the positive impact of CB [241]. In the last step the number of printed layers (from 7 to 10) was optimized, trying to achieve the most appropriate sensing platforms (Figure 101d and e). The highest anodic peak currents were recorded on IPEs with 8 and 9 layers of printing. However, 8 layers were selected as the suitable value taking into account the lower amount of ink required to print and the lower capacitive current recorded on the final electrode. Figure 101f showed images illustrating the quality of printed sensor platforms.

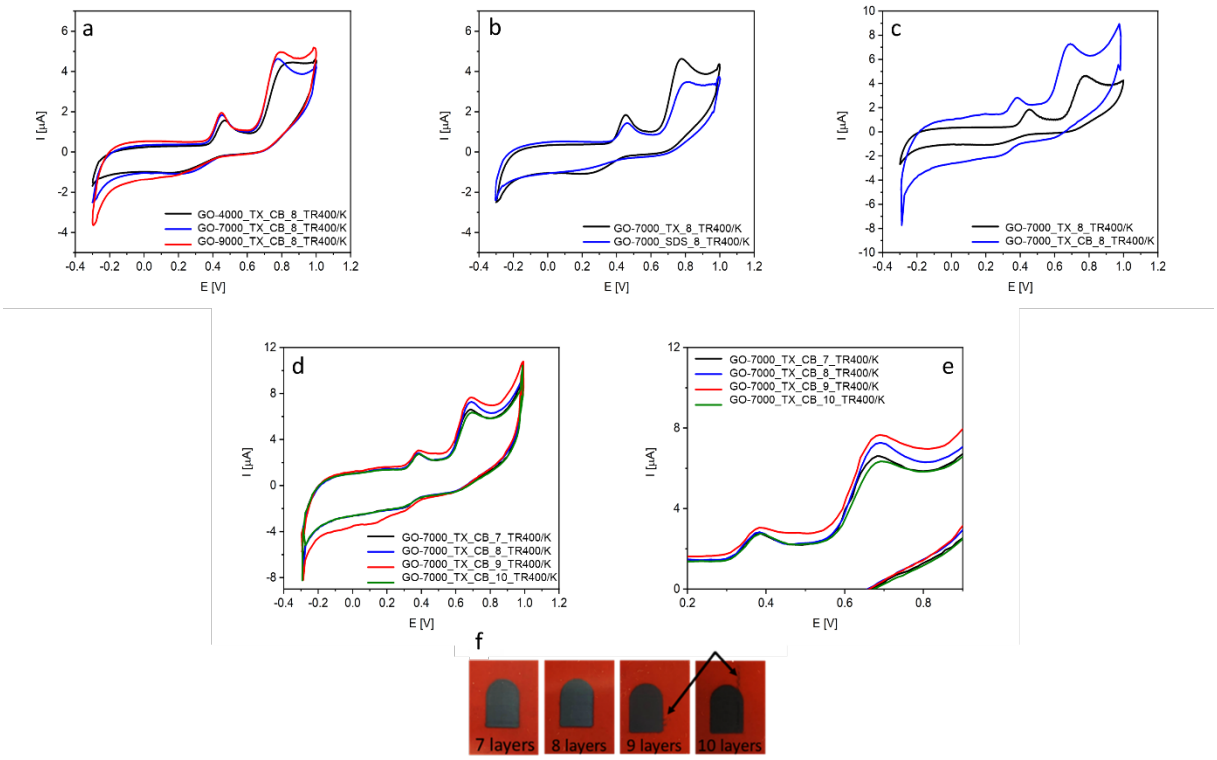

Figure 101. (a-e) CVs recorded on GO-X_S_CB_Y_TR400/K electrodes manufactured using different GO-based ink formulations. A 0.1 M PBS solution (pH 7.0) containing 100 µM DCF was used as electrolyte. (f) Images of GO-7000_TX_CB_Y_TR400/K electrodes differing in the number of GO-based printed layers (from 7 to 10).

The IPE manufactured using the optimized ink formulation was subsequently thermally treated (at 400 ºC) and its electrochemical performance for DCF sensing was compared to that from IPE before thermal treatment, using a 0.1 M PBS solution (pH = 7.0) containing 100 µM DCF (Figure 102a). Additionally, the electrochemical behavior of both IPEs was compared to that of widely used GO/GCE and TRGO400/GCE (Figure 102b). The anodic peak ascribed to the faradaic process of 2,2-hydroxyphenyl acetic acid was well-developed on the IPE after post-processing step (thermal treatment). In comparison with TRGO400/GCE, the IPE displayed a lower capacitive current which could be beneficial for its electrochemical performance.

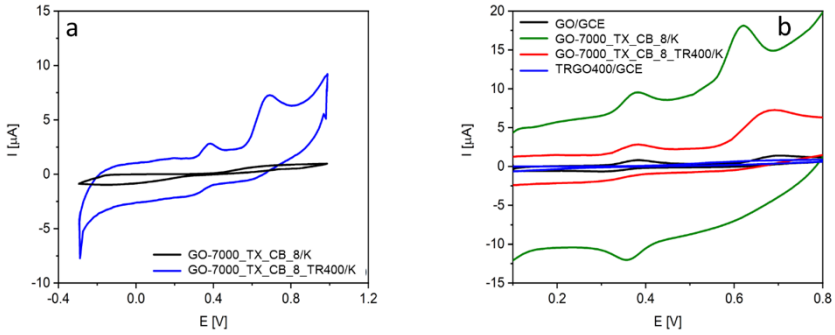

Figure 102. CVs recorded on (a) GO-7000_TX_CB_8/K and GO-7000_TX_CB_8_TR400/K sensors. (b) Comparison with GO/GCE and TRGO-400/GCE conventional electrodes. A 0.1 M PBS solution (pH 7.0) containing 100 µM DCF was used as electrolyte.

Figures 103a and b presented the baseline corrected DPVs recorded, in a 0.1 M PBS solution (pH 7.0) containing 100 µM DCF, on GO-7000_TX_CB_8_TR400/K and TRGO400/GCE, respectively. The anodic peak recorded on IPE resulted very broad, probably due to the overlapping of the response corresponding to first electroactive DCF reaction with the side reaction of 1-hydroxy-2-(hydroxyphenyl)ethanalate. However, well–resolved peaks were recorded TRGO400/GCE indicating improved electrochemical performance on this electrode. Nevertheless, IPEs and miniaturized setup shows promising potential for future application of this type of electrodes towards electrochemical detection of pharmaceutical environmental contaminants including DCF for which extended research is required in order to improve inks formulations and printing and/or post-printing parameters.

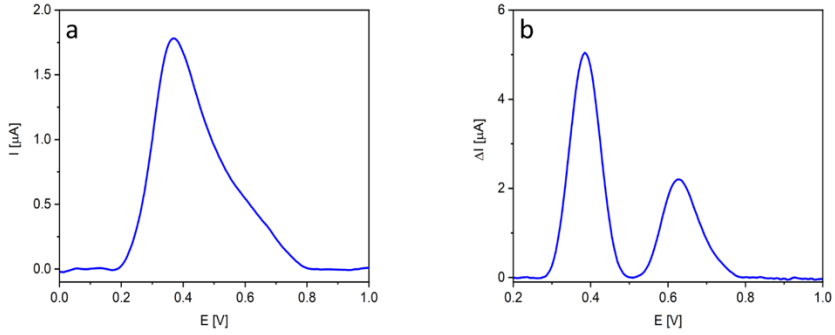

Figure 103. Baseline corrected DPVs recorded on (a) GO-7000_TX_CB_8_TR400/K and (b) TRGO400/GCE in a 0.1 M PBS solution (pH 7.0) containing 100 µM DCF.

Summary

A novel concept of miniaturized electrochemical setup based on IPEs was presented. Ink formulations starting from GO as active material were successfully prepared and their suitability towards inkjet-printing was assessed. The optimal water-based ink formulation ready to be printed on flexible Kapton® substrate consisted of GO (7000 ppm), Triton X-100 and carbon black which, after a post-processing thermal treatment, gave rise to an IPE (GO-7000_TX_CB_8_TR400/K). The oxygen content after thermal treatment decreased from 31.3 to 9.1 at. %. It was found that the chemical composition of GO-7000_TX_CB_8_TR400/K was similar to that corresponding to TRGO400 powder obtained using conventional thermal exfoliation/reduction of starting GrO. The selected electrode (GO-7000_TX_CB_8_TR400/K) was tested towards non-direct DCF electrochemical detection at pH 7.0 and compared with TRGO400/GCE. The preliminary results showed the potential of this type of novel electrodes for electrochemical sensing of different target analytes widening a range of available sensors.

6 Overall summary

In this thesis, great efforts have been focused on the improvement of sensors working parameters for electroactive species as neurotransmitter DA, its interfering compounds including AA and UA, and environmental pollutants such as pharmaceutical DCF. Potential working electrodes (GCEs) modifiers, mainly based on three groups of graphene material composites, and a novel miniaturized electrochemical setup based on inkjet-printing technology have been proposed to enhance the required sensing parameters to the above-mentioned analytes.

In the first step, NRGO was synthesized using hydrothermal treatment (180°C/12h) of GO in the presence of urea as a nitrogen source. Then, NRGO was modified with AuNPs using electrodeposition technique. For comparative purposes RGO was synthesized following the same hydrothermal treatment. The resultant materials were tested towards DA, AA, UA and their simultaneous detection. The impact of nitrogen contribution in the material structure on AuNPs distribution and subsequent electrochemical performance of proposed sensor was determined. According to the results, the electrochemical response from DA redox reactions was improved after nitrogen introduction into RGO structure. Further modification of NRGO/GCE with AuNPs led to a significant decrease of LOD of DA (812 vs. 385 nM). Determination of AA and UA using AuNPs/RGO/GCE and AuNPs/NRGO/GCE revealed that

last one performed better for detecting interfering species. Moreover, AuNPs acted as electrocatalysts resulting in a significant decrease of the overpotential of electrochemical reactions.

In the next step, PANI had been proposed to compare effectiveness of modification of graphene materials with conductive polymers with previously discussed modification with metallic nanoparticles. A series of TRGOs obtained by thermal exfoliation/reduction of GrO at 400, 700 and 1000ºC was used in this study, while PANI was prepared by oxidative polymerization. The next step consisted on PANI and TRGOs mixing and subsequent hydrothermal treatment (180°C/8h) to obtain final composites. Starting and as-synthesized materials were tested towards DA electrochemical detection. Significant differences in the distribution of PANI on and within graphene layers were revealed, comparing composites obtained applying different components ratio (1:3, 1:1 and 3:1) and thermal reduction temperature. The PANI:TRGO ratio was optimized and selected as 1:1. In addition, the optimal GrO reduction temperature was set as 700 °C, also ensuring the most homogenous PANI distribution. It has been revealed that PANI-TRGO7001:1/GCE performance for DA detection was as good as in case of AuNPs/NRGO/GCE (LODs 430 and 385 nM, respectively).

Willing to fill the literature gap concerning the suitability of graphene materials as GCE modifiers for DCF sensing, TRGOs were assessed. Electrochemical measurements revealed the most improved performance of TRGO700 (5.1 at. %) towards non-direct electrochemical detection of DCF resulting in a LOD of 61 nM. Moreover, the impact of PANI introduction into TRGO structure was also investigated. However, the sensor working parameters after PANI introduction were not improved, as LOD was as high as 442 nM.

Taking into account that AuNPs and PANI improved the electrochemical detection of DA, in the next step binary and ternary composites containing mixed Fe_2O_3-SnO_2 were synthesized, to replace AuNPs, as they possess electrocatalytical activity and are a cheaper alternative. Two-step hydrothermal treatment was proposed to introduce inorganics and PANI nanoparticles not only on the surface of graphene layers but also between them. Binary composites of Fe_2O_3-SnO_2 and RGO, with different contribution of inorganic part were prepared by hydrothermal treatment (180°C/8h) of a mixture containing $SnSO_4$, $Fe(NO_3)_3$ and GO to yield FSG composites (FSG15:85 - 15 wt.% of mixed Fe_2O_3-SnO_2 and 85 wt.% of RGO and FSG33:65 - 33 wt.% of mixed Fe_2O_3-SnO_2 and 67 wt.% of RGO). The ternary PFSG composite was obtained by subsequent hydrothermal treatment of FSG with PANI (180°C/12h) to have the same contribution of PANI (50 wt.%) as those composites previously optimized (PANI-TRGOs composites). The Fe_2O_3-SnO_2 content was set the same as in FSG15:85, as the recorded LOD

of DA on FSG15:85 was lower than on FSG33:67. PFSG presented the lowest LOD of DA detection among all materials studied in this work (76 nM), while the lowest LOD of UA determination was revealed on FSG15:85 (328 nM). Above results indicated an improved electrochemical sensing performance of PFSG towards DA and UA comparing to the composites tested in the first paragraph (AuNPs/RGO/GCE and AuNPs/NRGO/GCE).

Considering LOD, the most improved electrochemical sensing performance towards DA determination was recorded on the ternary PFSG composite (LOD = 76 nM). However, AA and UA were effectively detected using AuNPs/NRGO and FSG15:85, respectively. In non-direct DCF determination, TRGO700/GCE seemed to be the most effective sensing platform. Summarizing, the working parameters determined for all the sensors developed in this thesis are presented in Table 35.

Table. 35. Sensor working parameters of all tested materials towards individual determination of DA, AA, UA and DCF

Electrode material	Detected analyte	LOD nM	LR µM	Sensitivity µA µM^{-1}	Reproducibility RSD %	Repeatability RSD %
RGO	**DA**	9980	5-70	2.29	7.7	6.7
NRGO	**DA**	812	3-70	1.12	6.2	4.8
AuNPs/RGO	**DA**	700	1-100	1.78	7.6	6.4
	AA	56000	100-2000	0.004	7.8	7.3
	UA	17000	20-500	0.04	7.2	6.9
AuNPs/NRGO	**DA**	385	1-100	0.79	4.3	2.7
	AA	44000	200-1000	0.002	4.9	4.6
	UA	2700	1-100	0.10	4.5	3.8
PANI	**DA**	1570	1-25	4.34	7.9	3.8
TRGO400	**DA**	883	1.25	3.58	9.7	2.8
	DCF	2250	5-25	0.20	10.5	5.0
TRGO700	**DA**	965	1-25	1.92	7.2	2.5
	DCF	61	0.2-20	1.86	11.9	6.4
TRGO100	**DA**	1213	3-25	1.52	6.9	2.4
	DCF	4140	5-20	0.83	12.3	7.8
PANI-TRGO400 1:3	**DA**	1180	0.3-30	4.60	9.3	3.1
PANI-TRGO400 1:1	**DA**	701	0.3-30	3.63	6.6	5.5
PANI-TRGO400 3:1	**DA**	1550	1-30	3.59	4.0	1.6
PANI-TRGO700 1:1	**DA**	430	0.8-20	6.71	4.0	1.0
	DCF	442	0.2-25	1.57	12.1	11.0
PANI-TRGO1000 1:1	**DA**	506	0.8-20	4.28	5.1	3.4
FSG33:67	**DA**	1500	1-35, 35- 100	2.04; 0.72	15.1	7.9
	UA	1800	5-40; 40-150	1.2; 0.6	16.1	9.5
FSG15:85	**DA**	441	0.3-5;5-50	7.41; 1.49	15.9	8.9
	UA	328	3-20; 20-70	2.02; 0.78	16.2	6.3
PFSG	**DA**	76	0.1-20; 20-120	2.75; 0.87	3.2	3.3
	UA	1600	5-50; 50-200	1.1; 0.3	5.1	3.4
PFSG w/o nafion	**DA**	833	1-30; 30-90	6.74; 1.36	9.2	8.7

Bearing in mind the promising results for DCF sensing recorded on the TRGOs, they were also proposed as active materials for the formulation of inks required for IPE preparation. Furthermore, a novel miniaturized lab-made electrochemical setup based on IPEs, which can be an interesting alternative for real-time detection of pharmaceuticals in environmental samples was proposed. After optimizing several parameters (GO concentration, selection of surfactant, CB addition, number of printed layers) the finally selected water-based ink formulation was printed on flexible Kapton substrate consisted of GO (7000 ppm), Triton X-100 and carbon black (GO-7000_TX_CB_8_TR400/K). The number of printed layers was fixed as 8. The electrochemical response for DCF sensing recorded on GO-7000_TX_CB_8_TR400/K was highly distinctive.

7 Conclusions

- Hydrothermal treatment of GO in the presence of urea as nitrogen source (180°C for 12h) resulted in the introduction of a 6.4 at.% of nitrogen into the structure of resulting RGO. The presence of these nitrogen functionalities was crucial for the subsequent homogenous distribution of AuNPs, as they preferably were attached in the N-enriched areas of the material. The achieved homogenous distribution of AuNPs increased the number of electrocatalytically active sites, leading to improved sensor working parameters for DA, AA and UA sensing. Both materials (RGO and NRGO) modified with AuNPs presented an enhanced electrocatalytic activity, resulting in well-resolved anodic peaks during simultaneous DA, AA and UA detection. Moreover, AuNPs enhanced long-term stability of the active materials protecting N-groups from oxidation.
- Thermal reduction temperature of GrO had a marked impact on the morphology of PANI-TRGO composites. Introduction of 50 wt.% of conductive polymer led to an enhancement of sensor working parameters for DA detection. The most homogenous distribution of PANI in the composites was revealed on TRGO700, due to its highest exfoliation degree. Moreover, a tailored oxygen content in the GCE electrode modifier played a key role for maintaining a suitable balance between electrical conductivity and proper affinity of the electrode surface for cationic DA. Moreover, PANI introduction improved long-term stability, reproducibility and repeatability of the active materials for DA detection.
- TRGO700 presented improved sensor working parameters for DCF electrochemical detection due to its moderate oxygen content, enabling maintenance of a suitable electrical

conductivity and sufficient wettability of the electrode surface. Contrarily to DA detection, introduction of 50 wt.% of PANI into TRGO700 worsen sensor working parameters.

- PANI introduction enabled to obtain a better accessibility to the active sites within graphene layers, acting as pillars and resulting in a decreased oxidation potential of DA and UA, comparing to responses recorded on the binary FSG composites. Synergistic effect between composite counterparts in PFSG led to LOD of DA as low as 76 nM. PANI introduction into ternary PFSG composite resulted in an enhanced long-term stability of the electrode material comparing to the binary FSG composites. PFSG/GCE sensor performed satisfactory in real samples analysis showing negligible impact of interferences on the detection of DA and UA (an average detection efficiency of 104 and 86 %, respectively).
- An adjusted ink formulation, composed of GO-7000, Triton X-100 and CB, enabled to print high quality films on Kapton® substrate with desktop EPSON EcoTank ET-M2120 printer. Furthermore, thermal treatment of printed sensing platforms resulted in successful reduction of GO, comparable to that achieved on TRGO400 in a powder form (reduced by conventional flash-pyrolysis of GrO). The proposed novel miniaturized sensing setup allowed to detect DCF in small sample volumes.

8 Abbreviations and acronyms

AA – ascorbic acid

APS – ammonium persulfate

BDDEs – boron doped diamond electrodes

CB – carbon black

CE – counter electrode

CNS – central nervous system

CNT – carbon nanotube

CCC – controlled current coulometry

CPC – controlled potential coulometry

CPs – conductive polymers

CV – cyclic voltammetry

CVD – chemical vapor deposition

DA – dopamine

DAB – 2-(3,4-dihyroxyphenyl)benzotriazole

DCF – diclofenac

DDL – dielectric double layer

DME – dropping mercury electrode

DMF – dimethylformamide

DMSO – dimethyl sulfoxide

DODA – dimethyldioctadecylamonium

DPV – differential pulsed voltammetry

EA – elemental analysis

EB – emeraldine base

EIS – electrochemical impedance spectroscopy

ES – emeraldine salt

FSG – composite consisted of iron oxide – tin oxide and reduced graphene oxide

FTO – fluorine-doped tin oxide

GCE – glassy carbon electrode

GO – graphene oxide

GrO – graphite oxide

HFCVD – hot filament chemical vapor deposition

HOPG – highly oriented pyrolytic graphite

HPLC – high performance liquid chromatography

IPE – inkjet printed electrode

IPL – intense pulsed light

ITO – indium tin oxide

LOD – limit of detection

LR – linear range

LSV – linear sweep voltammetry

N-5 – nitrogen in pyrrolic bonds

N-6 – nitrogen in pyridinic bonds

N-C – nitrogen in amine/amide bonds

N-Q – nitrogen in the form of quaternary bonds

N-X – nitrogen in the form of pyridine oxides

NMP – N-methyl-2-pyrrolidone

NPs – nanoparticles

NPV – normal pulsed voltammetry

NRGO – nitrogen doped reduced graphene oxide

NSAIDs – nonsteroidal anti-inflammatory drugs

ORR – oxygen reduction reaction

PANI - polyaniline

PBS – phosphate buffer solution

PEDOT – poly(ethylene dioxythiphene)

PET – poly(ethylene terephthalate)

PFLGs – planar few layers nano-graphene

PFSG – composite consisted of polyaniline, reduced graphene oxide and iron oxide-tin oxide

PGEs – pencil graphite leads

PPy – polypyrrole

PRGO – phosphorous doped reduced graphene oxide

RE – reference electrode

REM – rapid eye movement

RF – riboflavin

RGO – reduced graphene oxide

RSD – residual standard deviation

SDS – sodium dodecyl sulphate

SEM – scanning electron microscopy

SPE – screen printed electrode

SPCE – screen printed carbon electrode

SWV – square wave voltammetry

TEM – transmission electron microscopy

TRGO – thermally reduced graphene oxide

TVD – thermal vapour deposition

TX – triton X-100

UA – uric acid

WE – working electrode

XPS – X-ray photoelectron spectroscopy

XRD – X-ray diffraction

9 References

[1] Z. Brzózka, W. Wróblewski, Sensory Chemiczne, *Oficyna Wydawnicza PW* Warszawa (1999).

[2] A.J. Bard, L.R. Faulkner, Electrochemical methods: fundamentals and applications, *John Willey & Sons, Inc*. United States of America (2001).

[3] A.K. Geim, K.S. Novoselov, The rise of graphene, *Nat. Mater.* 6 (2007) 183-191.

[4] K. Jackowska, P. Krysinski, New trends in the electrochemical sensing of dopamine, *Anal. Bioanal. Chem*. 405 (2013) 3753–3771.

[5] B.S. Dakshayini, K.R. Reddy, A. Mishra, N.P. Shetti, S.J. Malode, S. Basu, S. Naveen, A. V. Raghu, Role of conducting polymer and metal oxide-based hybrids for applications in amperometric sensors and biosensors, *Microchem. J*. 147 (2019) 7–24.

[6] R. Liu, Z.Y. Feng, D. Li, B. Jin, Y. Lan, L.Y. Meng, Recent trends in carbon-based microelectrodes as electrochemical sensors for neurotransmitter detection: A review, *TrAC - Trends Anal. Chem*. 148 (2022) 116541.

[7] S.N. Berger, P. Hashemi, Brain chemistry | neurotransmitters, Encyclopedia of Analytical Science (Third Edition)*, Elsevier* (2019) 316–331.

[8] K.L. Wasewar, S. Singh, S.K. Kansal, Process intensification of treatment of inorganic water pollutants, Inorganic Pollutants in Water*, Elsevier* (2020) 245–271.

[9] The Editors of Encyclopaedia Britannica, Catecholamine, *Encyclopedia Britannica.* https://www.britannica.com/science/catecholamine, Accessed 4 April 2023.

[10] T. Nagatsu, T. Yamakawa, The catecholamine system in health and disease-relation to tyrosine 3-monooxygenase and other catecholamine-synthesizing enzymes, *Proc. Jpn. Acad. Ser. B Phys. Biol. Sci*. (2006) 388-415.

[11] F. Haddad, M. Sawalha, Y. Khawaja, A. Najjar, R. Karaman, Dopamine and levodopa prodrugs for the treatment of Parkinson's disease, *Molecules* 23 (2018) 40.

[12] R. Daneman, A. Prat, The blood–brain barrier, *Cold Spring Harb. Perspect. Biol*. 7 (2015) a020412.

[13] J.A. Best, H.F. Nijhout, M.C. Reed, Homeostatic mechanisms in dopamine synthesis and release: A mathematical model, *Theor. Biol. Med. Model*. 6 (2009) 21.

[14] L.F. Reichardt, R.B. Kelly, A molecular description of nerve terminal function, *Annu. Rev. Biochem*. 52 (1983) 871–926.

[15] H. Juárez Olguín, D. Calderón Guzmán, E. Hernández García, G. Barragán Mejía, The role of dopamine and its dysfunction as a consequence of oxidative stress, *Oxid. Med. Cell. Longev*. 2016 (2016) 9730467.

[16] T. Kageyama, M. Nakamura, A. Matsuo, Y. Yamasaki, Y. Takakura, M. Hashida, Y. Kanai, M. Naito, T. Tsuruo, N. Minato, S. Shimohama, The 4F2hc/LAT1 complex transports L-DOPA across the blood-brain barrier, *Brain Res.* 879 (2000) 115-121.

[17] R. Franco, I. Reyes-Resina, G. Navarro, Dopamine in health and disease: Much more than a neurotransmitter, *Biomedicines* 9 (2021) 1–13.

[18] C. Vitrac, S. Péron, I. Frappé, P.O. Fernagut, M. Jaber, A. Gaillard, M. Benoit-Marand, Dopamine control of pyramidal neuron activity in the primary motor cortex via D2 receptors, *Front. Neural. Circuits* 8 (2014) 13.

[19] Z. He, Y. Jiang, S. Gu, D. Wu, D. Qin, G. Feng, X. Ma, J.H. Huang, F. Wang, The aversion function of the limbic dopaminergic neurons and their roles in functional neurological disorders, *Front. Cell. Dev. Biol*. 9 (2021) 713762.

[20] R. Pivonello, D. Ferone, G. Lombardi, A. Colao, S.W.J. Lamberts, L.J. Hofland, Novel insights in dopamine receptor physiology, *Eur. J. Endocrinol*. 156 (2007) 13-21.

[21] K. Dzirasa, S. Ribeiro, R. Costa, L.M. Santos, S.C. Lin, A. Grosmark, T.D. Sotnikova, R.R. Gainetdinov, M.G. Caron, M.A.L. Nicolelis, Dopaminergic control of sleep-wake states, *Neurosci J*. 26 (2006) 10577–10589.

[22] S.J. McCarter, M.J. Howell, Importance of Rapid Eye Movement Sleep Behavior Disorder to the Primary Care Physician, *Mayo. Clin. Proc*. 91 (2016) 1460–1466.

[23] R. Brisch, A. Saniotis, R. Wolf, H. Bielau, H.G. Bernstein, J. Steiner, B. Bogerts, K. Braun, J. Kumaratilake, M. Henneberg, T. Gos, The role of dopamine in schizophrenia from a neurobiological and evolutionary perspective: Old fashioned, but still in vogue, *Front. Psychiatry* 5 (2014) 47.

[24] L. C. Triarhou, Dopamine and Parkinson's Disease. *Madame Curie Bioscience Database* (2000–2013).

[25] C.P.C. Galts, L.E.B. Bettio, D.C. Jewett, C.C. Yang, P.S. Brocardo, A.L.S. Rodrigues, J.S. Thacker, J. Gil-Mohapel, Depression in neurodegenerative diseases: Common mechanisms and current treatment options, *Neurosci. Biobehav. Rev*. 102 (2019) 56–84.

[26] Institute of Health Metrics and Evaluation (IHME), *GBD.* Seattle, WA:IHME (2018).

[27] P. Belujon, A.A. Grace, Dopamine system dysregulation in major depressive disorders, *IJNP* 20 (2017) 1036–1046.

[28] D.F. Davidson, Elevated urinary dopamine in adults and children, *Ann. Clin. Biochem*. 42 (2005) 200-7.

[29] Dopamine ELISA Kit (ab285238), https://www.abcam.com/products/elisa/dopamine-elisa-kit-ab285238.html, Accessed 4 May 2023.

[30] E. M. Wightman, L.J. May, A.C. Michael, Dynamic, Detection of dopamine dynamics in the brain, *Anal. Chem*. 60 (1988) 769-780.

[31] D.D. Perrin, Dissociation constants of organic bases in aqueous solution, *Butterworths* London (1965).

[32] R.P. Bacil, L. Chen, S.H.P. Serrano, R.G. Compton, Dopamine oxidation at gold electrodes: Mechanism and kinetics near neutral pH, *Phys. Chem. Chem. Phys*. 22 (2020) 607–614.

[33] U. Chandra, B.E. Kumara Swamy, M. Kumar, A. Wagari Gebisa, M. Praveen, Simple flame etching of pencil electrode for dopamine oxidation in presence of ascorbic acid and uric acid, *Int. J. Nanotechnol*. 14 (2017) 739-752.

[34] K.A. Naidu, Vitamin C in human health and disease is still a mystery ? An overview, *Nutr. J.* 2 (2003) 7.

[35] R.B. Rucker, J. Morris, A.J. Fascetti, Clinical Biochemistry of Domestic Animals, 6th Edition, *Elsevier* (2003) Chapter 23.

[36] J.L. Silencio Barrita, M. del S. Santiago Sanchez, Oxidative stress and chronic degenerative diseases - a role for antioxidants, *IntechOpen* (2013).

[37] M. Malik, V. Narwal, C.S. Pundir, Ascorbic acid biosensing methods: A review, *Process Biochem.* 118 (2022) 11–23.

[38] C. Wang, J. Du, H. Wang, C. Zou, F. Jiang, P. Yang, Y. Du, A facile electrochemical sensor based on reduced graphene oxide and Au nanoplates modified glassy carbon electrode for simultaneous detection of ascorbic acid, dopamine and uric acid, *Sens. Actuators B Chem*. 204 (2014) 302–309.

[39] D. Léger, Scurvy Reemergence of nutritional deficiencies, *CFP* 54 (2008) 1403-6.

[40] S. Chambial, S. Dwivedi, K.K. Shukla, P.J. John, P. Sharma, Vitamin C in disease prevention and cure: An overview, *Indian J. Clin.Biochem*. 28 (2013) 314–328.

[41] A.M. Pisoschi, A. Pop, A.I. Serban, C. Fafaneata, Electrochemical methods for ascorbic acid determination, *Electrochim. Acta* 121 (2014) 443–460.

[42] G. van Gorkom, B. Gijsbers, E.J. Ververs, A. El Molla, C. Sarodnik, C. Riess, W. Wodzig, G. Bos, C. Van Elssen, Easy-to-use HPLC method to measure intracellular ascorbic acid levels in human peripheral blood mononuclear cells and in plasma, *Antioxidants* 11 (2022) 134.

[43] M.M. Kamel, E.M. Abdalla, M.S. Ibrahim, Y.M. Temerk, Electrochemical studies of ascorbic acid, dopamine, and uric acid at a DL-norvaline-deposited glassy carbon electrode, *Can. J. Chem*. 92 (2014) 329–336.

[44] D. Liu, Y. Yun, D. Yang, X. Hu, X. Dong, N. Zhang, L. Zhang, H. Yin, W. Duan, What is the biological function of uric acid? An antioxidant for neural protection or a biomarker for cell death, *Dis. Markers* 2019 (2019) 4081962.

[45] Q. Yan, N. Zhi, L. Yang, G. Xu, Q. Feng, Q. Zhang, S. Sun, A highly sensitive uric acid electrochemical biosensor based on a nano-cube cuprous oxide/ferrocene/uricase modified glassy carbon electrode, *Sci. Rep*. 10 (2020) 10607.

[46] B. Öndeş, S. Evli, Y. Şahin, M. Uygun, D.A. Uygun, Uricase based amperometric biosensor improved by AuNPs-TiS_2 nanocomposites for uric acid determination, *Microchem. J.* 181 (2022) 107725.

[47] W. Boumya, N. Taoufik, M. Achak, H. Bessbousse, A. Elhalil, N. Barka, Electrochemical sensors and biosensors for the determination of diclofenac in pharmaceutical, biological and water samples, *Talanta Open* 3 (2021) 100026.

[48] N. Vieno, M. Sillanpää, Fate of diclofenac in municipal wastewater treatment plant - A review, *Environ. Int.* 69 (2014) 28–39.

[49] R. Becker, Cattle drug threatens thousands of vultures, *Nature* (2016) 19839.

[50] Council of Europe European Pharmacopoeia Commission European Directorate for the Quality of Medicines & Healthcare, Diclofenac Sodium, *European Pharmacopoeia*. 7th ed. Strasbourg: Council Of Europe: European Directorate for the Quality of Medicines and Healthcare (2010).

[51] The United States pharmacopeia. The National formulary DCF. *Rockville, Md.:United States Pharmacopeial Convention, Inc*. (1979).

[52] G.Y. Aguilar-Lira, G.A. Álvarez-Romero, A. Zamora-Suárez, M. Palomar-Pardavé, A. Rojas-Hernández, J.A. Rodríguez-Ávila, M.E. Páez-Hernández, New insights on diclofenac electrochemistry using graphite as working electrode, *J. Electroanal. Chem.* 794 (2017) 182–188.

[53] F. Nadeem, J. Mandon, A. Khodabakhsh, S.M. Cristescu, F.J.M. Harren, Sensitive spectroscopy of acetone using a widely tunable external-cavity quantum cascade laser, *Sensors* 18 (2018) 2050.

[54] F. Duša, W. Chen, J. Witos, S.K. Wiedmer, Nanoplasmonic sensing and capillary electrophoresis for fast screening of interactions between phosphatidylcholine biomembranes and surfactants, *Langmuir* 34 (2018) 5889–5900.

[55] S. Xu, Y. Wang, D. Zhou, M. Kuang, D. Fang, W. Yang, S. Wei, L. Ma, A novel chemiluminescence sensor for sensitive detection of cholesterol based on the peroxidase-like activity of copper nanoclusters, *Sci. Rep*. 6 (2016) 39157.

[56] Z. Yaneva, N. Georgieva, Physicochemical and morphological characterization of pharmaceutical nanocarriers and mathematical modeling of drug encapsulation/release mass transfer processes, Nanoscale Fabrication, Optimization, Scale-up and Biological Aspects of Pharmaceutical Nanotechnology, *William Andrew Applied Science Publishers* (2017) 173–218.

[57] A. Hulanicki, S. Głab, F Ingman, Chemical sensors definitions and classification, *Pure & Appl. Chem*. 63 (1991) 1247-1250.

[58] L. Mariaamoretto, K. Editors, Environmental Analysis by Electrochemical Sensors and Biosensors, Volume 2: Applications, *Springer* London (2014).

[59] Y. Song, C. Xu, H. Kuroki, Y. Liao, M. Tsunoda, Recent trends in analytical methods for the determination of amino acids in biological samples, *J. Pharm. Biomed. Anal*. 147 (2018) 35–49.

[60] V.S. Bagot͡skiĭ, Fundamentals of electrochemistry, *John Wiley & Sons*. New York (2006).

[61] A. Kisza, Elektrochemia Elektrodyka II, *Wydawnictwo Naukowo Techniczne*. Warszawa (2001).

[62] B. Schumm, Encyclopedia of Applied Electrochemistry, *Springer* New York (2014).

[63] G. Canciani, Y. Davrain, M. Crozet, D. Roudil, S. Picart, Controlled Potential Coulometry for the accurate determination of plutonium in the presence of uranium: The role of sulfate complexation, *Talanta* 222 (2021) 121490.

[64] T. Trapp, B. Ross, K. Cammann, E. Schirmer, C. Berthold, Development of a coulometric CO_2 gas sensor, *Sens. Actuators B Chem*. 50 (1998) 97-103.

[65] S. Dzyadevych, N. Jaffrezic-Renault, Conductometric biosensors, in: Biological Identification: DNA Amplification and Sequencing, Optical Sensing, Lab-On-Chip and Portable Systems, *Elsevier* (2014) 153–193.

[66] P. Bharathi, S. Harish, M. Shimomura, S. Ponnusamy, M. Krishna Mohan, J. Archana, M. Navaneethan, Conductometric NO_2 gas sensor based on Co-incorporated MoS_2 nanosheets for room temperature applications, *Sens. Actuators B Chem*. 360 (2022) 131600.

[67] S. Halley, K.P. Ramaiyan, L. kun Tsui, F. Garzon, A review of zirconia oxygen, NO_x, and mixed potential gas sensors – History and current trends, *Sens. Actuators B Chem*. 370 (2022) 132363.

[68] H.J. Park, J.H. Yoon, K.G. Lee, B.G. Choi, Potentiometric performance of flexible pH sensor based on polyaniline nanofiber arrays, *Nano Converg*. 6 (2019) 9.

[69] J. Heyrovský, Polarographisches Praktikum, *Springer* Berlin, Heidelberg, (1960).

[70] J.E. Page, Applications of polarography in pharmaceutical analysis, *JPP* 4 (1952) 1-20.

[71] S. Chelly, M. Chelly, R. Zribi, R. Gdoura, H. Bouaziz-Ketata, G. Neri, Electrochemical detection of dopamine and riboflavine on a screen-printed carbon electrode modified by AuNPs derived from rhanterium suaveolens plant extract, *ACS Omega* 6 (2021) 23666–23675.

[72] F.R. Simões, M.G. Xavier, Electrochemical Sensors, Nanoscience and its Applications, *William Andrew* Norwich (2017).

[73] M. Mostafavi, M.R. Yaftian, F. Piri, H. Shayani-Jam, A new diclofenac molecularly imprinted electrochemical sensor based upon a polyaniline/reduced graphene oxide nano-composite, *Biosens. Bioelectron*. 122 (2018) 160–167.

[74] J. Cai, B. Sun, X. Gou, Y. Gou, W. Li, F. Hu, A novel way for analysis of calycosin via polyaniline functionalized graphene quantum dots fabricated electrochemical sensor, *J. Electroanal. Chem*. 816 (2018) 123–131.

[75] S.A. Hashemi, S. Bahrani, S.M. Mousavi, N. Omidifar, M. Arjmand, K.B. Lankarani, S. Ramakrishna, Simultaneous electrochemical detection of Cd and Pb in aquatic samples via coupled graphene with brominated white polyaniline flakes, *Eur. Polym. J*. 162 (2022) 110926.

[76] F. Tian, H. Li, M. Li, C. Li, Y. Lei, B. Yang, Synthesis of one-dimensional poly(3,4-ethylenedioxythiophene)-graphene composites for the simultaneous detection of hydroquinone, catechol, resorcinol, and nitrite, *Synth. Met*. 226 (2017) 148–156.

[77] L. Gao, R. Yue, J. Xu, Z. Liu, J. Chai, Pt-PEDOT/rGO nanocomposites: One-pot preparation and superior electrochemical sensing performance for caffeic acid in tea, *J. Electroanal. Chem.*. 816 (2018) 14–20.

[78] V. Beni, M. Ghita, D.W.M. Arrigan, Cyclic and pulse voltammetric study of dopamine at the interface between two immiscible electrolyte solutions, *Biosens. Bioelectron, Elsevier*. (2005) 2097–2103.

[79] P. Abraham, R. S, P. Vijayan, N. V, K. Sreevalsan, V. Anithakumary, Review on the progress in electrochemical detection of morphine based on different modified electrodes, *J. Electrochem. Soc.* 167 (2020) 037559.

[80] M. Mehrvar, M. Abdi, Recent developments, characteristics, and potential applications of electrochemical biosensors, *Anal. Sci*. 20 (2014) 1113-1125.

[81] Y. Yi, G. Weinberg, M. Prenzel, M. Greiner, S. Heumann, S. Becker, R. Schlögl, Electrochemical corrosion of a glassy carbon electrode, *Catal. Today* 295 (2017) 32–40.

[82] A.M. Abdel-Aziz, H.H. Hassan, I.H.A. Badr, Glassy carbon electrode electromodification in the presence of organic monomers: electropolymerization versus activation, *Anal. Chem*. 92 (2020) 7947–7954.

[83] J.D. Benck, B.A. Pinaud, Y. Gorlin, T.F. Jaramillo, Substrate selection for fundamental studies of electrocatalysts and photoelectrodes: Inert potential windows in acidic, neutral, and basic electrolyte, *PLoS One* 9 (2014) e0127338.

[84] K. Kordek, H. Yin, P. Rutkowski, H. Zhao, Cobalt-based composite films on electrochemically activated carbon cloth as high performance overall water splitting electrodes, *Int. J. Hydrogen Energy* 44 (2019) 23–33.

[85] M. Li, Y.T. Li, D.W. Li, Y.T. Long, Recent developments and applications of screen-printed electrodes in environmental assays-A review, *Anal. Chim. Acta*. 734 (2012) 31–44.

[86] Y. Gao, X. Guo, Z. Qiu, G. Zhang, R. Zhu, Y. Zhang, H. Pang, Printable electrode materials for supercapacitors, *ChemPhysMater*. 1 (2022) 17–38.

[87] S. Bhattacharya, A. Kumar, A. Nripen, C.A. Pandey, A. Kumar, S. Editors, Environmental, Chemical and Medical Sensors Energy, Environment, and Sustainability, *Springer* Singapore (2018).

[88] R.P. Tortorich, E. Song, J.-W. Choi, Inkjet-Printed Carbon Nanotube Electrodes with Low Sheet Resistance for Electrochemical Sensor Applications, *J. Electrochem. Soc*. 161 (2014) 3044–3048.

[89] K.S. Novoselov, V.I. Fal'Ko, L. Colombo, P.R. Gellert, M.G. Schwab, K. Kim, A roadmap for graphene, *Nature* 490 (2012) 192–200.

[90] H. Kim, A.A. Abdala, C.W. MacOsko, Graphene/polymer nanocomposites, *Macromolecules* 43 (2010) 6515–6530.

[91] A. Huczko, A. Dąbrowska, M. Kurcz, Grafen otrzymywanie charakterystyka właściwości, *Wydawnictwo UW* Warszawa (2016).

[92] Ł. Smędowski, R. Muzyka, Grafen-metody otrzymywania a zastosowanie i właściwości, *Karbo* 2 (2013) 128-136.

[93] N. Mishra, J. Boeckl, N. Motta, F. Iacopi, Graphene growth on silicon carbide: A review, *PSS (A)* 213 (2016) 2277–2289.

[94] P.R. Somani, S.P. Somani, M. Umeno, Planer nano-graphenes from camphor by CVD, *Chem. Phys. Lett*. 430 (2006) 56–59.

[95] A.A. Moosa, M.S. Abed, Graphene preparation and graphite exfoliation, *Turk. J. Chem*. 45 (2021) 493–519.

[96] H. Thiele, Die quellung des graphit an der anode und die mechanische zerstörung von kohleanoden, *Z. Elektrochem*. 40 (1934) 26–33.

[97] A. Siklitskaya, E. Gacka, D. Larowska, M. Mazurkiewicz-Pawlicka, A. Malolepszy, L. Stobiński, B. Marciniak, A. Lewandowska-Andrałojć, A. Kubas, Lerf–Klinowski-type models of graphene oxide and reduced graphene oxide are robust in analyzing non-covalent functionalization with porphyrins. *Sci. Rep*. 11 (2021) 7977.

[98] F. Liu, C. Wang, X. Sui, M.A. Riaz, M. Xu, L. Wei, Y. Chen, Synthesis of graphene materials by electrochemical exfoliation: Recent progress and future potential, *Carbon Energy* 1 (2019) 173–199.

[99] J. Zhang, Chemically derived graphene, functionalization, properties and applications, *RSC* (2013).

[100] A. M. Dimiev, S. Eigler (2016) Graphene oxide fundamentals and applications, *Willey* (2017).

[101] Z. Ismail, Green reduction of graphene oxide by plant extracts: A short review, *Ceram. Int.* 45 (2019) 23857–23868.

[102] A. Paudics, S. Farah, I. Bertóti, A. Farkas, K. László, M. Mohai, G. Sáfrán, A. Szilágyi, M. Kubinyi, Fluorescence probing of binding sites on graphene oxide nanosheets with Oxazine 1 dye, *Appl. Surf. Sci*. 541 (2021)148451.

[103] A. Jiříčková, O. Jankovský, Z. Sofer, D. Sedmidubský, Synthesis and applications of graphene oxide, *Materials* 15 (2022) 920.

[104] K.K.H. De Silva, H.H. Huang, M. Yoshimura, Progress of reduction of graphene oxide by ascorbic acid, *Appl. Surf. Sci*. 447 (2018) 338–346.

[105] H. Tong, J. Zhu, J. Chen, Y. Han, S. Yang, B. Ding, X. Zhang, Electrochemical reduction of graphene oxide and its electrochemical capacitive performance, *J. Solid State Electroch*. 17 (2013) 2857–2863.

[106] A. Zhou, J. Bai, W. Hong, H. Bai, Electrochemically reduced graphene oxide: Preparation, composites, and applications, *Carbon* 191 (2022) 301–332.

[107] M.J. McAllister, J.L. Li, D.H. Adamson, H.C. Schniepp, A.A. Abdala, J. Liu, M. Herrera-Alonso, D.L. Milius, R. Car, R.K. Prud'homme, I.A. Aksay, Single sheet functionalized graphene by oxidation and thermal expansion of graphite, *Chem. Mater*. 19 (2007) 4396–4404.

[108] S. Pei, H.M. Cheng, The reduction of graphene oxide, *Carbon* 50 (2012) 3210–3228.

[109] P. Álvarez, C. Blanco, R. Santamaría, P. Blanco, Z. González, L. Fernández-García, U. Sierra, M. Granda, A. Páez, R. Menéndez, Tuning graphene properties by a multi-step thermal reduction process, *Carbon* 90 (2015) 160–163.

[110] N. Díez, A. Śliwak, S. Gryglewicz, B. Grzyb, G. Gryglewicz, Enhanced reduction of graphene oxide by high-pressure hydrothermal treatment, *RSC Adv*. 5 (2015) 81831–81837.

[111] H.H. Huang, K.K.H. De Silva, G.R.A. Kumara, M. Yoshimura, Structural Evolution of Hydrothermally Derived Reduced Graphene Oxide, *Sci. Rep*. 8 (2018) 6849.

[112] M.R. Thalji, G.A. M Ali, S. Poh Lee, K. Feng Chong, Solvothermal synthesis of reduced graphene oxide as electrode material for supercapacitor application nanomaterials for energy storage applications, *Chem. Adv. Mater*. 4 (2019) 17-26.

[113] Y. Hu, C. Zhou, H. Wang, M. Chen, G. Zeng, Z. Liu, Y. Liu, W. Wang, T. Wu, B. Shao, Q. Liang, Recent advance of graphene/semiconductor composite nanocatalysts: Synthesis, mechanism, applications and perspectives, *Chem. Eng. J.* 414 (2021)128795.

[114] H.N. Tien, V.H. Luan, T.K. Lee, B.S. Kong, J.S. Chung, E.J. Kim, S.H. Hur, Enhanced solvothermal reduction of graphene oxide in a mixed solution of sulfuric acid and organic solvent, *Chem. Eng. J.*. 211–212 (2012) 97–103.

[115] S. Kaushal, M. Kaur, N. Kaur, V. Kumari, P.P. Singh, Heteroatom-doped graphene as sensing materials: A mini review, *RSC Adv*. 10 (2020) 28608–28629.

[116] X. Wang, G. Sun, P. Routh, D.H. Kim, W. Huang, P. Chen, Heteroatom-doped graphene materials: Syntheses, properties and applications, *Chem Soc Rev*. 43 (2014) 7067–7098.

[117] M. Inagaki, M. Toyoda, Y. Soneda, T. Morishita, Nitrogen-doped carbon materials, *Carbon* 132 (2018) 104–140.

[118] N. M. Santhosh, G. Filipič, E. Kovacevic, A. Jagodar, J. Berndt, T. Strunskus, H. Kondo, M. Hori, E. Tatarova, U. Cvelbar, N-graphene nanowalls via plasma nitrogen incorporation and substitution: the experimental evidence, *Nanomicro. Lett*. 12 (2020) 53.

[119] W.S. Jeon, C.H. Kim, J.H. Wee, J.H. Kim, Y.A. Kim, C.M. Yang, Sulfur-doping effects on the supercapacitive behavior of porous spherical graphene electrode derived from layered double hydroxide template, *Appl. Surf. Sci*. 558 (2021) 149867.

[120] Y. Tian, Z. Wei, K. Zhang, S. Peng, X. Zhang, W. Liu, K. Chu, Three-dimensional phosphorus-doped graphene as an efficient metal-free electrocatalyst for electrochemical sensing, *Sens. Actuators B Chem*. 241 (2017) 584–591.

[121] P. Wiench, Z. González, S. Gryglewicz, R. Menéndez, G. Gryglewicz, Enhanced performance of pyrrolic N-doped reduced graphene oxide-modified glassy carbon electrodes for dopamine sensing, *J. Electroanal. Chem*. 852 (2019). 113547.

[122] P. Wiench, Z. González, R. Menéndez, B. Grzyb, G. Gryglewicz, Beneficial impact of oxygen on the electrochemical performance of dopamine sensors based on N-doped reduced graphene oxides, *Sens. Actuators B Chem*. 257 (2018) 143–153.

[123] D. Wei, Y. Liu, Y. Wang, H. Zhang, L. Huang, G. Yu, Synthesis of n-doped graphene by chemical vapor deposition and its electrical properties, *Nano Lett*. 9 (2009) 1752–1758.

[124] G. Deokar, J. Jin, U. Schwingenschlögl, P.M.F.J. Costa, Chemical vapor deposition-grown nitrogen-doped graphene's synthesis, characterization and applications, NPJ 2D *Mater. Appl*. 6 (2022) 14.

[125] A. Jafari, M. Ghoranneviss, A. Salar Elahi, Growth and characterization of boron doped graphene by Hot Filament Chemical Vapor Deposition Technique (HFCVD), *J. Cryst. Growth*. 438 (2016) 70–75.

[126] W. Norimatsu, K. Matsuda, T.O. Terasawa, N. Takata, A. Masumori, K. Ito, K. Oda, T. Ito, A. Endo, R. Funahashi, M. Kusunoki, Controlled growth of boron-doped epitaxial graphene by thermal decomposition of a B_4C thin film, *Nanotechnology* 31 (2020) 145711.

[127] D. Long, W. Li, L. Ling, J. Miyawaki, I. Mochida, S.H. Yoon, Preparation of nitrogen-doped graphene sheets by a combined chemical and hydrothermal reduction of graphene oxide, *Langmuir* 26 (2010) 16096–16102.

[128] B. Grzyb, S. Gryglewicz, A. Śliwak, N. Díez, J. Machnikowski, G. Gryglewicz, Guanidine, amitrole and imidazole as nitrogen dopants for the synthesis of N-graphenes, *RSC Adv*. 6 (2016) 15782–15787.

[129] C. Zhang, N. Mahmood, H. Yin, F. Liu, Y. Hou, Synthesis of phosphorus-doped graphene and its multifunctional applications for oxygen reduction reaction and lithium ion batteries, *Adv. Mater*. 25 (2013) 4932–4937.

[130] Y. Wen, B. Wang, C. Huang, L. Wang, D. Hulicova-Jurcakova, Synthesis of phosphorus-doped graphene and its wide potential window in aqueous supercapacitors, *Chem. Eur. J*. 21 (2015) 80–85.

[131] S. Yoo, S.Y. Jeong, J.W. Lee, J.H. Park, D.W. Kim, H.J. Jeong, J.T. Han, G.W. Lee, S.Y. Jeong, Heavily nitrogen doped chemically exfoliated graphene by flash heating, *Carbon* 144 (2019) 675–683.

[132] K. Xia, Z. Huang, L. Zheng, B. Han, Q. Gao, C. Zhou, H. Wang, J. Wu, Facile and controllable synthesis of N/P co-doped graphene for high-performance supercapacitors, *J. Power Sources* 365 (2017) 380–388.

[133] X. Luo, A. Morrin, A.J. Killard, M.R. Smyth, Application of nanoparticles in electrochemical sensors and biosensors, *Electroanalysis* 18 (2006) 319–326.

[134] M.H. Naveen, N.G. Gurudatt, Y.B. Shim, Applications of conducting polymer composites to electrochemical sensors: A review, *Appl. Mater. Today* 9 (2017) 419–433.

[135] J. Polte, Fundamental growth principles of colloidal metal nanoparticles - a new perspective, *CrystEngComm*. 17 (2015) 6809–6830.

[136] C. Tan, X. Huang, H. Zhang, Synthesis and applications of graphene-based noble metal nanostructures, *Mater. Today* 16 (2013) 29–36.

[137] X. Cui, S. Wu, Y. Li, G.G. Wan, Sensing hydrogen peroxide using a glassy carbon electrode modified with in-situ electrodeposited platinum-gold bimetallic nanoclusters on a graphene surface, *Microchim. Acta* 182 (2015) 265–272.

[138] A. Benvidi, A. Dehghani-Firouzabadi, M. Mazloum-Ardakani, B.B.F. Mirjalili, R. Zare, Electrochemical deposition of gold nanoparticles on reduced graphene oxide modified glassy carbon electrode for simultaneous determination of levodopa, uric acid and folic acid, *J. Electroanal. Chem*. 736 (2015) 22–29.

[139] P. Bazylewski, A. Akbari-Sharbaf, S. Ezugwu, T. Ouyang, J. Park, G. Fanchini, Graphene thin films and graphene decorated with metal nanoparticles, in: crystalline and non-crystalline solids, *IntechOpen* (2016).

[140] M. Sookhakian, M.A. Mat Teridi, G.B. Tong, P.M. Woi, M. Khalil, Y. Alias, Reduced graphene oxide/copper nanoparticle composites as electrochemical sensor materials for nitrate detection, *ACS Appl. Nano Mater*. 4 (2021) 12737–12744.

[141] J. Li, J. Liu, G. Tan, J. Jiang, S. Peng, M. Deng, D. Qian, Y. Feng, Y. Liu, High-sensitivity paracetamol sensor based on Pd/graphene oxide nanocomposite as an enhanced electrochemical sensing platform, *Biosens. Bioelectron*. 54 (2014) 468–475.

[142] F. Zhang, S. Huang, Q. Guo, H. Zhang, H. Li, Y. Wang, J. Fu, X. Wu, L. Xu, M. Wang, One-step hydrothermal synthesis of Cu_2O/CuO hollow microspheres/reduced graphene oxide hybrid with enhanced sensitivity for non-enzymatic glucose sensing, *Colloids Surf. A Physicochem. Eng Asp*. 602 (2020) 125076.

[143] K. Namsheer, C.S. Rout, Conducting polymers: a comprehensive review on recent advances in synthesis, properties and applications, *RSC Adv*. 11 (2021) 5659–5697.

[144] M. Heydari Gharahcheshmeh, K.K. Gleason, Texture and nanostructural engineering of conjugated conducting and semiconducting polymers, *Mater. Today Adv*. 8 (2020) 100086.

[145] H. Behniafar, K. Malekshahinezhad, A. Alinia-pouri, One-pot methods for preparing polyaniline/Ag nanocomposites via oxidative polymerization of aniline, *J. Mater. Sci.: Mater. Electron*. 27 (2016) 1070–1076.

[146] S. Muralikrishna, D.H. Nagaraju, R.G. Balakrishna, W. Surareungchai, T. Ramakrishnappa, A.B. Shivanandareddy, Hydrogels of polyaniline with graphene oxide for highly sensitive electrochemical determination of lead ions, *Anal. Chim. Acta*. 990 (2017) 67–77.

[147] S.M. Naghib, F. Behzad, M. Rahmanian, Y. Zare, K.Y. Rhee, A highly sensitive biosensor based on methacrylated graphene oxide-grafted polyaniline for ascorbic acid determination, *Nanotechnol. Rev*. 9 (2020) 760–767.

[148] X. Wang, X. Gu, C. Yuan, S. Chen, P. Zhang, T. Zhang, J. Yao, F. Chen, G. Chen, Evaluation of biocompatibility of polypyrrole in vitro and in vivo, *J. Biomed. Mater. Res. A* 68 (2003) 411-22.

[149] Y. Yuan, T. Li, Z. Ye, Y. Feng, Z. Chen, Y. Wang, Y. Sun, H. Wu, Z. Yang, Y. Wang, Y. Zhang, L. Huang, B. Liang, A one-step electropolymerized biomimetic polypyrrole membrane-based electrochemical sensor for selective detection of valproate, *Front. Bioeng. Biotechnol*. 10 (2022) 851692.

[150] S.M. Oliveira, J.M. Luzardo, L.A. Silva, D.C. Aguiar, C.A. Senna, R. Verdan, A. Kuznetsov, T.L. Vasconcelos, B.S. Archanjo, C.A. Achete, E. D'Elia, J.R. Araujo, High-performance electrochemical sensor based on molecularly imprinted polypyrrole-graphene modified glassy carbon electrode, *Thin Solid Films* 699 (2020) 137875.

[151] J.A.L. Sánchez, R.P. Capilla, A.M. Díez-Pascual, High-performance PEDOT: PSS/hexamethylene diisocyanate-functionalized graphene oxide nanocomposites: Preparation and properties, *Polymers* 10 (2018) 1169.

[152] A. Wong, A.M. Santos, O. Fatibello-Filho, Determination of piroxicam and nimesulide using an electrochemical sensor based on reduced graphene oxide and PEDOT:PSS, *J. Electroanal. Chem*. 799 (2017) 547–555.

[153] X. Huang, W. Shi, J. Li, N. Bao, C. Yu, H. Gu, Determination of salivary uric acid by using poly(3,4-ethylenedioxythipohene) and graphene oxide in a disposable paper-based analytical device, *Anal. Chim. Acta*. 1103 (2020) 75–83.

[154] B. Demirkan, S. Bozkurt, K. Cellat, K. Arıkan, M. Yılmaz, A. Şavk, M.H. Çalımlı, M.S. Nas, M.N. Atalar, M.H. Alma, F. Sen, Palladium supported on polypyrrole/reduced graphene oxide nanoparticles for simultaneous biosensing application of ascorbic acid, dopamine, and uric acid, *Sci. Rep*. 10 (2020) 2946.

[155] G. Chen, J. Zheng, Non-enzymatic electrochemical sensor for nitrite based on a graphene oxide–polyaniline–Au nanoparticles nanocomposite, *Microchem. J*. 164 (2021) 106034.

[156] M. Li, W. Wang, Z. Chen, Z. Song, X. Luo, Electrochemical determination of paracetamol based on Au@graphene core-shell nanoparticles doped conducting polymer PEDOT nanocomposite, *Sens. Actuators B Chem*. 260 (2018) 778–785.

[157] S. Liu, X. Jiang, G.I.N. Waterhouse, Z.M. Zhang, L. min Yu, A Cu_2O/PEDOT/graphene-modified electrode for the enzyme-free detection and quantification of glucose, *J. Electroanal. Chem*. 897 (2021) 115558.

[158] S. Radhakrishnan, K. Krishnamoorthy, C. Sekar, J. Wilson, S.J. Kim, A promising electrochemical sensing platform based on ternary composite of polyaniline-Fe_2O_3-reduced graphene oxide for sensitive hydroquinone determination, *Chem. Eng. J*. 259 (2015) 594–602.

[159] R. Salahandish, A. Ghaffarinejad, S.M. Naghib, A. Niyazi, K. Majidzadeh-A, M. Janmaleki, A. Sanati-Nezhad, Sandwich-structured nanoparticles-grafted functionalized graphene based 3D nanocomposites for high-performance biosensors to detect ascorbic acid biomolecule, *Sci. Rep*. 9 (2019) 1226.

[160] Z. Liao, Y. Ma, S. Yao, J. Zhang, Y. Han, K. Xu, Honeycomb-patterned porous graphene film for electrochemical detection of dopamine, *Appl. Surf. Sci*. 605 (2022) 154725.

[161] Y.S. Hsieh, B. De Hong, C.L. Lee, Non-enzymatic sensing of dopamine using a glassy carbon electrode modified with a nanocomposite consisting of palladium nanocubes supported on reduced graphene oxide in a nafion matrix, *Microchim. Acta* 183 (2016) 905–910.

[162] R. Santhosh Kumar, K. Govindan, S. Ramakrishnan, A.R. Kim, J.S. Kim, D.J. Yoo, Fe_3O_4 nanorods decorated on polypyrrole/reduced graphene oxide for electrochemical detection of dopamine and photocatalytic degradation of acetaminophen, *Appl. Surf. Sci*. 556 (2021) 149765.

[163] C. Karuppiah, S. Cheemalapati, S.M. Chen, S. Palanisamy, Carboxyl-functionalized graphene oxide-modified electrode for the electrochemical determination of nonsteroidal anti-inflammatory drug diclofenac, *Ionics* 21 (2015) 231–238.

[164] K. Kimuam, N. Rodthongkum, N. Ngamrojanavanich, O. Chailapakul, N. Ruecha, Single step preparation of platinum nanoflowers/reduced graphene oxide electrode as a novel platform for diclofenac sensor, *Microchem. J.* 155 (2020) 104744.

[165] S.P. Nayak, S.S. Ramamurthy, J.K. Kiran Kumar, Green synthesis of silver nanoparticles decorated reduced graphene oxide nanocomposite as an electrocatalytic platform for the simultaneous detection of dopamine and uric acid, *Mater. Chem. Phys*. 252 (2020) 2020.123302.

[166] R. Chen, Y. Wang, Y. Liu, J. Li, Selective electrochemical detection of dopamine using nitrogen-doped graphene/manganese monoxide composites, *RSC Adv*. 5 (2015) 85065–85072.

[167] A. Kader Mohiuddin, M. Shamsuddin Ahmed, S. Jeon, Palladium doped α-MnO_2 nanorods on graphene as an electrochemical sensor for simultaneous determination of dopamine and paracetamol, *Appl. Surf. Sci*. 578 (2022) 152090.

[168] H. wei Yu, J. hui Jiang, Z. Zhang, G. cai Wan, Z. yong Liu, D. Chang, H. zhi Pan, Preparation of quantum dots CdTe decorated graphene composite for sensitive detection of uric acid and dopamine, *Anal. Biochem*. 519 (2017) 92–99.

[169] Z. Yang, X. Liu, X. Zheng, J. Zheng, Synthesis of Au@Pt nanoflowers supported on graphene oxide for enhanced electrochemical sensing of dopamine, *J. Electroanal. Chem*. 817 (2018) 48–54.

[170] K. Zhang, X. Chen, Z. Li, Y. Wang, S. Sun, L. Wang, T. Guo, D. Zhang, Z. Xue, X. Zhou, X. Lu, Au-Pt bimetallic nanoparticles decorated on sulfonated nitrogen sulfur co-doped graphene for simultaneous determination of dopamine and uric acid, *Talanta* 178 (2018) 315–323.

[171] Q. He, J. Liu, X. Liu, G. Li, P. Deng, J. Liang, Preparation of Cu_2O-reduced graphene nanocomposite modified electrodes towards ultrasensitive dopamine detection, *Sensors* 18 (2018) 199.

[172] D. Muthu, R. Govindaraj, M. Manikandan, P. Ramasamy, Y. Haldorai, R.T. Rajendra Kumar, Reduced graphene oxide supported monoclinic bismuth vanadate nanoparticles as an

electrocatalyst for selective determination of dopamine in human urine samples, *Mater. Chem. Phys*. 297 (2023) 127437.

[173] M. Gu, H. Xiao, S. Wei, Z. Chen, L. Cao, A portable and sensitive dopamine sensor based on AuNPs functionalized ZnO-rGO nanocomposites modified screen-printed electrode, *J. Electroanal. Chem*. 908 (2022) 116117.

[174] P. Manivel, M. Dhakshnamoorthy, A. Balamurugan, N. Ponpandian, D. Mangalaraj, C. Viswanathan, Conducting polyaniline-graphene oxide fibrous nanocomposites: Preparation, characterization and simultaneous electrochemical detection of ascorbic acid, dopamine and uric acid, *RSC Adv*. 3 (2013) 14428–14437.

[175] X. Chen, D. Li, W. Ma, T. Yang, Y. Zhang, D. Zhang, Preparation of a glassy carbon electrode modified with reduced graphene oxide and overoxidized electropolymerized polypyrrole, and its application to the determination of dopamine in the presence of ascorbic acid and uric acid, *Microchim. Acta*. 186 (2019) 407.

[176] Z. Rui, W. Huang, Y. Chen, K. Zhang, Y. Cao, J. Tu, Facile synthesis of graphene/polypyrrole 3D composite for a high-sensitivity non-enzymatic dopamine detection, *J. Appl. Polym. Sci*. 134 (2017) 44840.

[177] H. Teng, J. Song, G. Xu, F. Gao, X. Luo, Nitrogen-doped graphene and conducting polymer PEDOT hybrids for flexible supercapacitor and electrochemical sensor, *Electrochim. Acta* 355 (2020) 136772.

[178] G. Xu, Z.A. Jarjes, V. Desprez, P.A. Kilmartin, J. Travas-Sejdic, Sensitive, selective, disposable electrochemical dopamine sensor based on PEDOT-modified laser scribed graphene, *Biosens. Bioelectron*. 107 (2018) 184–191.

[179] S.H. Ko, S.W. Kim, Y.J. Lee, Flexible sensor with electrophoretic polymerized graphene oxide/PEDOT:PSS composite for voltammetric determination of dopamine concentration, *Sci. Rep*. 11 (2021) 21101.

[180] P. Sundaresan, T.Y. Lee, Facile synthesis of exfoliated graphite-supported cobalt ferrite (Co1.2Fe1.8O4) nanocomposite for the electrochemical detection of diclofenac, *Microchem. J*. 181 (2022) 107777.

[181] B. Mekassa, P.G.L. Baker, B.S. Chandravanshi, M. Tessema, Synthesis, characterization, and preparation of nickel nanoparticles decorated electrochemically reduced graphene oxide modified electrode for electrochemical sensing of diclofenac, *J. Solid State Electrochem*. 22 (2018) 3607–3619.

[182] O.K. Okoth, K. Yan, L. Liu, J. Zhang, Simultaneous electrochemical determination of paracetamol and diclofenac based on poly(diallyldimethylammonium chloride) functionalized graphene, *Electroanalysis* 28 (2016) 76–82.

[183] M.M. El-Wekil, S.A. Alkahtani, H.R.H. Ali, A.M. Mahmoud, Advanced sensing nanomaterials based carbon paste electrode for simultaneous electrochemical measurement of esomeprazole and diclofenac sodium in human serum and urine samples, *J. Mol. Liq*. 262 (2018) 495–503.

[184] W.S. Hummers, R.E. Offeman, Preparation of Graphitic Oxide, *J. Am. Chem. Soc*. 80 (1958) 11339.

[185] A. Moyseowicz, G. Gryglewicz, Hydrothermal-assisted synthesis of a porous polyaniline/reduced graphene oxide composite as a high-performance electrode material for supercapacitors, *Compos. B Eng*. 159 (2019) 4–12.

[186] S. Chutipongtanate, V. Thongboonkerd, Systematic comparisons of artificial urine formulas for in vitro cellular study, *Anal. Biochem*. 402 (2010) 110–112.

[187] H. Zhang, T. Kuila, N.H. Kim, D.S. Yu, J.H. Lee, Simultaneous reduction, exfoliation, and nitrogen doping of graphene oxide via a hydrothermal reaction for energy storage electrode materials, *Carbon* 69 (2014) 66–78.

[188] M. Gao, Y. Xu, X. Wang, Y. Sang, S. Wang, Analysis of electrochemical reduction process of graphene oxide and its electrochemical behavior, *Electroanalysi*s 28 (2016) 1377–1382.

[189] X.Y. Peng, X.X. Liu, D. Diamond, K.T. Lau, Synthesis of electrochemically-reduced graphene oxide film with controllable size and thickness and its use in supercapacitor, *Carbon* 49 (2011) 3488–3496.

[190] M. Song, J. Xu, C. Wu, The effect of surface functionalization on the immobilization of gold nanoparticles on graphene sheets, *J. Nanotechnol*. 2012 (2012) 329318.

[191] L. Sun, L. Wang, C. Tian, T. Tan, Y. Xie, K. Shi, M. Li, H. Fu, Nitrogen-doped graphene with high nitrogen level via a one-step hydrothermal reaction of graphene oxide with urea for superior capacitive energy storage, *RSC Adv*. 2 (2012) 4498–4506.

[192] D. Mollenhauer, N. Gaston, E. Voloshina, B. Paulus, Interaction of pyridine derivatives with a gold (111) surface as a model for adsorption to large nanoparticles, *J. Phys. Chem. C*. 117 (2013) 4470–4479.

[193] S.W. Moon, J.W. Ha, Influence of the capping material on pyridine-induced chemical interface damping in single gold nanorods, *Analyst*. 144 (2019) 2679–2683.

[194] K. Bera, S. Maiti, M. Maity, C. Mandal, N.C. Maiti, Porphyrin-Gold Nanomaterial for Efficient Drug Delivery to Cancerous Cells, *ACS Omega* 3 (2018) 4602–4619.

[195] Z. Hnatejko, Complexes of d-and f-metal ions with pyridine n-oxide and its derivatives: spectroscopic studies. *Wiad. Chem*. 65 (2011) 5-6.

[196] J.-P. Sylvestre, A. V. Kabashin, E. Sacher, M. Meunier, J.H.T. Luong, Nanoparticle size reduction during laser ablation in aqueous solutions of cyclodextrins, *Proc. SPIE*. 5339 (2004) 84-92.

[197] E. Taer, A. Agustino, R. Farma, R. Taslim, Awitdrus, M. Paiszal, A. Ira, S.D. Yardi, Y.P. Sari, H. Yusra, S. Nurjanah, S.D. Hartati, Z. Aini, R.N. Setiadi, The relationship of surface area to

cell capacitance for monolith carbon electrode from biomass materials for supercapacitor aplication, *J. Phys. Conf. Ser*. 1116 (2018) e32040.

[198] Y.C. Yeh, B. Creran, V.M. Rotello, Gold nanoparticles: preparation, properties, and applications in bionanotechnology, *Nanoscale* 4 (2012) 1871–1880.

[199] P. Muñoz, S. Huenchuguala, I. Paris, J. Segura-Aguilar, Dopamine oxidation and autophagy. *Parkinsons Dis*. 2012 (2012) 920953.

[200] S. Sundar, G. Venkatachalam, S.J. Kwon, Biosynthesis of copper oxide (CuO) nanowires and their use for the electrochemical sensing of dopamine, *Nanomaterial*s 8 (2018) 823.

[201] K.Y. Chan, D. Yang, B. Demir, A.P. Mouritz, H. Lin, B. Jia, K.T. Lau, Boosting the electrical and mechanical properties of structural dielectric capacitor composites via gold nanoparticle doping, *Compos. B Eng*. 178 (2019) 107480.

[202] J. Li, C.L. Sun, P. An, X. Liu, R. Dong, J. Sun, X. Zhang, Y. Xie, C. Qin, W. Zheng, H.L. Zhang, X. Jiang, Construction of Dopamine-Releasing Gold Surfaces Mimicking Presynaptic Membrane by On-Chip Electrochemistry, *J. Am. Chem. Soc*. 141 (2019) 8816–8824.

[203] E. Peltola, S. Sainio, K.B. Holt, T. Palomäki, J. Koskinen, T. Laurila, Electrochemical Fouling of Dopamine and Recovery of Carbon Electrodes, *Anal. Chem*. 90 (2018) 1408–1416.

[204] J. Clayden, N. Greeves, S. Warren, Organic chemistry. https://learninglink.oup.com/access/clayden2e, Accessed 15 May 2023.

[205] Y. Wang, L. Zhang, Recent developments in the chemistry of heteroaromatic N-oxides, *Synthesis* 47 (2015) 289-305.

[206] J. Zhang, C. Zhao, N. Liu, H. Zhang, J. Liu, Y.Q. Fu, B. Guo, Z. Wang, S. Lei, P.A. Hu, Tunable electronic properties of graphene through controlling bonding configurations of doped nitrogen atoms, *Sci. Rep*. 6 (2016) 28330.

[207] H. Cai, C. Xu, P. He, Y. Fang, Colloid Au-enhanced DNA immobilization for the electrochemical detection of sequence-specific DNA, *J. Electroanal. Chem.* 510 (2001) 78-85.

[208] W. Lyu, M. Yu, J. Feng, W. Yan, Facile synthesis of coral-like hierarchical polyaniline micro/nanostructures with enhanced supercapacitance and adsorption performance, *Polymer* 162 (2019) 130–138.

[209] C. Botas, P. Álvarez, C. Blanco, R. Santamaría, M. Granda, M.D. Gutiérrez, F. Rodríguez-Reinoso, R. Menéndez, Critical temperatures in the synthesis of graphene-like materials by thermal exfoliation-reduction of graphite oxide, *Carbon* 52 (2013) 476–485.

[210] A. Moyseowicz, Z. González, R. Menéndez, G. Gryglewicz, Three-dimensional poly(aniline-co-pyrrole)/thermally reduced graphene oxide composite as a binder-free electrode for high-performance supercapacitors, *Compos. B Eng*. 145 (2018) 232–239.

[211] I. Sengupta, S. Chakraborty, M. Talukdar, S.K. Pal, S. Chakraborty, Thermal reduction of graphene oxide: How temperature influences purity, *J. Mater. Res*. 33 (2018) 4113–4122.

[212] S. Golczak, A. Kanciurzewska, M. Fahlman, K. Langer, J.J. Langer, Comparative XPS surface study of polyaniline thin films, *Solid State Ion*. 179 (2008) 2234–2239.

[213] R. Dziembaj, Z. Piwowarska, X-ray photoelectron spectroscopy (XPS) as a useful tool to characterize polyaniline doped by 12-tungstosilicic, 12-tungstophosphoric and 12-molybdophosphoric acids, *Synth. Met*. 63 (1994) 225-232.

[214] J. Feng, Q. Li, J. Cai, T. Yang, J. Chen, X. Hou, Electrochemical detection mechanism of dopamine and uric acid on titanium nitride-reduced graphene oxide composite with and without ascorbic acid, *Sens. Actuators B Chem*. 298 (2019) 126872.

[215] S. Mahalakshmi, V. Sridevi, In situ electrodeposited gold nanoparticles on polyaniline-modified electrode surface for the detection of dopamine in presence of ascorbic acid and uric acid, *Electrocatalysis* 12 (2021) 415–435.

[216] F. Scholz, Electroanalytical Methods Guide to Experiments and Applications 2nd, *Springer* (2010).

[217] Y. Li, Z. Wang, Q. Wang, C. Wang, G. Xue, A facile and efficient route for coating polyaniline onto positively charged substrate, *Macromolecules* 43 (2010) 4468–4471.

[218] Y. Yuan, S. Wang, P. Wu, T. Yuan, X. Wang, Lignosulfonate in situ-modified reduced graphene oxide biosensors for the electrochemical detection of dopamine, *RSC Adv*. 12 (2022) 31083–31090.

[219] G. Zhou, C. Xu, W. Cheng, Q. Zhang, W. Nie, Effects of oxygen element and oxygen-containing functional groups on surface wettability of coal dust with various metamorphic degrees based on XPS experiment, *J. Anal. Methods Chem*. 2015 (2015) 467242.

[220] D.H. Jeon, Wettability in electrodes and its impact on the performance of lithium-ion batteries, *Energy Storage Mater*. 18 (2019) 139–147.

[221] J. Zhang, X.S. Zhao, Conducting polymers directly coated on reduced graphene oxide sheets as high-performance supercapacitor electrodes, *J. Phys. Chem. C*. 116 (2012) 5420–5426.

[222] P. Singh, S. Mandal, D. Roy, N. Chanda, Facile detection of blood creatinine using binary copper-iron oxide and rGO-based nanocomposite on 3D printed Ag-electrode under poc settings, *ACS Biomater. Sci. Eng*. 7 (2021) 3446–3458.

[223] A. Kousar, E. Peltola, T. Laurila, Nanostructured geometries strongly affect fouling of carbon electrodes, *ACS Omega*. 6 (2021) 26391–26403.

[224] J.Y. Lin, M.H. Chou, Y.C. Kuo, Rapid synthesis of tin oxide decorated carbon nanotube nanocomposities as anode materials for lithium-ion batteries, *J. Alloys Compd*. 589 (2014) 472–478.

[225] A. Lassoued, B. Dkhil, A. Gadri, S. Ammar, Control of the shape and size of iron oxide (α-Fe_2O_3) nanoparticles synthesized through the chemical precipitation method*, Results Phys.* 7 (2017) 3007–3015.

[226] A. Moyseowicz, A. Śliwak, E. Miniach, G. Gryglewicz, Polypyrrole/iron oxide/reduced graphene oxide ternary composite as a binderless electrode material with high cyclic stability for supercapacitors, *Compos. B Eng*. 109 (2017) 23–29.

[227] G.M. Neelgund, A. Oki, A facile method for the synthesis of polyaniline nanospheres and the effect of doping on their electrical conductivity, *Polym. Int*. 60 (2011) 1291–1295.

[228] T. Danno, D. Nakatsuka, Y. Kusano, H. Asaoka, M. Nakanishi, T. Fujii, Y. Ikeda, J. Takada, Crystal structure of β-Fe_2O_3 and topotactic phase transformation to α-Fe_2O_3, *Cryst. Growth Des*. 13 (2013) 770–774.

[229] A. Nafady, M.D. Albaqami, A.M. Alotaibi, CuO nanoparticles embedded in conductive PANI framework for periodic detection of alcohol from sweat, *Colloid Polym. Sci*. 301 (2023) 517-526.

[230] J. Li, M. Östling, Prevention of graphene restacking for performance boost of supercapacitors-a review, *Crystals* 3 (2013) 163–190.

[231] T. Yamashita, P. Hayes, Analysis of XPS spectra of Fe^{2+} and Fe^{3+} ions in oxide materials, *Appl Surf Sci*. 254 (2008) 2441–2449.

[232] K. Lee, S. Shin, T. Degen, W. Lee, Y.S. Yoon, In situ analysis of SnO_2/Fe_2O_3/RGO to unravel the structural collapse mechanism and enhanced electrical conductivity for lithium-ion batteries, *Nano Energy* 32 (2017) 397–407.

[233] C. Ma, J. Lee, Y. Kim, W. Cheol Seo, H. Jung, W. Yang, Rational design of α-Fe_2O_3 nanocubes supported $BiVO_4$ Z-scheme photocatalyst for photocatalytic degradation of antibiotic under visible light, *J. Colloid Interface Sci*. 581 (2021) 514–522.

[234] H. Wang, J. Lin, Z.X. Shen, Polyaniline (PANi) based electrode materials for energy storage and conversion, *J. Sci.: Adv. Mater. Dev*. 1 (2016) 225–255.

[235] M. Sajid, M.K. Nazal, M. Mansha, A. Alsharaa, S.M.S. Jillani, C. Basheer, Chemically modified electrodes for electrochemical detection of dopamine in the presence of uric acid and ascorbic acid: A review, *TrAC - Trends Anal. Chem*. 76 (2016) 15–29.

[236] N. Yusoff, Graphene–Polymer Modified Electrochemical Sensors, Graphene-Based Electrochemical Sensors for Biomolecules, *Elsevier* (2019) 155–186.

[237] Y.R. Kim, S. Bong, Y.J. Kang, Y. Yang, R.K. Mahajan, J.S. Kim, H. Kim, Electrochemical detection of dopamine in the presence of ascorbic acid using graphene modified electrodes, *Biosens. Bioelectron*. 25 (2010) 2366–2369.

[238] A. Celzard, J. F. Mareche, G. Furdin, F. Furdin, Surface area of compressed expanded graphite, *Carbon* 40 (2002) 2713-2718.

[239] E. Aliyev, V. Filiz, M.M. Khan, Y.J. Lee, C. Abetz, V. Abetz, Structural characterization of graphene oxide: surface functional groups and fractionated oxidative debris, *Nanomaterials* 9 (2019) 1180.

[240] H. Zhao, D. Zhao, J. Ye, P. Wang, M. Chai, Z. Li, Directional oxygen functionalization by defect in different metamorphic-grade coal-derived carbon materials for sodium storage, *Energy Environ. Mater*. 5 (2022) 313–320.

[241] D. Pantea, H. Darmstadt, S. Kaliaguine, L. Summchen, C. Roy, Electrical conductivity of thermal carbon blacks influence of surface chemistry, *Carbon* 39 (2001) 1147-1158.

10 Abstract

Nowadays, due to an increased awareness in the field of health state monitoring and environment protection, great research interest has been focused on the development of novel techniques for appropriate sensing of several analytes as neurotransmitters and pharmaceuticals. Electrochemical sensors appear as promising alternatives for currently applied methodologies as High-Performance Liquid Chromatography (HPLC) or spectroscopy techniques. The key element in achieving a suitable electrochemical sensing setup is the working electrode. Traditionally, non-modified working electrodes are characterized by weak current responses originated from redox processes of analytes of interest. One of the approaches to enhance recorded currents and resulting sensor working parameters is the development of novel and efficient active electrode materials. Moreover, great efforts have been focused on miniaturizing currently used setups, which would enable to test small sample volumes in real analysis time.

The aim of this work was develop and apply graphene-based materials and their composites as GCE modifiers, for electrochemical detection of dopamine (DA), ascorbic acid (AA), uric acid (UA) and diclofenac (DCF), which enable detection of above-mentioned analytes in low concentrations with high sensitivity. Three groups of materials based on reduced graphene oxide (RGO) were synthesized. The first group was based on nitrogen-doped RGO (NRGO) and its composites with gold nanoparticles (AuNPs/NRGO), the second group includes composites of thermally reduced RGO (TRGO) with polyaniline (PANI/TRGO), and the last group of materials covered binary and ternary RGO composites with iron and tin oxides and PANI (FSG and PFSG).

Synthesized composites and their components were thoroughly investigated using advanced analytical methods (FESEM, HRTEM, XPS, EA, N_2 sorption, XRD, sheet resistance measurements). The impact of the morphology and chemical composition of composites on the detection of above mentioned analytes using cyclic voltammetry (CV) and differential pulsed voltammetry (DPV) was defined, including determination of sensor working

parameters such as limit of detection (LOD), linear range (LR), sensitivity, selectivity and long-term stability.

Beneficial impact of nitrogen doping of the graphene material on the homogenous distribution of AuNPs and resulting electrochemical properties was revealed. Moreover, the amount of PANI in the PANI-TRGO composites was optimized and the impact of reduction temperature of TRGO on the PANI distribution was determined. |A synergistic effect between composite counterparts of PFSG was demonstrated. The most improved sensor working parameters in electrochemical DA detection were recorded on PFSG/GCE (LOD = 76 nM). The lowest LOD values in AA and UA detection were obtained for GCEs modified with AuNPs/NRGO (LOD = 44 μM) and FSG15:85 (LOD = 328 nM), respectively. Whereas, in simultaneous detection of DA, AA and UA, AuNPs/NRGO/GCE was the most effective. In case of DCF detection the lowest LOD was recorded on GCE modified with TRGO700 (LOD = 61 nM).

Moreover, a novel miniaturized setup using inkjet-printed electrodes for DCF detection was designed. Inkjet printed electrodes were prepared using graphene-based ink (GO) printed on Kapton® and then subsequently thermal reduction process was performed. The high effectiveness of reduction of GO on Kapton® was revealed.

The results of this thesis open a new line of research on novel electrochemical sensor based on modified graphene materials.

11 Streszczenie

Rosnąca świadomość społeczeństwa w aspekcie monitorowania stanu zdrowia i ochrony środowiska spowodowała znaczny wzrost zainteresowania nowoczesnymi technikami detekcji analitów z grupy neuroprzekaźników i farmaceutyków. Sensory elektrochemiczne są obiecującą alternatywą dla obecnie stosowanych technik analitycznych takich jak wysokosprawna chromatografia cieczowa (ang. High Performance Liquid Chromatography - HPLC) i techniki spektroskopowe. Głównym elementem sensora elektrochemicznego jest elektroda pracująca. Niemodyfikowana elektroda pracująca sensora elektrochemicznego charakteryzuje się słabą odpowiedzią prądową pochodzącą od wykrywanych analitów. Jednym z kierunków rozwoju prowadzących do wzmocnienia rejestrowanego sygnału, a tym samym do poprawy parametrów pracy sensorów elektrochemicznych, jest opracowanie nowoczesnych materiałów elektrodowych. Dodatkowo obiecującym kierunkiem badawczym jest

miniaturyzacja obecnie wykorzystywanych układów pomiarowych w celu testowania w czasie rzeczywistym próbek o małych objętościach.

Celem pracy było opracowanie i zastosowanie materiałów grafenowych i ich kompozytów do modyfikacji elektrod pracujących (GCE) sensorów elektrochemicznych dopaminy (DA), kwasu askorbinowego (AA), kwasu moczowego (UA) i diklofenaku (DCF), które umożliwią wykrycie wyżej wymienionych analitów w niskich stężeniach z wysoką czułością. W pracy zsyntezowano trzy grupy materiałów na bazie zredukowanego tlenku grafenu (RGO). Pierwsza z nich to domieszkowany azotem RGO (NRGO) i jego kompozyty z nanocząstkami złota (AuNPs/NRGO), druga grupa obejmuje kompozyty termicznie zredukowanego RGO (TRGO) z polyaniliną (PANI/TRGO), a trzecia grupa materiałów to dwuskładnikowe i trójskładnikowe kompozyty RGO z tlenkami żelaza i cyny oraz PANI (FSG i PFSG).

W badaniach stosowano szereg zaawansowanych technik analitycznych do charakteryzacji kompozytów i ich składników (FESEM, HRTEM, XPS, EA, sorpcja N_2, XRD, pomiary przewodnictwa elektrycznego). Określono wpływ morfologii i składu chemicznego kompozytów na detekcję wymienionych analitów z wykorzystaniem woltamperometrii cyklicznej (CV) i woltamperometrii pulsowo-różnicowej (DPV) wyznaczając takie parametry pracy czujnika jak limit detekcji (LD), zakres liniowej pracy (LR), czułość, selektywność i stabilność pracy.

W pracy wykazano korzystny wpływ domieszkowania materiału grafenowego azotem na homogeniczną dystrybucję AuNPs i na właściwości elektrochemiczne materiału. Zoptymalizowano ilość PANI w kompozytach PANI/TRGO i określono wpływ temperatury redukcji TRGO na jej dystrybucję. Przeprowadzone badania wskazują również na synergiczne działanie pomiędzy składnikami kompozytu PFSG mające korzystny wpływ na parametry pracy czujnika. Wykazano, że najlepsze parametry elektrochemicznej detekcji DA, w tym LD można uzyskać modyfikując elektrodę GCE materiałem PFSG (LD = 76 nM). Najniższe wartości LD w przypadku detekcji AA i UA uzyskano dla czujnika z elektrodą GCE modyfikowaną odpowiednio AuNPs/NRGO (LD = 44 μM) i FSG15:85 (LD = 328 nM). Natomiast w jednoczesnej detekcji DA, AA i UA najbardziej efektywny okazał się układ z elektrodą AuNPs/NRGO/GCE. Najniższy LD w detekcji DCF zarejestrowano dla elektrody GCE modyfikowanej TRGO700 (LD = 61 nM).

Zaprojektowano również zminiaturyzowany układ pomiarowy do detekcji DCF wykorzystujący elektrody przygotowane w oparciu o technologię inkjet-printed. Elektrody typu inkjet-printed przygotowano na bazie tuszu z tlenku grafenu (GO) nadrukowanego na

Kapton®, który następnie został poddany termicznej redukcji. Wykazano wysoką skuteczność procesu redukcji GO na Kaptonie®.

Prezentowane w pracy doktorskiej wyniki badań nadają nowy kierunek badaniom nad nowoczesnymi materiałami elektrodowymi sensorów elektrochemicznych wykorzystujących modyfikowane materiały grafenowe.

12 Scientific achievements

Scientific articles

1. **Daria Minta**, Zoraida González, Sonia Melendi-Espina, Grażyna Gryglewicz
   Easy-to-prepare graphene-based inkjet-printed electrodes for diclofenac electrochemical sensing.
   Progress in Organic Coatings 185:1-9, 2023 (IF = 6.206; MEiN = 100).
2. Thayset Mariño Peacok, Harold Crespo Sariol, Ángel Sánchez Roca, Jeamichel Puente Torres, Marian Rigñack Delgado, **Daria Minta**, Sofie Thijs, Liset Salomón García, Carleer Robert, Dries Vandamme, Peter Adriaensens
   Batch and dynamic acid regeneration evaluation of activated carbons used in water cleaning treatment system. A comparative study between advanced analytical methods and a new infra-red thermographic method.
   Journal of Environmental Chemical Engineering 11:1-15, 2023 (IF = 7.968; MEiN = 100).
3. Christophe Gueibe, Jos Rutten, Johan Camps, Dominique Moyaux, Wouter Schroeyers, Romano Plenteda, Nikolaus Hermanspahn, **Daria Minta**, Sonja Schreurs
   Xenon collection and separation from atmospheric air in silver-exchanged zeolites, activated carbon and metal-organic frameworks.
   Separation and Purification Technology 323:1-13, 2023 (IF = 9.136; MEiN = 140).
4. Adam K. Moyseowicz, **Daria Minta**, Grażyna Gryglewicz,
   Conductive polymer/graphene-based composites for next generation energy storage and sensing applications.
   ChemElectroChem 10:1-25, 2023 (IF = 4.782; MEiN = 100),
5. Katarzyna Gajewska, Adam K. Moyseowicz, **Daria Minta**, Grażyna Gryglewicz,
   Effect of electrolyte and carbon material on the electrochemical performance of high-voltage aqueous symmetric supercapacitors.
   Journal of Materials Science 58:1721-1738, 2023 (IF = 4.682; MEiN = 100), citations Scopus: 1,

6. Agata K. Moyseowicz, Zoraida González, Sonia Melendi-Espina, Beatriz Acevedo, Georgeta Predeanu, Sorin M. Axinte, Juan J. Fernandez, Marcos Granda, **Daria Minta**, Adam Moyseowicz, Grażyna Gryglewicz,
   Hydrothermal nitrogen doping of anthracene oil-derived activated carbons for wide voltage asymmetric capacitors.
   Journal of Energy Storage 60:1-9, 2023 (IF = 8.907; MEiN = 100).
7. **Daria Minta**, Zoraida González, Sonia Melendi-Espina, Grażyna Gryglewicz,
   Highly efficient and stable PANI/TRGO nanocomposites as active materials for electrochemical detection of dopamine.
   Surfaces and Interfaces 28:1-10, 2022 (IF = 6.137; MEiN = 70), citations Web of Science: 7, Scopus: 8,
8. **Daria Minta**, Adam K. Moyseowicz, Stanisław Gryglewicz, Grażyna Gryglewicz,
   A promising electrochemical platform for dopamine and uric acid detection based on a polyaniline/iron oxide-tin oxide/reduced graphene oxide ternary composite.
   Molecules 25:1-18, 2020 (IF = 4.412; MEiN = 140), citations Web of Science: 17, Scopus: 19,
9. **Daria Minta**, Zoraida González, Piotr Wiench, Stanisław Gryglewicz, Grażyna Gryglewicz, *N-doped reduced graphene oxide/gold nanoparticles composite as an improved sensing platform for simultaneous detection of dopamine, ascorbic acid, and uric acid.*
   Sensors 20:1-13, 2020 (IF = 3.576; MEiN = 100), citations Web of Science: 14, Scopus: 16,
10. **Daria Minta**, Piotr Wiench, Grażyna Gryglewicz,
    Enhanced performance of GCE/N-reduced graphene oxide-Au nanocomposite in dopamine sensing.
    Proceedings 15:1-4, 2019.

Conferences

1. **Daria Minta,** Zoraida González, Sonia Melendi-Espina, Grażyna Gryglewicz
   Graphene-based inkjet-printed electrodes as disposable electrochemical platforms for diclofenac sensing
   CESEP2023, 24-28 September 2023, Budapest, poster.
2. Christophe Gueibe, Jos Rutten, Johan Camps, Dominique Moyaux, Wouter Schroeyers, Romano Plenteda, Nikolaus Hermanspahn, **Daria Minta**, Sonja Schreurs

Unprecedented xenon collection and separation from air on silver-exchanged zeolites
ENVIRA 2023, 17-22 September 2023, Sevilla.

3. Zoraida González, **Daria Minta**, Lucía Quintana, Victoria Rocha, Grażyna Gryglewicz, Rosa Menéndez
   Nanocarbons as active electrode materials in novel electrochemical sensors for water emerging contaminants detection.
   Carbon2023, Cancun, 16-21 July 2023.
4. **Daria Minta**, Zoraida González, Grażyna Gryglewicz
   Graphene-based composites for the electrochemical detection of neurotransmitters. Interdisciplinary Doctoral Symposium: Rajd Doktoranta 2023, Przesieka, 12-14 May 2023, oral presentation.
5. **Daria Minta**, Zoraida González, Sonia Melendi-Espina, Grażyna Gryglewicz
   Thermally reduced graphene oxide and polyaniline composites for electrochemical dopamine detection.
   III Warsztaty Naukowe Polskiego Towarzystwa Węglowego "Nowe trendy w nauce o węglu", Kraków, 24 czerwca 2022, oral presentation.
6. **Daria Minta**, Zoraida González, Grażyna Gryglewicz
   Facile and efficient carbon nanotubes-based electrodes in diclofenac electrochemical detection.
   XIV Konferencja Naukowo-Techniczna: 18-21 października 2022, Ustroń, poster.
7. Grażyna Gryglewicz, Piotr Gauden, Jochen Settelein, Begüm Bozkaya, Sylwester Furmaniak, **Daria Minta**, Adam K. Moyseowicz
   Water adsorption isotherms - hysteresis loops – porosity.
   Materiały węglowe i kompozyty polimerowe: nauka - przemysł' 2022: XIV Konferencja Naukowo-Techniczna: 18-21 października 2022, Ustroń-Jaszowiec.
8. **Daria Minta**, Zoraida González, Adam K. Moyseowicz, Grażyna Gryglewicz
   Wpływ metody otrzymywania nanokompozytów polianiliny i zredukowanego tlenku grafenu na elektrochemiczną detekcję dopaminy.
   63. Zjazd Naukowy Polskiego Towarzystwa Chemicznego, Łódź, 13-17 września 2021, poster.
9. **Daria Minta**, Adam K. Moyseowicz, Zoraida González, Grażyna Gryglewicz
   Wpływ domieszkowania materiałów grafenowych polimerami przewodzącymi i nanocząstkami metali i tlenków metali na detekcję dopaminy.

XIII Konferencja Naukowo-Techniczna: 23-26 listopada 2021, Ustroń-Jaszowiec, oral presentation.

10. Adam K. Moyseowicz, **Daria Minta**, Agata K. Moyseowicz
    Właściwości i charakterystyka elektrochemiczna kompozytów siarczku żelaza z węglem aktywnym.
    XIII Konferencja Naukowo-Techniczna: 23-26 listopada 2021, Ustroń-Jaszowiec.
11. **Daria Minta**, Zoraida González, Adam K. Moyseowicz, Grażyna Gryglewicz: *Polyaniline/thermally reduced graphene oxide nanocomposites for DA sensing.*
    Current Trends in Electrochemistry: 41st Meeting of the Electrochemisty Group of the Spanish Royal Society of Chemistry: 1st French-Spanish Atelier/Workshop on Electrochemistry, 6th July - 9th July 2021, Paris, multimedia poster (short presentation).
12. **Daria Minta,** Adam K. Moyseowicz, Zoraida González, Grażyna Gryglewicz
    Enhanced Performance of ternary polyaniline/iron oxide-tin oxide/reduced graphene oxide composites for dopamine and uric acid detection.
    ANM2021 Conference (session: Advanced Graphene Materials), 22-24 July 2021, Aveiro., oral presentation.
13. **Daria Minta**, Grażyna Gryglewicz
    Elektrochemiczna detekcja dopaminy z wykorzystaniem materiałów grafenowych i ich kompozytów z nanocząstkami złota.
    XIV Wrocławskie Sympozjum Chemiczne, 18-19.05.2019, Wrocław., oral presentation.
14. **Daria Minta,** Katarzyna Chomiak, Grażyna Gryglewicz
    Magazynowanie wodoru na węglach aktywnych z surowca lignocelulozowego.
    Ogólnopolska Konferencja Technologii Chemicznej i Biotechnologii KonTeCh, 9-10.06.2018, Wrocław., poster.

Research Internships

1. **04.04. – 07.06.2022** – scientific internship in the Institute of Carbon Science and Technology (INCAR), CSIC, Oviedo (Spain), internship financed from ERASMUS+ program.
   Tittle of an internship: „*Inkjet-printed electrodes based on graphene materials as working electrodes of electrochemical diclofenac sensor”.*
2. **15.09. – 11.12.2020** – scientific internship in the Institute of Carbon Science and Technology (INCAR), CSIC, Oviedo (Spain), internship financed from ERASMUS+ program.

Tittle of an internship: *„Testing of graphene-based composites as dopamine electrochemical sensors”.*

Participation in research projects

1. *ZABAT – Next generation rechargeable and sustainable zinc-air batteries*, NCN M-ERA.NET 3, member of consortium prof. Grażyna Gryglewicz.
2. *Investigations of the effect of carbon surface functional groups on electrochemical behavior of lead-carbon electrodes,* joint project with Fraunhofer Institute for Silicate Research ISC, Consortium for Battery Innovation (CBI), leader prof. Grażyna Gryglewicz.
3. *Kompozyty siarczków metali z nanostrukturalnymi materiałami węglowymi do zastosowania w superkondensatorze*, SONATA NCN, leader dr. Agata Moyseowicz.